UNIVERSITY OF SOUTHAMPTON

Radio Spectral Properties of Faint Source Populations

Derek Moss

Submitted for the degree of Doctor of Philosophy

SCHOOL OF PHYSICS AND ASTRONOMY
FACULTY OF SCIENCE

March 17, 2008

UNIVERSITY OF SOUTHAMPTON

ABSTRACT

FACULTY OF SCIENCE

SCHOOL OF PHYSICS AND ASTRONOMY

Doctor of Philosophy

Radio Spectral Properties of Faint Source Populations

by Derek Moss

In this thesis, the radio spectral properties of the faint sources in two deep extragalactic radio survey areas are investigated to aid in the discrimination between AGN and starbursts.

The detailed 4–point radio spectra of two X-ray bright, optically quiescent sources in the 13^H XMM/*Newton*/*Chandra* survey area are measured, and found to be flat in one case, and steep ($\alpha \sim -0.6$) in another.

Deep imaging of both the 13^H and 1^H XMM/*Newton*/*Chandra* survey fields at 610 MHz with the GMRT are presented. To detection limits of ~320 and 300μJy beam^{-1}, 206 and 223 sources are discovered in the 13^H and 1^H fields respectively.

A deep 1.4 GHz survey of the 1^H field is performed with the VLA. To a detection limit of 45 μJy, 432 sources are discovered.

The source counts at both 610 MHz and 1.4 GHz agree with those in other deep fields, and can both be fit with similar models consisting of standard AGN source count models combined with a population of steep spectrum ($\alpha = -0.7$) starburst galaxies undergoing power law evolution with an index of 2.5 and 2.6 at 1.4 GHz and 610 MHz respectively.

The catalogues of these three surveys are combined with the results of an earlier deep 1.4 GHz survey of the 13^H field to calculate useful radio spectral indices for 192 faint radio sources. Assuming that starburst galaxies exhibit spectra within $-1 < \alpha < -0.4$; 83 sources can be identified as AGN on radio spectral grounds.

Contents

List of Figures

List of Tables

Acknowledgements

This work is the sum of the efforts of many people. Along with the reduction of data used herein, discussion of the principles and techniques involved has encompassed a wide menagerie. I'd like to thank my supervisor, Ian M^{c}Hardy, for his kind and skilled introduction to radio astronomy, his sage wisdom, his boundless enthusiasm, and his determination to offer tea and coffee.

Nick Seymour, as any who have read this all the way through will realise, was a key contributor, both in providing the work that forms the foundation for these radio surveys and for his frequent and useful discussions on all matters AIPS, radio and cricket. Katherine Gunn also helped enormously in the early days, and more recently, Tom Dwelly has provided insightful comments and advice. Thanks also to Mat Page, and Nic Loaring.

I would also like to thank the Particle Physics and Astronomy Reasearch council for the funding which made this richly interesting and enjoyable work possible, and the staff of the GMRT who were wonderfully friendly and helpful.

Simon Harris, the computer support chap for the astronomy group requires special thanks. To complete the Southampton acknowledgments, the Andy's Witham and Barnes need thanking for tolerating me and my constant humming, clicking and being quiet, and for sharing plentiful laughs.

Thanks also to my colleges of a Purbeckian nature, for providing innumerable fits of giggles, and a suitably shambacerack vocabulary.

Many thanks go to Ronni, the best use the universe has ever put a pile of carbon to.

Most of all, many tanks to my family, especially Mum and Dad, Linds and Gran. This is for you. Pay attention, there will be a quiz later.....

Derek Moss, 2007

Chapter 1

Introduction

In this first chapter, I offer an introduction to extragalactic taxonomy, and the motivation behind deep surveys. A brief history of radio astronomy is then given. The basics of radio interferometry are discussed, and the state of deep radio surveys reviewed. The two extragalactic survey fields studied herein are introduced, and the long term science goals of the extended project presented.

1.1 Introduction

This thesis is concerned with the understanding the faint radio population of the universe, as seen in deep surveys. It is concerned with understanding the origin of radio emission, particularly from AGN and starburst galaxies, and distinguishing between those two classes of object using a variety of radio, IR and X-ray diagnostics. In order to provide a suitable background to this subject, this chapter begins with an introduction to extragalactic taxonomy, providing a grounding in the terminology and phenomenology met throughout later chapters.

To place this study within its context, a fuller discussion of the motivation behind deep surveys, and radio surveys in particular, then follows. The degree to which the following chapters rely on the techniques and complexities of radio astronomy also motivate a brief history of radio astronomy which is then given along with an introduction to the concept of radio interferometry and aperture synthesis.

1.2 Taxonomy of Extragalactic Sources

Most galaxies are detected in the optical region of the electromagnetic spectrum via the thermal radiation emitted by their constituent stars. This spectral component peaks in the near infrared (NIR) at around 1μm for most stellar populations. Other spectral components provide information about other properties of the host galaxy. Dust emits in the mid infrared (MIR), and stellar accretion processes can emit in the ultraviolet, X-ray and sometimes radio.

1.2.1 AGN

Many galaxies have been found to emit in a manner that implies the existence of a source of radiation other than the stars, dust, and binary systems that constitute normal stellar populations. Now known as Active Galactic Nuclei (AGN), these sources of non-stellar radiation can be seen to emit across the electromagnetic spectrum from from the radio to gamma rays, and go by a number of names, which are often more closely related to the method of their discovery than any physical properties they portray. The following is a brief taxonomy of the types of AGN.

1.2.1.1 Seyferts

In the 1940's Carl Seyfert had noticed (Seyfert 1943) that the central point-like excess seen in some spiral galaxies (see Fig. 1.1) showed broad emission lines. It was eventually noticed that the spectra of the cores of these Seyfert galaxies could be broadly classified into one of two types (Khachikian & Weedman 1974). Both contained narrow emission features (widths of several hundreds of kilometres per second) of both forbidden and permitted atomic transitions (e.g. OIII, NeIII) - implying low densities, as required to avoid collisional de-excitation. Some also contained broad emission lines of Hα, Hβ, Hγ, and Hδ with widths implying velocities of up to 10^4km s^{-1}. The spectra that contained both sets of lines are known as Seyfert 1's, whilst those only exhibiting narrow lines are known as Seyfert 2's. The spectrum of a typical example of a Seyfert 1, with both sets of lines, can be seen in Fig 1.2.

1.2.1.2 Quasars

First noted as point-like optical counterparts to sources in the first radio surveys (Matthews & Sandage 1963), Quasi-Stellar Objects (QSOs, or quasars) were found

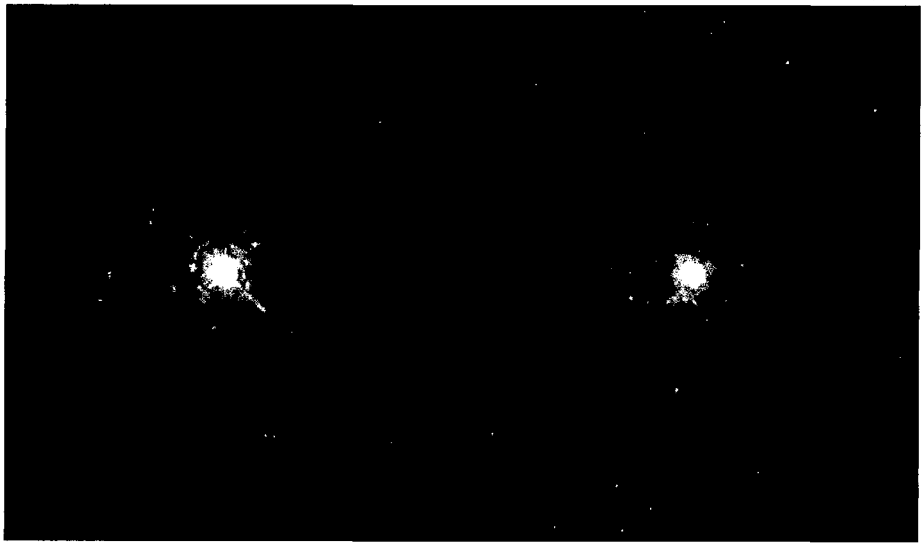

Figure 1.1: a) The optical morphology of the Seyfert 1 galaxy NGC5548. b) The optical morphology of the quiescent galaxy NGC3277.

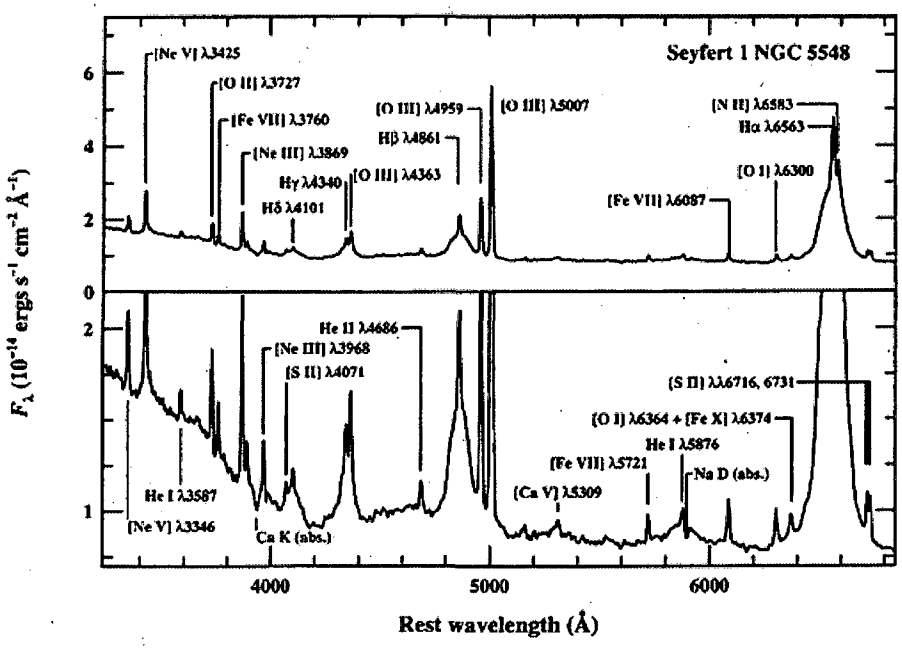

Figure 1.2: The optical spectrum of the Seyfert 1 galaxy NGC5548 (from Peterson 1997).

to have broad emission lines in the optical, which initially puzzled observers. It was eventually realised (Schmidt 1963) that the emission spectra were of standard atomic transitions, though at very high redshifts. The implied luminosities made quasars the brightest known non-transient objects. As methods for selecting them in other wavebands became better understood, it became clear that the majority of quasars did not emit in the radio, leading to the labels of Radio Loud QSO and Radio Quiet QSO.

1.2.1.3 Radio Galaxies

Many radio sources are discovered to lie in giant elliptical galaxies, and show extension on the sky from the central optical source. The radio emission is considered to be synchrotron radiation from electrons spiralling in the magnetic fields of jets that protrude from the centre of the optical galaxy into the surrounding medium. The optical spectra of the host galaxies often exhibit broad and/or narrow emission lines and as such they can be referred to as Broad Line Radio Galaxies (BLRGs) or Narrow Line Radio Galaxies (NLRGs).

Fanaroff and Riley (1974) studied the radio morphology and radio luminosity of these sources in depth, and concluded that they fall broadly into 2 types, which are labelled FRI and FRII.

The less luminous of the the two types, Fanaroff-Riley Type I (FRI) sources are dominated by emission closer to the centre of the optical galaxy, which tapers away to the extremities.

The emission from FRII sources is dominated by the ends of the jets furthest from central galaxy and is, in total, more luminous than that shown by FRI's. The cut-off in luminosity is taken to be $L_{1.4\ GHz} = 10^{32}$ erg s^{-1} Hz^{-1} (Bridle and Perley 1984). These hot spots are shocks formed as the material in the jet collides with the surrounding medium (intra-cluster gas).

1.2.1.4 Blazars

The object designated BL Lac - which was originally thought to be a variable star, hence the designation - is a variable point source of radio, infrared and optical radiation. When a detailed spectrum was acquired, it became apparent that BL Lac was extragalactic. The timescale of its variability and simple energetic arguments imply that the power source is small, and very massive. Several objects have been found with similar properties.

Optically Violent Variables (OVV) are less powerful, and along with the BL Lac objects make up the class of objects known as blazars.

1.2.1.5 XBONGs

Discovered in numbers in the first deep *Chandra* surveys, X-ray Bright, Optically Normal Galaxies (XBONGs) are luminous X-ray sources with X-ray spectra that are not dissimilar to quasars, but which exhibit the optical spectra of standard galaxies, that of stars and stellar absorption only. (e.g. Hornschemeier et al. 2001; M^{c}Hardy et al. 2003).

1.2.1.6 Unification - AGN

The current standard paradigm (Antonucci et al. 1993; Urry and Padovani 1995) is that all of the above are the result of a central supermassive black hole (SMBH) of mass $\sim 10^6$ to 10^9 solar masses, and are generically known as Active Galactic Nuclei (AGN). A central engine, comprising of a SMBH surrounded by an accretion disk, is surrounded by a torus of obscuring dust, as shown in Fig. 1.3. Situated near the disk, clouds of dense, fast moving gas are responsible for the broad emission lines seen in quasar and Seyfert 1 galaxies, and are known as the Broad Line Region (BLR). Further from the disk, sparse clouds of gas are responsible for the narrow emission lines in Seyfert 2 spectra, and are called Narrow Line Regions (NLR).

The only intrinsic variables that change from object to object are the luminosity of the central engine, and the presence or lack of jets. Orientation accounts for the remaining disparity in observed properties.

To illustrate the point, under this paradigm, a Seyfert 1 is a low luminosity counterpart of a radio quiet quasar. Both are viewed from a similar position, as indicated by the directions labelled *Sey 1* and *Radio Quiet QSO* in Fig. 1.3, so that both the broad and narrow line regions can be seen without obscuration by the torus. In the radio loud (either FRI or FRII) case, an AGN viewed from this direction would be appear to be a BLRG or radio loud QSO.

Similarly, a Seyfert 2 is a low luminosity, radio quiet version of an FRI or NLRG. Both are viewed from a similar direction with respect to the obscuring material (as shown by the *Sey 2* and *NLRG* labels in Fig. 1.3) such that the emission from the BLR is prevented from reaching the observer. A blazar is an AGN with a jet, viewed down the axis of the jet, as illustrated by the *BL Lac* and *OVV* labels in Fig. 1.3. FRI's and FRII's are therefore the parent population of blazars, but viewed from

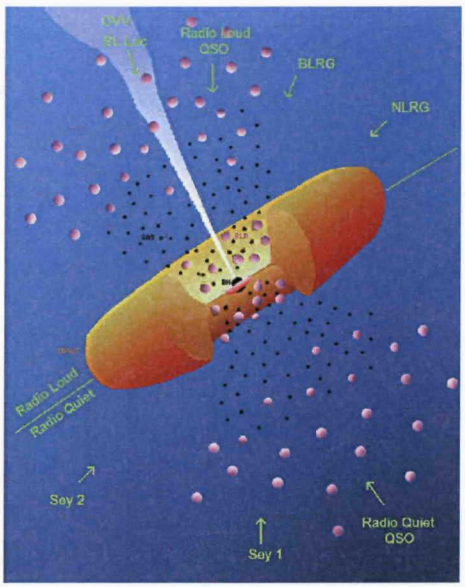

Figure 1.3: A cartoon representation of the standard unification model, adapted by M. Polletta from fig. 1 of Urry and Padovani (1995). The directions from which we are viewing this standard configuration when we observe the various types of AGN are illustrated.

the same position as a Seyfert 2 or NLRG.

This simple picture leads to a basic classification of any AGN into Type 1, where no obscuration is present, or Type 2 where some of the standard components are obscured. While there exist many objects which cannot easily be reconciled with this simple model it does provide a useful framework in which to consider the AGN phenomenon.

1.2.1.7 AGN SEDs

Armed with the simple standard model for AGN, it is possible to construct a library of possible Spectral Energy Distributions (SEDs).

The broadband spectrum of the emission from stars is merely a superposition of the thermal spectra of each star, and peaks in the near infrared. The emission from an accretion disk is also the superposition of many thermal spectra - those of differing positions in the disk and therefore differing temperatures. For AGN this is centred in the blue/UV part of the spectrum. X-ray emission from AGN generally have power-law spectra and is hypothesised to be from a corona of hot electrons surrounding the inner regions of the accretion disk. These hot electrons Compton scatter the thermal photons from the accretion disk into the X-ray range.

The energy absorbed from the AGN in both the X-ray and the UV/optical is re-emitted by the obscuring material in the infrared.The AGN that show signs of having jets emanating from them (FRI, FRII, radio galaxies, Blazars, radio loud quasars) emit in the radio via synchrotron emission, from electrons spiralling the the magnetic fields required to collimate the jets. This synchrotron emission can extend all the way to the X-ray and beyond, but the power-law shape of its spectrum means that it is outshone by other components of the host galaxy at frequencies above that of the radio. The exception to this is the case of a blazar, where the large velocities of the emitting material along the line of sight cause Doppler boosting of the radiation and the synchrotron component can dominate across the spectrum. Indeed Compton scattering of the synchrotron photons off the emitting high energy electrons can lead to jets emitting into the hard γ-ray band. For more details of the physics and observed phenomena of synchrotron spectra, see Section 1.7.

The relative contribution of the stars and AGN components can vary almost arbitrarily from galaxy to galaxy as the luminosity of the AGN changes. This is illustrated by the difference between the point like radio quiet quasars and Type 1 Seyfert galaxies, which are believed to both be similarly composed and viewed from similar angles within the standard paradigm. As mentioned above, the synchrotron component can also vary relative to the other components from system to system, as the viewing angle changes.

1.2.2 Other Non-Thermal Sources

Other non-transient objects emit radiation not from standard stellar processes. For example, the gas trapped in the gravitational well of groups and clusters of galaxies emits X-rays via bremsstrahlung radiation, but its comparison with optical images can confirm its non-galactic origin. In another example, the hyperfine transition of hydrogen at 21cm means that sparse neutral gas emits in the radio.

1.2.2.1 Star Formation

A source of non-thermal radiation that originates within a host galaxy is star formation. The star formation process requires reservoirs of fuel (gas), and a triggering mechanism. Once these are supplied (e.g. by galaxy mergers or AGN outflow), stars can form. The most massive stars are the most luminous, and shortest lived, and can form high-mass X-ray binaries (where X-ray emission is produced by accretion). These massive stars evolve, and explode, leaving supernova remnants (SNRs), which

emit in the radio. Hence, a burst of star formation will lead to a galaxy becoming brighter than normal in the X-ray and the radio. The young, hot stars also heat any dust in the region, increasing the mid IR emission relative to a quiescent galaxy.

1.3 Deep Surveys: Introduction to Cosmology and Current Motivations

An in-depth introduction to cosmology is beyond the scope of this work. See Bothun (1998), Peacock (1998), and Rowan-Robinson (2000) for introductions to the field.

In brief, the universe is currently believed to have expanded out of a singularity approximately 13.5 billion years ago. The early expansion saw a number of phase transitions of the constituent energy, matter and the space in which it resided, and was driven by a period of inflation.

Quantum fluctuations in the early universe lead to over densities which collapsed to form the structures that we see today. While the temperature was such that baryonic matter was still supported by radiation pressure, only dark matter (which doesn't interact with radiation) could collapse. Once the average temperature of the universe dropped below that required to ionise hydrogen, matter formed neutral atoms and decoupled from the radiation. This radiation went on to form the Cosmic Microwave Background, while the baryonic matter was now free to collapse into the dark matter halos.

As matter collapsed into over densities, stars, galaxies, and groups and clusters of galaxies were formed. In the bottom-up scenario (e.g. Searle and Zinn 1978), the smallest components (the globular clusters) formed first, and hierarchically merged to form larger and larger structures.

The universe continued to expand, while slowing under its own self gravity. At some later point, the expansion began accelerating. It is theorised that a cosmically ubiquitous fluid with a negative pressure became the dominant energy in the universe at that point as the mass energy became diluted by expansion. This 'dark energy' provides for an expansion of space-time, and hence drives the acceleration of the universal expansion. The exact equation of state of dark energy and precise parameters of the acceleration are the motivation behind many ongoing deep survey research efforts, as they have key effects upon structure formation.

The spectra of high redshift ($z \sim 6$) quasars contain large absorption features which are not seen in the spectra of lower redshift quasars. These features imply

that large quantities of neutral hydrogen purveyed inter galactic space at early times, and then became re-ionised (Gunn and Peterson 1965). The source of the ionising radiation that was responsible for the re-ionising of the universe is currently a matter of intense interest. Both star and AGN activity have the potential to perform the required re-ionisation. Currently a large amount of effort is being invested in both theoretical and observational exploration of this issue. To predict the amount of potential ionising radiation provided by both AGN and stars at the time of re-ionisation, both the accretion history and the star formation history of the universe need to be studied and accurately quantified.

In conclusion, the cosmic history of both accretion and star formation can offer insights into both re-ionisation and, through their tracing of structure formation, cosmological physics.

1.3.1 Accretion History

The accretion history of universe is one of the motivations behind deep X-ray surveys. X-rays are a good waveband in which to select AGN without bias, and large samples over a wide spread in redshift allow the evolution of the AGN luminosity function to be measured (e.g. Ueda et al. 2003). Modelling of the X-ray colours of the detected AGN with respect to the spectrum of the Cosmic X-ray Background (CXB) also provides some information about the AGN luminosity evolution (see e.g. Dwelly et al. 2005), as well as helping to discern the nature of the CXB.

1.3.2 Star Formation History

Massive stars emit in the ultraviolet and therefore are the stars most likely to be responsible for re-ionisation. They are also the shortest lived, and so star formation rate is a good indicator of the ionising ability of stellar populations.

The star formation history was studied in depth by Lilly et al. (1996) and Madau et al. (1996). The star formation rate density rises sharply with redshift, as seen in Fig. 1.4. The data used to construct Fig. 1.4 are based on observations at a variety of wavelengths (Hopkins et al. 2004). UV observations probe the hottest and therefore most massive and short lived stars, and so can provide measurements of the star formation rate in a galaxy. The rest frame UV passes into the optical band with increasing redshift. However, assumptions need to be made about dust obscuration, and the corrections required to account for it.

The luminosity of a galaxy in Hα can also be used to measure its star formation

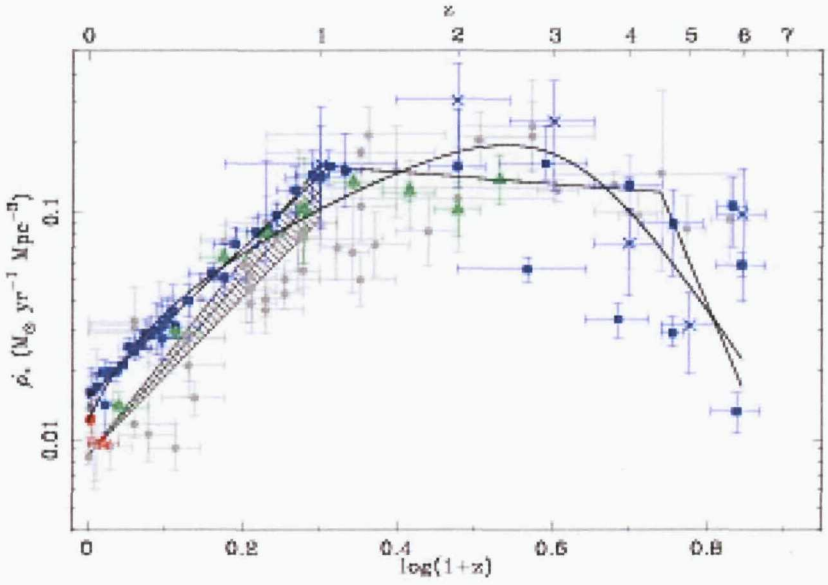

Figure 1.4: The evolution of the star formation rate density. A compilation of measurements taken from Hopkins et al. (2004).

rate, but is again subject to biases in both sample selection and correction factors. Fitting the broad band SEDs of galaxies can, along with stellar population modelling, give measurements of star formation rate - young stars are hot, and so skew the cumulative colour of the stellar population to the blue.

Current deep optical surveys (e.g. Bouwens et al. 2006) are beginning to study the star formation rate out to redshift of ~5–6, and may soon be able to probe the era of re-ionisation.

The star formation history is also important in terms of the study of structure formation. When did the majority of stars form? Where did they form? In large or small galaxies? What triggers star formation? Recent evidence (Juneau et al. 2005; Zheng et al. 2007) seems to indicate that the peak of the star formation rate density seems to shift from high mass galaxies at a redshift of ~2 to smaller galaxies at the present epoch. Known as 'down-sizing', this seems to contradict the hierarchical merging that is the standard model of structure formation.

1.3.3 Other Motivations

Another interesting facet of structure formation is the discovery of high redshift radio galaxies. Radio galaxies are hosted by the most massive elliptical galaxies at most epochs, so their discovery at very high redshifts ($z > 3$) provide tantalising

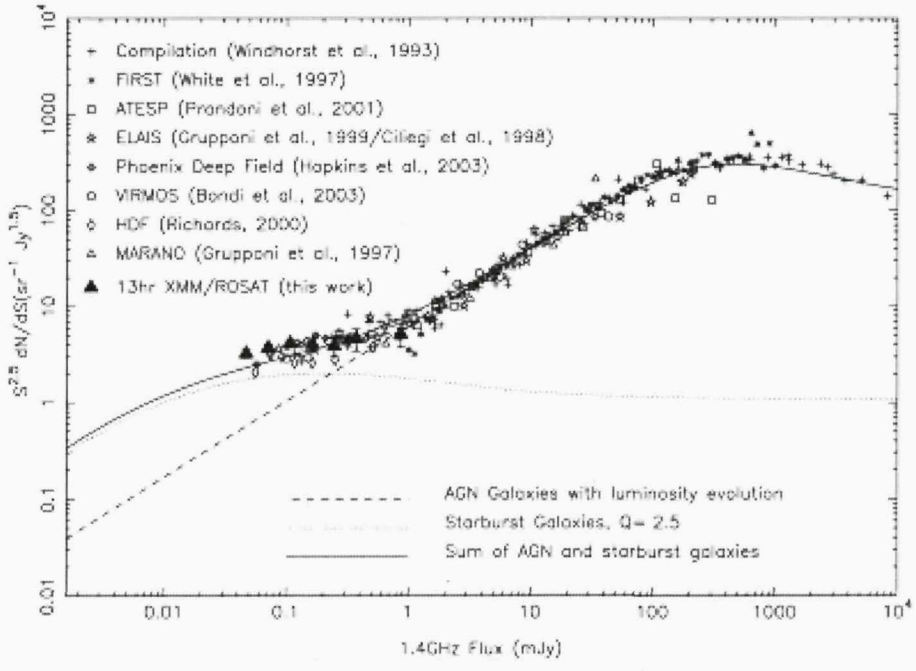

Figure 1.5: The Euclidean normalised differential source counts at 1.4 GHz. This figure is taken from Seymour et al. (2004). The origins of the data are shown in the legend.

clues about the merging rate and early structure formation history (e.g. De Breuck et al. 2004).

One motivation that drives all deep surveys is the discovery of new phenomena. New classes of object, new extreme examples of known classes, objects detected in new wavelength ranges, and entirely new populations are all of scientific interest. One such unexpected population was discovered as radio surveys achieved detection limit of below ∼1 mJy (e.g. Condon 1984). Above ∼1mJy the 1.4 GHz differential source counts can be well modelled by a single population of AGN undergoing luminosity evolution.

Below ∼1mJy, there is an upturn in the Euclidean normalised counts (e.g. Condon 1989). This upturn, shown in Fig. 1.5, has been attributed to the emergence of a new population of radio emitting objects. One suggestion is that this population consists of sources where the radio emission is dominated by star formation (e.g. Condon 1989; Benn et al. 1993; Rowan-Robinson et al. 1993; Hopkins et al. 1998).

Electrons accelerated by supernova remnants (SNRs) and spiralling in galactic magnetic fields emit synchrotron radiation in the radio waveband. Since only the most massive - and therefore shortest lived - stars explode in supernova explosions,

detectable radio emission from distant galaxies without AGN indicates a burst of recent star formation.

1.4 Radio Astronomy

1.4.1 History

The discipline of radio astronomy was in its infancy in the early years of the 20th Century. Since Maxwell had formulated his equations describing the behaviour of electromagnetic radiation, people had attempted to detect signals in radio band from astronomical sources. Technological limitations and high backgrounds limited any success until the work of Karl Jansky. Working at the Bell telephone laboratories, Janksy was investigating the sources of interference in communication. He discovered three main sources: local thunderstorms, distant thunderstorms, and a mysterious third source which he could not initially identify. Eventually the fact that the interference was variable, and began 4 minutes later every day lead him to conclude that its source was outside solar system, allowing its identification with the galactic centre (Jansky 1933). Karl Janksy's achievements were later held in such high regard that the unit of flux density (the janksy, abbreviated to Jy, and equal to 10^{-26} $\mathrm{Wm^{-2}Hz^{-1}}$) was named after him.

The next development came when Grote Reber built a steerable reflector and mapped the sky at radio wavelengths.

The advent of the Second World War delayed further developments in radio astronomy but pushed technological innovation in the area, with the demand for better radar and communications capabilities. At the cessation of hostilities, several of the scientists who had been working on these technologies moved into academia and turned their attention to the sky.

In 1944, van de Hulst calculated that the hyper fine hydrogen spin-flip transition line lay at at 21cm. This knowledge, along with the fact that radiation at this wavelength suffers little absorption, allowed the tracing of the motion of the gas within the Milky Way, and a mapping of its spiral arms. Rotation maps of the gas in other other galaxies also became possible, often extending to greater radii than those available at other wavelengths, and allowed the discovery of further evidence for the existence of dark matter.

Soon, the lack of resolution afforded by radio dishes, relative to that offered by shorter wavelengths, lead to the development of interferometers, the operation of

which is addressed in the following section.

Another phenomenon discovered as radio detectors improved were pulsars. First noticed in 1967 (Hewish et al. 1968), they emit regular radio pulses, and are believed to be beamed radiation from neutron stars.

1.4.2 Interferometry

The diffraction limited resolution of a telescope is proportional to λ/D where λ is the wavelength of the radiation, and D is the diameter of the aperture. Hence, imaging at longer wavelengths requires larger apertures. For example, for the Subaru optical telescope operating in the B band, $\lambda \sim 450$nm, and D=8.2m, the diffraction limited resolution is therefore 0.02 arcsec. In actuality, the resolution is limited by atmospheric seeing to $\sim$0.5 arcsec. To achieve a similar resolution at 1.4 GHz, an aperture of $\sim$ 100 km is required, which is not feasible from either an engineering or a financial point of view. The practical resolution of this problem became apparent in the late 1940s with pioneering work in Cambridge and Sydney (Ryle & Vonberg 1946, and observations by Pawsey). By combining the signals from two radio dishes, it is possible to synthesise the resolving power of a single aperture with an effective diameter equal to the separation between the two dishes. The signals from the two antennas are fed to a correlator, where one is multiplied by the complex conjugate of the other. Real signals correlate and are amplified by the multiplication, while noise is averaged out. Essentially, the correlation is the measure the coherence of the electromagnetic field over large areas, and represents a sinusoidal wave of sensitivity to real sources on the sky (a fringe).

Baselines (pair of antennas) of differing lengths sample different spatial scales, and as the Earth rotates and carries the antennas around a plane with respect to the target source, that scale is sampled in different directions on the sky. Modern interferometer arrays attempt to sample this plane, known as the *uv* plane, as densely as possible. Longer baselines provide higher resolution. However, the small spatial scales sampled by longer baselines can become insensitive to extended spatial structure relative to shorter baselines. Since each baseline is sensitive to emission within a sinusoidal pattern across the sky, only sources with sizes far smaller than the spatial wavelength of this sensitivity fringe will invoke the response of the interferometer that accurately represents their true flux. Once source sizes are a sizable fraction of a sensitivity fringe wavelength, the baseline which generates that fringe records a lower than ideal response as it is not fully sensitive to all the emission from

the source. For this reason, interferometer arrays include short baselines to retain sensitivity to extended emission.

The spatial scale sampled is actually that of the baseline projection onto a plane perpendicular to the direction to the source. Since the antennas that constitute each baseline are fixed to the surface of the Earth, this projection varies with hour angle, and delays need to be added to the signal of one antenna to effectively move it into the perpendicular plane.

Further introduction into the use of interferometers will be given in Chapter 2.

1.4.3 Modern Interferometers

There are many functioning interferometric arrays. They vary in location, element aperture size, array configuration, maximum baseline and sensitivity. Details on a selection of the interferometers relevant to this study, and to work similar to it, are given below.

1.4.3.1 VLA

Inaugurated in 1980, the Very Large Array (VLA) is operated by the National Radio Astronomy Observatory (NRAO). Situated in the Plains of San Augustin near Socorro, New Mexico, it comprises of 27 antennas each of 25 m diameter, operating from 74 MHz to 48 GHz. The antennas are placed in the shape of a "Y" and can be moved along tracks to alter the array configuration, changing the baseline lengths. The A-array is the widest spread configuration with maximum baselines of up to 36 km. As the array configuration names progress through the alphabet from A through to D, the antennas are more closely spaced, offering lower resolution, but higher sensitivity to extended emission.

1.4.3.2 ATCA

Originally a purely linear East-West array, the Australian Telescope Compact Array (ATCA), situated in New South Wales, consists of six 22 metre dishes. It operates from $\sim$1 to 100 GHz, with a maximum baseline of 6km, and now includes some North-South Baselines.

1.4.3.3 GMRT

The Giant Meterwave Radio Telescope (GMRT), of India's National Centre for Radio Astrophysics (NCRA), is situated near Pune, in India. Its array is formed of

30 wire mesh antennas, each of 45 m diameter, and operates from 150 to 1450 MHz. Half the antennas are arranged within a central square of approximately 1 square kilometre. The remaining 15 are split between 3 arms which stretch out from the central square in a "Y" configuration providing a maximum baseline of 25 km. The GMRT has been moved into full operation since 2002, and its combination of resolution and sensitivity have opened a new window onto the low frequency sky.

1.4.3.4 MERLIN

The 7 antennas of the Multi-Element Radio Linked Interferometer Network (MERLIN) are spread across England giving a maximum baseline of 217km. The dishes used vary in size, and the array can operate from 151 MHz to 24 GHz.

1.4.3.5 WSRT

Located in the Netherlands, the Westerbork Synthesis Radio Telescope (WSRT), is a linear East-West array of 14 antennas with a maximum baseline of 2.7 km. It operates between 120 MHz and 8.3 GHz.

1.4.3.6 VLBI

Very Long Baseline Interferometers (VLBI) take baseline length to the extreme. They cover large areas of the Earth's surface to attain the longest possible baselines. The Very Long Baseline Array (VLBA) covers the continental United States, with outlying antennas in Hawaii and Pueto Rico giving a maximum baseline of ~8600 km. The European VLBI Network (EVN) covers Europe including antennas in the UK, Spain, Finland, Italy, Germany and Poland. Radio dishes located in China, South Africa, and the VLBA array can also be included in the array.

These arrays achieve the highest resolution possible on Earth, but suffer in terms of sensitivity compared with the massed antennas of the smaller arrays such as the VLA.

1.4.4 Deep Radio Surveys

As with all surveys, the specific strategy of radio surveys are defined by a trade off between depth and area coverage within a finite amount of observing time. Deep surveys detect faint (both intrinsically and distance dimmed) and therefore interesting sources, but are usually limited in area. Small areas mean that numbers of

sources are limited, especially at brighter fluxes, where surface densities are generally lower. Wider, shallower surveys detect many more sources, but miss the fainter objects.

The first large scale surveys were performed using various interferometric arrays at Cambridge, and many radio sources are known by their Cambridge Survey catalogue number. As sensitivity improved, the 4C and 5C catalogues detected fainter and fainter sources. The advent of the VLA in the late 1970s increased sensitivity further. The NRAO VLA Sky Survey (NVSS), a northern hemisphere sky survey has been conducted with the D-array of the VLA at 1.4 GHz (Condon et al. 1998) reaches to a detection limit of 2.5 mJy over 82 percent of the celestial sphere with a resolution of 45 arcsec. At higher resolution (5.4 arcsec), the Faint Images of the Radio Sky at Twenty centimetres (FIRST, White et al. 1997) survey achieved a noise limit of 0.15 mJy over a smaller area of sky (10,000 square degrees).

Since the late 1990s several deep, narrow surveys have been undertaken to compliment deep surveys at higher frequencies and to probe the faint radio sky. Of these, the deepest have been the result of observations with the VLA, which has been used to survey the Hubble Deep Field North (HDF-N, Richards 2000; Biggs & Ivison 2006), the Lockman Hole and ELAIS N2 field (Biggs & Ivison 2006), the SSA13 Field (Fomalont 2006), and the 13^H field (Seymour et al. 2004) at 1.4 GHz, all to below $\sim 10\mu$Jy rms in single pointings.

Slightly larger areas have been covered to $\sim 20\mu$Jy, including the Spitzer First Look Field (SFLS, Condon et al. 2003), the VIRMOS VLA Deep Survey (VVDS, Bondi et al. 2003), and the COSMOS field (Schinnerer et al. 2004).

In the southern hemisphere, the Phoenix Field (Hopkins et al. 1998; Hopkins et al. 2003), the HDF-S (Norris et al. 2005, Huynh et al. 2005) and the southern half of the Great Observatories Origins Deep Survey (GOODS, Norris et al. 2006) are covered by ATCA at 1.4 GHz to levels similar to the deepest VLA pointings, and covering similar areas. The larger ATESP field (Prandoni 2000b) is also the subject of wider ATCA observations.

Deep imaging has also been achieved at 4.8 GHz with VLA imaging of the Lockman Hole (Ciliegi 2003) and ATCA imaging of the ATESP field (Prandoni et al. 2006).

1.5 The Fields Observed in this Thesis

The 13^H Field (13:34:42, 37:54:44) was the target of one of the deepest *ROSAT* surveys (M^{c}Hardy et al. 1998) aimed at resolving the CXB. This is a diffuse glow in the X-ray sky, first discovered by rocket bound X-ray astronomy missions, is suggested to be due to a large population of sources that earlier imaging systems could not resolve. These coordinates were chosen because they are the location the lowest galactic obscuration in the IRAS 100μm cirus maps.

The advent of XMM-*Newton* and *Chandra* in the late 1990's heralded a leap forward in both sensitivity and resolution in X-ray imaging. The 13^H, and 1^H (at 1:45:27, -4:34:42) fields are members of a new generation of deep X-ray surveys using these observatories. Specifically, the XMM-*Newton* observations of these fields were designed to study the nature of the sources that constitute the knee the the X-ray source counts. Radio observations were performed throughout the 1990's to provide further information on the nature of the sources, particularly those with optical counterparts too faint for spectroscopic follow-up.

1.5.1 X-ray Data

Both the 13^H, and 1^H field are the target of a 200 ks XMM-*Newton* pointing, as reported in Loaring et al. (2005) and analysed in Dwelly et al. (2005). Each contain $\sim$220 X-ray sources within 15 arcmin of the pointing centre. The high throughout of XMM-*Newton* allows the study of the X-ray spectra of many of these sources (Page et al. 2006).

A mosaic of four 50 ks *Chandra* pointings overlaps the XMM-*Newton* coverage for each field, providing excellent angular resolution, essential for the unambiguous identification of the optical counterpart to the X-ray sources (M^{c}Hardy et al. 2003).

1.5.2 Radio Data

To gain more information about the nature of the sources discovered in the X-ray, deep 1.4 GHz radio observations of the 13^H field were conducted throughout the 1990s with the VLA in both A and B arrays. At the time, these were the deepest 1.4 GHz images made, and they are presented in Seymour (2002) and Seymour et al. (2004). The observations included 24 hours of good time on source and reached 7.5μJy beam^{-1} rms noise. To a 4σ detection limit of 30μJy, in an area of 15 arcmin radius, 449 sources were discovered.

The field was also the target of 4.8 GHz VLA D array observations (Seymour 2002). The smaller primary beam of the VLA antennas at 4.8 GHz meant that a mosaic of 51 pointings was required to cover the XMM/VLA survey area and ~100 sources were detected above a 3σ limit of 100μJy. Of these, 53 have counterparts at 1.4 GHz, and so provide radio spectra. It should be noted that the observations at these two frequencies are not matched either in resolution or image properties, and so do not provide exact spectral information, as flux can be resolved out of the higher resolution 1.4 GHz maps.

The majority of the XMM/VLA survey area is covered by the four deep observations with MERLIN with each 4 day observation covering a field of $\sim 10 \times 10$ arcmin, to a noise level, of $\sim 27\mu$Jy beam^{-1}.

1.5.3 Infrared Data

The 13^H field is the target of one of the deepest *Spitzer* observations, performed in GTO time (P.I. G. Rieke). The Mid Infrared Photometry System (MIPS, Rieke et al. 2004) provides MIR coverage to 19th magnitude (AB) at 24μm, and the InfraRed Advanced Camera (IRAC, Fazio et al. 2004) provide deep images to AB magnitudes of 23, 22.6, 20.8 and 20.7 at 3.6, 4.8, 5.8, and 8μm respectively.

1.5.4 Optical Data

The 13^H field has deep optical imaging from the SuprimeCam 8k×10k mosaic camera (Miyazaki et al. 1998) on the Subaru telescope in the B, R, I and Z filters to AB mags of 27, 26 (see M^{c}Hardy et al. 2003 for details), 26 and 25 respectively. Deep u', g' and i' images of the same field to 26th, 27th and 25th magnitudes (AB) respectively are available from the MEGACAM instrument on the Canada France Hawaii Telescope (CFHT).

In the Near InfraRed (NIR), the 13^H field is covered by imaging in the K band to 23rd magnitude (AB) from the Wide Field Camera (WFCAM) on the United Kingdom InfraRed Telescope (UKIRT).

The Wide field InfraRed Camera (WIRC) on the Palomar 200 inch telescope provides imaging to J of 22.6, and the Wide-field InfraRed Camera (WIRCam) on the CFHT gives H band imaging to 22.7.

The 1^H field is covered in the B, I, and Z filters to similar depths as the 13^H field by SuprimeCam. R band coverage is provided by a mosaic of pointings of the Primary Focus Camera (PFC) on the William Herschal Telescope. Images with the

WIRC instrument at K_s reach 23, and J and H band observations proposed to reach 22.8 and 22.5 respectively are currently being undertaken with WFCAM.

Optical spectroscopy has been acquired for essentially all the radio and X-ray sources with optical counterparts brighter than 23rd R-band magnitude. The excellent optical coverage allows photometric redshift estimates to be calculated for the remainder, work which is currently ongoing.

1.6 The Wider Goals of this Study

This study is aimed at using radio data to discern the nature of the faint sources discovered in the two fields.

As described in Section 1.3, recent decades have seen the discovery of a new population of sources at faint 1.4 GHz fluxes, as witnessed by the upturn in the Euclidean normalised differential source counts below ~1mJy (see Fig. 1.5).

If the new population consists mainly of starburst dominated sources, they may provide an independent measure of the star formation rate density history of the universe. In the case that the radio emission from a galaxy contains no contamination from an AGN, radio luminosity is an unbiased measure of star formation rate.

It is important to highlight that the criterion for the radio luminosity being a measure of star formation rate is that there is *no* contribution from an AGN to the radio emission, not that there is no AGN present. Since only a fraction (~10-20 percent, Jiang et al. 2007) of AGN are radio loud, it is quite possible for a galaxy to host a radio quiet AGN while still having its radio emission dominated by star formation.

If all the sources that make up the sub-mJy bump can be individually identified as either AGN or starformers, it is possible to study the two populations separately. This has three important benefits. Firstly, the evolution of the luminosity of radio loud AGN can be studied out to greater redshifts, as contamination from the sources that form the bump can be removed.

Secondly, modelling of the source counts for this removed contribution (the sources where star formation dominates the radio emission) separately will measure the evolution of the radio luminosity function of the star formation in a statistical manner.

Finally a large, clean sample of sources whose radio emission is due to star formation can be used to accurately measure the starforming radio luminosity function.

The excellent NIR to optical coverage of the 13 and 1^H fields mean that the redshifts (either spectroscopic or photometric) required to calculate the luminosity of any individual source are available. Binning in redshift space allows the form of the evolving luminosity function to calculated. As radio luminosity is an unbiased measure of star formation rate, a radio luminosity function can be converted into a universal star formation rate at each binned epoch. Hence, a measure of the star formation history of the universe (see Section 1.3 and Fig 1.4) can be made, independent of the biases and uncertainties inherent in the current calculations.

To perform such measurements, a clean sample of sources whose radio emission is due to star formation is required. The selection of this sample relies critically on the ability to discriminate between sources whose radio emission is due to an AGN, and sources whose radio emission is from the SNR associated with star formation. Many methods exist to perform this discrimination, but it is their combination that provides the most useful information. The plethora of methods described below also provide sufficient redundancy to allow checks of the classification of each source.

1.6.1 AGN/Starburst Discrimination

For each source of radio emission, two questions need to be answered: 1) Is there an AGN in the galaxy? If not, then the radio emission is likely to be from star formation. 2) If there is an AGN in the galaxy, is that AGN responsible for the radio emission? If not, the radio emission is likely to be due to star formation.

1.6.1.1 Detailed Optical Spectroscopy

High resolution optical spectroscopy is an invaluable method for discriminating between AGN and starbursts. As discussed in Section 1.2, AGN exhibit both broad and narrow emission lines, while star formation is indicated by narrow emission lines, with limits on the values of various line ratios. The AGN spectral indicators can signify the presence of an AGN, not that the detected AGN is responsible for the radio emission since the optical spectroscopic emission of a radio quiet AGN can dominate over the optical spectral signatures of star formation.

The practical time limitations inflicted by the faint nature of the optical counterparts of sources detected in deep radio surveys mean that the acquisition of spectra of sufficiently high signal to noise to perform line ratio diagnostics for many sources is not feasible.

1.6.1.2 X-ray luminosity

In the unification scheme, AGN emit X-rays from coronae of high energy electron that surround the inner accretion disk. Indeed, X-ray surveys are excellent method for AGN sample selection. A point source X-ray detection at the centre of the optical galaxy which is emitting the radio flux is a good indication that an AGN is present. Once again, X-ray detection is an indication that an AGN in present, not that it responsible for the radio emission.

The most massive stars are relatively short lived, and rapidly evolve to form the supernova remnants responsible for the radio emission from star formation. The same massive stars are responsible for the accretion in High Mass X-ray Binaries (HMXBs). A burst of star formation therefore produces increased radio and X-ray emission, the expected ratio of which can be estimated (see Simpson et al. 2006 and references therein). A source with a radio to X-ray flux ratio differing significantly from this theoretical value must harbour an AGN, although as before, this AGN may not be the dominant source of radio emission.

1.6.1.3 Optical Colours

The massive, short lived stars that are present in large numbers only during a burst of star formation are also the hottest, and therefore their thermal spectrum peaks higher frequencies. In general, the older and cooler the stellar population, the redder the appearance of the galaxy which hosts them. A red optical colour of a galaxy which hosts radio emission is therefore an indication that an AGN is the source.

1.6.1.4 IRAC colours

Galaxies whose optical/NIR emission is dominated by star light fall off in flux as one progresses to longer wavelengths through the IRAC bands. Over the same range in wavelength, the spectrum of an AGN is a power law, and therefore falls in a different region of IRAC colour-colour space. This diagnostic is well calibrated at low redshift (Stern et al. 2005), but less well constrained at higher redshift, and once again can imply the presence of an AGN, not determine weather it is responsible for the radio emission.

1.6.1.5 Radio/MIR relation

In star formation, both radio emission and Mid InfraRed (MIR) is due to the same underlying phenomenon. Short lived massive hot stars heat dust (which gives rise

to MIR emission) and rapidly evolve to supernovae (which provide the means for radio emission). This leads to a correlation between the radio and MIR flux (e.g. Helou & Bicay 1993), the practical measurement of which is dependent on redshift as PAH features move through the 24μm band which is used to estimate the MIR flux. It is reasonable to assume that the radio emission from any source which does not obey this correlation is from an AGN. A limitation of this method is the fact that AGN can fall on this relation. The 'radio loudness' - the radio to optical, or indeed any other waveband, ratio - of an AGN is arbitrary, and so the radio to MIR flux ratio for an AGN can have a wide variety of values, including that predicted by the radio-MIR correlation for starbursts.

1.6.1.6 Radio/Optical relation

Since the radio emission from star formation and the thermal light from galaxies are (indirectly) from the same population, the ratio between flux in the two bands is somewhat constrained. For an AGN, both the radio to stellar optical flux ratio, and the radio to AGN optical flux ratio are less constrained. So, objects with extreme radio to optical flux ratios can be identified with a radio bright AGN.

1.6.1.7 Radio Polarisation

Since the synchrotron emission from AGN is from electrons spiralling in collimated, aligned jets, AGN radio flux can show a measurable degree of polarisation. The radio emission from a galaxy undergoing starformation is not expected to show any net polarisation. However, due to the inefficient use of observing time required to detected enough polarised flux to measure polarisation, it is impractical to employ this method in deep surveys.

1.6.1.8 Radio Luminosity

The radio luminosity of AGN varies hugely. Starbursts more limited in luminosity. The local radio luminosity function of starburst galaxies falls steeply with luminosity from 10^{22} W Hz^{-1} and continues to steepen to the highest measurement at $10^{23.5}$ W Hz^{-1} (Mauch and Sadler 2007). Any radio sources more luminous that this are likely to be AGN. Below this limit, the emission could be either AGN or starburst. To calculate the radio luminosity, the radio flux of the source, the radio spectrum of the source (for K-correction), and the distance to the source are all required. This last factor requires a redshift for the source, and an assumption about the

geometry of the universe. For the rest of this study, I assume a 737 (concordance) cosmology with $H_0 = 73$ km s^{-1} Mpc^{-1}, $\Omega_m = 0.3$, $\Omega_\lambda = 0.7$ (Spergel et al. 2003). As mentioned in Section 1.5, spectroscopic redshifts are available for many radio sources. Photometric redshifts provide estimates of the distance to the remainder. The calculation of photometric redshifts involves template fitting to source optical magnitudes derived from images taken through broad band filters. The coverage of both fields from B through to K_s allows the calculation of photometric redshifts for all of the 1.4 GHz sources, and hence radio luminosities are available for the entire sample.

1.6.1.9 Radio Morphology

The morphology of a radio source can discriminate between AGN and starburst emission. Extension of the radio emission, in one dimension, outside the extent of the optical emission of the emitting galaxy implies that the radio emission is from the jets associated with an AGN (see Fig 1.6). Radio emission extended in both dimensions across the emitting optical galaxy is likely to be from star formation (see Fig 1.7). The limit of this discriminant is that it sensitively depends on the resolution of radio imaging. In reasonable resolution radio images (~3 arcsec) typical of deep radio surveys, both AGN and star formation can appear point like. AGN with very small, young jets can remain unresolved, and therefore appear point like. Starbursts often occur in the very centre of galaxies. Such nuclear or circum-nuclear starbursts can also appear point like and therefore indistinguishable from AGN on morphology alone. Higher resolution images from VLBI instruments can extend the usefulness of this discriminant - as shown by ongoing work on the MERLIN maps of the 13^H field (Zoghbi et al, in prep).

1.6.1.10 Radio Spectrum

Radio emission from both AGN and starbursts is primarily synchrotron in origin. Optically thin synchrotron radiation is expected to have a spectral index of $\alpha = -0.7 \pm 0.2$, where $S \propto \nu^\alpha$, and S represents flux, and ν frequency. Optically thick synchrotron radiation suffers self absorption and can lead to flatter spectra (higher values of α). For further detail on synchrotron radiation, and radio spectra, see Section 1.7. In brief, radio emission from star formation is optically thin and therefore the radio spectra of galaxies whose radio emission is due to star formation is expected to provide measurements of α of around -0.7 to -0.8. The range of

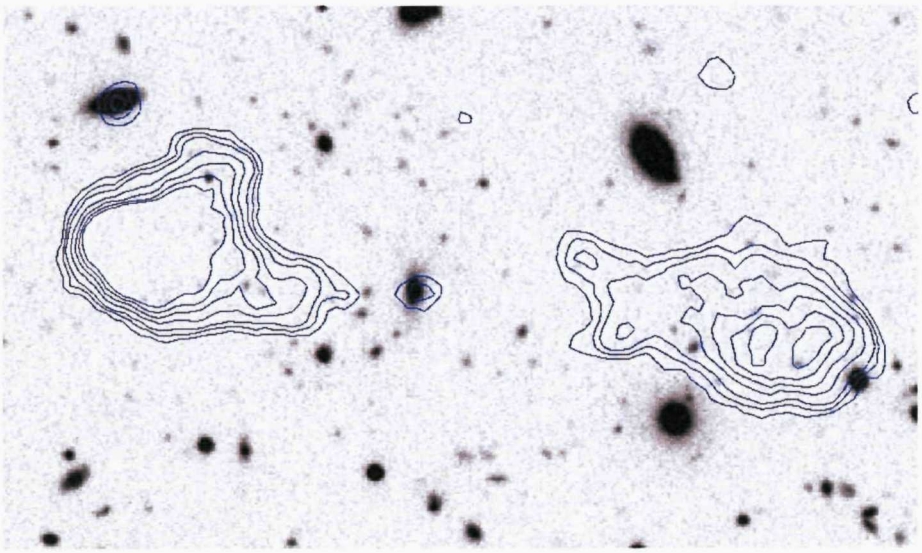

Figure 1.6: 1.4 GHz radio emission (contours), overlaid on I band optical image of a 3×2 arcmin region surounding a galaxy hosting a radio loud AGN. The jets can be seen to be extended primarily in one dimension, and outside that of the optical emission.

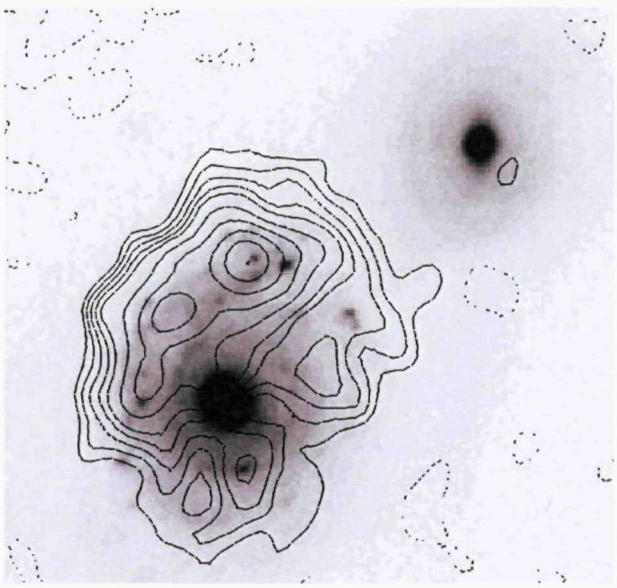

Figure 1.7: 1.4 GHz radio emission (contours), overlaid B band image of source R32, the 32nd brightest X-ray source in the ROSAT survey of the 13^H field (M^{c}Hardy et al. 1998, Gunn et al. 2001). The radio emission is extended in two dimensions and traces the optical galaxy. An AGN cannot emit radio from the disk of the host galaxy - so the radio emission in this case must be due to star formation

expected radio spectra for AGN is much greater, varying from flat spectra ($\alpha \sim 0$ or more) to very steep ($\alpha \sim -1.2$ or steeper). Conservatively, any source with a radio spectra outside of the range $-0.5 > \alpha > -1$ is likely to be an AGN. Hence, with radio flux measurements at two or more frequencies, radio emitting AGN can be positively identified. As the range $-0.5 > \alpha > -1$ can include values of α that are valid for the spectra of AGN, this discrimination cannot rule out AGN contribution to the radio emission, but can positively state that an AGN does contribute.

It is worthwhile at this point to reiterate that radio polarisation, radio luminosity, the radio/MIR relation and radio spectra are the only discriminants listed above that can provide information about the *radio luminosity* of any AGN present. The remainder of the diagnostics can merely indicate the presence of an AGN in the host galaxy, not confirm that it is the dominant source of radio emission, which is the key factor for the extended study of which this work forms a part. Hence, it is the combination of as many of these discriminants as possible that will give the most accurate picture of the nature of each individual radio source.

This work focuses on the acquisition, analysis, and use of radio spectra to study the faint radio population, both statistically, and on a source by source basis. Detailed radio spectra are used to study two interesting sources (XBONGs) from the X-ray catalogue of the 13^H field in Chapter 2. The remainder of this work deals with the wide field imaging of both the 13^H and 1^H fields at two frequencies to provide spectra for many of the faint radio sources, for the purpose of selecting a pure starburst sample to measure the cosmic star formation history. Observations of the 13^H field at 1.4 GHz have previously been published (Seymour et al. 2004). Here, 1.4 GHz imaging of the 1^H field with the VLA is presented, along with deep observations of both fields at 610 MHz with the GMRT.

The radio maps are resolution matched to gain accurate radio spectra for a sample of radio sources, which can be used as discriminants to construct a clean star forming radio sample.

An interesting aside to note at this point is that such large samples of radio spectra are useful for discovering Ultra Steep Spectrum (USS) ($\alpha < -1.3$) radio sources. Populations of USS source have been found (De Breuck et al. 2004) to be a good sample to select from in the search for high redshift radio galaxies, often hosted in the most massive galaxies at each epoch, and so interesting from the point of view structure formation.

1.7 Synchrotron Spectra

Since the majority of this work deals with the detection of synchrotron emission, and measuring its spectrum in the radio waveband, it is worthwhile at this point to provide a brief review of the physics and phenomenology involved.

When any charged particle undergoes acceleration, it emits electromagnetic radiation. For charged leptons spiralling in magnetic fields, this acceleration is their centripetal acceleration and the radiation is know as cyclotron. If the spiralling electrons are highly relativistic, the radiation is channelled into a tight cone of emission, the opening angle of which is proportional to their energy, and is known as synchrotron emission, after the type of particle accelerators in which it was first noticed.

The synchrotron emission from AGN is caused by high energy electrons spiralling in the magnetic fields of the jets which are launched from the central engine. In star forming galaxies, high energy electrons formed in supernova spiral in galactic magnetic fields.

The spectrum of the synchrotron radiation depends primarily on energy distribution of the emitting electrons. In both jets and SNR, the electrons are theorised to be accelerated by shocks, which lead to power-law electron energy distributions (Blandford & Eichler 1987) and power law spectral indices for optically thin synchrotron radiation. The majority of extragalactic sources do, indeed, have power law spectra, with a canonical spectral index of $\alpha \sim -0.7$.

Since the power emitted by the electrons spiralling in the magnetic field is proportional to the energy of those electrons, higher energy electrons radiate their energy faster. Hence, the population of emitting electrons at the highest energies can become depleted, and the spectrum fall off steeper than $\alpha = -0.7$ at high frequencies. High redshift radio galaxies have this steeper section of their radio spectrum redshifed into the frequency ranges typically used to make deep radio surveys. Indeed, $\alpha < -1.3$ is a good criteria upon which to select high redshift galaxies (De Breuck et al. 2004).

At lower frequencies, the emitting material becomes optically thick and leads to a turn over in the $\alpha \sim -0.7$ synchrotron spectrum below a characteristic frequency. Below this frequency, the spectrum falls off as $S \propto \nu^{5/2}$. The frequency at which this turnover occurs varies with the density and energy distribution of the electron population which is responsible for it. If many populations each with their own typical turn over frequency are contained within one observation resolution element,

they can superimpose to form a flat spectrum. This is often the case in observations of distant AGN, where the radio emission from different regions in the jets appear point-like at typical interferometry resolutions.

The radio spectra of AGN can therefore take a wide range of values, from very steep ($\alpha < -1.3$) – where the energy loss steepened region of the spectrum is redshifted into the centimetre bands – to the very flat, where many optically thick components of differing properties are superimposed.

Radio emission from star forming galaxies is optically thin and generally has a spectral index of 0.7 as determined both empirically (see Condon 1992 for a review) and by theory (Thompson et al. 2006).

It should be noted that star forming galaxies can emit in the radio with flat spectra. Thermal free-free emission from electrons in photo-ionised gas surrounding hot stars has a flat spectrum. However, this component is generally weaker than the synchrotron component, and only detectable at frequencies higher than those considered here (Condon 1992).

1.7.1 Measurement of Radio Spectra

The simple power law spectra of extragalactic source make estimates of their spectral indices relatively simple. Flux measurements at two frequencies are sufficient to estimate the spectral shape. However, when using maps of radio emission constructed from interferometers (as is essential when considering sources of the fluxes and sizes of those found in deep surveys), the fluxes need to be measured from images made at similar resolutions. High resolution maps can resolve out flux from extended structure as the spatial sensitivity scale of their longer baselines fails to recover the total flux of the object. Since higher frequencies allow higher resolution images to be made with greater ease (resolution $\propto \lambda$), this can have the effect of artificially steepening the calculated spectrum.

Another limitation upon the estimation of spectra from simple two point flux measurements come from the temporal domain. The radio emission of AGN can vary, especially if the jet is aligned close to the line of sight. If the two flux measurements are not made simultaneously, the calculated spectral index may not be a good estimate of the true spectrum.

Both this variation, and the aforementioned possibility that a starburst can have a flat radio spectrum illustrate that radio spectra alone and not ideal discriminants. It is when radio spectral information is combined with other diagnostics that AGN

and starburst can be efficiently disentangled. This study aims at acquiring the radio spectra to contribute thus.

1.8 Thesis Outline

The remainder of this thesis is arranged as follows. In Chapter 2, the detailed, pseudo-simultaneous radio spectra of two interesting sources detected in the X-ray surveys of the 13^H field are presented as a further introduction to the techniques of radio interferometry. Later chapters then move to deep, wide field, multi-frequency imaging to acquire simple radio spectra of the many sources discovered therein. Chapter 3 presents a 610 MHz survey of the 1^H field, and modelling of the 610 MHz source counts. The 1^H field is again the subject of Chapter 4, with deep 1.4 GHz imaging and a compilation of the 1.4 GHz source counts being presented. Chapter 5 completes the two field, two frequency sample by surmising the 1.4 GHz survey of the 13^H field of Seymour et al. (2004) and discussing 610 MHz observations of this field. The multi-field 610 MHz source counts are modelled. The various catalogues are then cross-correlated and radio spectra, and limits thereon, are calculated. A preliminary analysis of the optical properties of the radio populations are presented in Chapter 6. The conclusions of the thesis are summarised in Chapter 7, and future work discussed.

Chapter 2

Radio Spectra of X-ray Bright Absorption Line Galaxies

This chapter examines the detailed radio spectra of two specific sources as a means of further introducing the techniques and uses of radio interferometry. The sources are the two brightest absorption line galaxies discovered as X-ray sources in the 13^H field. Data at 1.4, 4.8, 8.4 and 14 GHz, acquired from the VLA, are used to generate pseudo-simultaneous radio spectra. These are combined with data from other wavebands to construct spectral energy distributions.

2.1 Introduction

The first deep Chandra surveys (e.g. Mushotzky et al. 2000; Hornschemeier et al. 2000, 2001) showed that a new population of absorption line elliptical galaxies was a major contributor to the medium energy X-ray background (XRB). However the origin of the central, point-like X-ray emission in these X-ray Bright, Optically Normal Galaxies (XBONGs) was a mystery.

The source of X-rays from AGN is considered to be a corona of hot electrons surrounding the inner regions of an accretion disk. The detection of X-rays from a galaxy is therefore usually accompanied by the detection of optical signatures of AGN activity (a point-like central excess and emission lines). Indeed, the majority of galaxies discovered to emit X-rays in deep surveys are identified as AGN in this manner, although stars, galaxy clusters and the X-ray emission from star formation have also been detected (e.g. M^{c}Hardy et al. 2003, Gunn et al. 2001).

It is strange, therefore, to discover X-ray emission from a galaxy which shows no signs of AGN activity in its spectra. Several other potential sources of X-rays are

easily excluded as being the source of emission in this case.

Halos of hot gas have been seen in the gravitational potential wells of elliptical galaxies. They emit in the X-ray, but are generally resolved by *Chandra*, and therefore distinguishable from sources within a host galaxy.

High Mass X-ray Binary star systems (HMXBs) and Low Mass X-ray Binaries (LMXBs) within the stellar population of host galaxies can emit X-rays. Once again these would have properties not seen the currently considered population. The discrete, multiple nature of emission would either be resolvable with the excellent spatial resolution of *Chandra*, or offset from the galaxies nucleus. Also, HMXBs and the high mass stars that they contain, are short lived and therefore only expected to be found in large numbers in galaxies undergoing star formation - not absorption line ellipticals.

Other possibilities that are harder to rule out include advective flows in the central engines, hidden AGN, and low luminosity AGN and blazars.

In the standard AGN unification paradigm (See Section 1.2.1.6), the central engine consists of an SMBH surrounded by an accretion disk. This disk can have two configurations. The first to be considered in depth (e.g. Salpeter 1964) was an optically thick, geometrically thin disk where viscous heating heats the material in the disk which emits thermally. A corona of hot electrons is thought to be responsible for the X-ray emission in this configuration.

In recent years, observational evidence has motivated the consideration of a second configuration of the accretion material. Called an Advection Dominated Accretion Flow (ADAF), or a Radiatively Inefficient Accretion Flow (RIAF) the accreting material is optically thin, so any radiation escapes without interaction or causing the associated thermalisation (e.g. Shakura & Sunyaev 1973). Such accretion flows are characterised by little optical emission, and hard X-ray spectra.

As described in Section 1.2.1.6, much of the multitude of AGN phenomenology can be explained by various orientations, with respect to the line of sight, of a torus of obscuring material. X-rays are attenuated less by dust than radiation of longer wavelengths, so the optical signatures of an AGN can be lost to absorption while X-ray light escapes. A large absorbing column between an AGN and an observer can therefore explain the detection of X-rays from the core of a galaxy without any optical signs of activity. The increase with photon energy of transparency to radiation of the obscuring material also means that the X-rays observed from obscured AGN generally show a hard spectrum.

In a blazar, a jet from an AGN is orientated towards the line of sight. The emis-

sion from any such jet would be subject to Doppler boosting by the bulk motion. With such boosting, it is possible that the X-ray flux from the source is actually synchrotron emission from the base of said jet, rather than the regions surrounding the accretion disk. This provides an explanation for the X-ray detection of absorption line galaxies, as the X-ray emission is Doppler boosted, whereas any optical emission lines associated with the central engine are not, and can be outshone by the stellar population. If this is the case, the X-ray spectra can take many forms, depending on the energy distribution of the emitting electrons, the speed of motion in the jet, and the exact orientation of the jet to the angle of sight. However, several objects, including Mrk421 (e.g. Warwick et al. 1986) have steep, soft spectra over the sensitivity ranges of *Chandra* and *XMM*.

Although the deep *Chandra* surveys in which XBONGs were first detected did not produce detailed X-ray spectra, the sources were generally hard, thereby favouring advective flows or obscured AGN.

Comastri et al. (2002a) reported on detailed multi-wavelength study of CXOU J031238.9-765134, an optically inactive early-type galaxy identified with a $\sim 3 \times 10^{-14}$ erg s^{-1} cm^{-1} (2-10 keV) Chandra source, and concluded that heavy obscuration explained the lack of optical activity. It has also been claimed (Yuan and Narayan 2004) that this source, along with another (XMM J021822.3-050615.7) can be fitted with a Radiatively Inefficient Accretion Flow (RIAF).

The study of many objects is required to infer the nature of a population which may itself consist of several differing types of sources, especially given the ambiguity in the nature of the few that have been studied in depth. Indeed, in a study of 12 XBONGs by Georgantopoulos and Georgakakis (2005) concluded that XBONGs comprise of a mix of objects including type-1 AGN outshone by the host galaxies star light, and low luminosity AGN. Preliminary results of studies into 10 XBONGs (Comastri et al. 2002b) find that of the 7 of these that are covered by observations at radio wavelengths, only one is bright enough to be considered 'radio loud'.

Conclusions about the nature of even the best studied XBONGs are therefore not unique. Several similar XBONGs were discovered in the *Chandra* survey of the 13^H field (M^{c}Hardy et al. 2003). In this Chapter, a review of the previous observations covering the two optically brightest of these sources (known as Chandra 4 and Chandra 33, hereafter C4 and C33 respectively) in the radio, optical and X-rays is presented. Detailed radio spectral observations of the C4 and C33, utilising data from the VLA, and the GMRT, are then presented. The broad band Spectral Energy Distribution (SED) of each source is constructed and compared to simple

SED models of various AGN types combined with elliptical galaxy templates.

2.2 Previous Observations

2.2.1 X-ray Observations

2.2.1.1 ROSAT and Chandra Observations

The two *Chandra* X-ray sources, C4 and C33, were first noted in the *ROSAT* survey of M^{c}Hardy et al. (1998) where they are listed as sources 51 and 36 respectively. As both *ROSAT* and *Chandra* surveys list sources in flux order it can be seen that *ROSAT* source 51 is relatively much brighter in the higher energy Chandra survey (source C4). This brightening could be a spectral effect resulting from a hard X-ray spectrum, or could simply be due to variability. Although *ROSAT* spectra are not particularly informative for relatively faint sources like these ones, C4 was determined to be softer than C33 which indicates that variability may be the more likely cause of the relative flux change. The *Chandra* observations showed, unambiguously, that the two X-ray sources were both coincident with the nuclei of bright elliptical galaxies, ruling out the possibility that the X-rays are from thermal gas in the potential of the associated galaxy.

2.2.1.2 XMM Spectra

XMM-*Newton* observations of the *ROSAT* field, totalling 200 ks, were performed in June of 2001. See Page et al. (2006) for details. Although small variations are visible in the light curves, the sources are consistent with being constant.

The extracted source spectra were fitted with a powerlaw continuum plus intrinsic absorption at the redshift of each galaxy. Fig. 2.1 shows the XMM-*Newton* spectrum of C4, for which the best fitting model is a powerlaw with photon index $\Gamma = 2.40^{+0.06}_{-0.08}$ (1σ errors). The best fitting column density is $N_H = 2.4^{+2.0}_{-1.6} \times 10^{20}\,\mathrm{cm}^{-2}$ which, at its lower bound, is consistent with the Galactic column density in this field of $N_H = 7 \times 10^{19}\,\mathrm{cm}^{-2}$ (Dickey & Lockman 1990). See Fig. 2.2 for the XMM-*Newton* spectrum of C33. The corresponding powerlaw index and absorbing column density are $\Gamma = 2.24^{+0.20}_{-0.14}$ and $N_H = 9.0^{+3.2}_{-4.5} \times 10^{20}\,\mathrm{cm}^{-2}$, which is definitely above the Galactic column density.

There is no evidence of an iron line in C4 but there is a slight excess above the powerlaw in C33 between 5 and 6 keV. However, if we fix a Gaussian line at 5.2

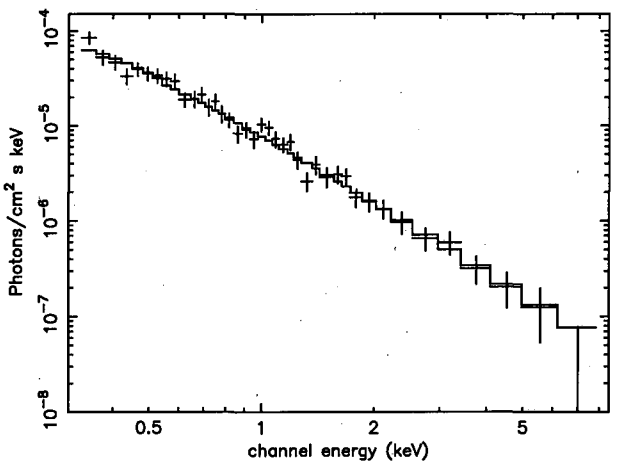

Figure 2.1: XMM spectrum of Chandra 4, showing the powerlaw plus Galactic absorption best fitting model.

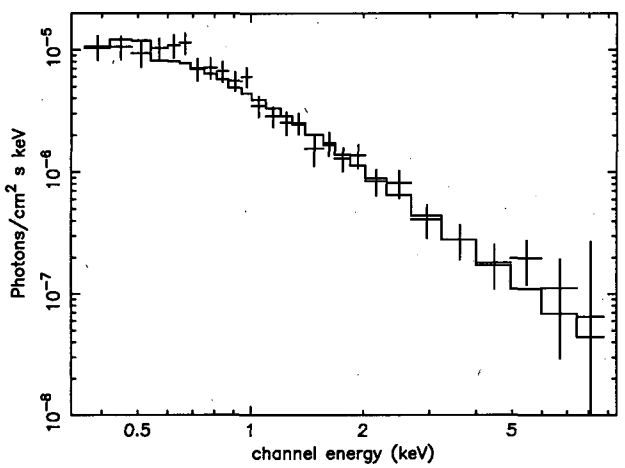

Figure 2.2: XMM spectrum of Chandra 33, showing the powerlaw plus intrinsic absorption best fitting model.

keV (the position expected of 6.4 keV line at the redshift of the galaxy) the F-test indicates that the line is only significant at the 78% confidence limit (i.e. about 1.5σ).

2.2.2 Optical Identification

2.2.2.1 Imaging

Optical counterparts for C4 and C33 were taken from the catalogue of sources extracted from the Subaru SuprimeCam R-band image using SExtractor (Bertin & Arnouts 1998). The magnitudes of both galaxies, as determined by SExtractor using its 'best' magnitude parameter, are identical at $R = 17.7$mag. Similar analysis of the SuprimeCam B band image yields magnitudes of C4 and C33 as 19.9 and 19.8 respectively. Both objects therefore have similar B-R colours of 2.15.

2.2.2.2 Optical Morphology

Using the IRAF task *ellipse*, the 1-D profiles for C4 and C33 have been determined. Both are extremely good fits to standard de Vaucouleurs elliptical galaxy profiles. Disc models are a very bad fit.

2.2.2.3 Optical Spectra

In Figs 2.3 and 2.4, the optical spectra of Chandra 4 and 33 respectively are shown. These spectra were obtained in 1994 and 1995 using the MOS spectrograph (Le Fevre et al. 1994) at the Canada France Hawaii telescope in the process of identifying *ROSAT* sources. (see M^{c}Hardy et al. 1998) for details. Their redshifts are 0.257 and 0.229 respectively.

The spectra of C4 and C33 show prominent absorption features, including the 4000Åbreak but, with the exception of a possible weak [OII] 3727 line (leading to the GAL/NELG classification in M^{c}Hardy et al. 1998) there are no strong emission lines. There is no sign of H_α in C4 but the CFHT spectrum of C33 (Fig. 2.4) does not extend far enough to detect H_α. However, a WHT spectrum of C33, although of lower S/N, does cover Hα and shows no strong H_α line.

2.2.3 Radio Detection

Radio emission is not affected by absorption, and so is an excellent diagnostic for investigating possible obscured AGN.

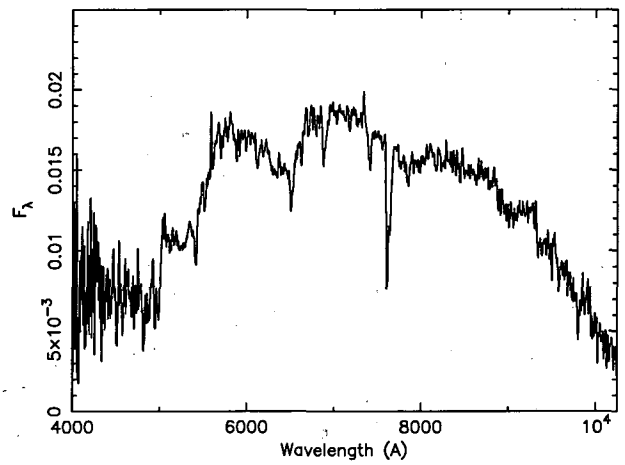

Figure 2.3: Optical spectrum of Chandra 4, taken using the CFHT MOS spectrograph.

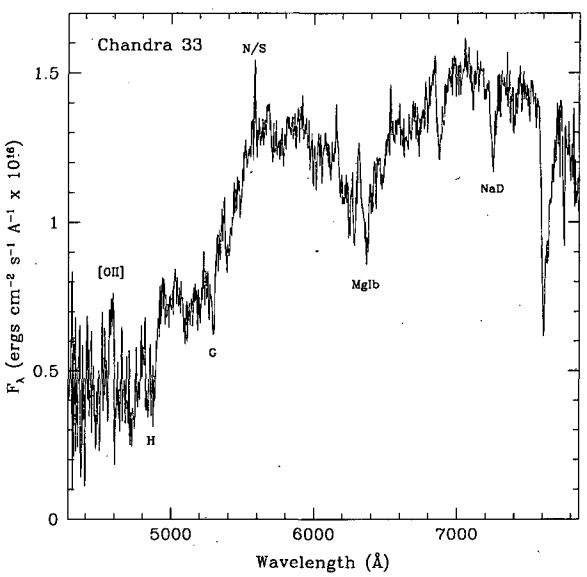

Figure 2.4: Optical spectrum of Chandra 33, taken using the CFHT MOS spectrograph.

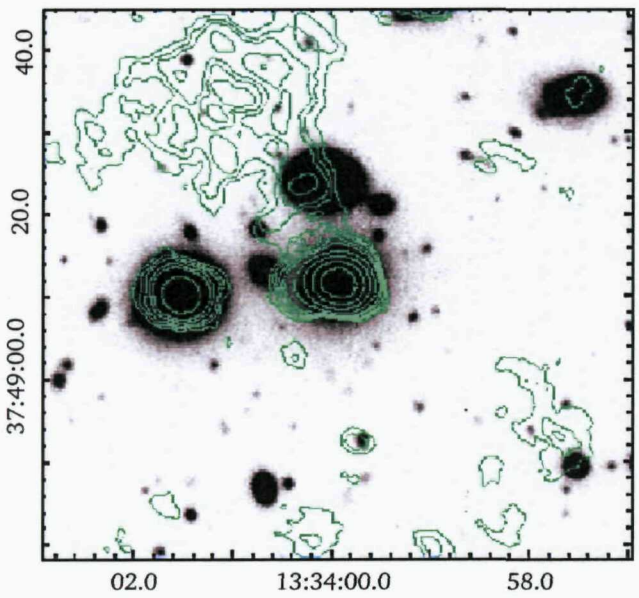

Figure 2.5: VLA 20cm radio contours (logarithmic) overlaid on a 70″ × 70″ Subaru SuprimeCam R-band image of Chandra 4, showing the complex environment of this source. C4 lies at the centre of the image. Approximately 20" east of C4 is the 16 mag Narrow Emission Line Galaxy (NELG) which was originally suggested as the identification of the ROSAT source R51. Note that this NELG is also a strong radio source.

Both sources were observed extensively as part of the deep VLA and MERLIN survey of the *XMM/Chandra/ROSAT* survey area. The analysis of the VLA observations is described in Seymour (2002) and Seymour et al. (2004), and is summarised in Section 5.5. Both sources were detected at high levels of significance.

The 20cm VLA survey maps of C4 and C33, made with natural weighting, are shown in Figs. 2.5 and 2.6, overlaid on *R*-band images.

2.2.3.1 Radio Morphology

There are a number of other weaker radio sources in the field of C4, together with some diffuse extended (∼35 arcsec) emission north of its position, as can be seen in Fig. 2.5. The bright region of emission does itself show a slight extension to the East.

In the catalogue of Seymour et al. (2004), C33 is listed as having a width (deconvolved from the ∼3 arcsec beam) of 1.8 arcsec, though close inspection of the image suggests that this extension may be purely due to the effect of bandwidth smearing.

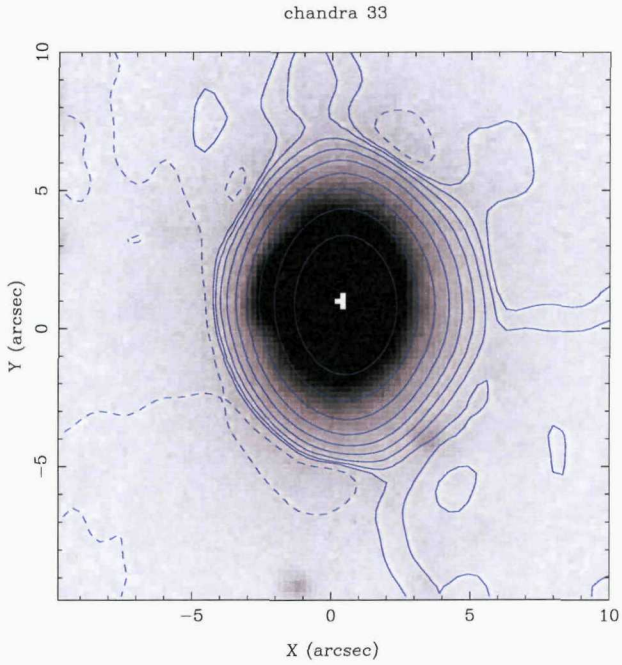

Figure 2.6: VLA 20cm radio contours overlaid on a $10'' \times 10''$ Subaru SuprimeCam R-band image of Chandra 33.

The 13^H field is also covered by a deep MERLIN survey (Zoghbi et al. in prep). Preliminary analysis of this observation shows that while the VLA emission from C4 has a maximum extent of $\sim 7''$, MERLIN shows a partially resolved compact core coincident with the nucleus of the elliptical galaxy. This core-halo morphology is typical of BL Lac objects (see e.g. Antonucci & Ulvestad 1985). C33 is seen as an unresloved core coincident with the core of the associated optical galaxy.

2.3 Radio Spectra

Radio spectra can be used to distinguish between AGN and starbursts (see Section 1.7), as starbursts are expected to have a limited range of spectral indices ($-0.5 < \alpha < -1$, where $S \propto \nu^{\alpha}$). The elliptical morphology, red colour and passive optical spectrum of both C4 and C33 mean that star formation is highly unlikely to be the source of radio and X-ray emission. Radio spectra are, however, illustrative for non-star formation diagnostics. For example, a flat radio spectrum ($\alpha > -0.5$) is indicative of the superposition of the optically thick synchrotron spectra of populations of electrons with many differing energy distributions (See Section 1.7). Such a configuration is explainable by, for example, a jet orientated towards the observer

and therefore suggests that any X-ray emission may be Doppler boosted synchrotron.

2.3.1 Observations and data reduction

To gain pseudo-simultaneous radio spectral information, both C4 and C33 were observed by the A-array of the VLA at 20, 6, 3.5 and 2 cm (equivalently 1.4, 4.8, 8.4 and 14 GHz respectively) in July of 2003. The observations were in standard continuum mode, with 2 Intermediate Frequencies (IFs) and 50 MHz of bandwidth. Calibration observations of 3C286 and 1327+434 at each frequency were interspersed between pointings on-target which themselves were spread throughout the observing window to increase *uv* coverage.

Reduction was performed in the National Radio Astronomy Observatory's (NRAO) Astronomical Image Processing System (AIPS) software.

2.3.1.1 Calibration

Accurate interferometric observations require the measurement of the amplitude and phase of the varying electromagnetic field to be measured at each antenna in a consistent manner. Due to the sensitive nature of the equipment therefore involved – the antenna feeds and the electronics behind them – its response to both amplitude and phase of incoming radiation varies in time. Atmospheric turbulence can also effect the accurate recording of phase information.

Primary flux calibration was performed using 3C286. This source is one of 3 which has been extensively monitored with the VLA, and who's flux at any of the VLA's operating frequencies can therefore be calculated using the extended scale of Barrs et al. (1977). Regular observations of this source can therefore calibrate the amplitude response of the system to a source of known flux. By constraining the observations of it to be of such resolution that 3C286 appears as a point source to the interferometer, the phase difference between any two antennas can be assumed to be zero – the plane radio wave from a source at infinity, which is located at the phase tracking centre, reaches all antennas simultaneously at the same phase, once phase lags have been inserted into the signal paths to project all the antennas into a plane orthogonal to the direction to the source. All baselines should then report a flux equal to that calculated. Least squares fitting of the complex gain (amplitude and phase) of each antenna to this model then produces an amplitude calibration scale which can then be extrapolated to the other pointings. This is an oversampled fit, as there are N(N-1) baselines measuring the flux response from N antennas.

The amplitude response of the interferometer is mainly a function of the hardware involved, and controls the flux scale of the resulting map. The phase response, on the other hand, is effected by both the electronics and the atmosphere. Since the recorded phase at any antenna is used to calculate a phase lag relative to another, and therefore the direction from which a plane wave is incident on the (projected) array plane, the accuracy of the recorded phases control the location of flux in any image, and therefore is the main factor in the image quality. An useful analogy from the optical band is that the observations of 3C286 provide the photometric calibration (similar to that from a standard star), while the phase calibration is similar to the focusing of the instrument. Extrapolation of the gain calibration from the primary flux calibrator can remove any smoothly varying phase instability in the electronics, but it cannot account for phase variation caused by the atmosphere. Plasma can cause distortions in the path of an electromagnetic wave. The ionosphere contains plasma which can effect the path of radio waves at the frequency used in radio astronomy. Since interferometry is based in the assumption of a plane wave from infinity incident on a projected perpendicular array plane, the effect of the atmosphere needs to be removed from observations. Any atmospheric disturbance will vary with position on the sky, and so the usual strategy adopted is to observe a known point source a small angular distance from the source of interest, who's radiation detected at the interferometer interacts with the same region of atmosphere as that from the target source. The VLA calibrator source 1327+434, located only 5.8 degrees from C4 and 5.3 degrees from C33, was used for this purpose. It was observed at each frequency, and used to calibrate the phase response of each antenna. Its flux was then bootstrapped to that of 3C286 at each frequency, and the gain solutions extrapolated across the times of the target observations.

The *uv* data were carefully edited to remove corrupted data. Bursts of Radio Frequency Interference (RFI) and cross-talk between the antennas can increase recorded amplitudes above that expected from astronomical sources. Pointing errors, electronics glitches, and correlator problems can reduce the amplitude of a visibility (a single recorded baseline correlation). The observations of the calibration sources – with known structure and therefore known visibility flux and phase response – were inspected to reveal any such problems, and the data from any possibly corrupt antenna or baseline removed ('flagged' in radio interferometry parlance) from both the calibration and target datasets. Calibration was repeated with this newly flagged data, and images made.

2.3.1.2 Imaging and Deconvolution

Since the visibility recorded from each baseline is the response to a sinusoidal wave of sensitivity (who's direction and spatial scale are determined by the direction between the two contributing antennas in the plane projected perpendicular to the vector pointed at the source, and their separation in that plane, respectively), the *uv* dataset can be considered a Fourier transform of the flux distribution on the sky. The process of imaging is the inversion of this Fourier transform. This transform can be evaluated at any arbitrary set of positions, and as such the pixel scale of the resulting image is user defined. The restrictions upon it are computational expense and the fact that the synthesised beam needs to be Nyquist sampled. Pixel scales of 0.3, 0.1, 0.06 and 0.03 were used for the images made at 1.4, 4.8, 8.4 and 14 GHz respectively, as required for the main lobe of the synthesised beam to be covered by at least 4 pixels in each direction.

Since the spatial scale sampled by any one baseline is dependant upon the wavelength, as discussed in Chapter 1, higher frequency, shorter wavelength observations achieve higher resolution with the same array configuration. The resolutions of the clean maps were 1.3, 0.4, 0.2, and 0.1 arcsec in the 1.4, 4.8, 8.4, and 14 GHz bands respectively.

These initial ('dirty') images made from the transform of the *uv* data consist of maps of the brightness distribution of the sky convolved with the 'dirty beam' – the transform of the *uv* coverage achieved during the observation. A hypothetical full *uv* coverage, where an infinite number of infinitesimal antennas covered the *uv* plane and sampled the coherence function at all spatial scales in all directions, would recover the true sky brightness distribution. Such coverage is impractical, so the dirty beam always has some effect which needs to be corrected for. Since the dirty beam is merely the Fourier transform of the known *uv* coverage, its shape can be calculated. This known shape, along with the assumption that the true brightness distribution consists of patches of positive brightness imposed on a background of zero flux allows the 'dirty image' to be cleaned.

The CLEAN algorithm (Högbom 1974; Clark 1980; Schwab 1984) employed in AIPS to perform the deconvolution of the dirty beam further assumes that the true emission can be represented by a series of *point* sources. The dirty image is searched for the highest valued pixels, where the response of the interferometer implies the location of a real source. At this location, a CLEAN component (CC) is placed. The effect of the dirty beam can then be subtracted from this location in either the *uv* or the image plane. In the *uv* plane subtraction method, a model of a point source at

this position, with flux of a user defined fraction of the measured pixel value (typically 10%) is removed from the *uv* database, and the imaging repeated. The new image is searched for the next highest pixel (potentially at the same location), and the process repeated. Deconvolution in the image plane involves broadly the same procedure, except that an image of the dirty beam (constructed by making an image from the observed *uv* coverage, but with visibility amplitudes and phases of 1 and 0 respectively at all samples points) at the location of the point is subtracted from the dirty image. Since re-imaging is not required, this image plane deconvolution is quicker. Once the CLEANing processes is stopped (usually after a set number of iterations or once the flux properties of the CCs reach a certain level), images of the 'clean beam' are placed into the residual map at the locations and with the fluxes of the CCs. This clean beam (also known as the restoring beam) is an estimation of the response of the interferometer to a point source with full coverage inside that of the longest baseline, and is usually a Gaussian, and is similar to the main lobe of the dirty beam.

In practise, a combination of these two forms of deconvolution is performed. Several iterations of image plane CLEANing (minor cycles) remove the effects of the dirty beam in the image plane and then search for further peaks. After a certain number of minor cycles, a major cycle is performed, where point source models of all the identified CCs are removed from the *uv* database, the dataset is re-imaged and further sets of minor cycles performed if required. This system has the advantage of the speed of image plane deconvolution, as simple arithmetic functions are used to locate the CCs, but retains the accuracy of full *uv* subtraction.

The CLEAN algorithm, as described above, is good at deconvolving images that consist mainly of point sources, but performs less well for extended emission like that seen in FRIIs. Other methods exist for the deconvolution of such images, but will not be discussed here as they are not required either here or in later chapters, where the majority of the sources are, to a good approximation, point-like.

2.3.1.3 Self Calibration

The calibration strategy discussed previously performs well for removing amplitude and long timescale phase variations within the electronics, and the phase errors from large sky position variation. However, further calibration can improve the final maps. Variations of the complex gain on timescales shorter than the time between calibrator scans remain in the recorded data. Any variation in atmospheric conditions across the angular distance between the phase calibrator and science

targets also remains. Self calibration is a method that can improve such errors.

If one is confident that the external calibration provides an accurate image of the science target source, this image can be used to construct a model to which the complex gains of the antennas can be fit. This is analogous to the point source model fitting done in the initial calibration stage, and allows the higher time resolution gain solutions to be calculated, as well as calibrating for phase variations within the correct patch of atmosphere. Caution is required in the construction of the model used. The CCs defined in the CLEANing can be used to construct a simple set of point sources, the *uv* modelling of which is not overly complicated. Careful selection of CCs to not include any noise spikes caused by the imperfect initial calibration is required, and the total flux of the model needs to be bright enough to give confident fits.

In none of the observations of C4 was it bright enough to allow self calibration. C33, on the other hand, allowed self calibration at all four frequencies. At 1.4, 4.8, and 8.4 GHz, two iterations of self calibration were performed. Only the antenna phases were allowed to vary in the fit to the first model. This was then re-imaged, and both the phases and amplitudes allowed to vary for the second fitting, though the total amplitude of all visibilities was constrained to not vary. At 14 GHz, only 1 iteration of phase only self calibration was performed. In all cases, good solutions were found when a model of a single point source at the position of C33 was used. It should be noted that if the point source model assumed was incorrect, fitting of the recorded amplitude gains to an observations of a non-point source would lead to poor and or failed solutions.

2.3.1.4 Other considerations

All interferometric observations are modulated in sensitivity by the response of the individual array elements – the so-called primary beam. Since the targets of all observations discussed in this chapter were located at the pointing centre, and are not extended on a scale comparable to that of the primary beam, no correction has been made for this effect.

Other instrumental effects can further remove the response of an array from that of a perfect interferometer. Bandwidth smearing (analogous to chromatic aberration at shorter wavelengths), time delay smearing and 3D smearing can all reduce the measured flux of sources. Since the targets of these observations are all small in extent with respect to the primary beam, and are located at the phase and tracking centre, none of these degrading effects are relevant and so are not considered further

here, but will be discussed in length in later chapters.

Each antenna has two receivers for each frequency – one that is sensitive to right hand circularly polarised radiation, and another for left hand polarisation. The feeds from these receivers can be combined in a variety of ways to acquire different information about the observed targets. However, this thesis is concerned purely with the total flux of each source detected, and so in all cases the two polarisations were combined into images of total intensity, known as a 'Stokes I'.

2.3.1.5 Analysis

The images of C4 at 1.4, 4.8, 8.4 and 14 GHz can be seen in Fig. 2.7, in panels a, b, c and d respectively. Similarly, Fig. 2.8 shows the maps of C33.

As can be seen in Fig. 2.7, there is no emission from C4 visible at 14 GHz. The remaining images were analysed using the AIPS task JMFIT, which fits a two dimensional Gaussian to the pixel values centred on a user defined location. The initial guess for the size and shape of the Gaussian is that of the restoring beam. Least squares fitting of the pixels values predicted by this model Gaussian to the map pixel values is performed. Once a best fit has been reached, the peak pixel value (in Jy beam^{-1}) of the fit is taken to be the peak flux density of the source (this includes information from many pixels, and so is less susceptible to the effects of noise than the single peak pixel in the map). The pixel values of all pixels within the fitted Gaussian are summed and the result divided by the beam area (in pixels) to calculate a total flux density. The size and shape of the fitted Gaussian is compared to the restoring beam to identify any resolution. For high signal to noise observations, this beam shape can be reliably deconvolved from the fitted source shape.

As expected from the self calibration procedure, C33 is unresolved at all four frequencies, confirming that the slight resolution of this source seen at the lower noise levels of the 1.4 GHz deep survey image is merely the result of bandwidth smearing.

At frequencies higher than 1.4 GHz, C4 is too dim to confidently believe the size of the source as deconvolved from the restoring beam by JMFIT. At 1.4 GHz, JMFIT determines a deconvolved size of 1.3 arcsec, and a total flux 44 percent greater that the peak flux, both implying some extension – as seen in the deep survey image.

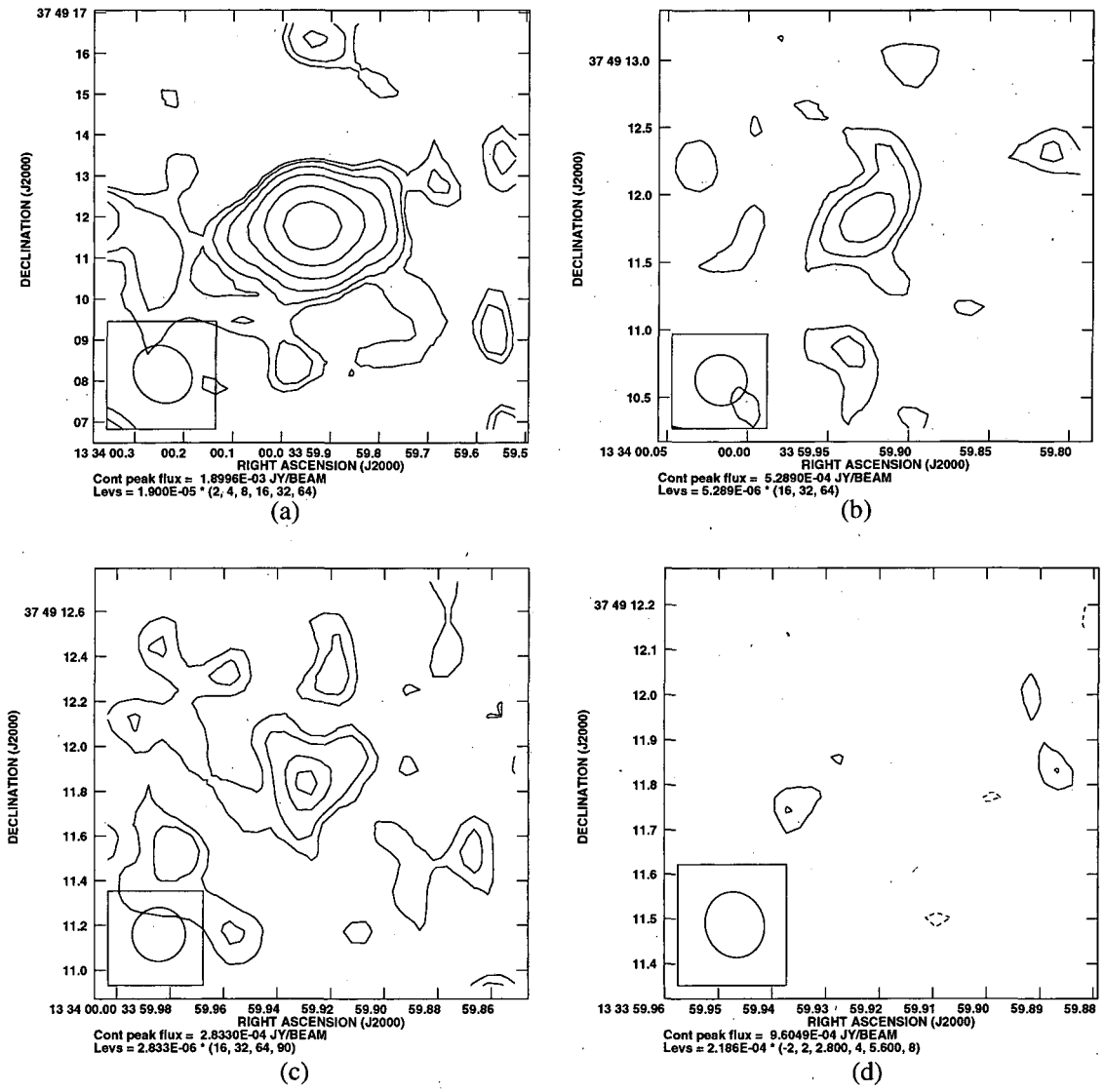

Figure 2.7: Contour maps of the intensity of C4 at 1.4, 4.8, 8.4 and 14 GHz in panels a, b, c and d respectively. The images are 10, 3, 1.8 and 0.9 arcsec on a side. As indicated below each map, contours are shown at 2, 4, 8, 16, 32 and 64 times the peak flux at 1.4 GHz, 16, 32 and 64 at 4.8 GHz and 16, 32, 64, and 90 at 8.4 GHz. In the 14 GHz image of panel (d), contours are shown at -2, 2, $2\sqrt{2}$, 4, $4\sqrt{2}$, and 8 times the rms noise of the image. The size of the restoring beam is shown in the lower left of each panel.

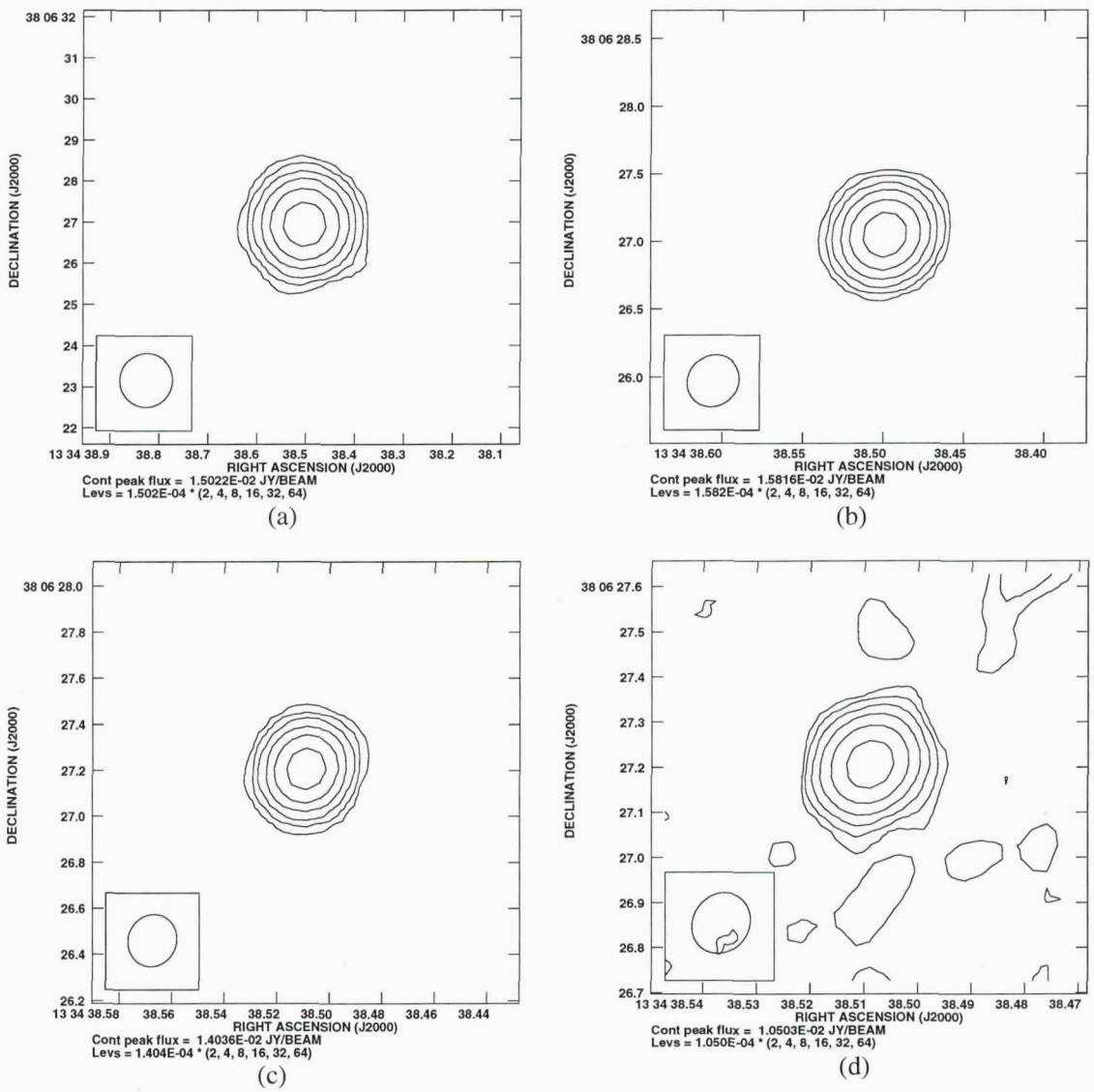

Figure 2.8: Contour maps of the intensity of C33 at 1.4, 4.8, 8.4 and 14 GHz in panels a, b, c and d respectively. The images are 10, 3, 1.8 and 0.9 arcsec on a side. As indicated below each map, contours are shown at 2, 4, 8, 16, 32 and 64 times the peak flux.

2.3.2 610 MHz measurement

Additionally, the XMM survey area is the target of a deep observation at 610 MHz with the Giant Metrewave Radio Telescope (GMRT) of India's National Centre for Radio Astrophysics (NCRA). See Chapters 3 and 5 for details of the observations and data reduction. A preliminary reduction of a portion of the *uv* data taken in 2004 achieved an rms noise level of $\sigma \sim 90\mu$Jy/beam with a $\sim 6''$ beamwidth. Both sources are clearly detected above this noise level, and JMFIT was again used to estimate their properties. Both appear point-like (owing to the low comparative resolution of these observations. It should be noted that these flux measurements were taken $\sim$1 year after those at 1.4, 4.8, 8.4 and 14 GHz discussed above, so variability may have some effect.

2.3.3 Radio Spectra

As discussed in Section 1.7, synchrotron spectra are expected to be of a power-law shape with flux density, $S \propto \nu^{\alpha}$. Functions of this form were fit (using the minimum χ^2 method) to the flux densities reported by JMFIT, and are discussed below.

The computation of a source's radio spectrum requires the measurement of the flux of the source in each frequency to sample that flux equally. As discussed in Section 1.7, this creates and added complication when determining the spectra of sources as measured with interferometer arrays. Since the resolution of an array varies with frequency, the maps shown in Figs. 2.7 and 2.8 are not resolution matched. The fact that interferometer images are constructed from the combination of many individual baselines, each with sensitivity to differing spatial scales means that high resolution imaging can 'resolve out' some flux from extended sources.

2.3.3.1 The Radio spectrum of C33

C33 appears as an unresolved point source at all frequencies, and so the fluxes measured at each frequency (from the images presented in Figs. 2.8) can be directly compared, as each image is sensitive to all flux from the source. These are given in Table 2.1 and shown in Fig. 2.9. Simplistic fitting of the expected spectral function described above to these fluxes gives a spectral index, $\alpha = -0.10 \pm 0.02$ implying a flat spectrum typical of BL Lacs where the jet orientated towards the line of sight contains many electron energy distributions who's superimposed self absorption flattens the optically thin synchrotron spectrum of $\alpha = -0.7$. However, examination

Table 2.1: Radio properties of C4 and C33. Data are the integrated fluxes in mJy. An upper limit of C4 at 2cm is given at the 3 sigma level.

Source	RA (J2000)	Dec (J2000)	S^{20cm} (mJy)	S^{6cm} (mJy)	S^{3cm} (mJy)	S^{2cm} (mJy)
Chandra 4	13 33 59.95	37 49 11.64	2.7	0.8	0.5	<0.6
Chandra 33	13 34 38.50	38 06 27.01	15.3	16.3	14.0.	10.4

of Fig. 2.9 illustrates that such a simplistic spectral model does not adequately describe the data. Above 4.8 GHz, the spectrum falls with frequency, whereas below this frequency the spectrum is flat. Inclusion of the 610MHz data (where C33 is a point source with a flux of 12.6 mJy) further accentuates the departure from a simple power-law. This 610 MHz flux does not conform to the pseudo-simultaneity that the remaining measurements share, and so should be taken with a note of caution. In the catalogue of Seymour et al. (2004), C33 has a 1.4 GHz flux of 10.90 ± 0.02 mJy while here it is measured at 1.4 GHz as 15.3 ± 0.4 mJy, implying that the source does vary on a timescale of 5 years. However, should the source have not varied significantly over the 12 months between the observations at 610 MHz and those of 2003, this measurement confirms the spectral shape below 4.8 GHz is different to that above that frequency. Indeed, the 8.4 to 14 GHz spectral index of C33 is -0.6, close to that expected from optically thin synchrotron emission, and steeper than the index measured between the simultaneous 1.4 and 4.8 GHz observations. It is likely therefore that the frequency range covered here is sampling the turn over in the radio spectrum of C33 from steep to self absorbed. In this property, it is similar to the class of objects known as Giga-Hertz Peaked Sources (GPS). GPS's are radio sources with peaks in their radio spectrum around 1 GHz, steep spectra higher frequencies, and are theorised to be the young jets of FRI and FRII's (Tingay et al. 2003). This spectrum does not sample a sufficiently wide frequency space to categorically state that C33 is a classical GPS, though a GPS would not be expected to show signs of variability (Snellen et al. 2002).

2.3.3.2 The Radio spectrum of C4

C4 shows extended structure at 20cm, both here and in the more sensitive image of Seymour et al. (2004). As such, the possibility of higher resolution images losing sensitivity to the full flux density of the source as the long baseline 'resolve out' flux needs to be considered. The *uv* data used to make the 4.8, 8.4 and 14 GHz images shown in Figs. 2.7 where re-imaged, with the contribution of the longer

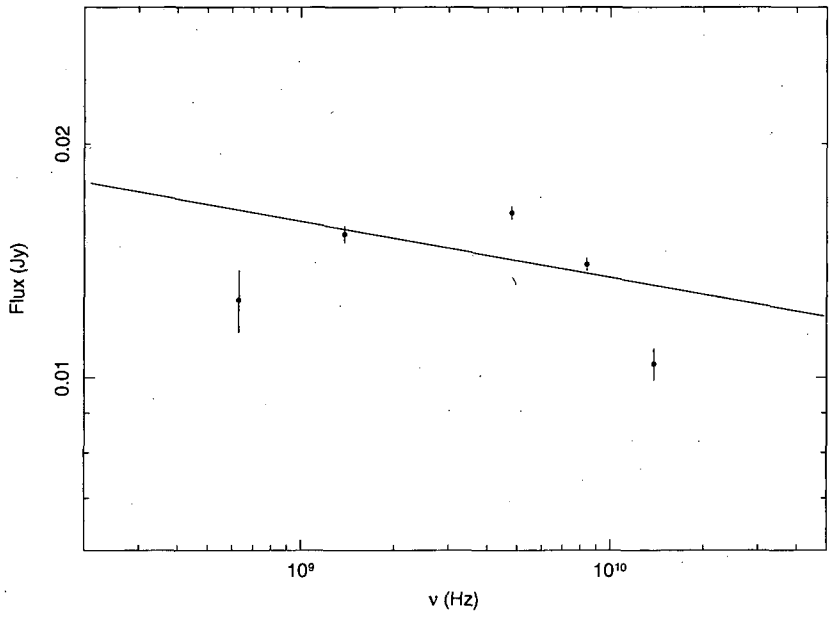

Figure 2.9: The radio spectrum of C33. The line plotted is the spectrum best fit by the data, if a simple power-law is assumed

baselines down weighted. This is known as tapering the *uv* data, and resulted in images of lower sensitivity, but with resolutions matching that at 1.4 GHz. The flux of C4, where it was detected, was measured from these images, and the results are shown in Table 2.1. A 3σ upper limit of the 14 GHz flux was taken and the fluxes fitted with a powerlaw of the same form used for C33. The best fit was gained with $\alpha = -0.70 \pm 0.16$, typical of optically thin synchrotron emission. Including the 610 MHz flux to the integrated flux spectrum gives a fit of $\alpha = -0.57 \pm 0.09$ which can be seen in Fig. 2.10, along with the measured fluxes. This value, derived from non-simultaneous data, is still steep and likely to be due to optically thin emission.

So, while C33 shows the flat spectrum expected from several superimposed, self-absorped synchrotron spectra (with $\alpha > -0.1$), C4 shows a spectrum more akin the canonical optically thin value of $\alpha = -0.7$, with $\alpha = -0.7$ for the fully simultaneous spectrum, and $\alpha = -0.6$ when including the 610 MHz detection made 1 year later.

2.4 Dilution of the Optical Spectra

As presented in Section 2.2.2.3, the optical spectra of both C4 and C33 show none of the emission lines traditionally taken to be signs of AGN activity.

AGN can, however, have other effects on the optical spectrum of their host galax-

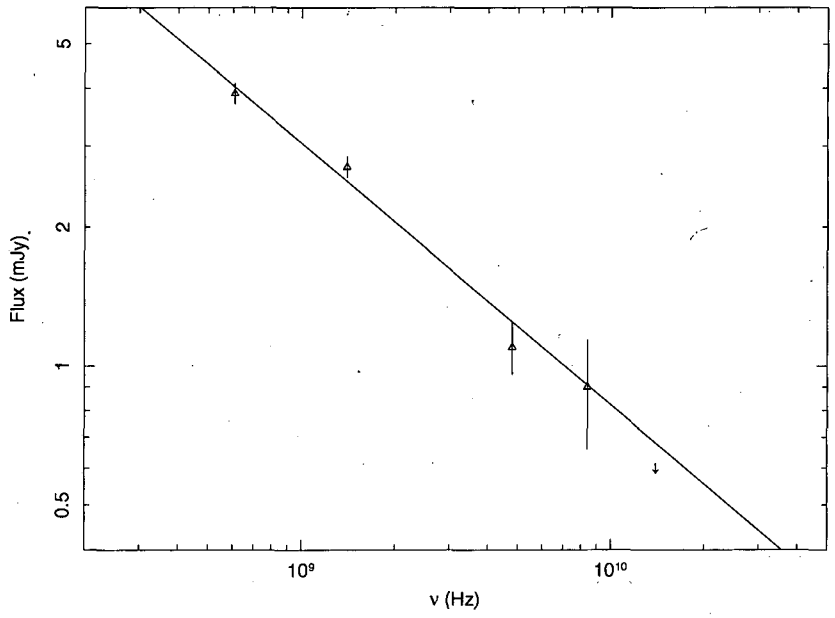

Figure 2.10: The radio spectrum of C4. The line plotted is that of the simple power-law spectrum best fit by the data.

ies. Stellar absorption lines and spectral breaks from interstellar material are the optical spectral components of a quiescent stellar population. Any contribution from an AGN can weaken the appearance of these spectral breaks.

To quantify the degree of dilution by any non-thermal continuum, the 4000 angstrom break contrast of the spectra of C4 and C33 were examined using the contrast parameter in a method similar to that of Anton et al. (2004) and references therein. First order polynomials were fitted to 200 angstrom sections either side of the break and used to calculate C, the contrast parameter, defined as

$$C = (F_\nu^+ - F_\nu^-)/F_\nu^+ \tag{2.1}$$

where F_ν^+ and F_ν^- are the flux densities red-ward and blue-ward of the break respectively. For normal early type ellipticals with no non-thermal dilution, C > 0.4. and $< C >= 0.49 \pm 0.10$ (Dressler and Shectman 1987). The values for C4 and C33 are 0.36 ± 0.17 and 0.48 ± 0.13 respectively. C33 therefore shows no sign of dilution, and C4 shows some marginal signs, but errors on the determination include the possibility of zero dilution.

Hence, any AGN emission is much dimmer than that of the stellar population of C33. This test cannot rule out a marginally detectable AGN contribution to the optical light of C4.

2.5 Discussion

The small angular scale concentration of the radio flux and *Chandra* X-ray flux in the core of each host elliptical galaxy is indicative that the source of the observed activity in both cases is in the nuclear regions. The 1.4 GHz isotropic rest frame luminosities of C4 and C33 at are 5.9×10^{23} and $2.2 \times 10^{24} WHz^{-1}$ respectively, putting them at the lower end of AGN radio luminosity function. The flat radio spectrum exhibited by C33 is indicative of unresolved, optically thick synchrotron radiation, and therefore possibly of a jet aligned close to the line of sight. The core-halo radio morphology of C4 is also indicative of a jet aligned close to the line of sight, however its spectrum implies optically thin synchrotron emission.

At optical wavelengths, no central excess above a de Vaucouleurs profile is seen, and the spectra of the two galaxies show none of the emission line signatures of activity. Neither do the spectra show any significant dilution by a non-thermal continuum. Any such continuum must be of low amplitude relative to the galaxy continuum, either because it is of intrinsically low luminosity or because it is absorbed.

Several possibilities exist to explain the observed properties of C4 and C33. A central engine comprising of an either an intrinsically low luminosity AGN/jet, or a radiatively inefficient advective accretion flow could reside within the nuclei, or a high degree of obscuration could be masking the optical signature of the AGN.

The X-ray spectra of C4 and C33 are much steeper than is expected from an advective dominated flow (di Matteo et al. 1999), ruling out any explanation involving radiatively inefficient accretion.

The lack of absorption seen in the X-ray spectrum of C4, and the small amount seen in C33 are not indicative of an obscured AGN. In the case of any such obscuration, the energy absorbed is re-processed in the infrared, and we would expect brighter measured IR fluxes, especially at 24μm (see Section 2.6 below).

The origin of the X-rays from AGN can either be synchrotron emission from a jet (i.e. a BL Lac type object), or UV disk emission Compton up-scattered by a corona surrounding the central engine. The steep X-ray spectra of both sources suggest that the X-rays originate within a jet.

The likely misidentification of low luminosity BL Lacs inside bright elliptical host galaxies, whose light would far outweigh that of the BL Lac, has been pointed out by Marcha and Browne (1995). Although such objects may have been detected in radio surveys (Caccianiga et al. 2002), they have not yet been detected in X-ray

surveys.

2.5.1 Radio Variability

As mentioned in Section 2.3.3, the sources have been seen to vary. With the combination of all data taken on the 13^H field, 1.4 GHz fluxes can be measured for both sources from 1998 and 2003. Although not resolution matched, 4.8 GHz measurements are available from 1991 and 2003. As already discussed, the 1.4 GHz flux of C33 is measured to have varied from 10.90 ± 0.02 to 15.3 ± 0.4 mJy between 1998 and 2003, which is an increase of ~ 30 percent. The change in its measured 4.8 GHz flux between 1991 and 2003 is +10 percent, and its point-like appearance should mean that differing resolutions (~ 14 and ~ 1.4 arcsec respectively) are not important. The 1.4 GHz flux of C4 was 3.9 ± 0.5 and 2.70 ± 0.14 mJy in 1998 and 2003 respectively, though the relative resolutions may mean that the more recent measurement may underestimate the flux. Its 4.8 GHz flux changes from 2.5 mJy in 1991 to 0.8 mJy in 2003, though once again, the higher sensitivity of the 1991 VLA D-array image to extended structure may explain the difference.

Tapering the 2003 1.4 GHz observations of C4 confirms that the full resolution image at this frequency is not missing flux relative to that from 1998, as the flux remains 2.7 mJy. The large difference between the 2003 VLA A-array 4.8 GHz observations and the 14 arcsec resolution of those conducted in 1991 with the D-array precludes the acquisition from the 2003 data of a comparable flux. The complex environment of C4 is also likely to have caused source confusion to have some effect of its flux in the 14 arcsec resolution image from 1991.

C33 is therefore seen to vary, in a manner not expected to be due to measurement errors, by ~ 20 percent on the timescale of a few years, a behaviour consistent with that exhibited by blazars (e.g. O'Dell et al. 1988). Once again, the observations are such that such a statement cannot be made for C4.

2.6 Spectral Energy Distributions

The wide frequency range over which both C4 and C33 are covered (610 MHz to 10 keV $\sim 1 \times 10^{18}$ Hz) allows the broad spectral energy distribution (SED) of both sources to be studied. Coverage of this range allows the identification of the majority of the potential components of the sources' emission, from synchrotron to accretion disk coronal emission, and the relative contribution of each.

To accurately constrain the effect of any possible AGN components in the optical, further flux measurements in the NIR to UV are required.

2.6.1 Infrared Observations

Fluxes for C4 and C33 at 3.6, 4.5, 5.6 and 8 μm were taken from the catalogue of sources from the IRAC observations of the 13^H field, made using SExtractor in dual image mode with the 3.6μm image used for source detection (see Seymour et al. in prep. for details).

Simple aperture photometry was used to measure the properties of the sources in the 24μm MIPS image. Neither source is detected in the MIPS 70 or 160μm images, either due to confusion by nearby sources (C4), or due to the higher noise level of these images (C33).

Further flux measurements were acquired from the 2MASS archive. Total J, H, and K_s magnitudes for C33 were taken from the Extended Source Catalogue. C4 does not appear in the Extended Source Catalogue, but does have an entry in the point source catalogue.

2.6.2 Optical photometry

The survey field was also observed in u, g, and i bands with the MegaCam instrument on the CFHT in November of 2004. Previously constructed SExtractor catalogues were searched for the counterparts of C4 and C33, giving magnitudes measurements of 21.5, 19.7, and 17.9 for C4 in the u, g, and i bands respectively. The corresponding magnitudes for C33 are 21.1, 19.6, and 17.8.

SExtractor catalogues constructed from the further observations of the 13^H field with SuprimeCam on the Subaru telescope made in the I and Z bands were examined for further optical flux measurements.

2.6.3 SED Construction

The flux measurements mentioned above were combined to form the radio to X-ray SEDs of C4 and C33, which can be seen in Figures 2.11 and 2.12.

2.6.4 SED Modelling

Various simple model SEDs were compared to the data to test weather the various AGN types mentioned previously, at the the levels constrained by the radio and

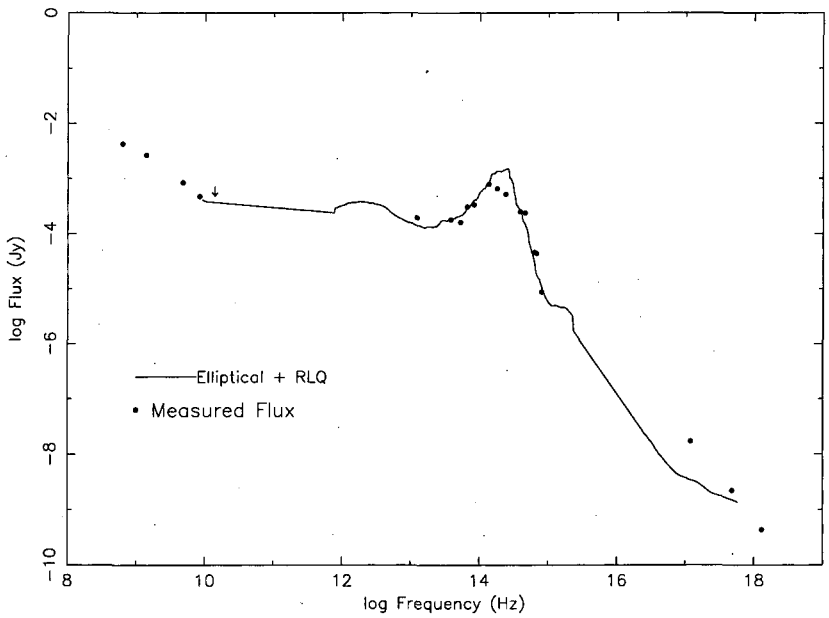

Figure 2.11: The SED of C4 compared to a simple model produced by combining the SED of an elliptical galaxy with the MED of the RLQs of Elvis et al. (1994).

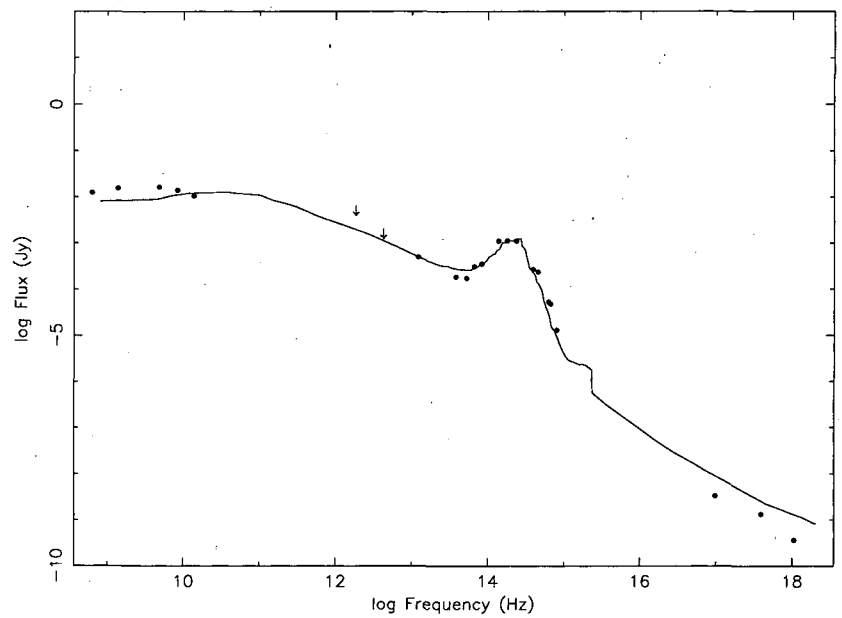

Figure 2.12: The SED of C33 compared to a simple model combining an elliptical galaxy with a low frequency peaked blazar (3C279).

X-ray measurements, could be consistent with there being no signs of AGN activity in the optical.

Models were constructed by summing the contributions of the SED of an elliptical galaxy (taken from Polletta et al. 2000) with examples of various AGN SED. These models were then redshifted to the redshift of the source, and simply examined by eye to determine which broad class best matched the observed SEDs.

Models tested included the Mean Quasar Energy Distributions (MED) of both Radio Loud Quasars (RLQ) and Radio Quiet Quasars (RQQ), taken from Elvis et al. (1994). NGC4945 was used as an example of a highly obscured AGN, with data provided by the NASA Extragalactic Database. Both a high frequency peaked blazar and a low frequency peaked blazar were also tested, Mkn421 (Brodie et al. 1987; George et al. 1988) and 3C279 (Böttcher et al. 2001) respectively. The model SEDs of C4 and C33 can be found in Figures 2.11 and 2.12 respectively. In each case, the most representative model is shown. C33 shows remarkable similarity to a low frequency peaked blazar combined with an elliptical galaxy, further suggesting that its X-ray and radio properties can be explained by synchrotron emission from a beamed jet, originating from a low luminosity AGN which is outshone by its galactic starlight.

The case of C4 is not as clear. Of the simple models tested, that which best resembles the SED of C4 is that of an elliptical galaxy combined with a RLQ. The steep, optically thin radio spectrum is the main reason for this.

2.7 Implications

The steep X-ray spectrum, lack of X-ray absorption, and relatively bright radio emission of C4 suggest the existence of a low luminosity AGN, which is outshone in the optical by the integrated starlight of the host galaxy. The radio core-halo morphology suggests that this jet may be orientated towards the line of sight, though the steep radio spectrum contradicts this. Likewise, the steep X-ray spectrum and relative radio brightness of C33 are each indicative of an unresolved, low luminosity synchrotron jet. The flat radio spectrum, radio variability, and the similarity of the SED of C33 to that of a BL Lac object within an elliptical galaxy imply that the jet is orientated towards the line of sight.

2.8 Conclusions

The calibration, editing, imaging, and deconvolution of data from radio interferometers has been introduced using the example of simple continuum VLA observations undertaken to gain radio spectral information for two interesting X-ray sources. The two sources, identified as quiescent elliptical galaxies in the optical, each have 5 point radio spectra measured. The radio-brighter object (C33) has a flat spectrum, which combined with its radio morphology, optical spectrum, broad-band SED, and indications of radio variability suggest that its X-ray emission may be akin to a low luminosity blazar. The second source (C4) has a steep radio spectrum consistent with optically thin emission, and is more likely to be a low luminosity AGN with small radio jets viewed side-on.

Chapter 3

The 610 MHz Survey of the 1 Hour Field

In this chapter, the results of a deep 610 MHz survey of the 1^H XMM-*Newton* / *Chandra* survey area with the GMRT are presented. The resulting maps have a resolution of $\sim 7''$and an rms noise limit of 60 μJy. To a 5σ detection limit of 300 μJy, 223 sources are detected within a survey area of diameter 64 arcmin. The 610 MHz source counts are computed and compared to those at other radio wavelengths. The well know flattening of the Euclidean-normalised 1.4 GHz source counts below $\sim$2 mJy, usually explained by a population of starburst galaxies undergoing luminosity evolution, is seen at 610 MHz. The 610 MHz source counts are modelled by the same populations that explain the 1.4 GHz source counts, assuming a spectral index of -0.7 for the starburst galaxies and the steep spectrum AGN population that are combined with a flat spectrum AGN population. A similar dependence of luminosity evolution on redshift for the starburst galaxies is found at 610MHz as is found at 1.4 GHz (i.e. the powerlaw index in (1+z), 'Q' $= 2.3^{+0.3}_{-0.5}$).

3.1 Introduction

As introduced in Chapter 1, the nature of the sources that constitute the sub-mJy bump in the 1.4 GHz normalized differential source counts remains unclear after two decades of study. The possibility that galaxies undergoing star formation are responsible provides the potential to use radio observations to measure the star formation rate density in an independent, unbiased manner. A clean sample of galaxies whose radio emission is due to star formation is required for this measurement, and among the many possible discriminants, radio morphology, radio to infrared ratio

and radio spectra are key to determining the nature of the *radio* emission.

The 13^H field is the target of one of the deepest 1.4 GHz surveys (Seymour et al. 2004), and as such has an excellent sample of sources with which to *measure* the star formation rate density, as the sub-mJy population is well sampled. The 1^H field is also the subject of a deep 1.4 GHz survey (see Chapter 4), and both have a plethora of multi-wavelength followup data to assist with source characterisation. Discrimination between AGN and starbursts is key to studying the population which constitutes the sub-mJy bump, and radio spectra are an important indication of the nature of the radio emission. Simple radio spectra can be estimated with flux density measurements at two differing radio frequencies, so 610 MHz observations of both fields have been conducted with the Giant Metre-wave Radio Telescope (GMRT), of India's National Centre for Radio Astrophysics, to compliment those at 1.4 GHz.

At low frequencies (i.e. below 1.4 GHz), where steep spectrum sources such as starburst galaxies are expected to make a larger contribution relative to flatter spectrum AGN, radio surveys have, until recently, been limited to relatively bright flux limits ($\sim$ 2.5 mJy, Valentijn 1980). This limit has been primarily due to the lack of a radio telescope with the sensitivity and angular resolution required to reach to faint flux densities without being limited by source confusion. However, the GMRT now provides the necessary capabilities at low frequency.

The previous deepest radio surveys at 610 MHz were made with the Westerbork Synthesis Radio Telescope (WSRT) in the 1970s. Katgert (1979) combined several such surveys to compute source counts down to 22 mJy. Later WSRT surveys of galaxy clusters achieved lower detection limits (e.g. 2.5 mJy, Valentijn 1980). However, none of these surveys was sufficiently deep to reveal the upturn in the source counts.

This study is part of a new generation of GMRT 610 MHz surveys conducted to compliment higher frequency imaging (Bondi et al. 2007; Garn et al. 2007). In this chapter, the initial 610 MHz survey of the 1^H field is presented. Later chapters will deal with 13^H field and the use of radio spectra of individual sources to discriminate between AGN and star formation. Here, it will be shown that, in combination with similar calculations at 1.4 GHz, modelling of the source counts at 610 MHz can provide information about the average spectral index of the sources which make up the sub-mJy bump.

3.2 Observations and Data Reduction

3.2.1 Observations

In August of 2004, the 1^H field was observed for approximately 4.5 hours at 610 MHz with the GMRT. Unlike the configuration of the VLA used to acquire the observations presented in Chapter 2, the GMRT correlator operates in spectral line mode, splitting the observed bandwidth into many spectral channels and recording visibilies as a function of frequency. Observations were carried out in dual band, spectral line mode, the former to maximize bandwidth and the latter to minimize chromatic aberration.

The principle of interferometry assumes that the radiation being observed and interfered is monochromatic. The spatial scale sampled by each baseline depends upon the baseline lengths (the distances between antenna pairs in the plane project perpendicular to the direction to the source) and the wavelength of the radiation (c.f. resolution $\propto \lambda/D$). The spatial scale used in the inversion back to the sky plane is then calculated using this frequency. However, finite bandwidths are required to actually record any data. Once frequencies other than the central frequency of the band are accepted, the inversion of the fourier transform performed in imaging is no longer entirely accurate. Radiation recorded at $\nu + \delta\nu/2$ (where ν is the observing frequency and $\delta\nu$ is the bandwidth) contributes to the amplitude of the recorded visibility which is then included in the image as a sinusoidal wave whose spatial wavelength is calculated at ν. The actual spatial scale at $\nu + \delta\nu/2$ should be smaller (higher resolution). Similarly, the spatial scale at $\nu - \delta\nu/2$ should be larger that that used for the visibility. The net result is a smearing of the response of the interferometer to a point source, with the magnitude of the smearing being dependent upon the bandwidth of the accepted radiation. Hence, to minimize bandwidth smearing, small bandwidths are ideally used. However, larger bandwidth allows more information about the sky brightness distribution to be recorded. The balancing of these two considerations motivates the recording of visibilities in many narrow channels. In this case, 128 spectral channels of 125 kHz were centred on both 602 and 618 MHz to give a total of 32 MHz bandwidth, with two independent circular polarizations recorded. The GMRT uses separate correlators for the two frequency bands at which data is recorded and transmitted. Known as the Lower and Upper SideBands (LSB and USB), these are the frequency blocks centred on 602 and 618 MHz respectively. Calibration, initial imaging and self calibration were performed on each sideband separately.

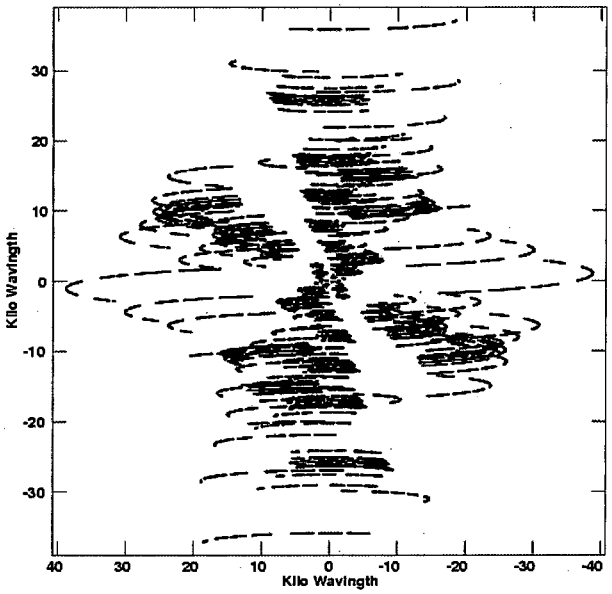

Figure 3.1: The *uv* coverage achieved by the GMRT with the 4.5 hr observation of the 1^H field.

Visibilities were recorded every 17 seconds. Observations were made of the phase calibration source 0054+035 every 40 minutes. The bandpass and absolute flux calibration were provided by several observations of 3C48.

The *uv* coverage achieved during the observations of the 1^H field is shown in Fig. 3.1. While not a complete synthesis (a full rotation cycle), the observing strategy provides reasonable sampling of the *uv* plane, and therefore reasonable sensitivity to extended structure on all position angles.

3.2.2 Calibration

The *uv* data were carefully inspected and bad data flagged. Like at the VLA, the first few visibilities recorded in each scan with the GMRT are poor due to pointing errors. Power outages meant that two antennas were lost throughout. Initial calibration of 3C48 was performed on a dataset created by averaging over 5 RFI free channels in each sideband (centred on 607 and 617 MHz), and calculating a flux density of 29.51 and 29.19 mJy in the LSB and USB respectively from the extended scale of Baars et al. (1977). The baselines used in the antenna gain fitting were restricted to those with *uv* separation less than 30kλ. Several iterations of flagging and calibration were performed to identify and flag bad baselines effected by correllator glitches, power outages, and other problems. Any baseline or antenna which showed suspect

data was removed for all times between those where it was known to be operating adequately.

Similar flagging and calibration iterations were performed on the phase calibration source 0054-035. Located 12 degrees from the centre of the 1^H field and observed frequently between science pointings, these observations provide good calibration for the phase response of the atmosphere and shorter timescale electronic variations.

The amplitude of 0054-035 was bootstrapped to that of 3C48, and calculated to be 4.84 and 4.77 Jy in the LSB and USB respectively.

3.2.2.1 Bandpass Calibration

While the calibration discussed above can correct for variations in the complex gain response of the interferometer elements with time, further calibration is required for the response as a function of frequency across the 256 spectral channels that constitute the observed bandwidth. The previously derived gain responses are defined for the frequency at the centre of those channels averaged to make the calibration dataset. Any variation of gain with frequency can be removed by dividing by the normalized frequency response to a source with a known spectrum. The observations of 3C48 were used for this purpose. The AIPS task BPASS was used to generate an initial bandpass calibration. With this applied, all channels of each baseline were inspected for signs of RFI. Any anomalously high channels were flagged for all times in between those where it was clear that there was no RFI. Also, the unreliable 4 channels with the highest and lowest frequencies in each sideband were flagged. Once all RFI had been removed, BPASS was rerun, and the resultant bandpass calibration interpolated over the observations of the phase calibrator and the science field.

Each baseline of the observations of both of these targets were searched for remaining RFI, and any high channels flagged, leaving a clean and calibrated set of *uv* data from the 1^H field.

3.2.3 Imaging Strategy

All 128 channels of each sideband were combined into one *uv* plane during the imaging process. An image pixel scale of 1 arcsec was chosen to well sample the synthesized beam achieved with the *uv* coverage shown in Fig. 3.1.

The interferometric inversion assumes that radiation from the sky consists of plane waves incident on the projected plane of the interferometer. For this assump-

tion to hold, a requirement is that a plane exist onto which all baselines can be projected though the adding of phase lags to the signals from the various antennas. For an linear array of antennas aligned East-West, this plane is one perpendicular to the Earth's axis of rotation. For snap shots observations with 2 dimensional arrays such as the VLA and the GMRT, this plane is that tangential to the Earth's surface at the location of the interferometer.

For an observation with a 2 dimensional array which lasts for an appreciable fraction of an Earth rotation, the array of baselines occupies the surface of a sphere rather than a plane. Phase delays are inserted into the signal path to translate the instantaneous locations of the antennas into a plane perpendicular to the direction to the source, and altered to keep it pointing thus. This phase 'targeting' can only be pointed in one direction at one time – the phase tracking centre of the field. With observational setups with wide primary beams, like the 45m GMRT antennas operating at 610 MHz (43 arcmin FWHM), sources at the edge of the primary beam are sufficiently far from the phase tracking centre that the plane into which the antennas are projected is not perpendicular to direction to these distant sources. As such, the wavefronts reaching the interferometer plane are not simultaneously co-incident on both elements of a baseline, and the assumption that they are leads to an incorrect location of the recieved flux in an inverted map. The net result is a smearing of flux, the magnitude of which increases with radius from the phase centre and is known as 3D smearing. This effect can be mitigated by altering the phases of the visibilities to reproject the interferometer plane at different angles. In practice, the celestial sphere is approximated by a series of flat image facets with the *uv* data re-phased to the centre of each one. Imaging was therefore performed over a five by five grid of 1024×1024 arcsec facets to ensure that no point on any image would be more that 10 arcmin from a tangential pointing.

Deconvolution of the dirty beam was performed with the Clean algorithm as implemented in the AIPS task IMAGR and discussed in Chapter 2. Special care was taken to remove the effects of bright sources located within the side lobes of the primary beam. Small images were made of all surrounding sources found at 1.4 GHz in the NRAO VLA Sky Survey (NVSS, Condon et al. 1998), including them in the cleaning process to ensure that their side lobes were fully removed from the science images.

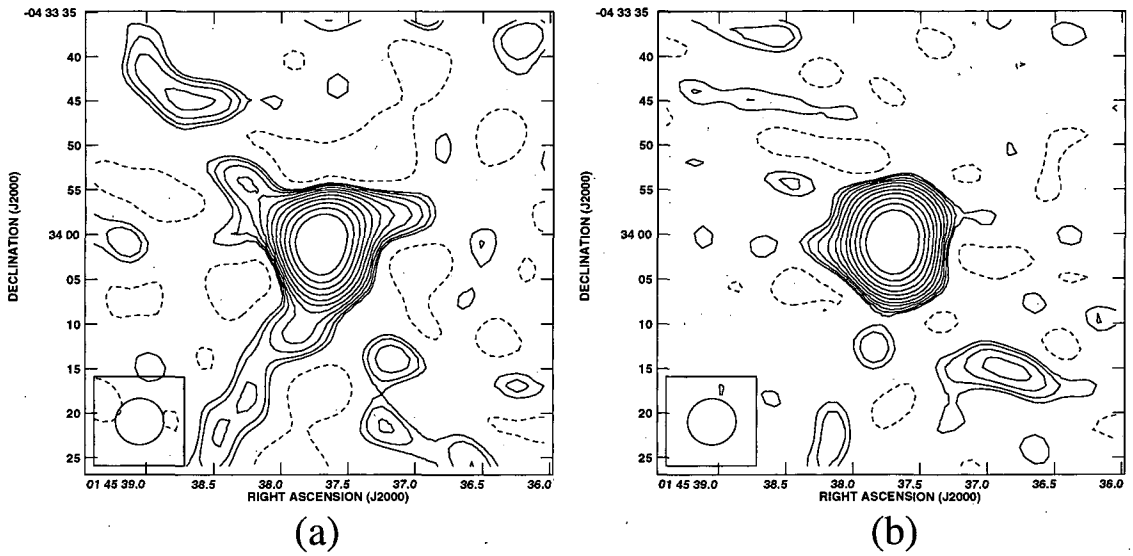

Figure 3.2: The effect of self calibration. Contours of radio brightness in the region surrounding the brightest source both before (panel a), and after (panel b) self calibration. Contours are shown at -2 and at $2^{1+n/2}$ (where n=1,2,3..) times 100μJy.

3.2.4 Self Calibration

As discussed in Chapter 2, self calibration of *uv* data can improve the quality of the images made from it. Once external calibration has enabled the construction of an adequately accurate model of the the sky flux distribution (i.e., an image), this can be used to calibrate out variations in the atmospheric conditions between the phase calibrator and science target, and temporal variations in the electronics on timescales shorter that the time between phase calibrator observations. In practice, the Clean Components (CCs) created during the Cleaning process were used to define a simple model of the sky flux distribution. CCs from each of the 25 primary facets and the images of the 5 brightest external sources were used. All CCs up to the first of negative flux were included. As spectral variation can cause differing fluxes, and therefore model *uv* data, a model was constructed thus for each sideband separately, and used in a least squares fitting of the antenna phases in that sideband. Solutions were computed every 15 minutes. Further iterations of self calibration, with more detailed models and shorter solution intervals, did not further improve the quality of the images.

Contours of the region surrounding the brightest source both before and after self calibration are shown in panels (a) and (b) respectively of Fig. 3.2, and clearly illustrate the improvement in image quality given by improved phase calibration.

3.2.5 Final Imaging

The self calibrated *uv* data for both sidebands were combined using AIPS tasks DBCON, BLOAT, and the customised AIPS task UVFLP, provided by Dave Green (http:www.mrao.cam.ac.uk/~dag/UVFLP), giving a final *uv* dataset of 256 channels. These were gridded onto one *uv* plane, as discussed in section 3.2.3.

Calibrated *uv* data can be weighting in several different ways, each giving the final image different characteristics. In the 'natural' weighting scheme, each visibility is given its intrinsic weight, based on system temperature, which achieves the highest possible sensitivity. The design of interferometer arrays usually means that there are many more short baselines than long ones – meaning that these short baselines dominate the response of the array. This is the case with the GMRT, where half of the antennas are located in a central square. Weighting each visibility by the inverse of the local density of *uv* measurements alleviates this short *uv* bias - giving the longer baselines greater weight and recovering the full resolution of the array. This scheme is known as uniform weighting. Natural weighting therefore produces a map of lower noise, at the cost of resolution. Since it is expected the majority of the sources within our field to be point like (see Seymour 2002) at the highest resolution achievable with the GMRT at 610 MHz of $\sim$ 5 arcsec, resolution is not important. Lower noise, however, improves the detection limit of the survey, and so full natural weighting was used, resulting in a restoring beam of 7.33 by 6.05 arcsec.

The final imaging consisted of 30,000 iterations of Cleaning. Images and CC locations were inspected at 5000 iteration intervals, and the Cleaning process stopped at a stage where a significant number of CCs had been placed in regions not showing 3σ sources.

The maps of the individual facets were combined into a final image using the AIPS task FLATN, with no correction made for the degradation of the primary beam sensitivity. This final map can be seen in Figs. 3.3 and 3.4.

Areas of high noise can be seen around the brightest sources. As discussed in Section 3.3, several of these are extended. The side lobes of extended sources are difficult for the Clean algorithm to remove, as it operates under the assumption that all sources of radio emission are point like. As such, residual effects of the dirty beam are present around the brighter extended sources. The remaining high noise can be explained by small remaining phase errors in the *uv* data.

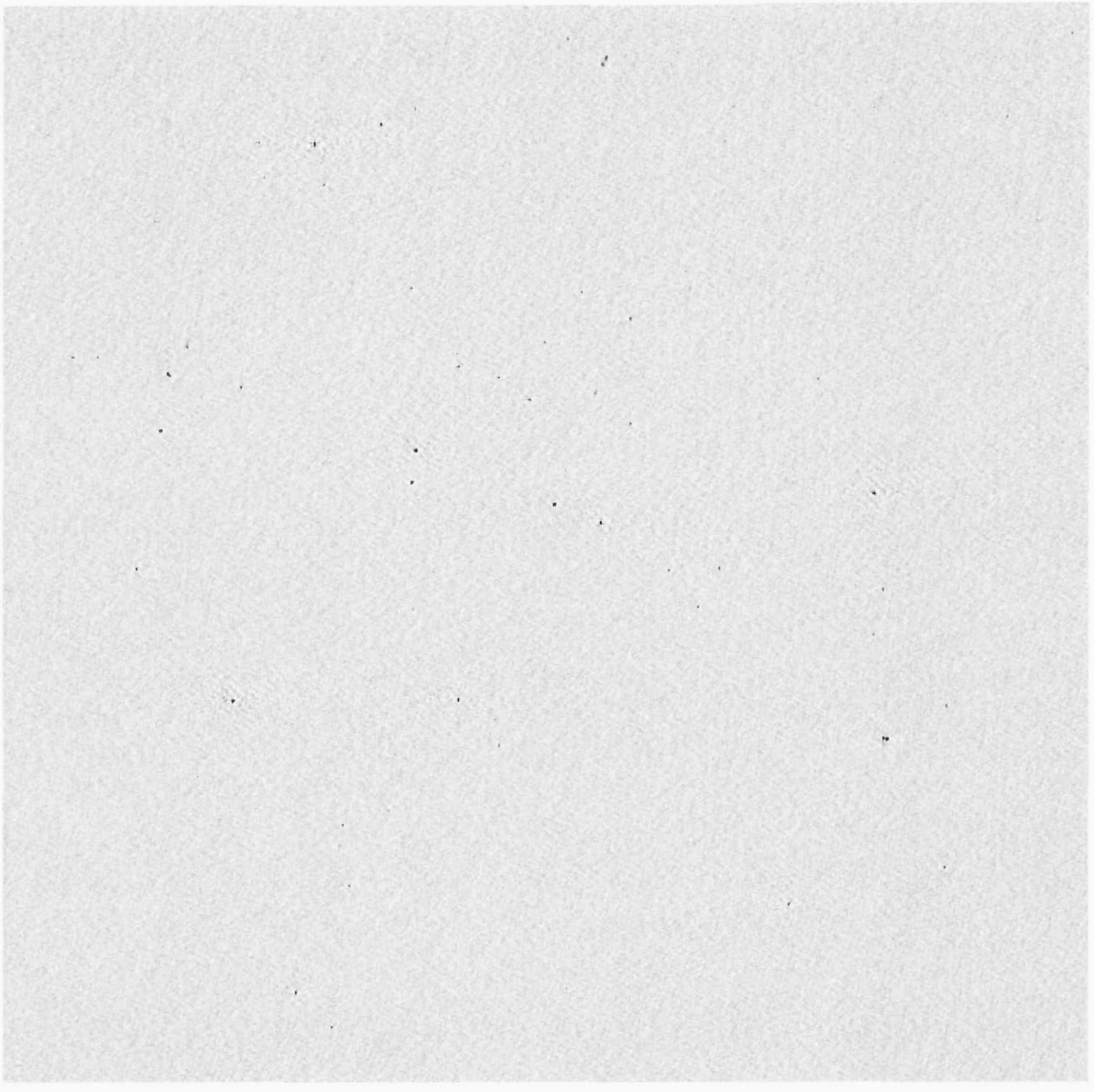

Figure 3.3: The image of the whole primary beam 1^H field at 610 MHz. This image was made with natural weighting, has a resolution of 7.33 by 6.05 arcsec, and has not been corrected for the degradation in sensitivity of the primary beam.

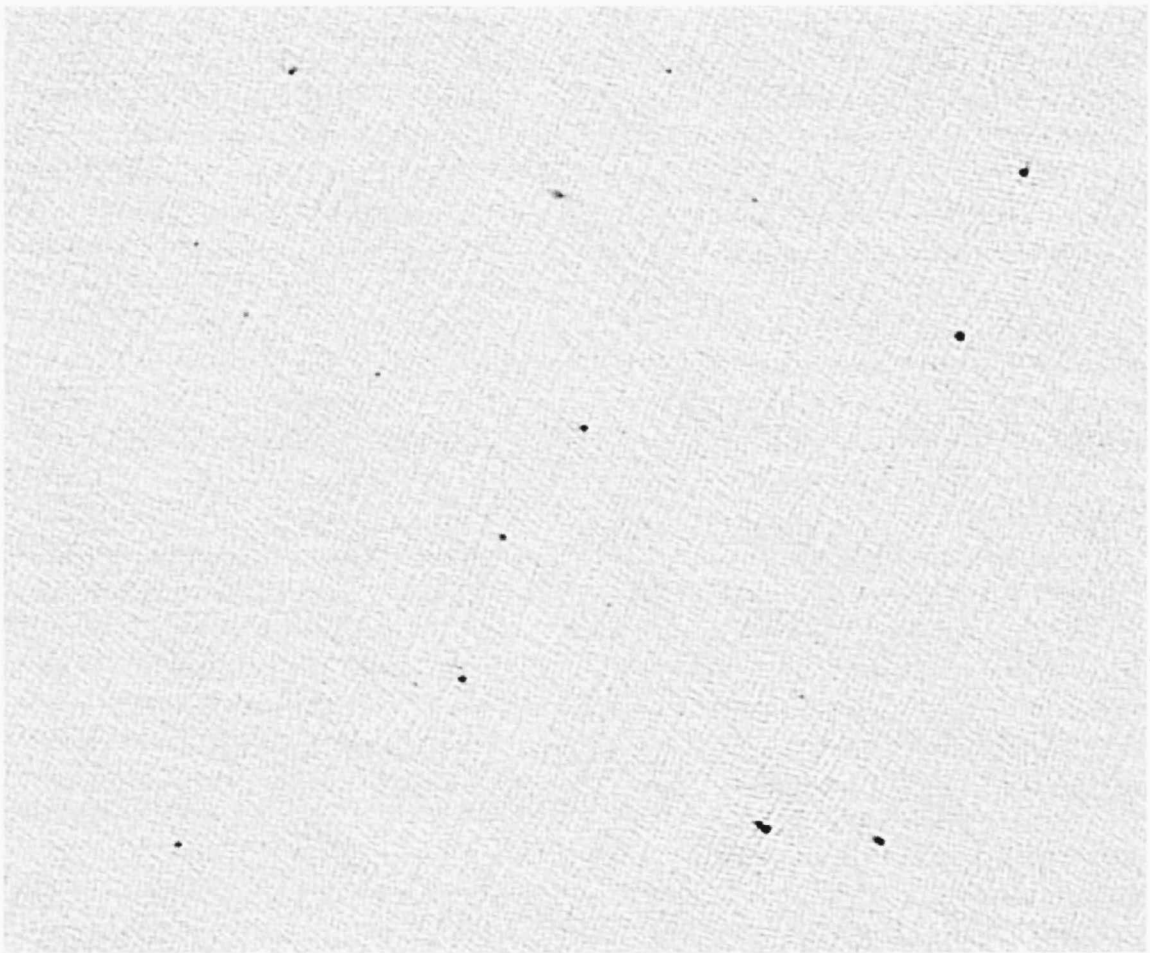

Figure 3.4: A 25 by 20 arcmin region near the centre of the 1^H field at 610 MHz.

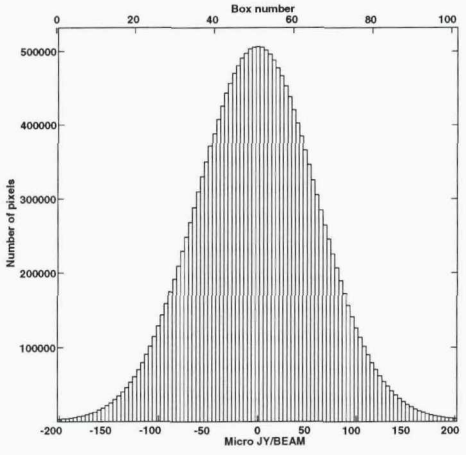

Figure 3.5: Histogram of the pixel values of the science image shown in Fig. 3.3.

3.3 Catalogue Construction

The image shown in Fig. 3.3 is a combination of the radio emission from real sources and noise caused by thermal motion in the electronics, the dynamics of the atmosphere and a few small remaining calibration errors. A rigorous method of differentiating between real sources and noise spikes is required. In the presence of noise with a Gaussian distribution of pixel values, the probability that pixels with values more than 3 times the root mean square (rms, often referred to as σ) value of that distribution are due to noise is 2.3×10^{-3}. Similarly, the probability that a 5σ pixel value is due to noise is 5×10^{-7}. If a pixel with such a value is detected, it is therefore unlikely to be part of the noise distribution, and therefore a real source.

It should be noted that within the 32 arcmin radius of the primary beam, there are $\sim 1 \times 10^7$ pixels, so a very small number of noise pixels may exist above 5σ. Since the source extraction routine used (see below) fits Gaussians to the areas around peak pixels, the effect of noise is averaged over several pixels, reducing the number of spurious sources due to noise.

A histogram of the distribution of pixel values of Fig. 3.3 is shown in Fig. 3.5, and does indeed have a Gaussian shape. The rms of the image, as determined by fitting a Gaussian to this distribution, is 60μJy. A 5σ limit of 300μJy was used as a cutoff between believable sources and noise spikes.

It should be noted that this noise level is greater than that expected. The limiting sensitivity of such an observation is expected to be the thermal noise – random signals generated by the finite internal energy of the electronic components of the

instrument. The theoretical thermal noise level in these images, given the system temperatures claimed at the time, is 23 μJy. The actual noise level achieved is a factor of 2.6 greater than this. At the time of the observations, little was known about the sensitivity of the GMRT when used in long integrations. The effect of RFI on deep observations had not been quantified, and the thermal noise limit had not been tested in deep imaging. During the course of the observations, 2 to 4 antennas were generally not operational at any one time, and RFI caused a not insignificant amount of *uv* data to be flagged. However, neither of these seem likely to have caused such a large increase over the expected thermal noise.

Bondi et al. (2007) have since presented similar observations. In 5.5 hours on source, they reach $\sim 50\mu$Jy, a noise level not dissimilar to that achieved with 4.5 hours here, and a factor of 2.4 greater than the expected thermal noise. However, Garn et al. (2007) reach the thermal noise limits, achieving $\sim 27\mu$Jy with 3.3 hours on source. The major difference between their observations and those presented here is the time between phase calibration scans. Garn et al. (2007) took short scans of a phase calibration source every twenty minutes, whereas these observations of the 1^H field used 40 minute scans, after consultation with local experts, and in an attempt to efficiently exploit observing time. Self calibration assists the removal of any phase instability in the atmosphere and/or electronics between phase calibrator scans, and should therefore alleviate any differences between the two schemes. Once again, Garn et al. (2007) perform self calibration on shorter time intervals that those applied here, though the quality of their image near bright objects (a measure of the quality of the phase calibration) is not dissimilar to that in the image shown in Fig. 3.3, implying that better phase calibration is not the only cause of the difference in sensitivities.

Both the observations of the 1^H field, and those reported in Bondi et al. (2007) were conducted in August of 2004 and reach noise levels of similar factors above the expected thermal noise. The observations reported in Garn et al. (2007) were conducted in March of that year. The stability and sensitivity of the electronics and power supply at the GMRT are not as good as those of the long established VLA (which reaches the thermal limit as a matter of course), due to its location. Given the coincidence of the two August observations both being approximately the same factor worse that those of Garn et al. (2007), it is possible that variation in the performance of the instrument – possibly relating to locate climate variation – is the source of the disparate sensitivities. However, since the source of the thermal noise is a large array of many electronic components, it seems unlikely that such a large

decrease in performance is solely due to the common fluctuation of so many individual elements. The Spitzer First Look Survey field, the target of the observations reported in Garn et al. (2007) is, unlike the 1^H field, in a region devoid of bright sources. Since the thermal noise in the electronics of a radio interferometer effects the quality of the calibration of the antenna gains, and these gains are then used to determine the response of the array to real objects, the dynamic range (the ratio of the brightest part of the image and the noise level) of an image derived from an interferometer is limited by the accuracy of the calibration, and the achievable noise level is therefore limited by the flux of the brightest few sources within the field of view. Within 30 arcmin of the pointing centre of the 1^H field lay 5 sources with peak fluxes greater than 50 mJy beam^{-1} and several other bright sources lie just outside this region, where the array antennas are still sensitive. Since the effect of any residual calibration errors on the noise level of a map is related to the brightness of the sources they are convolved with, these may well make a contribution to the high noise level seen.

The high noise level in the final image is therefore likely to be due to a combination of small remaining residual calibration errors caused by the long times (relative to Garn et al. 2007) between both calibration scans and self calibration solutions, some small variation in the condition of the instrument, and dynamic.range issues caused by the prevalence of relatively bright sources in the field.

3.3.1 Source Extraction

Sources were extracted with the AIPS task SAD. SAD searches throughout an image for pixels greater than a user defined value. The Gaussian fitting routine used in the task JMFIT, and discussed in Chapter 2, is then applied to the pixel values in a 10 by 10 pixel box around the position of that peak pixel. The peak pixel value (Jy beam^{-1}), total flux (total pixel value of all the pixels within the best-fitting Gaussian, corrected by the beam area, in Jy), Right Ascension, Declination, major axis FWHM, minor axis FWHM and position angle of this best fitting Gaussian model are recorded.

The map in Fig 3.3 was searched for all pixels with values (in Jy beam^{-1}) above 270μJy. These were then fitted with Gaussians, and only sources with *fitted* peak pixel values greater than a conservative 5σ limit (of 300μJy) were accepted. Using this fitted value means that information from many pixels is exploited in the determination the critical peak value, decreasing the likelihood that noise spikes could

be erroneously identified as real sources. In the areas surrounding the five brightest sources, detection was performed separately with higher detection thresholds to account for the higher rms noise. Within the 20 percent power radius of the GMRT primary beam at 610 MHz (32 arcmin), 213 sources were discovered above 5σ. In order to determine the success of the SAD source extraction, both the science images and the residual noise maps were carefully inspected. There were 8 extended sources where the Gaussian model fitted by SAD inadequately described the data.

The characteristics of these sources were determined using the AIPS task TVSTAT, which sums all flux within a user defined area. This area was, by hand, defined as that delimited by the 2σ contours of emission from a source. Contour plots of these sources are shown in Fig 3.6. Five of these appear to contain two peaks joined by extended emission, i.e. double lobe sources.

Five further pairs of sources are separated by less than 20 arcsec, and could potentially be components of a double source. Given the density of sources across the entire primary beam, the number of sources detected within 20 arcsec of any one source is expected to be $\sim$0.02 – implying that, from the information contained within the radio image alone, it is likely that these pairs of sources with small separations are related. However, inspection of i' band imaging from SuprimeCam on the Subaru telescope, and the Digitised Sky Survey (DSS) images shows that for four of these cases, potential optical counterpart candidates are present within a few arcsec of one or both sources of radio emission, with no optical object detected between them as a candidate for an AGN giving rise to double lobes – suggesting that they are unrelated.

It should be noted that the high sky density of objects in the i' band image means that chance coincidences are possible. However, where potential optical counterparts are discovered near a radio source contained within one of these 4 potential pairs, they are between 1 and 2 arcsec from the peak of the radio emission. Even at the source densities detected in the deep Subaru i' band imaging, only $\sim$0.1 chance coincidences are expected within this radius.

The exact nature of the objects responsible for the emission in these cases is therefore not clear. Although chance coincidence within the radio image is unlikely, the information from the optical indicates that they may be separate, and so they have been retained as separate sources in the catalogue.

The emission from the two sources constituting the remaining potential double is separated by 17 arcsec and shows no sign of extension in the direction linking the two. No optical counterpart is visible for either emission region, and neither is

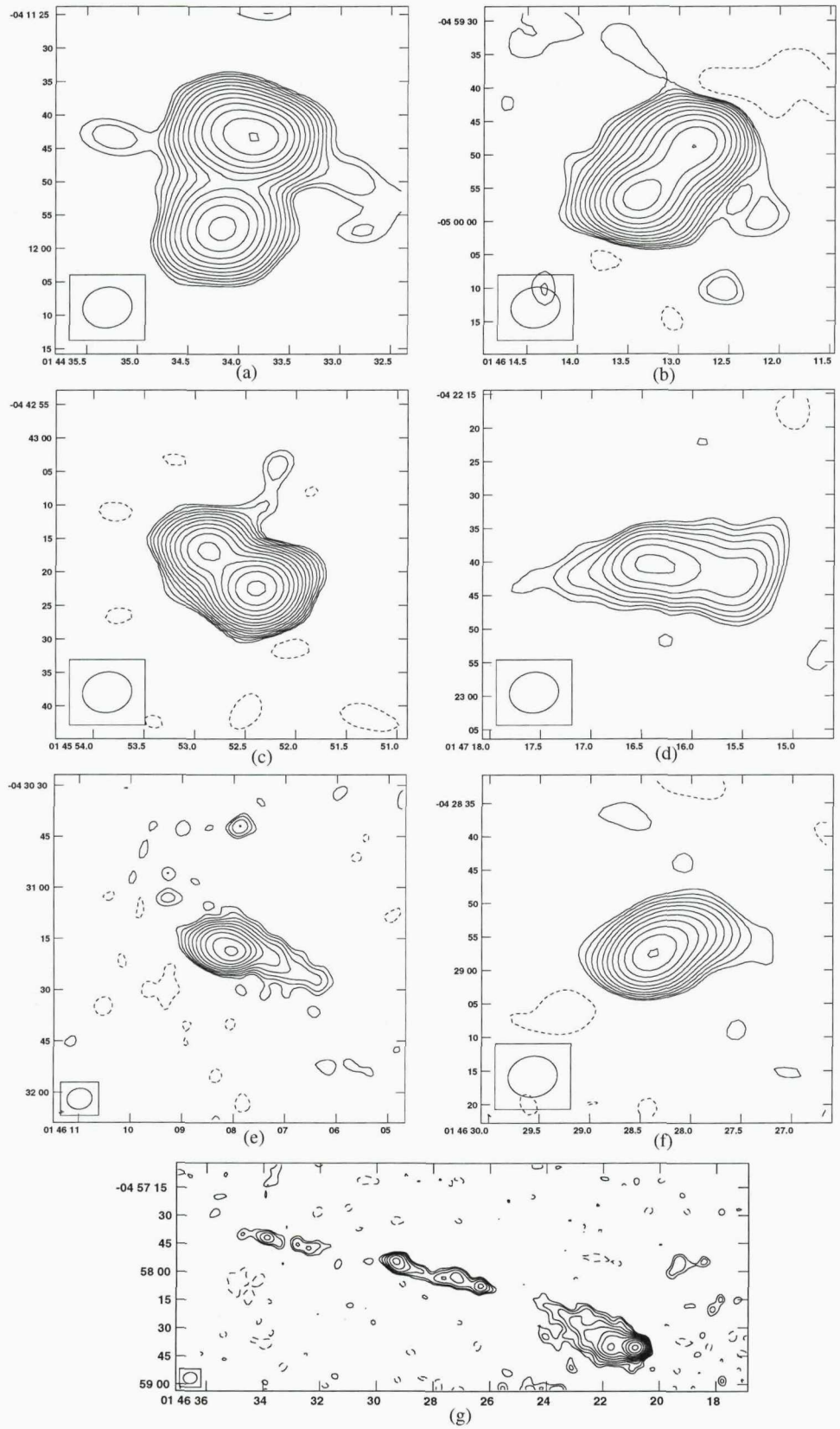

Figure 3.6: Plots of the contours of radio emission from sources 1, 5, 8, 16, 23 and 24 are shown in panels (a), (b), (c), (d), (e), and (f) respectively. Panel (g) shows sources 10 (consisting of the two elongated patches of emission in the middle and top left) and 20 (to the bottom right). Contours are shown at -2, and at $2^{1+n/2}$ (where n=1,2,3..) times the local noise.

any object detected between the two, though the region containing these sources is beyond that covered by the deep i' band image, and so all optical information is provided by the much shallower DSS image. For consistency, they have also been included in the catalogue separately, as sources 106 and 149.

3.3.2 Tapered Map

The incomplete spatial sampling of interferometers means that not all flux is always detected. Baselines with fringes that have spatial wavelengths comparable to, or smaller than, that of a source 'resolve out' some of the flux from that source, as areas of true flux are covered by areas of low sensitivity in the visibility fringe. Large sources therefore invoke a lower amplitude response from the longer baselines in an array, whose inclusion in inversion therefore weakens the response of the entire array to extended emission. This effect is most important, in terms of completeness, at the lowest flux densities where real, low surface brightness, extended sources can be missed.

To search for such low surface brightness extended sources, a low resolution map was made using a similar strategy to that presented in Section 3.2.5, but with the uv visibility data tapered to down-weight the contribution of the longer baselines. Tapering the statistical weights of the visibilities by a elliptical Gaussian with 30 percent radius of 17 and 13 kλ in the u and v directions respectively produced a map with a restoring beam of 12×12 arcsec, and an rms noise of 72 μJy. Ten further sources were discovered above 5σ, and added to the catalogue.

3.3.3 Resolution

In the analysis of low signal to noise detections, noise spikes near a source can cause Gaussian fitting routines such as SAD to poorly fit the width of a source. Since the total flux density is calculated from the sum of the pixel values in the fitted Gaussian (then corrected for the beam size), inaccurate fitted widths necessarily imply inaccurate measured flux densities. The ratio of the total to peak flux density (S_{tot}/S_P) is often used to probe this effect. In Fig. 3.7, S_{tot}/S_P is plotted against S_P. Under the assumption that the measurement of any source as having $S_{tot} < S_P$ is due to the effect of noise, the distribution of S_{tot}/S_P is used to define a criterion for a source to be considered resolved. An envelope that contains 98 percent of the sources with $S_{tot}/S_P < 1$ is defined as $S_{tot}/S_P = 0.88^{2.5/S_P}$, where S_P is measured in mJy. This envelope is then mirrored about $S_{tot}/S_P = 1$. Any source within this

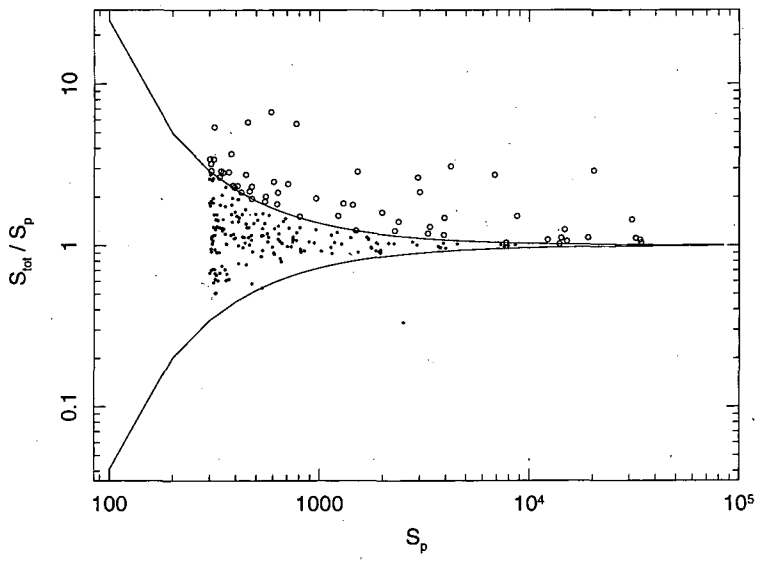

Figure 3.7: The ratio of S_{tot} to S_P as a function of S_P. The lower solid line is the envelope defined to contain 98 percent of the sources with $S_p > S_{tot}$. The upper solid line is that envelope mirrored about $S_{tot}/S_p = 1$, and used to define an unresolved source. Open circles are those sources considered resolved, while dots indicate those considered unresolved.

envelope is considered unresolved, and its fitted peak flux density taken as the best measure of its true flux density.

To confirm that this method offers the most accurate measurement of the flux of a source, a series of simulations were performed. Sources of known flux were inserted into the residual noise of the final image, and their fluxes measured by a variety of methods. One hundred point sources were inserted into the residual map and extracted. This was repeated 5 times each for sources of at 400, 500 and 800μJy. For each source in the resultant map, the integrated flux from SAD, the fitted peak flux from SAD, and the peak pixel value (as would be recorded by SExtractor) were recorded. Fig. 3.8 shows the resulting distributions of flux measurements. The 3 histograms in the left most column are the results of the simulations with sources inserted at 400μJy. The top panel shows the results from the SAD integrated fluxes. The middle panel shows the SAD peak fluxes, and the lower panel the peak pixel values. The central column of histograms are the same plots for sources inserted at 500μJy. The right most three plots are for sources inserted at 800μJy. The results are summarised in Table 3.1. As can be seen in all cases, the integrated fluxes from SAD are indeed less reliable than the various measurements of the peak flux, with offsets between the mean measured flux the known inserted flux, and

	400		500		800	
	mean	σ	mean	σ	mean	σ
SAD S_{tot}	424	131	511	129	804	143
SAD S_p	404	52	500	56	799	57
peak pixel	402	60	499	63	797	64

Table 3.1: The means and standard deviations of the measured fluxes of sources inserted into the residual noise to test the best treatment of sources not considered to be reliably resolved.

have much wider distributions about the mean measured flux. The means of both measurements of the peak flux provide excellent estimations of the true fluxes at 500μJy (8σ) and above. At smaller signal to noise ratios, both suffer from small but similar offsets. At each flux, the distribution is narrower about the mean for the SAD peak fluxes. The single pixel value is more susceptible to the noise influencing the measured value. As SAD fits Gaussians to the pixel values across regions of flux, the noise is effectively averaged over the number of pixels used in the fit, reducing its effect.

3.3.4 Flux Density Corrections

There are a number of potential systematic effects which can cause erroneous measurements of flux density in deep radio observations. The impact of each is evaluated as follows.

3.3.4.1 Bandwidth Smearing

As explained in Section 3.2, bandwidth smearing is the result of channels of finite bandwidth being used in an interferometric inversion that assumes monochromatic radiation, and is analogous to chromatic aberration at shorter wavelengths. Bandwidth smearing manifests itself as a radial blurring where the total flux density of a source is conserved, but the peak flux density is reduced. The effect increases with distance from the phase tracking centre.

The strategy of keeping the 128 channels of each sideband separate until the *uv* gridding process ensured minimal bandwidth smearing, as the bandwidth over which this effect is relevant is the channel width of 125kHz rather than the total sideband bandwidth of 16MHz. Following Chapter 18 of Taylor et al. (1999), and approximating the *uv* coverage to a Gaussian tapered circle, and the bandpass as

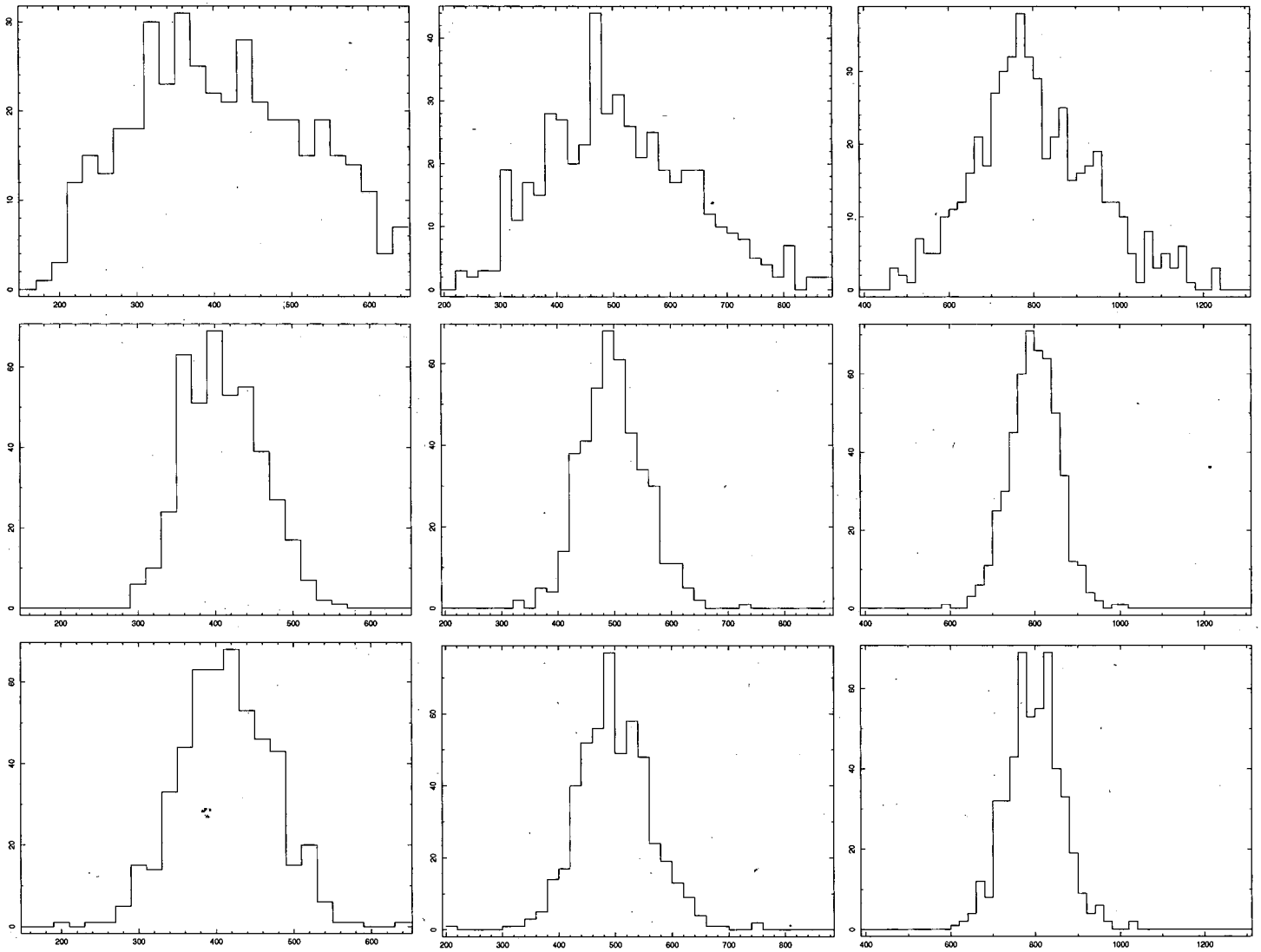

Figure 3.8: The distribution of fluxes of model point source as measured by a variety of methods. From left to right, 400, 500 and 800μJy. Top to bottom SAD total fluxes, SAD peak fluxes, peak pixel values.

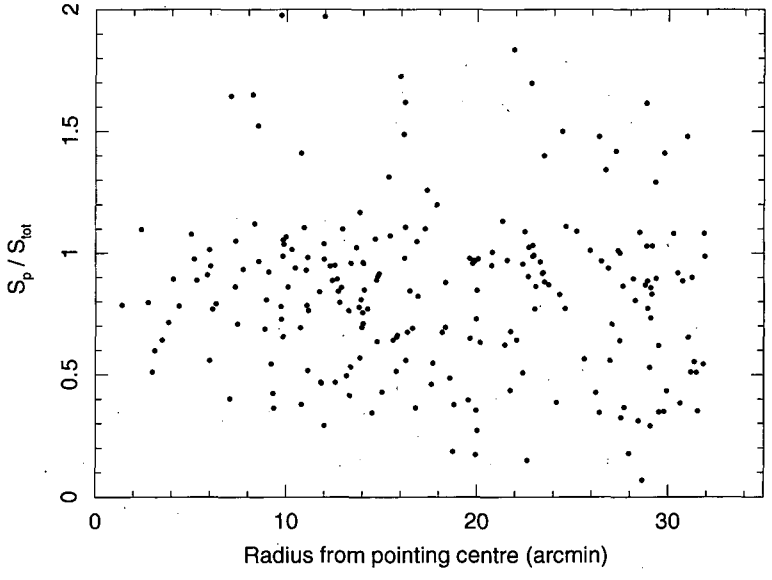

Figure 3.9: The variation of S_p/S_{tot} across the primary beam. Any time or bandwidth smearing effecting the data would manifest itself as a decline of the S_p to S_{tot} ratio with radius, which is not seen.

square, the maximal theoretical effect of bandwidth smearing (at the edge of the survey area) for this data is $\left|(S_p - S_p^{true})/S_p^{true}\right| < 0.0003$ where S_p is the measured peak intensity and S_p^{true} is the true, unsmeared peak flux density. Thus, bandwidth smearing is not considered further.

3.3.4.2 Time delay Smearing

Sources rotate in the sky during the 17 second integration of each of the recorded visibilities. In the simplified case of a target at a celestial pole, the effect is essentially a smearing of each source in a direction tangential to that towards the phase tracking centre. In this simplified case, and approximating to a circular *uv* coverage with Gaussian tapering (again following Taylor et al. 1999), the maximum theoretical effect at the edge of the survey area is a decrease of peak flux density of 4%, which for the majority of sources is smaller than the flux density measurement uncertainties.

Fig. 3.9 shows the ratio of measured peak to measured total flux density of the observed sources. There is no apparent dependence of this ratio on radial distance from the phase tracking centre, as would be apparent should either of these smearing effects be important. A Pearson's correlation test gives a value of -0.07, implying no significant correlation. This result confirms that neither bandwidth nor time delay smearing has a significant effect on the quality of the images, and hence neither

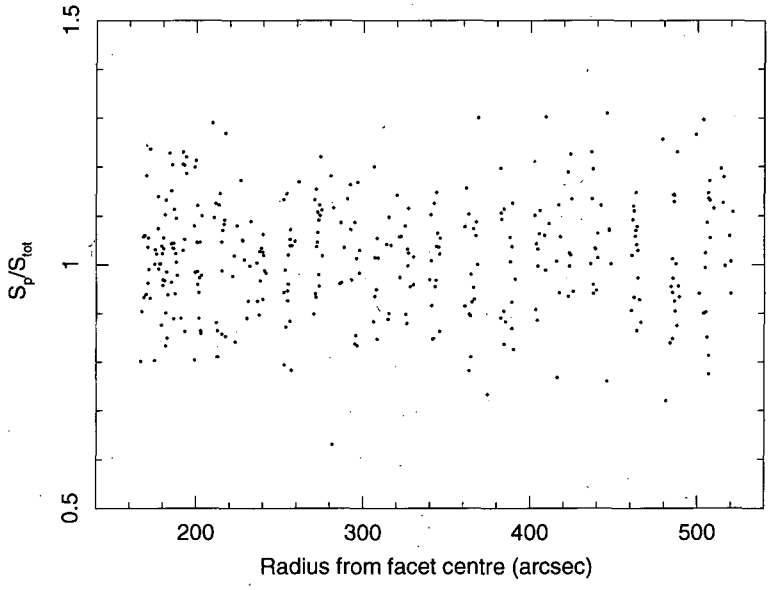

Figure 3.10: The ratio of S_p to S_{tot} for simulated sources, plotted against radial distance from the local facet tangent pointing centre at radii where any effect, if present, would be most noticeable. If 3D smearing were important, S_p/S_{tot} would show a decrease with radius from the local pointing centre.

effect was considered further.

3.3.4.3 3D Smearing

Sources far from the tangential pointing have their flux smeared out due to the inaccuracy of the assumption of a coplanar array in the interferometric Fourier transform relation. The imaging strategy adopted was expected to minimize this effect (see Section 3.2.3), but simulations were carried out to discover the magnitude of any remaining 3D smearing. A series of fake point sources were inserted into the *uv* coverage at a constant radius from the phase tracking centre of the field. This strategy isolates 3D smearing across a facet from the radially dependent bandwidth and time delay smearing across the primary beam. This modified *uv* data was then imaged with the same strategy as used for the science images. The ratio of S_p to S_{tot} of these fake sources showed no dependence on distance from the local facet tangential pointing centre, as seen in Fig. 3.10. A Pearson's correlation test gives 0.03, indicative of no significant correlation. This result confirms that 3D smearing is not important, and so it is not considered further.

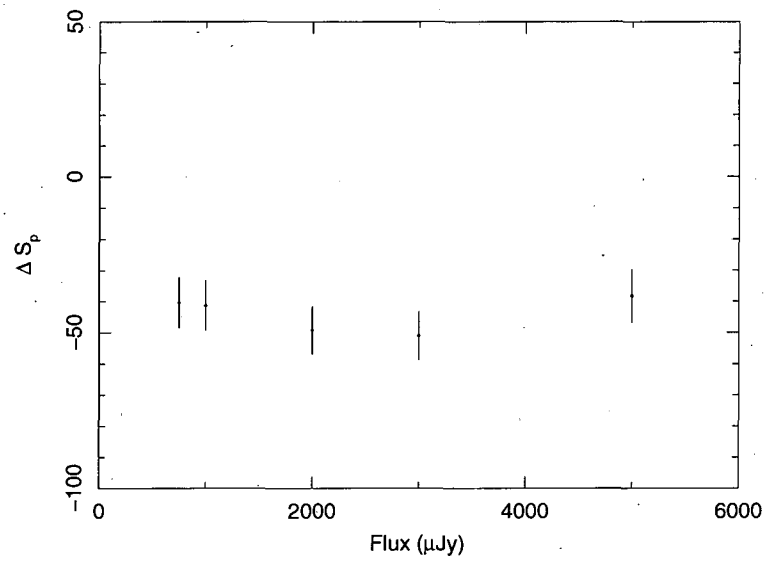

Figure 3.11: The average measured decrease in total flux density, for model sources inserted into the *uv* data, imaged, and detected by SAD, as a function of peak flux density. Error bars give the uncertainty on the determination of the mean.

3.3.4.4 Clean Bias

The Clean algorithm used to deconvolve the dirty beam can, in presence of noise, reduce the measured flux of sources. The superposition of a noise spike with a sidelobe from a real source can lead to the placing of clean components at positions not occupied by real sources. The removal of the dirty beam from this position can then remove flux from real sources, and lead to systematic underestimation of their flux densities (Condon et al. 1998; Prandoni et al. 2000a; Huynh et al. 2005). To quantify the effect of this Clean bias on the source measurements, a series of fake sources with known flux densities were inserted randomly into the full *uv* data at positions not coincident with any real sources. Imaging was then conducted in a manner similar to that used for the science images, and source extraction repeated. The measured flux densities of these model sources were then compared to the input model source parameters and the average offset as a function of flux is shown in Fig. 3.11. The average measured offsets are consistent within the errors on the determination of the mean at each flux. The fitting of a simple constant to the offsets at these fluxes gives 44 μJy as the amount by which the imaging, cleaning and source extraction processes have reduced the true model source flux densities. The flux densities of the real sources have been corrected thus, before any correction for the degradation in sensitivity of the primary beam.

3.3.4.5 Primary Beam Attenuation

Any interferometric observation is modulated by the primary beam pattern of the array elements. The flux densities of all objects were corrected for the GMRT 610 MHz primary beam response using an eighth order polynomial provided by N. Kantharia and A. Pramesh Rao (Addendum to GMRT Technical Report R00185).

3.3.5 Catalogue

The full catalogue is given in Table 3.2, in order of descending flux density, giving: (1) source number; (2) right ascension (J2000); (3) declination (J2000); (4) detection signal to noise ratio; (5) angular size in arcsec (as determined from the deconvolution of the clean beam by SAD, with the exception of the 8 extended sources whose flux densities were extracted using TVSTAT, in which case the distance in arcsec between the 2σ contours along the line of greatest extent is given) for those sources considered reliably resolved; (6) peak flux density, S_p in μJy beam^{-1} for those sources considered reliably resolved; (7) flux density, S in μJy, the best determination of the flux of the source; (8) error on S_{tot} for those resolved. Sources whose properties were extracted by hand using TVSTAT are marked with a †.

3.4 Source counts

This 610 MHz survey was designed to compliment the deep imaging at 1.4 GHz and provide spectral information to be combined with high resolution radio morphology and observations at other wavelengths to determine the nature of the faint radio population. Such comparison will be presented in later chapters, while this chapter shall concentrate upon the ability of this survey to probe the faint source counts at 610 MHz.

Integrated source counts, the surface density of sources apparently brighter than a certain flux, are used in many wavebands to characterize the population of sources found in survey images. Differential source counts approximate the number of sources at each flux by counting the number of sources within flux bins. The differential source counts from deep surveys are a probe of source evolution and cosmic dynamics.

Early radio surveys detected evolution in the luminosity of the AGN (e.g. Longair 1966) which formed the majority of the detections. An upturn in the number of sources at what, at the time, were considered low flux densities was interpreted as

Table 3.2: The complete catalogue of sources. Source Number, RA, Dec, detection signal to noise ratio (SNR),angular size in arcsec (see Section 3.3.5) and peak flux density S_p in μJy beam^{-1}, both for sources considered reliably resolved, best flux density S in μJy, and the error on the best determination of the flux density, in μJy.

Source	Right Ascension	Declination	SNR	θ (arcsec)	S_p (μJy b^{-1})	S (μJy)	ΔS (μJy)
1 †	01:44:34.04	-04:11:50.2	338.9	32.0	55383.1	160804.3	450.6
2	01:47:15.93	-04:50:09.8	537.8	3.73	138106.8	153572.6	285.5
3	01:44:44.31	-04:55:34.9	562.6	3.67	72536.4	78817.5	140.0
4	01:45:40.56	-04:12:35.0	570.5	2.29	68278.8	71533.8	125.3
5 †	01:46:13.17	-04:59:53.4	114.2	19.51	20786.1	56590.3	453.9
6	01:43:49.26	-04:18:17.9	237.2	3.29	50278.1	56077.4	236.3
7	01:47:21.13	-04:45:41.6	204.4	3.07	48648.2	52916.9	258.8
8 †	01:45:52.63	-04:43:19.1	515.1	5.16	35946.5	51873.4	99.0
9	01:45:57.8	-05:00:26.4	252.4	2.23	42551.8	45389.3	179.7
10 †	01:46:21.34	-04:58:39.7	70.5	21.23	12659.7	38896.4	505.1
11	01:45:20.33	-05:02:00.9	126.9			22403.5	176.4
12	01:45:32.86	-04:30:54.0	318.3	3.07	19557.7	21884.5	68.7
13	01:45:37.7	-04:34:00.8	246.2	4.27	14965.6	18768.6	74.9
14	01:46:09.6	-04:55:3.0	143.1			17914.9	125.1
15	01:44:44.84	-04:40:26.8	232.8	2.5	16903.4	17331.7	74.4
16 †	01:47:16.3	-04:22:40.7	25.3	12.71	5728.9	16109.8	593.5
17	01:44:43.09	-04:07:45.6	65.3	3.13	13582.1	15794.5	241.6
18	01:45:43.78	-04:43:36.3	146.0	7.01	9982.9	15183.6	100.5
19	01:44:14.79	-04:45:06.5	132.4			14394.5	108.7
20 †	01:46:29.25	-04:57:55.4	12.8	10.24	2516.3	13578.0	1000.8
21	01:46:15.42	-04:40:29.6	129.3	1.74	9875.9	10289.8	79.5
22	01:45:01.1	-04:59:47.7	61.3			9650.2	157.2
23 †	01:46:08.1	-04:31:17.9	49.2	10.51	3490.1	9157.1	173.5
24 †	01:46:28.34	-04:28:57.1	65.8	7.38	5696.1	8420.8	123.6
25	01:46:06.1	-04:35:44.2	122.2			8362.8	68.4
26	01:47:06.7	-04:53:31.5	16.0	10.6	4292.4	8233.8	487.9
27	01:47:28.46	-04:41:37.2	20.5	7.04	5334.7	8058.5	379.6
28	01:44:05.8	-04:24:36.6	9.7	27.92	1273.8	8019.3	743.1
29	01:45:14.49	-04:12:00.1	62.9			7892.5	125.4
30	01:45:20.36	-04:22:58.3	50.2	8.67	3671.0	7823.5	147.9
31	01:46:36.93	-04:43:39.7	75.7			7707.5	101.8
32	01:47:11.08	-04:50:18.3	30.9			7343.6	237.1
33	01:47:25.36	-04:43:23.2	28.0			6987.8	249.2
34	01:47:04.7	-04:49:29.2	32.0			6386.3	199.2
35	01:45:02.3	-04:12:38.6	48.6			6115.7	125.8
36	01:46:11.81	-04:16:21.7	33.1	8.33	3825.1	6099.6	177.6
37	01:43:54.29	-04:18:25.2	24.9	3.78	4888.8	6034.9	238.0
38	01:43:54.45	-04:47:44.4	35.6			5929.3	166.3
39	01:45:10.0	-04:24:22.8	56.0	4.52	4010.5	5236.4	91.8
40	01:45:52.66	-05:05:24.3	10.4	7.85	2914.3	5122.7	468.1
41	01:46:41.06	-04:25:12.2	46.3			5079.1	109.6
42	01:45:04.4	-04:03:18.8	17.0			4885.3	287.0
43	01:46:12.35	-04:37:48.5	54.8	3.8	3990.4	4732.0	86.2
44	01:45:45.17	-04:58:54.7	32.5			4681.4	143.6
45	01:46:18.47	-04:19:28.8	7.5	19.57	854.7	4588.2	548.6
46	01:44:49.19	-04:31:43.9	66.5			4584.5	68.8
47	01:46:22.29	-04:10:09.1	23.5			4581.7	194.5
48	01:44:31.42	-04:36:49.5	39.7	6.58	3148.9	4405.4	108.8

Table 3.2 continued

Source	Right Ascension	Declination	SNR	θ (arcsec)	S_p (μJy b^{-1})	S (μJy)	ΔS (μJy)
49	01:45:46.33	-04:13:41.0	37.7			4366.7	115.6
50	01:45:19.85	-04:26:20.3	65.0			4339.5	66.6
51	01:47:04.1	-04:50:55.8	18.9			4062.0	214.9
52	01:44:10.86	-04:48:12.2	31.1			4057.3	130.3
53	01:44:31.97	-04:43:27.4	24.0	7.94	2112.3	3731.1	150.1
54	01:44:32.53	-04:37:44.6	38.1	3.61	3010.3	3705.8	95.5
55	01:47:19.81	-04:42:1.0	5.0	12.71	1180.7	3694.7	677.8
56	01:45:09.3	-04:17:33.5	21.6	7.17	2042.5	3679.3	161.3
57	01:44:46.36	-05:02:24.7	5.6	11.98	1376.2	3677.6	601.7
58	01:46:15.28	-05:00:27.2	5.0	14.81	1128.4	3312.9	602.0
59	01:46:36.53	-04:24:58.0	31.4			3300.8	104.9
60	01:47:33.08	-04:32:01.3	6.1	23.87	1127.7	2991.8	540.3
61	01:45:00.0	-04:11:20.3	20.2			2878.9	141.9
62	01:46:19.59	-04:08:40.9	13.0			2841.9	217.3
63	01:46:40.35	-04:30:40.0	5.2	20.76	575.8	2804.8	485.0
64	01:45:39.55	-05:00:43.3	6.8	19.37	1230.9	2728.2	453.5
65	01:44:43.33	-04:07:55.7	12.5			2674.2	214.1
66	01:45:27.68	-04:37:41.3	7.9	14.76	1418.4	2663.0	384.4
67	01:46:02.8	-04:37:18.6	6.4	18.44	1176.6	2614.1	456.9
68	01:46:53.83	-04:36:42.2	6.6	17.27	1195.6	2589.6	444.6
69	01:44:29.93	-04:20:38.9	6.3	13.99	728.7	2490.6	362.6
70	01:44:50.17	-04:46:22.7	28.6			2357.4	82.3
71	01:46:35.59	-04:32:13.6	25.4			2339.7	91.9
72	01:44:33.15	-04:05:45.3	7.7			2334.2	302.1
73	01:46:21.85	-04:34:42.5	29.3			2310.7	78.6
74	01:45:59.78	-04:28:57.2	32.6			2277.9	69.8
75	01:46:20.86	-04:24:26.5	24.8			2245.6	90.3
76	01:46:15.59	-04:40:15.4	11.8	10.81	950.8	2210.5	175.8
77	01:45:22.17	-04:22:47.6	29.5			2190.5	74.1
78	01:46:29.58	-04:46:50.2	19.6			2078.0	105.6
79	01:47:10.9	-04:42:28.5	11.2			2037.8	177.6
80	01:43:31.56	-04:35:51.3	8.8			1913.4	216.3
81	01:47:20.45	-04:48:32.2	6.4			1886.5	279.2
82	01:46:31.82	-04:33:35.0	21.2			1869.6	87.9
83	01:46:34.24	-04:33:44.5	7.4	14.5	716.5	1859.3	232.2
84	01:44:40.94	-04:51:01.1	5.8	19.35	673.8	1770.8	283.8
85	01:45:34.23	-04:19:00.1	13.4	5.86	1185.0	1759.3	127.2
86	01:45:04.0	-05:01:42.8	8.9			1747.4	193.9
87	01:47:00.8	-04:34:13.7	12.4			1695.7	136.1
88	01:47:22.37	-04:39:01.3	7.4			1681.9	221.6
89	01:46:0.0	-04:26:13.3	10.5	8.55	814.9	1675.6	150.0
90	01:45:52.86	-04:31:50.6	10.1	9.59	695.0	1662.2	153.9
91	01:47:21.78	-04:48:40.2	5.2			1627.1	299.1
92	01:43:29.38	-04:34:40.3	6.8			1603.8	233.6
93	01:43:31.15	-04:34:44.0	7.2			1598.4	222.4
94	01:45:39.32	-04:17:21.7	7.7	10.49	772.3	1596.5	194.6
95	01:47:12.91	-04:18:27.8	5.5			1580.5	283.6
96	01:44:48.09	-04:23:13.9	7.9	8.8	703.1	1557.4	184.2
97	01:46:40.06	-04:30:04.7	5.5	12.05	610.1	1503.8	251.4
98	01:44:28.84	-05:00:52.6	5.9			1503.4	236.8
99	01:46:00.1	-04:44:57.9	9.2	8.3	753.8	1467.1	150.5
100	01:46:37.38	-04:59:47.8	5.2			1429.2	256.1
101	01:46:05.7	-04:15:14.1	11.5			1404.0	118.9

Table 3.2 continued

Source	Right Ascension	Declination	SNR	θ (arcsec)	S_p (μJy b^{-1})	S (μJy)	ΔS (μJy)
102	01:46:16.36	-04:39:58.9	9.1	8.12	753.0	1363.5	141.9
103	01:45:01.9	-04:44:55.3	5.2	11.73	433.0	1355.6	238.4
104	01:47:17.19	-04:35:01.8	6.8			1344.8	196.4
105	01:46:04.7	-05:02:57.0	5.2			1327.7	251.9
106	01:44:28.99	-04:52:11.8	9.9			1305.4	131.5
107	01:45:49.67	-04:40:50.9	19.1			1301.9	68.1
108	01:45:31.02	-04:48:40.4	15.7			1282.7	81.5
109	01:43:58.77	-04:22:23.5	8.0			1281.2	160.6
110	01:47:15.38	-04:24:21.8	5.5			1281.1	226.2
111	01:45:53.26	-04:31:24.8	19.0			1271.1	66.7
112	01:45:58.83	-05:01:00.5	6.3			1258.2	192.0
113	01:45:24.72	-04:47:28.8	16.0			1244.8	76.9
114	01:45:52.63	-04:49:07.1	6.8			1241.8	207.4
115	01:45:38.31	-04:20:28.7	5.1	9.96	462.7	1232.1	224.3
116	01:45:58.66	-04:14:52.6	10.1			1221.5	120.3
117	01:44:26.48	-04:39:23.8	6.7			1220.1	210.8
118	01:46:46.48	-04:13:43.7	5.3			1219.1	229.7
119	01:45:10.1	-04:15:22.3	11.0			1203.9	108.9
120	01:45:02.9	-05:03:35.2	6.6			1201.0	211.2
121	01:47:16.85	-04:44:22.5	5.0			1193.2	223.8
122	01:46:17.36	-04:33:52.9	7.0	8.76	577.5	1172.1	156.5
123	01:45:35.85	-04:37:49.2	6.4			1165.7	214.9
124	01:45:23.79	-04:07:44.6	6.3			1160.3	209.0
125	01:45:49.09	-04:58:39.9	7.5			1155.7	151.4
126	01:44:39.5	-04:37:58.1	14.9			1142.9	76.9
127	01:46:52.34	-04:29:29.7	8.8			1114.2	125.7
128	01:46:19.02	-04:40:36.1	13.4			1113.5	81.6
129	01:46:59.14	-04:36:44.6	7.9			1084.0	136.6
130	01:45:21.28	-05:01:21.9	5.7			1069.4	187.5
131	01:46:08.3	-04:49:18.0	10.8			1064.2	98.5
132	01:46:58.83	-04:36:58.8	7.7			1052.1	134.7
133	01:45:25.16	-04:52:02.7	10.9			1049.1	95.9
134	01:46:45.23	-04:32:20.1	9.6			1045.8	105.7
135	01:45:12.74	-04:57:56.6	7.1			1022.4	142.6
136	01:45:16.98	-04:54:28.9	9.1			1017.6	109.0
137	01:44:51.87	-05:00:29.9	5.1			1015.0	199.4
138	01:44:09.8	-04:40:45.7	8.9			1011.2	109.1
139	01:45:15.3	-04:50:54.1	10.6			983.8	91.6
140	01:45:09.2	-04:47:46.8	11.9			977.4	80.8
141	01:44:46.38	-04:42:05.6	12.4			971.1	78.2
142	01:45:09.4	-04:43:31.0	13.5			970.9	71.9
143	01:46:04.2	-04:40:41.1	12.9			963.6	74.5
144	01:45:44.11	-04:58:46.1	6.0			937.6	155.8
145	01:47:08.3	-04:42:17.2	5.0			927.1	185.4
146	01:46:04.8	-04:21:27.7	10.0			922.6	91.6
147	01:45:16.32	-04:30:27.2	14.1			921.2	65.3
148	01:46:04.3	-04:39:05.6	12.2			894.3	73.2
149	01:44:29.96	-04:52:21.5	6.5			888.6	135.9
150	01:46:06.7	-04:24:49.9	10.6			882.3	81.7
151	01:44:54.23	-04:10:25.0	5.0			875.0	166.5
152	01:45:17.55	-04:34:15.9	13.5			866.8	63.9
153	01:46:13.57	-04:20:31.6	8.4			865.7	99.9
154	01:44:45.21	-04:33:39.6	10.8			799.2	74.1

Table 3.2 continued

Source	Right Ascension	Declination	SNR	θ (arcsec)	S_p (μJy b^{-1})	S (μJy)	ΔS (μJy)
155	01:45:49.13	-04:49:07.1	8.9			795.2	89.3
156	01:45:03.0	-04:34:15.2	11.7			783.5	66.9
157	01:47:01.2	-04:29:01.1	5.0			777.9	145.3
158	01:44:55.78	-04:12:17.3	5.1			775.7	149.7
159	01:44:51.16	-04:56:24.7	5.2			765.7	147.6
160	01:44:45.56	-04:27:49.5	9.5			754.6	79.0
161	01:45:26.94	-04:47:25.1	9.4			752.5	79.6
162	01:46:03.0	-04:24:09.4	8.7			736.1	83.9
163	01:45:45.22	-04:12:19.5	5.2			734.5	141.2
164	01:44:38.59	-04:45:10.6	7.9			729.9	92.1
165	01:43:58.49	-04:33:39.0	5.4			723.2	129.2
166	01:45:40.38	-04:49:5.0	8.2			721.0	84.4
167	01:45:40.56	-04:16:52.3	6.9			713.9	100.5
168	01:44:52.15	-04:55:20.6	5.2			711.7	130.1
169	01:45:04.4	-04:32:59.9	10.6			711.4	67.2
170	01:46:52.66	-04:41:48.6	5.1			704.2	138.4
171	01:46:43.79	-04:28:58.8	5.9			689.7	115.3
172	01:44:34.23	-04:26:47.4	7.4			672.7	90.2
173	01:45:03.8	-04:48:14.9	7.6			671.2	87.6
174	01:45:26.93	-04:36:05.2	10.2			658.5	63.7
175	01:45:35.16	-04:40:22.8	9.4			641.7	67.9
176	01:44:30.64	-04:34:53.1	7.3			631.5	85.8
177	01:45:44.22	-04:16:37.2	5.7			618.5	102.3
178	01:46:35.9	-04:24:21.5	5.1			609.2	118.5
179	01:44:48.52	-04:32:57.4	8.1			600.3	72.6
180	01:45:42.99	-04:36:29.8	8.9			595.7	65.7
181	01:46:45.42	-04:34:58.0	5.1			593.5	107.7
182	01:44:22.33	-04:32:55.7	6.1			588.1	95.4
183	01:46:03.1	-04:35:48.6	7.9			578.1	73.1
184	01:44:31.25	-04:37:02.2	6.4			563.5	86.4
185	01:45:56.0	-04:51:32.7	5.1			553.0	107.6
186	01:44:40.96	-04:40:03.2	6.6			545.2	82.3
187	01:45:31.59	-04:23:36.8	6.8			533.7	74.4
188	01:46:12.01	-04:22:27.5	5.3			527.2	96.1
189	01:44:38.81	-04:27:44.3	5.9			516.5	83.4
190	01:44:46.83	-04:47:22.0	5.3			512.4	96.8
191	01:44:46.47	-04:48:09.8	5.0			509.7	100.3
192	01:45:31.35	-04:29:29.9	7.2			499.9	68.5
193	01:46:02.6	-04:21:52.6	5.2			496.9	91.5
194	01:45:39.56	-04:34:36.8	7.4			496.4	64.4
195	01:45:00.9	-04:38:20.4	6.8			489.7	69.8
196	01:45:53.73	-04:27:07.9	6.3			483.2	76.2
197	01:44:58.9	-04:22:38.1	5.4			482.7	85.8
198	01:44:53.16	-04:46:41.4	5.3			481.7	90.9
199	01:45:37.97	-04:32:29.5	7.1			481.1	65.2
200	01:46:06.8	-04:39:41.9	6.0			477.5	79.2
201	01:45:00.7	-04:23:31.9	5.5			470.2	84.8
202	01:46:20.58	-04:28:20.7	5.1			468.7	91.8
203	01:46:03.1	-04:44:25.9	5.4			466.6	84.5
204	01:45:22.98	-04:45:24.8	5.9			464.3	78.6
205	01:45:12.26	-04:45:08.6	5.8			463.3	78.3
206	01:44:45.25	-04:42:18.4	5.3			451.0	84.7
207	01:45:52.05	-04:44:55.0	5.3			441.4	82.5

Table 3.2 continued

Source	Right Ascension	Declination	SNR	θ (arcsec)	S_p (μJy b^{-1})	S (μJy)	ΔS (μJy)
208	01:45:19.82	-04:44:15.2	5.7			438.9	75.5
209	01:44:59.38	-04:29:05.9	5.8			434.5	73.0
210	01:44:52.98	-04:31:50.3	5.7			431.1	74.4
211	01:46:07.8	-04:30:41.9	5.4			430.6	79.8
212	01:45:19.23	-04:41:31.3	5.9			430.3	72.0
213	01:45:46.94	-04:33:17.1	6.0			418.7	69.8
214	01:45:45.11	-04:26:05.9	5.3			409.6	77.3
215	01:45:58.49	-04:37:13.3	5.4			407.0	74.4
216	01:44:52.84	-04:34:19.1	5.3			403.4	75.1
217	01:45:46.73	-04:31:16.1	5.6			400.2	68.1
218	01:45:56.88	-04:29:02.2	5.0			389.5	71.7
219	01:45:15.98	-04:41:55.6	5.2			385.1	74.2
220	01:45:40.73	-04:43:16.6	5.0			385.0	73.5
221	01:45:48.18	-04:38:09.8	5.3			383.8	71.0
222	01:45:41.37	-04:39:41.1	5.2			374.9	70.9
223	01:44:58.01	-04:36:03.1	5.0			373.8	73.8

an indication that AGN were, on average, radio brighter in the past. The source counts from further, deeper radio surveys detected a downturn in the number of sources per flux bin at lower fluxes, interpreted as due to the expansion of the universe.

The source counts at 1.4 GHz have been studied extensively (e.g. Windhorst et al. 1985; Hopkins et al. 1998; Richards 2000; Seymour et al. 2004) and show a flattening of the Euclidean normalised counts below ~1 mJy (a second upturn in the *non-normalized* counts – see Section 3.4.2 for more details on Euclidean normalization). This survey is among the first of a new generation of 610 MHz extragalactic surveys that are able to reach the depth required to confirm or deny the existence of this 'sub-mJy' bump at lower frequency.

3.4.1 Completeness

To be compared meaningfully to other results and with models, several completeness corrections need to be made to convert the raw source numbers into a sky density as a function of flux density.

3.4.1.1 Primary Beam Attenuation

The dominant effect is the loss of sensitivity relative to that at the pointing centre due to the attenuation of the primary beam. This loss is corrected for in the binning process by assigning weights to each source proportional to the area over which they

could have been detected, see Section 3.4.2.

3.4.1.2 Source Detection Completeness

Sources are detected based on peak flux density in a map of finite noise. The detected peak flux density of a source is the superposition of its intrinsic peak flux density and any noise flux at its position. This effect can be sufficient to move sources in and out of the flux bins that correspond to their intrinsic fluxes. The important number in terms of completeness is the net gain or loss on the number of sources in each bin and is know as Eddington bias. Since the source counts are rising steeply with decreasing flux, the number of low flux sources scattered up is likely to be greater that the number scattered down. To correct for this effect, some knowledge of the number of sources below the detection threshold is needed (Eddington 1913). Hence, the discussion of this Eddington bias, which is small, is left until section 3.4.4, after the modelling of the source counts is addressed and an extrapolation has been performed.

3.4.1.3 Instrumental Effects

Bandwidth and time delay smearing reduce the peak flux density of a source while conserving the total flux density. Such a reduction of peak flux density can cause a source with a total flux density that is relevant to the calculation of source counts to be missed by a peak signal source extraction. As was shown in Section 3.3.4, neither bandwidth nor time delay smearing is important in the current study, and so no corrections have been made.

3.4.1.4 Resolution Bias

Source counts are calculated based on total flux density, from a catalogue selected on peak flux density, and so some sources of intrinsic low surface brightness may be missed. As in previous deep surveys (Richards 2000, Seymour et al. 2004), tapered, low-resolution, maps were searched for such sources and a small number have already been included in the catalogue.

For any value of S_{tot}, an upper angular size limit exists whereby the peak flux density of a source of that total flux still exceeds the detection limit of the survey. Using the relation

$$\frac{S_{tot}}{S_P} = \frac{\theta_{maj}\theta_{min}}{b_{maj}b_{min}} \tag{3.1}$$

where θ_{maj} and θ_{min} are the major and minor axes of the detected source respectively and b_{maj} and b_{min} are the major and minor axes of the restoring beam (Prandoni et al. 2000b), the size limits relevant to the full resolution and tapered maps can be calculated.

At detected fluxes above 360μJy, the tapered map provides excellent sensitivity to extended sources, where all sources smaller than 12 arcsec should be detected. Further, very large sources will still be missed. Due to the differing detection limits between the two maps, in the flux density range of 300 to 360μJy, the smaller beam of the full resolution means that sources larger than $\sim$7 arcsec are missed. Fig. 3.12 shows the angular size distribution of the sources in the catalogue, plotted against S_{tot}, with the detectable size limits of both the full resolution and tapered maps plotted as dashed and dotted lines respectively. Sources with properties that place them above these limits will not be detected in the survey observations, and the number thereof constitutes the resolution bias. As can be seen from the angular size distribution of the detected sources, few sources would be expected to reside in the zone where resolution bias would exclude them from the catalogue.

Little is known about the angular size distribution of sub-mJy sources at 610 MHz, but the angular size distribution of sources found in higher resolution deep surveys at 1.4 GHz over a similar flux range of 0.15 to 1mJy (the region in 610 MHz flux space for which resolution bias may have an effect, adjusted for a spectral index of -0.7, and at sufficiently high flux that these 1.4 GHz surveys are not themselves effected unduly by resolution bias) can provide some information about the expected population. Bondi et al. (2003) fit the 1.4 GHz angular size distribution of the sources in the VLA-VIRMOS Deep Field over a flux range not expected to be affected by resolution bias (0.4 to 1mJy). Using their formulation, this survey is expected to miss $\sim$3 percent of the sources above the tapered resolution bias limit in this flux range. Assuming this angular size distribution holds to lower 1.4 GHz flux densities, it is expected that only $\sim$7 percent of sources which lie between the detection limits of our full resolution and tapered 610 MHz maps will be missed. Inspecting the size distribution of sources in the 3.4 arcsec resolution VLA A+B array 1.4 GHz map of the 13^H deep field (Seymour 2002, see Chapter 5) provides similar estimates of the fraction of sources that may be missed. Hence, the effect of resolution bias is conservatively estimated as 7 percent below a detected flux of 360μJy, and 3 percent between 360μJy and 1mJy. It should be noted that the likely steep spectrum of extended emission implies that the radius out to which an extended source could be detected is greater at 610 MHz than at 1.4 GHz, implying

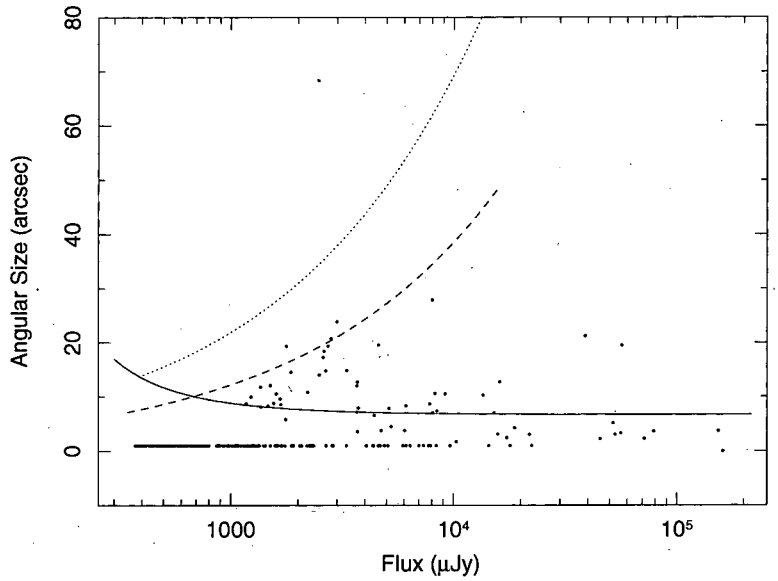

Figure 3.12: The angular size distribution of the sources detected at 610 MHz in the 1^H field. For sources confidently considered resolved, the sizes shown are the deconvolved sizes reported by SAD. All sources taken as unresolved are arbitrarily plotted at 1 arcsec. The solid line shows the minimum *observed* size for which a source can be confidently considered resolved as a function of flux density (see Section 3.3.3). The dashed and dotted lines show the maximum detectable size resolution bias limits in the full resolution and tapered maps, respectively.

larger angular sizes at the lower frequency. Another limitation of examining the 1.4 GHz angular size distribution is that higher resolution images can resolve out flux from low surface brightness sources. Nevertheless, the study of the 1.4 GHz size distribution as a guide to that at 610 MHz, while not without problems, is informative.

3.4.2 Construction of the Source Counts

The sources were binned in total flux density with the lowest bin having a lower flux limit of 344 μJy. Bins of width 0.3 dex, were chosen to provide good flux resolution while retaining a reasonable number of sources per bin. The highest two flux bins were widened to 0.6 dex to compensate for the lower number of sources per decade at high flux densities.

Each source was weighted by the inverse of the area over which it could have been detected – any departure from the full survey area being caused by primary beam attenuation and the areas of high rms noise surrounding the bright sources –

and for the fraction of sources missed at that flux by resolution bias. These weights were then summed for all the sources in each bin, and divided by the bin width.

Traditionally, differential radio source counts have been plotted after normalization to those expected in a homogeneously populated, static, Euclidean universe. With sources of a uniform luminosity and density, the total number of sources detected by a stationary observer above a certain flux varies purely as a function of the distance to the source. The observed flux of any detected source varies with the distance to it (to the power of minus 2). The number of sources detected above a certain flux therefore goes as flux to the power of 3/2, the 3 in the numerator coming from the increased volume of a sphere in which source can be detected above the detection limit, and the 2 in the denominator from the decrease in flux due to the intervening distance. This is the expected form of the integrated source counts – the total number seen with flux above a certain limit. The number seen within certain flux bins is the differential of this, i.e. $dN/dS \propto S^{-2.5}$. In a plot of differential source counts normalised thus, the source counts derived from a population of sources of uniform density and luminosity in a static, flat universe will appear as a constant with flux density. Any departures from such a constant indicate the invalidity of the assumption of either uniform density, uniform luminosity or static flat cosmology. The source counts at 1.4 GHz shown in Fig. 1.5 indeed show such a departure. Above 10 Jy, a flux density range where only the local universe is sampled, the differential source counts are indeed flat, but below this (within the flux range shown in the figure), significant departures are apparent. The increase in the counts as the flux decreases from 10 Jy to 300 mJy is caused by luminosity evolution in the AGN population – radio loud AGN were brighter in the past. The drop off below 100 mJy is due to the expansion of the universe. As discussed in Chapter 1, the upturn below $\sim$1 mJy is attributed to the emergence of a second population of sources, rather than a second, more violent, bout of luminosity evolution of the AGN population.

To normalise the 610 MHz counts to those expected from a Euclidean static universe, the summed weight of each bin was divided by $S_{mid}^{-2.5}$, where S_{mid} is the flux density at the log centre of the bin. The bin flux limits, log bin centres, numbers of sources, and normalised differential source counts are tabulated in Table 3.3, and plotted in Fig 3.13. The given uncertainty estimates are calculated from the square root of the number of sources within the bin. Also plotted are the 610 MHz source counts determined from a number of Westerbork survey fields of Katgert (1979), which can be seen to agree well with the current observations. A prominent bump

Bin (mJy)	S_{mid} (mJy)	N_s	$S^{2.5}dN/dS$ ($Jy^{1.5}sr^{-1}$)
0.283 – 0.564	0.39	38	11.9 ± 3.0
0.564 – 1.12	0.80	64	15.9 ± 2.3
1.12 – 2.24	1.59	39	15.9 ± 2.6
2.24 – 4.47	3.18	17	18.3 ± 4.5
4.47 – 8.91	6.34	22	57.9 ± 12
8.91 – 17.8	12.6	12	88.9 ± 26
17.8 – 35.5	25.2	10	209 ± 66
35.5 – 282	100	10	474 ± 150

Table 3.3: Tabulated 610 MHz source counts. The columns show bin flux limits (mJy), log bin centre, number of sources, and Euclidean normalised dN/dS with Eddington correction applied – see Section 3.4.4

at sub-mJy levels can indeed be seen at 610 MHz, where the normalised counts flatten below ~ 3 mJy. Fig 3.13 also includes a compilation of the source counts at 1.4 GHz (see Seymour et al. 2004 and references therein). The counts at 610 MHz follow a similar shape to those at 1.4 GHz, with a higher normalisation as expected when an average steep spectral index of synchrotron emission shifts each source to higher flux bins, and alters the normalising flux. See Section 3.4.3 for a more detailed discussion of the relationship between the source counts in the two bands.

3.4.3 Modelling the 610 MHz Source Counts

The modelling of source counts has long been a method of constraining cosmological evolution of radio populations, particularly those too optically faint to be spectroscopically identified (e.g. Longair 1966; Rowan-Robinson 1970; Hopkins et al. 1998; Seymour et al. 2004).

The 610 MHz source counts presented here are modelled in a manner similar to that of Seymour et al. (2004). Following previous authors (Condon 1984, Saunders et al. 1990, Rowen-Robinson et al. 1993, Hopkins et al. 1998), it is assumed that the evolution of luminosity function of radio sources $\phi_z(L)$ can be deconvolved into luminosity and density evolution:

$$\phi_z(L) = g(z)\phi_0 \left(\frac{L}{f(z)} \right) \tag{3.2}$$

where $g(z)$ and $f(z)$ represent the density and luminosity evolution of the radio luminosity function with redshift, z.

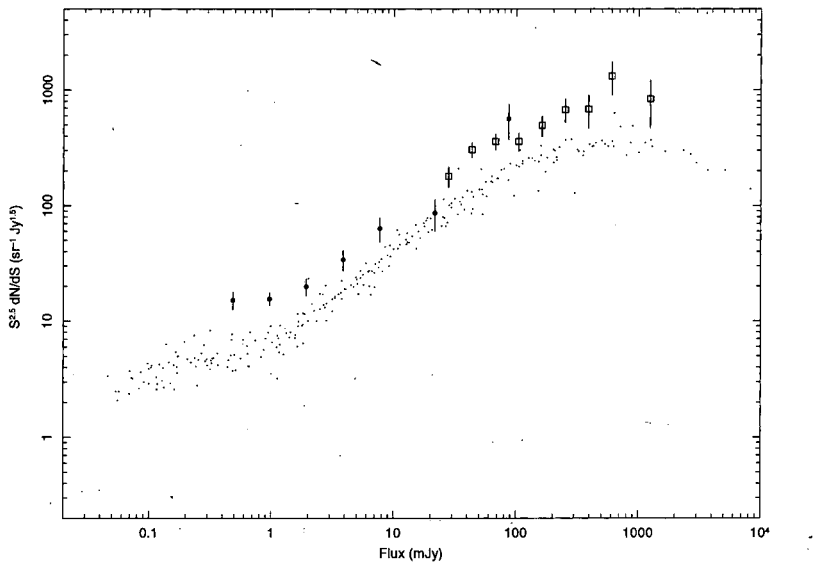

Figure 3.13: The differential Euclidean-normalised 610 MHz source counts as determined in the present study (filled circles), plotted at the log bin centre, S_{mid}, and those of Katgert 1979 (empty squares) overlaid on those at 1.4 GHz (dots) from the compilation of Seymour et al. 2004.

Above $\sim$ 3mJy, the extragalactic 1.4 GHz radio population is dominated by AGN, an observation confirmed spectroscopically, and through simple modelling of the source counts (Dunlop and Peakock 1990). It has been postulated (e.g. Hopkins et al. 1998; Seymour et al. 2004) that the upturn in the normalised differential source counts is due to the detection of a second population of sources – galaxies undergoing star formation. These two populations form the basis for the models fitted to the 610 MHz source counts here. The flux density distribution of sources can be determined by integrating their luminosity functions over volume. Here, the local luminosity function of both AGN and starburst galaxies are modified by evolutions as parameterised in Eq. 1 and integrated over volume.

The density evolution, $g(z)$, and the luminosity evolution $f(z)$ remain to be defined. The luminosity evolution is parameterised separately for the two populations and will be addressed later. It is assumed that any density evolution can be parameterized similarly for the two populations, as a power law function of redshift, $g(z) \propto (1+z)^P$. The integration by volume is converted to a integration over redshift, with luminosity transformed into flux and redshift (see Seymour 2004), and the counts normalised to Eucidean giving, as the counts due to each population:

$$S^{2.5}\frac{dN}{dS} \propto S^{1.5} \int \phi_0(S,z)h(z)(1+z)^P dz \tag{3.3}$$

where

$$h(z) = D_H \frac{(1+z)^{-2} D_L^2}{(\Omega_M(1+z)^3 + \Omega_k(1+z)^2 + \Omega_\Lambda)^{\frac{1}{2}}} \tag{3.4}$$

and D_H is the Hubble distance (c/H_o), Ω_M the matter density parameter, Ω_Λ the cosmological constant parameter and Ω_k the curvature term (Hogg 1999).

Once suitable parameterisations for the local luminosity function and evolution of the the two populations have been determined, this function can then be integrated across redshift to give the expected differential source count at each flux.

The AGN luminosity function and evolution function are taken from Rowan-Robinson et al. (1993) whose 1.4 GHz functions are based on survey work at 2.7GHz by Dunlop and Peacock (1990). They split the local AGN population into two types, characterised by flat and steep radio spectra. Here, the steep spectrum luminosity function was shifted to 610 MHz assuming an average spectral index of $\alpha = -0.7$. The flat spectrum population (with $\alpha = 0$) was taken to be the same as that at 1.4 GHz.

The local starburst radio luminosity function was taken from Sadler et al. (2002), who take a sample of 242 radio sources detected in the NVSS which are identified as starburst galaxies in the 2dF Galaxy Redshift Survey. The Sadler et al. (2002) radio luminosity function was shifted to 610 MHz assuming an average spectral index of $\alpha = -0.7$, suitable for the optically thin synchrotron radiation expected from supernova remnants associated with rapid star formation. Following previous authors, the luminosity evolution was parametrized as $(1+z)^Q$.

In order to fit this model to the 610 MHz counts, and obtain useful errors on Q, previous authors are followed, and the contribution to the counts of the AGN populations is fixed. The 610 MHz source counts above ~4 mJy are well described by the model of the combined AGN population luminosity and evolution functions as taken from Rowan-Robinson et al. (1993). Also, zero density evolution is assumed, and hence the only parameter left free to vary is the power law index of the starburst population luminosity evolution (Q). A χ^2 fit was performed, and the best-fitting value is $Q = 2.7^{+0.15}_{-0.25}$, where the errors are given at the 1σ level.

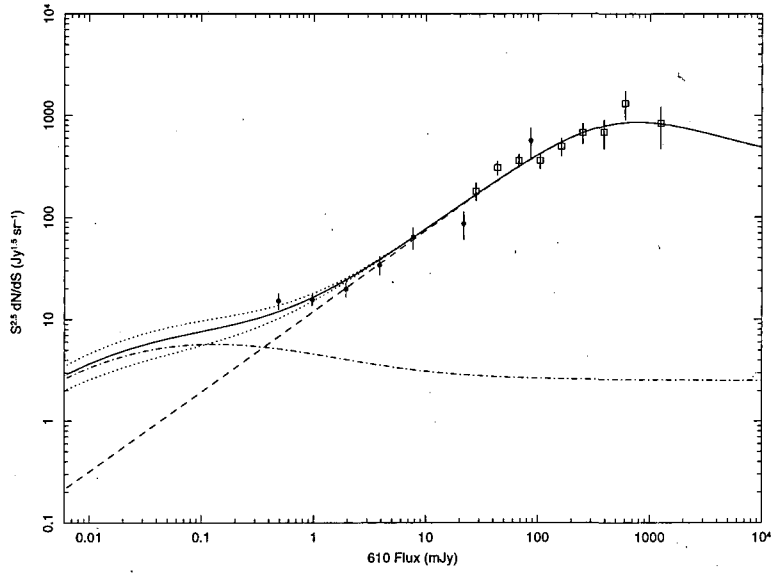

Figure 3.14: The 610 MHz source counts shown with the model fitted at 610 MHz. The solid line and accompanying dotted lines show the best-fitting model with the AGN contribution fixed, that with the power law index of starburst luminosity evolution $Q = 2.4^{+0.3}_{-0.4}$. The dashed lines show the relative contribution of the AGN and starburst populations.

3.4.4 Eddington Bias and Detection Completeness

When source counts are rising steeply with decreasing flux density it is likely that a larger number of sources will have their true fluxes boosted by the effect of noise towards brighter fluxes than reduced to dimmer fluxes. This effect is expected to be greatest at the flux limit of the survey. At 1.4 GHz, where source counts are available for many fields and from surveys of many detection thresholds, the effect of Eddington bias not critical for model fitting. However, when models are fitted to the few bins of source counts from one single survey, such as here, the bias can have a significant effect upon the results. To quantify the effect that such Eddington bias has on the measured source counts, an estimation of the number of sources below the survey detection threshold is required. The best-fitting source count model of Section 3.4.3 was extrapolated to 57μJy and used as such a prediction of the number of sources below the detection limit. A population of fake sources with a flux density distribution determined from this model were inserted randomly into a residual noise map of the entire survey area which had not been corrected for primary beam attenuation, i.e. a map with flat noise characteristics. The input flux density of each source was reduced, dependent upon position, to account for the

attenuation of the primary beam sensitivity. Sources were then extracted from these maps and counts constructed from these detections, following the same method as used for the real sources in Section 3.4.2, and the process repeated 20 times. The difference between the average detected differential source count and that of the input model gives an estimate of the net up-scatter, i.e. the Eddington bias, and any incompleteness in the source detection routine.

Only the lowest flux bin shows a significant offset, with the average measured differential source count overestimating the inserted model value by 21 percent. As a first-order approximation to the true source counts the observed counts in the lowest flux bin were therefore reduced by 21 percent and the model refitted, obtaining a value of $Q = 2.45$.

It should be noted that the 21 percent correction factor is actually slightly larger than should be applied to return to the true source counts as it is based on an *overestimate* of the real value of Q, corresponding to a steeper unnormalised source count and hence to a larger number of up-scattered sources than is the case in reality. This overestimate comes from the fact that the model of the source counts used ($Q = 2.7$) is that best fit to data which includes the effect of the bias. However the 21 percent factor is not a great deal too high as can be seen by repeating the simulations described above, assuming $Q = 2.45$. In this case the simulated source counts exceeded the model, in the lowest flux bin, by 19 percent thereby almost, but not quite, returning us to our starting position. Since the original 21 percent correction was an overestimate of the effect, this value is an underestimate, as too few model sources below the detection limit have been inserted into the simulations. Thus an intermediate correction factor of 20 percent is adopted and applied to the counts in the observed lowest flux bin which, when refitted, still provides $Q = 2.45^{+0.25}_{-0.4}$. The corrected source counts and best fitting model are shown in Fig. 3.14.

In order to test the requirement of an additional starburst population to provide an adequate fit to the observed source counts, a model with no second population (i.e. AGN only) was also tested. An f-test shows that the starburst population is required at the 99.3 percent confidence level.

3.4.5 Comparison with other determinations

At 1.4 GHz and following similar methodology, Rowan-Robinson et al. (1993) find $Q = 2.5 \pm 0.5$, Hopkins et al. (1998) find $Q = 3.1 \pm 0.8$, Condon et al. (2002) find $Q = 3.0 \pm 1$, Seymour et al. (2004) find $Q = 2.5 \pm 0.5$, and Huynh et al. (2005) find $Q = 2.7$.

A study of IRAS sources believed to be tracing starforming galaxies by Saunders et al. (1990) found evidence for luminosity evolution of $Q = 3.2 \pm 0.1$. Hopkins (2004) finds $Q = 2.7 \pm 0.6$ and $P = 0.15 \pm 0.60$ (where P is the powerlaw index of density evolution) as the best-fitting evolutionary scenario when both 1.4 GHz source counts and other star formation rate indicators are considered simultaneously.

The best-fitting value of Q at 610 MHz ($2.45^{+0.25}_{-0.4}$) is therefore consistent, within errors, with the results from the plethora of measurements at 1.4 GHz. This agreement suggests that observations at both frequencies are probing similar source populations, and that the sources which constitute the 'sub-mJy bump' can be explained by the an evolving population of starburst galaxies with steep ($\alpha \sim -0.7$) radio spectra.

The basic two population model used here may over simplify the true situation in faint radio sources. AGN and starburst activity can occur simultaneously in the same galaxy, and their common requirement of gas reservoirs would indicate that they are not entirely independent. However, it has been shown (Seymour et al. 2004, and this work) that such a model does provide a reasonably good representation of the observed source counts at both 1.4 GHz and 610 MHz.

3.5 Conclusions

In a ~4.5 hour 610 MHz observation of the 1^H XMM-*Newton* / *Chandra* survey area, 223 sources are detected down to a 5 σ detection limit of 300 μJy within a 32 arcmin radius.

It is shown that the 610 MHz source counts show the upturn in Euclidean normalised differential counts at faint fluxes (here, below 2mJy) familiar from extensive studies at 1.4 GHz. The 610 MHz counts are reasonably well fitted by a model similar to those fitted at 1.4 GHz, assuming a spectral index of $\alpha = -0.7$ for both steep spectrum AGN and a population of starburst galaxies undergoing luminosity evolution which dominate below $\sim$ 1 mJy. The best-fitting value for Q, the power law index of the starburst luminosity evolution, is $2.45^{+0.25}_{-0.4}$. This is consistent with the determinations at 1.4 GHz.

Chapter 4

The 1.4 GHz Survey of the 1 Hour Field

In this chapter, the 1.4 GHz imaging of the 1^H field is presented. With a noise level of 11.2 μJy beam^{-1}, 432 sources are discovered to 4σ. Source counts are computed, compared with other deep 1.4 GHz surveys, and modelled in a manner similar to Chapter 3.

4.1 Introduction

As introduced in Chapter 1, radio spectra can be used as diagnostics of the nature of the *radio* emission from the faint sources discovered in deep radio surveys. Chapter 3 illustrated that modelling of the source counts at 610 MHz can provide information about the average spectral index of the faint population. However, the observations presented in Chapter 3 were performed with the intention of acquiring radio spectra for individual sources discovered in deep 1.4 GHz imaging of the 1^H field. This 1.4 GHz VLA A-array observation forms the basis of this chapter.

The greater sensitivity possible with the VLA at 1.4 GHz compared to the GMRT at 610 MHz allows a much better sample of the sub-mJy population. Also, the high resolution imaging possible at 1.4 GHz with the VLA in A-array can help discriminate on a morphological basis, and provide accurate positions for the identification of optical counterparts. The trade off for these benefits is the reduction of field of view with respect to the GMRT at 610 MHz.

The observations are summarised in Section 4.2, data reduction discussed in Section 4.3, and image analysis in Section 4.4. Section 4.5 discusses source extraction, the catalogue resulting from which is presented in Section 4.6. The 1.4 GHz source

counts and morphological discrimination provided by these images are discussed in Sections 4.7 and 4.8 respectively.

4.2 Observations

Observations of the 1^H field at 1.4 GHz totalling 9.6 hours were conducted with the A-array of the VLA in August of 1999. A further 17 hours of data were taken in February and March of 2006. The pseudo-continuum 4IF mode of the VLA correlator was used, similar to the deep observations of the 13^H field (Seymour et al. 2004) and the Hubble Deep Field (Richards 2000).

4.3 Data Reduction

Reduction was performed in a manner similar to that of the 13^H field presented in Seymour (2002), and Seymour et al. (2004), and differs only slightly from that discussed in the previous chapter due to differences in the observational set up of the VLA compared to the GMRT.

4.3.1 Calibration

Flux calibration was performed using observations of 3C48, and phase calibration with regular observations of 0141-094. 3C48 is heavily resolved by the A-array configuration of the VLA at 1.4 GHz. As such, not all baselines can be used in the fitting of the antenna gains to a point source model during the calibration process. To retain all the antennas in the fitting process and thereby acquire a robust calibration solution, antenna gains were fitted to a model of 3C48 provided by the NRAO, rather than to a single point source.

The phase calibrator, 0141-094, is essentially a point source when observed with this configuration of the VLA. As per the VLA calibration manual, the *uv* range of baselines used in the fitting to a point source during calibration was restricted to those above 45kλ to avoid contamination by a small amount of confusing emission.

The pseudo continuum mode of the VLA correlator used during the observations provides 8 channels of 3.125 MHz bandwidth (of which only 7 are generally usable) in each of 2 IFs. This leads to a total bandwidth of 43MHz. The wide channels (cf. the 125 kHz channels of the GMRT) means that bandwidth smearing is more important, in terms of both imaging defects and completeness, than in the survey presented in

Chapter 3. From a calculation similar to that in Chapter 3, and once again following Taylor et al. (1999) by approximating the *uv* coverage to a tapered Gaussian and the channel bandwidth to a unit top hat function of width 3.125 MHz, the maximal effect of bandwidth smearing on this data (at the edge of the field) should be a reduction in peak flux density of 0.57. The total flux density is unaffected. The effect this smearing has on the resultant maps, and efforts to mitigate such effect, will be discussed in more detail in Section 4.5. Calibration of the bandpass was performed using the observations of 3C48.

The response of each baseline as a function of time and frequency was examined to locate and remove the effect of any RFI. Very little flagging was required, with only isolated examples of possible interference.

4.3.2 Initial Imaging

The smaller restoring beam and differing configuration of these A-array VLA observations compared to those made with the GMRT in Chapter 3 mean that a different imaging strategy is required to minimise 3D smearing. To be ensure consistency between the two fields, a strategy similar to that used by Seymour (2002) and Seymour et al. (2004) was employed. A 3×3 grid of 676×676 arcsec^2 facets covered the primary beam of the VLA antennas. Care was taken to ensure that the points of maximal emission from the brightest sources were located where possible on pixel centres, to ensure accurate and efficient deconvolution of the dirty beam. Further, smaller, fields were centred on sources outside the primary beam whose sidelobes could potentially pollute the main survey area. These were selected from the NVSS (Condon et al. 1998), and from the wider image of the field at 610 MHz presented in Chapter 3.

A pixel size of 0.33×0.33 arcsec was selected to accurately sample the 1.5×1.2 arcsec restoring beam of the A-array of the VLA.

4.3.3 Self Calibration

As described in Chapters 2 and 3, initial images made using calibration performed with known point sources can be used as models for self calibration. This process can correct for both spatial atmospheric variations between the phase calibrator and the science pointing, and for fluctuations in the atmosphere and electronics on time scales shorter than that between calibrator scans.

After several rounds of self calibration in each of several strategies (with differing

numbers of CCs being taken to construct the *uv* calibration model, and differing solution intervals), no noticeable improvement in image quality or reduction in noise level was seen. The failure to improve the image characteristics may be due the limited amount of flux that could be included in the CC models due to the sinc-like sidelobes detected around the brightest sources (see below). The noise level achieved in the highest sensitivity maps (see below) is only 15 percent over the expected thermal noise for these observations. This implies that the calibration achieved with the external source is very good, and reduces the importance of self calibration.

4.3.4 Final Imaging

4.3.4.1 Weighting

As introduced in Chapter 3, the distribution of spacing of antennas pairs in interferometers often leads to a large number of Fourier samples of long spatial extent compared to those short spatial extent (i.e. many more short baselines than long ones). As such, if an image is made by inverting all the visibilities of an interferometric observation, it has high sensitivity but less than optimal resolution. Several weighting schemes (e.g. natural, uniform) have been developed to compromise between these two considerations.

These 1.4 GHz observations of the 1^H field have three purposes. Firstly, they aim to detect as many of the faint radio population as possible – to increase the sample size of sources in the 'sub-mJy bump', potential contributors to the cosmic star formation history. Secondly, they aim to provide morphological information about those sources – to assist in the accurate separation of AGN from starburst galaxies. Finally, they aim to provide flux measurements at 1.4 GHz that can be accurately compared to those at 610 MHz to calculate spectral indices – a further AGN/starburst discriminator.

To address these three issues, several maps were made of the 1^H field at 1.4 GHz, with the weighting and tapering schemes altered to tailor the resulting map to the relevant science goal. The first objective, maximum sensitivity, is achieved with natural weighting of the *uv* data. In actuality little difference in rms noise was seen between maps made with natural weighting, and those with the ROBUST parameter in the AIPS task IMAGR set to 0, while the ROBUST 0 map produced a simpler, and therefore more easily deconvolved, dirty beam. This robust weighting scheme is a trade-off between natural and uniform weighting, and is explained in full in

Briggs (1995).

The second, maximum resolution, is achieved with uniform weighting. Once again, the Robust 0 map provided a good enough compromise between resolution and sensitivity to use for this purpose.

As described in Chapter 1, the accurate calculation of radio spectral indices from fluxes derived from images at two differing frequencies requires those two images to be of similar resolution. High resolution images can "resolve out" flux from extended sources leading to underestimates of their flux, and artificially steepening their spectra. The third objective therefore requires a map made with similar synthesised beam properties as the 610 MHz map – achieved by tapering the *uv* data such that a restoring beam of $\sim 6 \times 6$ is generated. The required tapering was performed by applying a Gaussian weighting function to the data, with 30% levels at 17 and 13 $k\lambda$. The loss of large amounts of long baseline data increases the noise considerably, reducing the chance of detecting many of the faint sources. As such, an intermediate resolution map was made with resolution of 3×3 arcsec by similar weighting with corresponding 30% of 45 and 35 $k\lambda$.

4.3.4.2 Cleaning

The Robust 0 map was imaged first. Cleaning was performed in blocks of 5000 iterations, and continued until a significant number of CCs were placed away from real sources. This resulted in 20,000 iterations of cleaning. Similar cleaning was performed on both of the tapered maps.

The 9 image facets containing the science images were combined with the AIPS task FLATN, and the highest sensitivity image is shown in Fig. 4.1, with no correction applied for the degradation in sensitivity of the primary beam. The centre of the image is shown in more detail in Fig. 4.2.

4.4 Image Analysis

The Robust 0 scheme used to make the high sensitivity map led to a restoring beam of 1.5×1.2 arcsec. The central rms noise is 11.2μJy beam^{-1}. A histogram of the pixel values can be seen in Fig. 4.3, and is well described by a Gaussian.

The low resolution, highly tapered map achieved the desired restoring beam of 6×6 arcsec, with the noise increased to 31μJy. The intermediate resolution tapered map has a restoring beam of 3×3 arcsec, with the noise increased to 17μJy.

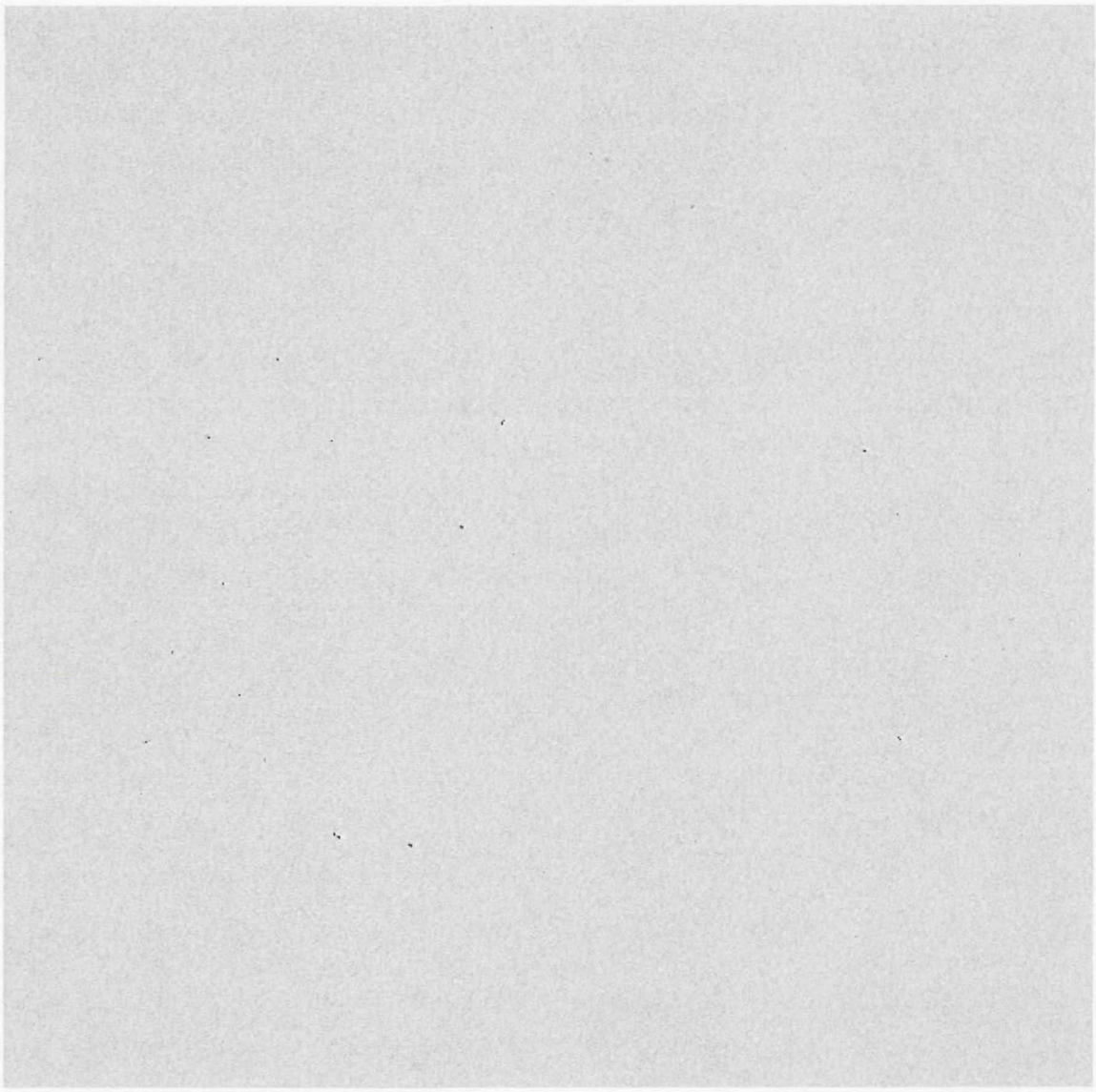

Figure 4.1: The entire 1.4 GHz image of the 1^H Field. This image has had no correction for for primary beam degradation applied.

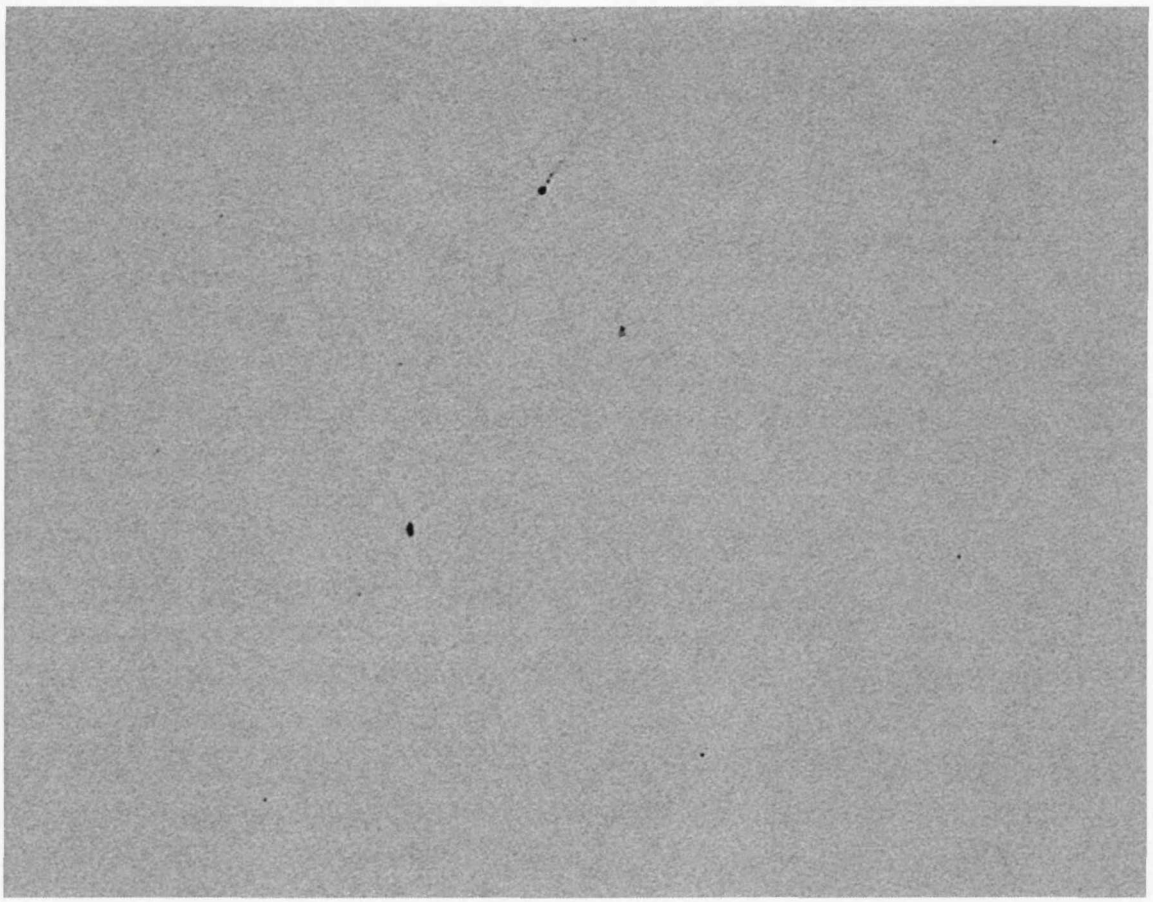

Figure 4.2: A central region ($\sim 8 \times 8$ arcmin) of the 1.4 GHz image of the 1^H Field.

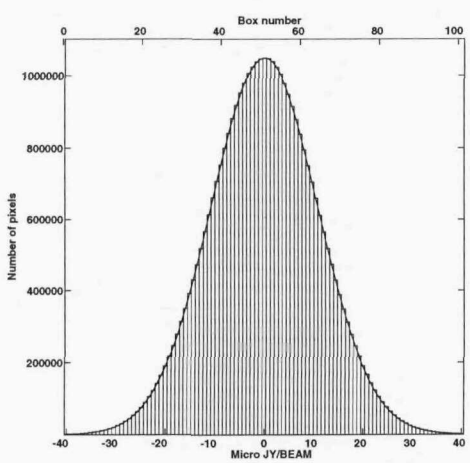

Figure 4.3: A histogram of the pixel values in the 1.4 GHz map of the 1^H field made with the Robust 0 weighting scheme.

As can be seen from close inspection of the image shown in Fig 4.1, sources further from the centre of the image are blurred out radially from that centre. This is the residual effect of the bandwidth smearing induced by the 3.125 MHz channel width. Details on how this effect was corrected for in terms of its effect on both the measured properties of the individual sources and the completeness of the survey, can be found in Section 4.5.

4.4.1 Sinc-like Sidelobes

One interesting artefact that should be noted is the approximate sinc function which is convolved with the bright sources in Fig. 4.1. The lobes of this artifact always point towards the phase centre, and have a maximal amplitude of $\sim$ 10 percent of the peak of the source they surround. Fig. 4.4 illustrates their effect on the source at 1:46:06.2, -4:35:45.4. The magnitude of the effect varies with radial distance from the pointing centre, and the magnitude is slightly greater in the direction to the centre than away from it.

While not present in the 1.4 GHz VLA survey of the 13^H field, similar ripples have been seen in other deep VLA surveys. Richards (2000) and Biggs & Ivison (2006) discovered the same pattern around bright sources in the 1.4 GHz survey of the HDF-N. Richards (2000) concludes that it is due to a problem with the 3.3 second sampling of the VLA correllator. Biggs and Ivison confirm that the effect is entirely local, having no effect on the rms noise in the remainder of the image, and hence take no further action to remove it, though they have noticed similar ripples with data sampled at 5 seconds (private communication).

In the 1^H field data, these ripples are present in images made with either IF, any one or more channels, and any weighting and cleaning strategy. The radial nature of the effect implies this may be a bandpass effect. The sinc function is the Fourier transform of a single wavelength square wave. Both the total bandpass and each individual channel is square, which is indicative that some problem with the frequency response of the data both here and in the HDF-N may be responsible. To test this hypothesis, further images were made with Hanning smoothing applied to the bandpass - effectively smoothing the edges of both the total bandpass, and each channel. Fig. 4.5 shows the contours of emission from the same source in this map. The smoothing has removed the sinc-like ripples, confirming that this is a bandpass effect. Such smoothing does have other, less welcome, effects on the maps. Hanning smoothing convolves the bandpass with a triangular function of the type 1/4, 1/2,

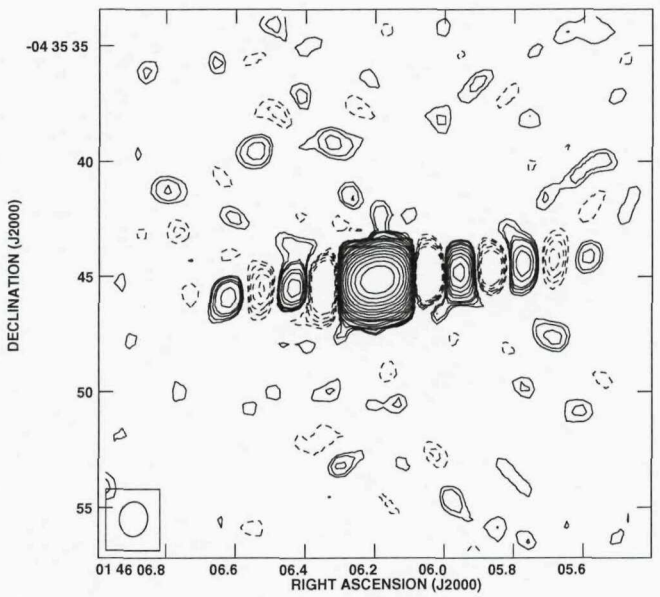

Figure 4.4: Contours of emission of source 3, illustrating the sinc – like sidelobes present around the brightest sources. The phase tracking centre is located to the right of this figure.

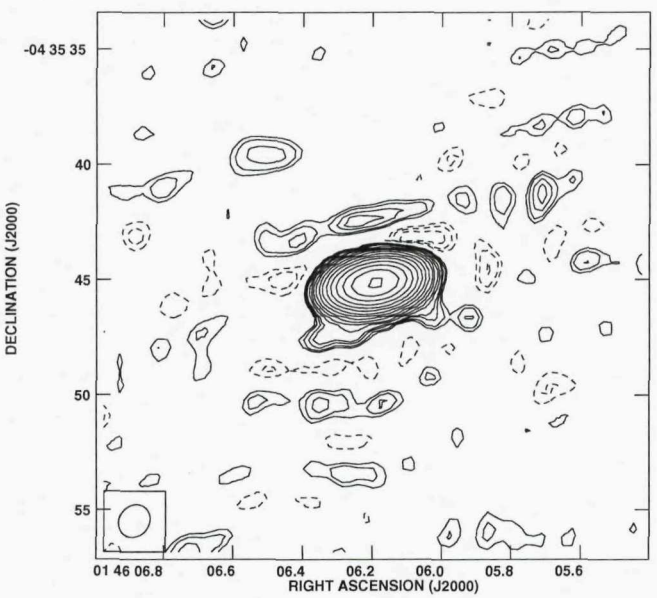

Figure 4.5: Contours of emission of source 3 in a map with Hanning smoothing applied to the bandpass. The sinc – like sidelobes are no longer present, but the effect of the increased bandwidth smearing can be seen in the elongation of the source.

1/4. Such averaging means that the channels lose their independence. This has two effects. Firstly, the effective bandwidth is increased, thereby increasing bandwidth smearing. In Fig. 4.5, the source has been smeared radially from the pointing centre (which is located to the right of the image) compared to the image constructed with full spectral resolution. Secondly, the noise in the Hanning smoothed images is unbelievably low ($\sim$ 70% of the theoretically expected thermal noise level). The AIPS task IMAGR treats each channel as independent. Applying the smoothing invalidates this assumption, and hence the images constructed by averaging over all channels suffer from unrealistic noise characteristics.

The ripples associated with the bright sources are small in extent ($\sim 10\times2$ arcsec), and have no perceivable effect beyond this distance. Hence, the final maps were made at full spectral resolution, with no attempt to remove them.

Their only remaining effect is a possible bias on the measurement of the source fluxes. Flux from the real sources may be spread into the sidelobes, meaning that Gaussian fitting to the central bright source underestimates the true flux. Also, the proximity of reasonably bright artifacts around sources can increase the clean bias as CCs are placed at the positions of non-real flux. These two effects may not only effect the bright sources (around which the ripples are visible above the noise) as the sidelobes will be lost in the noise for any source below 10σ.

Measurements of the flux density of various bright sources as estimated by various methods were compared to analyse the magnitude of this effect. Firstly, Gaussians were fitted to the central lobes of the brightest sources in the maps made with full spectral resolution. Secondly, TVSTAT was used to sum all the flux (both positive and negative) within the sinc pattern that was perceivable above the noise in these maps. Thirdly, TVSTAT was used to measure only the positive flux. Finally, both Gaussian fitting and TVSTAT were used to measure the flux of the bright sources in the Hanning smoothed map, and the maps tapered to lower resolutions.

For the bright, isolated sources, the flux densities measured from the tapered maps are, to within 1 percent, the same as the total flux measured across the entire perceivable sinc pattern in the map made with full spectral resolution. They are $\sim$7 percent lower than flux in the central lobe of the pattern. This implies that the effect of the sinc pattern on the measured flux is present in the tapered maps, but is not noticed due to the low resolution.

The average flux of these same sources as measured from the Hanning smoothed map is 3 percent greater than the total flux measured across the entire perceivable sinc pattern in the full spectral resolution map. It is 5 percent lower than that of

the central lobe of the pattern.

Since it is unlikely that any defect will *increase* the flux of a source, and the smoothed fluxes lie between the central and full pattern fluxes, the flux recorded in Table 4.1 for the sources with percievable sinc-like sidelobes is that of the central lobe of the function. These sources are marked with a S in the flag column. The average difference between these fluxes, and those measured across the entire sinc pattern (and, hence those in the tapered maps) is 7 percent. An error of 7 percent has therefore been added to the estimation of the errors on the measured fluxes from the effect of noise on the Gaussian fitting. This error has been applied to all sources because although the sinc-like sidelobe pattern may not be noticeable above the noise for any but the brightest sources, it may be present for all of them.

4.5 Source Extraction

Source extraction was again performed with the AIPS task SAD. The highest sensitivity (11.2 μJy beam^{-1}) map was used to construct an initial source list. The tapered maps were then analysed to measure a closer approximation to the zero-spacing flux of all the sources detected in the highest sensitivity map, and to locate any new sources whose emission is of sufficiently low surface brightness to be resolved out of the full resolution map.

In the full resolution map, Gaussians were fitted to the emission surrounding all pixels of a 3.5σ limit of 38 μJy. Sources were accepted as real if their fitted peak flux density was greater that a 4σ limit of 45μJy. Within a 15 arcmin radius of the pointing centre (the radius at which the sensitivity of the primary beam pattern drops to 50 percent), 389 sources were extracted.

Inspection of residual maps showed that the Gaussian fitting used by SAD failed to represent a further 20 sources sufficiently accurately. These include the 6 sources which suffer from the noticeable sinc function sidelobes discussed in Section 4.4.1 and 14 further sources with emission that is extended. The properties of the extended sources were extracted, by hand, from the high sensitivity map with TVSTAT, including the flux in all pixels that appeared to constitute the source, and measuring the size as the furthest extent between 2σ contours. The flux of the sources with the sinc-like sidelobes, discussed previously, was taken to be that of their central lobe, with the errors on all measured fluxes being increased to account for their effect. In these cases, the sidelobes inhibit an accurate determination of the size of the object, and a ?? has been included in the catalogue.

4.5.1 Doubles

There are several cases of regions of emission occurring in close proximity, potentially composing the double lobes of a AGN viewed side on. Most of these cases also showed low level emission connecting the two sources, and as such were among the number extracted by hand using TVSTAT. The contours of such emission were overlaid on the optical i band imaging of the 1^H field (see Appendix A). Sources seen as having connecting emission in the highest resolution map were taken as components of the same object, and assigned one entry in Table 4.1. In the cases of source pairs 35 and 229, 41 and 346, 55 and 267, 111 and 132, and 211 and 279, the two patches of radio emission are coincident with separate optical galaxies, with no emission seen between them. As such, they were retained as separate sources in Table 4.1.

The remaining case is that of sources 4 and 23, shown in Fig 4.6. Source 23 consists of two regions of emission separated by $\sim$ 4 arcsec. 7 arcsec to the south west, source 4 appears to consist of a pair of lobes centred on a dim optical object. The two components of source 23 seem to be associated with the bright, point-like optical object to the upper right of 4.6. A patch of faint i' band emission is located near the centre of the emission taken to be source 4. Since separate potential optical counterparts exist for the different regions of radio emission, they are recorded in Table 4.1 as two separate sources. It should be noted that in the 610 MHz image, the emission identified as source 23 in this map appears to be merely an extension of that from source 4. This confusion, caused by the lower resolution of the 610 MHz map, means that the measured fluxes, and hence radio spectra, for these source are uncertain.

4.5.2 Resolution

As discussed in Chapter 3, the sizes and integrated flux densities measured by Gaussian fitting routines at low signal to noise ratios are unreliable. Once again, the population with peak flux density exceeding total flux density were used as a guide to the magnitude of this effect. Unlike the 610 MHz observations presented in Chapter 3, these observations suffer from significant band width smearing. For the S_{tot} to S_P ratio to be meaningfully compared for sources across the entire field, the peak fluxes were corrected for bandwidth smearing (see Section 4.5.3 below for details) before the computation of this ratio. An envelope was defined to contain these in S_p/S_{tot} vs S_p space and mirrored about the $S_p = S_{tot}$ line to encompass

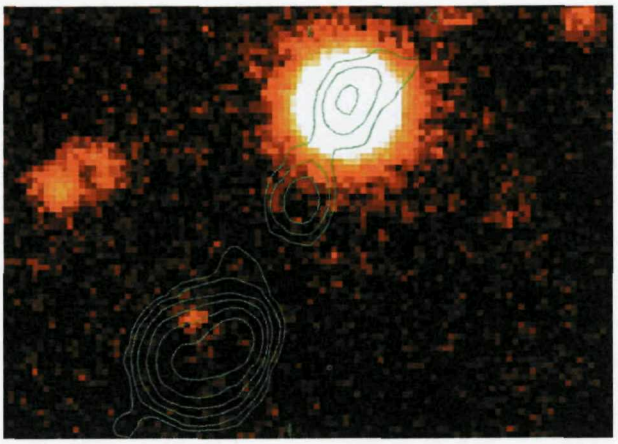

Figure 4.6: Contours of 1.4 GHz emission of sources 4 and 23 overlaid on an i' image. Source 4 is taken to be the emission to the lower left of the figure. A faint optical object is visible near the centre of the emission. While the remaining regions of emission are assumed to be separate, and associated with the bright optical source to the upper right.

98 percent of the sources whose resolution is questionable. Within this envelope, sources were taken to be unresolved points, while outside, measured widths and total flux densities were accepted. These functions, and the initial measured flux density ratios can be seen in Fig. 4.7.

4.5.3 Corrections to Source Properties

4.5.3.1 Primary Beam

The flux measurements of each source were corrected for the degradation in sensitivity of the primary beam at their location. The function used was that of the eighth order polynomial supplied by the AIPS task PBCOR.

4.5.3.2 Bandwidth smearing

As can be seen in Fig. 4.1, sources far from the centre are extended in the direction radial from the image centre. This is the effect of bandwidth smearing – where total flux of any real source is conserved but blurred out, reducing the peak flux. This effect has been studied in detail by Richards (2000), who use an observational set-up identical to that used for these observations. Following the method of Richards, and Seymour et al. (2004), the effect is approximated by the function:

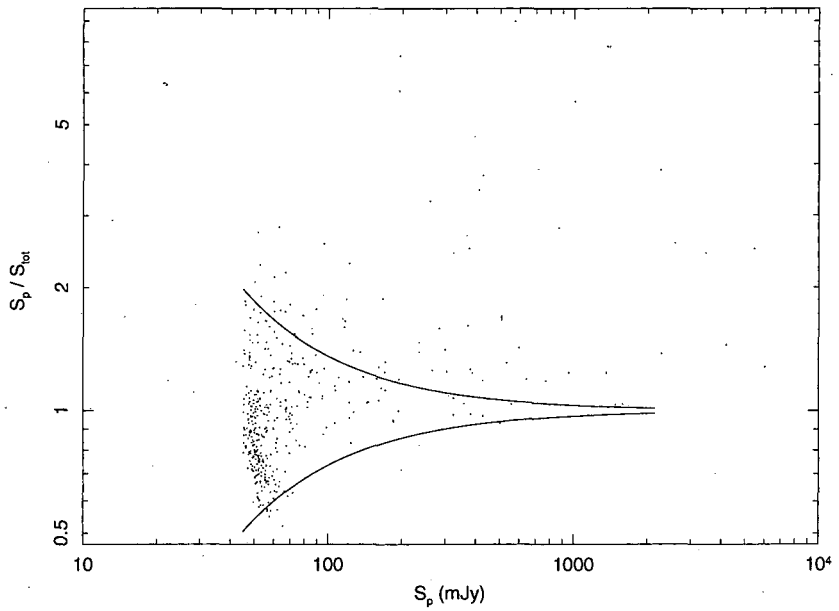

Figure 4.7: The ratio of the measured S_p to measured S_{tot} for sources detected in the 1^H field at 1.4 GHz. The envelopes used to define confident resolutions as a function of flux are shown as the solid lines.

$$\frac{S_{tot}}{S_p} = \left(1 + \left(\frac{r}{16.19}\right)^2\right)^{-0.5} \tag{4.1}$$

This has been used to correct the peak flux density of each source. The measured values of total flux do not require correction, as this property is conserved by bandwidth smearing.

4.5.3.3 Time delay Smearing

As mentioned in Chapter 3, the rotation of sources within the visibility integration time can lead to smearing which, in the simplified case, is perpendicular to the direction to the pointing centre. Each visibility in this dataset is the average of a 3.3 second correlation of the baseline feeds. With such a short averaging time, this effect is minimal. The maximal expected effect is a reduction in the measured peak flux by 0.4 percent.

4.5.3.4 Clean Bias

Maps with Robust=0 weighting were made with 5000, 10000, 20000, 30000 and 100000 clean iterations. The flux of several sources were measured in each of these

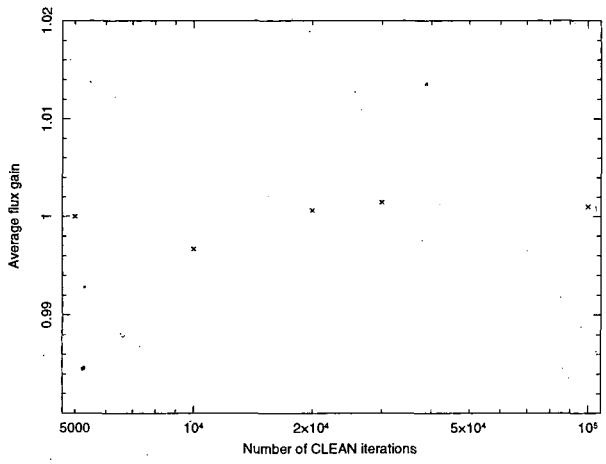

Figure 4.8: The average flux ratio of several bright, isolated sources measured in maps with various numbers of clean iterations. The ratio is defined as relative to the source's flux as measured in the 5000 iteration map.

maps, and average gains are plotted in Fig. 4.8. The measured flux density was not seen to reduce with increasing number of Clean iterations.

As a further check, simulations similar to those presented in Chapter 3 were performed. Sources of known flux density were inserted into the full *uv* data at regions constrained to lie more than 10 arcsec from a real source. This data was then imaged and analysed in a way similar to the science data, and the measured flux of sources compared to their known inserted flux. For 100 sources at 250μJy, the average measured flux was 249.6 ± 0.2, where the error is on the determination of the mean. The effect of Clean bias is therefore only important at the 0.2 percent level, insignificant compared to the errors from source fitting, noise, and the sinc-like sidelobes, and has therefore not been considered further.

4.5.4 Tapered Maps

The high resolution provided by the A-array of the VLA provides the opportunity to study the arcsec scale morphology of the sources detected. However, it also looses sensitivity to low surface brightness objects, from which some of the flux is resolved out by the longer baselines.

The 3×3 arcsec tapered map, made as an compromise between high sensitivity and 610 MHz matching resolution, provides greater sensitivity to such extended sources, as the influence of these long baselines is down weighted. This map has Gaussian noise, and was searched for sources in the same manner as discussed above,

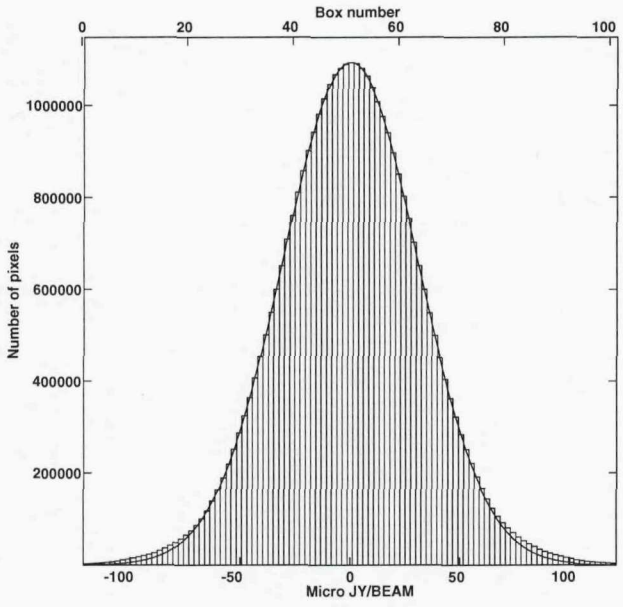

Figure 4.9: The distribution of pixel values (in μJy beam^{-1}) in the map tapered to 6x6 arcsec resolution. The wings of the distribution are higher than the values predicted by the Gaussian fitted to the distribution as a whole.

with the flux densities at this lower resolution recorded. SAD extracted 151 sources well fitted by Gaussians, and the properties of the further 20 extended sources were determined by hand. Of these, 148 were the tapered counterparts of sources already discovered in the full spatial resolution map. There were no significant detections in the full resolution map at the location of the remaining 23 sources detected at the 3×3 arcsec resolution. These non-detections imply that the contribution to the image of the many long baselines of the VLA A-array has resolved out the flux of these extended, low surface brightness objects. The 23 new sources were added to the catalogue.

As can be seen in Fig 4.9, the distribution of pixel vales in the map tapered to a resolution of 6×6 arcsec is not well described by a Gaussian. In the wings of the distribution, the number of pixels with a certain flux per beam exceeds the Gaussian profile that has been fitted to the whole distribution, and is over plotted. As such, the calculation of a simple detection limit as 4 times the σ of the distribution provides an unrealistically low detection threshold, as many pixels which contain purely noise would be counted as real sources. This is confirmed by the unrealistic number of new sources ($\sim$ 50) discovered above 4σ in this 6×6 arcsec map but not in the higher sensitivity 1.5×1.2 and 3×3 arcsec maps. As such, a different approach is

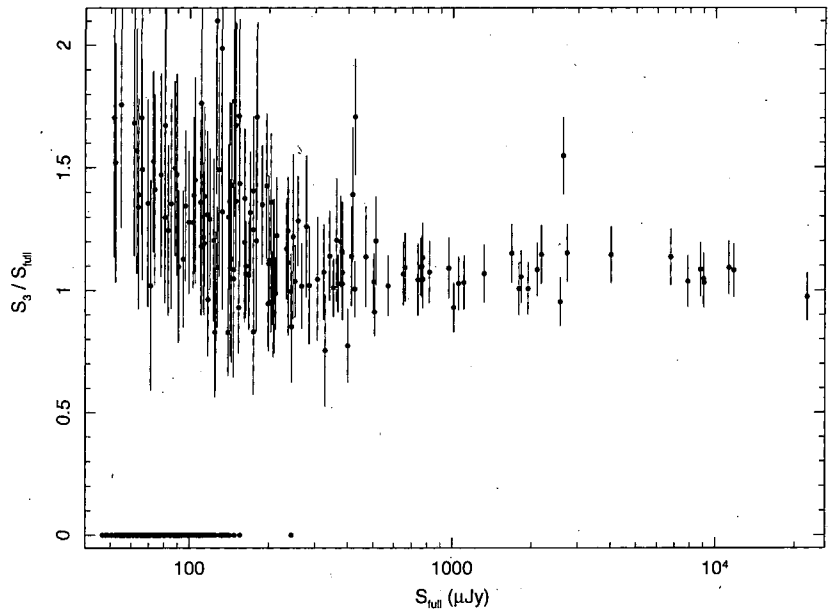

Figure 4.10: The ratio of the fluxes measured from the 3×3 arcsec and full resolution maps, plotted against detected peak flux in the full resolution, high sensitivity map.

required for defining a detection limit in this map. The map was examined to find the most negative pixel. Since any negative flux is necessarily the result of noise, this was taken to be the maximal extend of the negative part of the noise distribution. Since the noise distribution shown in Fig. 4.9 is reasonably symmetric, this value of 180 μJy was mirrored about mean of the distribution and hence a detection limit of 180 μJy was adopted. Above this level, 66 sources were detected, all of which had already been seen in the higher spatial resolution, higher sensitivity maps. In two cases, the low resolution of this map caused sources to be confused, and hence made individual flux densities impossible to measure accurately. This 6×6 arcsec source list was cross correlated with the list of 432 sources discovered in the maps of higher resolution.

The average increase in measured flux between the full resolution and 3×3 arcsec map is 1.21. As can be seen in Fig. 4.10, sources whose detection is of high significance in both maps usually appear to have the same flux in both. Only at faint fluxes, and therefore with less accurate flux measurements, does the distribution of gains widen. Sources with fluxes between the detection limits in the two maps are missed, depopulating the low flux, gain < 1 region in Fig. 4.10, increasing the average of the distribution above one.

In cases where the ratio of S_{3x3}/S_{full} is greater than unity by more than the error on S_{3x3}/S_{full} (from the combination of the errors on the flux measurements in each

map), the increase in flux is taken as significant, and the 3×3 arcsec flux is recorded in the catalogue. In 76 of the 409 cases of sources detected in the full resolution map, S_{3x3} was taken as significantly brighter. Similarly, if the flux measured in the 6×6 arcsec map is significantly brighter than that measured in either the full resolution or the 3×3 arcsec map, this is also recorded. 14 sources were taken as significantly brighter thus.

4.6 Catalogue

Table 4.1 is the catalogue of all sources discovered at 1.4 GHz in all maps of the 1^H field. The columns contain: Number; a source extraction flag (H meaning that the source properties were extracted by hand using TVSTAT, T meaning that the source was first seen in the 3×3 arcsec map, and S meaning that the source noticeably suffers from the sinc–like sidelobes); RA; Dec; the signal to noise ratio of the detection; peak flux in μJy $beam^{-1}$ for sources reliable resolved; the size of the source in arcsec, if it is reliably resolved (the deconvolved size reported by SAD for source adequately described by a Gaussian, and the greatest distance between 2σ contours for those sources extracted by hand. A ?? means that any measure of the source's extent is hampered by the sinc-like sidelobes); total flux in μJy, in the full spatial resolution map; flux in μJy, in the 3×3 arcsec resolution map for sources which are significantly brighter in it than in the full resolution map; flux in μJy, in the 6×6 map for sources which are significantly brighter in it than in maps at higher resolution; The best measurement of the flux in μJy; the error on the best flux, in μJy. Sources are ordered based on the best estimation of their total flux density.

4.7 Source counts

The 1.4 GHz source counts from the 1^h field were corrected and computed in a manner similar to that in Chapter 3. Sources with detection of 5σ and above were binned on total flux, and weighted by the area over which they could be seen.

Table 4.1: The full catalogue of sources detected at 1.4 GHz in the 1^H field. Columns are: Number; Flag; RA; Dec; SNR; size; S_p in μJy $beam^{-1}$; S_{tot} in μJy in the full resolution map; flux from the 3 arcsec resolution map for sources significantly brighter therein; flux from the 6 arcsec resolution map for sources significantly brighter therein; S_{Best}, the best measurement of the flux, in μJy; error in this best flux, in μJy. Flags are: H=source parameters extracted by hand; T=source first detected in the tapered map; S=source noticably effected by a sinc-like sidelobe pattern.

Source	Flag	Right Ascension	Declination	SNR	S_p μJy b^{-1}	θ arcsec	S_{tot} μJy	S_3 μJy	S_6 μJy	S_{Best} μJy	ΔS μJy
1	H	01:45:52.69	-04:43:20.5	478.4	8995.5	15.0	22387.4			22387.4	1567.5
2	HS	01:44:44.85	-04:40:28.0	368.3	7779.0	??	11280.1		12816.3	12816.3	897.1
3	HS	01:46:06.2	-04:35:45.2	529.1	9179.8	??	11757.2			11757.2	823.7
4	H	01:45:32.88	-04:30:54.9	303.7	3729.3	6.0	9066.0			9066.0	635.2
5	H	01:45:37.7	-04:34:01.4	197.6	2331.4	10.0	9030.6			9030.6	632.7
6	HS	01:44:49.2	-04:31:44.7	88.5	1541.5	??	8791.6			8791.6	616.3
7	HS	01:46:15.43	-04:40:30.3	200.4	4910.4	??	6772.1	7689.0	8015.6	8015.6	561.0
8	H	01:45:43.79	-04:43:37.5	50.3	875.8	12.0	7866.9			7866.9	551.7
9	H	01:46:08.0	-04:31:19.9	76.4	1437.1	23.0	4020.9	4602.1	4530.7	4530.7	317.1
10	H	01:45:20.36	-04:22:59.3	17.1	357.5	14.0	2641.3	4086.5	4087.9	4087.9	286.1
11	H	01:45:10.02	-04:24:23.8	37.3	727.5	10.0	2735.3	3153.2	3207.2	3207.2	224.5
12		01:44:50.17	-04:46:23.8	52.6	1532.3	1.135	2183.5	2502.6	2706.1	2706.1	0.0
13	H	01:46:12.37	-04:37:48.2	36.1	744.2	9.0	2576.3			2576.3	184.3
14	H	01:44:32.51	-04:37:45.1	28.4	738.6	7.0	1794.4		2193.0	2193.0	153.5
15		01:45:19.85	-04:26:21.2	129.8	2036.7	0.54	2106.1			2106.1	147.4
16		01:45:59.79	-04:28:58.0	83.7	1472.8	0.715	1825.8		1973.8	1973.8	0.0
17	H	01:44:31.54	-04:36:51.2	22.8	597.4	10.0	1942.2			1942.2	143.2
18	HS	01:45:22.19	-04:22:48.5	67.5	1422.0	??	1683.5	1937.3	1924.4	1924.4	134.7
19		01:46:21.84	-04:34:43.3	32.4	819.3	1.275	1321.6			1321.6	106.3
20		01:46:04.3	-04:39:06.3	46.8	845.7	0.86	1107.0		1215.9	1215.9	48.5
21		01:45:24.73	-04:47:29.7	33.9	781.5	0.96	968.0		1111.7	1111.7	61.8
22		01:44:52.85	-04:34:20.5	56.4	883.9	0.655	1056.1			1056.1	79.1
23	H	01:45:32.57	-04:30:46.5	32.9	406.4	12.0	1012.3			1012.3	75.9
24		01:46:19.01	-04:40:36.3	14.5	393.9	1.63	739.7		1002.9	1002.9	72.7
25		01:45:31.0	-04:48:41.0	23.2	612.6	1.04	769.5		879.7	879.7	70.7
26		01:45:49.69	-04:40:51.5	48.8			756.9		876.9	876.9	41.7
27	T	01:46:00.0	-04:26:13.5	9.6				823.9		823.9	111.1
28		01:44:45.59	-04:27:50.3	26.3	579.4	0.985	817.8			817.8	71.1
29		01:44:39.47	-04:37:58.8	20.6	449.3	1.105	660.0		807.1	807.1	58.6
30		01:44:45.26	-04:33:40.7	33.3	610.9	0.715	771.0			771.0	63.4
31	HS	01:44:48.52	-04:32:58.1	37.4	645.4	??	765.4			765.4	63.2
32	H	01:45:09.5	-04:43:32.6	10.7	186.1	4.5	426.2	727.3	743.2	743.2	52.0
33		01:46:03.0	-04:24:09.7	15.0	387.1	1.015	511.2	614.5	705.4	705.4	69.3
34		01:45:53.29	-04:31:25.5	24.7	358.0	1.13	569.3		657.2	657.2	38.8
35		01:46:06.8	-04:39:43.5	26.7	520.5	0.83	649.7			649.7	57.4
36		01:46:04.2	-04:40:42.2	8.4	162.9	1.995	417.3	580.1	613.7	613.7	52.0
37		01:46:06.8	-04:24:50.8	7.8	204.5	1.515	362.3		566.5	566.5	70.4
38		01:45:04.5	-04:33:00.9	20.6	273.8	0.92	381.3		549.9	549.9	69.6
39	H	01:45:09.2	-04:47:48.3	5.5	142.1	7.0	399.8		543.9	543.9	38.0
40		01:44:46.34	-04:42:06.7	10.2	229.7	1.4	380.3		509.9	509.9	60.3
41		01:45:26.97	-04:36:6.0	43.9			505.6			505.6	37.1
42		01:45:35.16	-04:40:24.8	37.3			502.1			502.1	37.5
43		01:45:40.38	-04:49:05.8	10.1	292.7	1.535	468.1			468.1	67.3
44	T	01:46:17.44	-04:33:53.9	5.1				451.8		451.8	102.5
45		01:45:59.44	-04:26:27.7	14.9	301.8	0.785	375.0	449.4		449.4	43.6
46		01:45:03.1	-04:34:15.6	28.4			379.8	440.8	443.8	443.8	35.8
47		01:45:15.96	-04:41:56.2	16.9			251.9		429.6	429.6	77.0
48		01:45:16.33	-04:30:28.2	33.3			425.6			425.6	32.2
49		01:44:30.6	-04:34:53.9	11.1	293.9	1.01	412.6			412.6	57.5
50		01:46:05.9	-04:43:56.5	7.5	184.9	1.32	285.2		389.7	389.7	65.8
51		01:44:40.97	-04:40:04.6	10.0	227.3	1.355	381.3			381.3	55.6
52		01:44:58.91	-04:22:39.3	7.5			196.2	279.7	378.0	378.0	69.9
53		01:45:17.59	-04:34:17.0	31.3			366.8			366.8	28.1
54		01:45:42.98	-04:36:30.6	28.3			352.6			352.6	27.5

Table 4.1 continued

Source	Flag	Right Ascension	Declination	SNR	S_p μJy b^{-1}	θ arcsec	S_{tot} μJy	S_3 μJy	S_6 μJy	S_{Best} μJy	ΔS μJy
55		01:44:59.38	-04:29:06.9	13.8	222.6	0.63	267.0		346.7	346.7	43.2
56		01:45:22.99	-04:45:25.8	14.1	266.6	0.99	340.8			340.8	41.9
57		01:45:19.86	-04:44:16.6	15.0			258.4	331.7		331.7	34.6
58		01:46:24.25	-04:39:05.8	5.2	154.3	2.315	327.9			327.9	76.9
59		01:44:45.63	-04:41:30.5	12.2	267.6	1.02	324.0			324.0	44.4
60		01:45:31.55	-04:23:38.3	9.7			188.7	254.6	313.7	313.7	52.0
61	T	01:44:53.12	-04:46:42.4	6.9				310.0		310.0	46.2
62		01:45:03.9	-04:48:16.6	6.2			180.3	307.7		307.7	47.9
63		01:44:38.73	-04:27:45.9	6.9	179.1	1.505	306.4			306.4	59.8
64		01:45:49.2	-04:23:32.7	10.6			236.6	294.2		294.2	38.9
65		01:44:52.54	-04:36:01.2	5.8	92.6	1.18	161.7		283.0	283.0	60.0
66		01:44:43.53	-04:43:25.7	7.8	202.9	0.965	278.2			278.2	52.0
67		01:45:29.82	-04:48:21.5	8.0			203.8	277.0		277.0	42.4
68		01:46:02.1	-04:24:12.0	6.1			154.1	263.6		263.6	41.5
69		01:45:18.12	-04:49:31.2	4.4			132.5	263.4		263.4	47.8
70		01:45:11.63	-04:48:59.9	5.1			147.9	261.9		261.9	46.8
71		01:45:38.62	-04:28:56.0	5.2	72.2	1.185	126.6	265.9	257.6	257.6	36.9
72		01:44:30.92	-04:32:47.5	5.6			149.6	250.2		250.2	43.1
73		01:45:20.13	-04:49:09.6	6.1	171.6	1.295	247.5			247.5	56.2
74		01:44:46.47	-04:42:53.1	7.4			174.6	245.3		245.3	39.0
75		01:44:44.81	-04:42:15.1	4.6	107.4	2.445	244.4			244.4	64.7
76		01:46:07.9	-04:30:42.9	5.8	112.2	1.645	244.2			244.2	53.1
77		01:45:39.54	-04:34:37.4	17.0	203.5	0.595	243.0			243.0	28.1
78		01:46:03.1	-04:44:25.5	6.3	153.8	1.23	237.3			237.3	51.5
79	T	01:44:48.19	-04:23:15.5	5.0				237.2		237.2	46.1
80		01:45:18.62	-04:46:24.8	11.1			233.6			233.6	26.0
81		01:45:25.15	-04:45:05.7	9.3			169.9	223.8		223.8	31.4
82		01:45:25.8	-04:23:01.5	7.9			161.9	222.5		222.5	33.9
83		01:45:00.8	-04:23:32.0	6.6			155.0	222.4		222.4	38.1
84		01:46:03.1	-04:35:49.5	10.6			174.6	217.9		217.9	28.7
85		01:45:26.92	-04:47:25.7	9.4			214.3			214.3	26.3
86		01:45:44.62	-04:31:09.2	16.1			212.6			212.6	19.6
87		01:45:00.9	-04:38:21.9	14.4			210.1			210.1	20.3
88		01:46:13.18	-04:38:45.4	5.2	113.2	1.505	209.5			209.5	52.1
89		01:45:16.49	-04:21:23.0	5.7	142.6	1.33	207.9			207.9	50.6
90		01:45:07.9	-04:36:13.8	16.1			205.9			205.9	19.0
91		01:46:13.69	-04:38:46.2	6.5			144.2	205.9		205.9	35.7
92		01:45:53.67	-04:27:08.9	8.4			149.8	204.4		204.4	30.0
93		01:44:47.86	-04:30:53.8	6.1	112.0	1.455	203.8			203.8	44.9
94	T	01:45:29.11	-04:49:07.7	4.6				203.7		203.7	42.4
95		01:45:19.27	-04:41:32.0	14.0			200.8			200.8	19.7
96		01:45:40.83	-04:22:34.0	4.6	104.8	1.725	199.8			199.8	54.9
97		01:45:38.06	-04:32:30.5	11.8	143.1	0.75	199.1			199.1	28.4
98		01:44:31.3	-04:37:02.9	4.1			110.8	195.4		195.4	40.5
99		01:46:19.61	-04:39:13.3	5.0			129.3	192.9		192.9	40.8
100	T	01:46:00.0	-04:44:59.0	4.9				187.7		187.7	35.9
101	T	01:45:57.75	-04:23:11.0	4.5				183.7		183.7	39.9
102		01:45:46.55	-04:24:49.6	7.3			140.6	182.7		182.7	31.4
103	T	01:46:18.84	-04:39:6.0	4.5				179.9		179.9	38.4
104	T	01:45:15.42	-04:22:22.6	5.0				179.8		179.8	35.4
105		01:45:27.4	-04:22:23.5	5.2	114.9	1.25	179.4			179.4	46.6
106	T	01:45:20.95	-04:47:01.2	5.0				177.3		177.3	33.5
107		01:45:17.08	-04:41:14.5	4.5	64.0	1.875	175.0			175.0	46.9
108	T	01:44:54.52	-04:42:26.6	5.5				170.6		170.6	31.6
109		01:45:33.29	-04:44:50.9	9.3			167.9			167.9	21.1
110		01:45:46.91	-04:33:18.5	12.7			163.9			163.9	16.9
111		01:45:31.71	-04:29:31.6	12.6			163.4			163.4	17.0
112		01:44:53.01	-04:31:51.4	6.9			112.0	161.0		161.0	26.6
113		01:44:50.8	-04:28:18.5	5.8			113.9	157.6		157.6	30.6
114		01:45:47.24	-04:22:48.5	6.6			155.7			155.7	25.1
115		01:45:41.53	-04:26:36.7	7.4			119.3	154.0		154.0	25.7
116		01:44:59.69	-04:32:13.1	10.6			153.7			153.7	17.6

Table 4.1 continued

Source	Flag	Right Ascension	Declination	SNR	S_p μJy b^{-1}	θ arcsec	S_{tot} μJy	S_3 μJy	S_6 μJy	S_{Best} μJy	ΔS μJy
117		01:46:01.2	-04:42:30.3	5.1			105.0	152.2		152.2	32.1
118		01:44:48.58	-04:35:51.5	6.4			110.1	149.7		149.7	27.4
119		01:46:15.08	-04:26:07.4	5.1			148.1			148.1	29.8
120	T	01:45:39.76	-04:46:11.7	4.4				147.8		147.8	32.4
121		01:44:55.26	-04:40:10.3	8.6			146.9			146.9	19.5
122		01:45:49.51	-04:44:41.1	4.0	80.8	1.395	146.8			146.8	47.3
123	T	01:44:48.83	-04:40:15.9	4.8				146.3		146.3	30.0
124	T	01:44:39.95	-04:34:14.2	4.4				145.9		145.9	31.3
125		01:45:12.29	-04:45:11.1	4.0	77.9	1.455	144.4			144.4	46.5
126		01:45:57.27	-04:36:20.5	7.0			103.8	144.1		144.1	24.3
127		01:44:58.39	-04:27:39.5	5.0	88.8	1.255	142.8			142.8	39.1
128		01:44:36.04	-04:27:34.0	5.0			141.9			141.9	28.1
129		01:46:03.3	-04:23:20.0	5.0			141.7			141.7	29.0
130		01:44:57.97	-04:47:9.0	5.1			141.0			141.0	28.6
131	T	01:44:42.26	-04:33:49.9	4.5				140.8		140.8	29.4
132		01:45:31.35	-04:29:31.0	10.8			140.0			140.0	15.9
133		01:44:44.63	-04:43:30.6	5.4			138.6			138.6	26.6
134		01:46:20.58	-04:28:20.5	4.7			137.3			137.3	28.7
135	H	01:45:16.9	-04:43:51.6	4.2			71.1		136.3	136.3	9.5
136		01:45:26.84	-04:24:33.0	4.5			80.8	135.2		135.2	27.2
137		01:45:09.6	-04:20:46.7	4.8			135.1			135.1	29.0
138		01:44:55.93	-04:24:04.6	5.6			133.6			133.6	24.6
139		01:45:55.93	-04:46:35.6	5.1			133.0			133.0	26.3
140		01:46:14.9	-04:28:45.4	5.4			132.9			132.9	25.5
141	T	01:45:56.93	-04:29:03.8	5.0				132.7		132.7	25.8
142	T	01:46:00.9	-04:40:12.6	4.7				132.7		132.7	27.2
143		01:46:16.35	-04:38:16.8	5.7			132.0			132.0	24.2
144		01:46:10.6	-04:24:32.8	4.5			131.9			131.9	29.8
145		01:44:53.31	-04:45:00.9	5.4			131.8			131.8	25.1
146		01:45:13.13	-04:37:20.3	8.3			103.1	131.8		131.8	20.7
147		01:45:52.76	-04:31:56.7	6.2			87.9	131.7		131.7	22.0
148		01:45:26.64	-04:43:53.1	5.4			89.4	131.7		131.7	26.2
149		01:44:44.3	-04:44:09.8	4.8			130.8			130.8	27.8
150		01:45:38.75	-04:39:49.9	7.2			96.3	129.5		129.5	21.8
151		01:45:58.51	-04:37:13.9	8.2			127.4			127.4	17.3
152		01:45:29.89	-04:49:28.5	4.3			125.7			125.7	29.5
153		01:45:22.77	-04:46:23.9	6.0			125.7			125.7	21.9
154		01:45:00.8	-04:35:43.8	4.3	60.7	1.605	125.6			125.6	37.2
155		01:45:37.14	-04:30:32.3	5.5	70.8	1.145	124.8			124.8	31.3
156		01:45:55.78	-04:46:59.0	4.6			123.9			123.9	27.6
157		01:45:00.9	-04:46:50.1	4.8			123.7			123.7	26.4
158		01:44:49.01	-04:41:18.1	6.1			123.4			123.4	21.0
159		01:44:54.06	-04:46:18.3	4.5			122.9			122.9	27.6
160		01:44:37.11	-04:41:53.9	4.4			121.2			121.2	28.0
161		01:46:12.04	-04:34:39.8	6.1			121.1			121.1	20.9
162		01:45:38.9	-04:20:27.6	4.3			120.6			120.6	28.5
163		01:46:15.12	-04:41:57.4	4.5			119.3			119.3	26.9
164		01:44:48.77	-04:25:18.8	4.8			119.1			119.1	25.2
165		01:44:48.71	-04:45:10.7	4.4			118.0			118.0	27.4
166		01:44:35.71	-04:37:37.7	4.9			118.0			118.0	24.6
167		01:45:55.92	-04:22:43.8	4.5			117.7			117.7	26.8
168		01:45:10.83	-04:29:08.7	8.3			117.4			117.4	15.9
169		01:45:26.94	-04:21:00.5	4.6			117.2			117.2	26.0
170		01:44:40.9	-04:27:49.3	4.7			117.1			117.1	25.2
171	T	01:44:57.04	-04:29:54.8	4.6				116.8		116.8	24.8
172		01:45:20.28	-04:45:17.5	6.2			116.8			116.8	19.8
173	T	01:44:58.26	-04:39:54.3	4.5				116.1		116.1	25.2
174		01:44:44.89	-04:38:44.7	5.8			114.9			114.9	20.8
175		01:44:55.77	-04:35:11.4	5.2			77.9	114.6		114.6	23.1
176		01:44:43.36	-04:27:58.5	4.9			113.5			113.5	23.7
177		01:44:53.6	-04:31:27.0	7.0			113.5			113.5	17.4
178		01:45:59.89	-04:30:01.8	6.7			112.6			112.6	17.9

Table 4.1 continued

Source	Flag	Right Ascension	Declination	SNR	S_p μJy b^{-1}	θ arcsec	S_{tot} μJy	S_3 μJy	S_6 μJy	S_{Best} μJy	ΔS μJy
179		01:46:10.51	-04:27:34.7	4.8			112.5			112.5	23.8
180		01:46:03.2	-04:25:01.8	4.6			112.4			112.4	24.8
181		01:46:15.71	-04:31:14.5	4.9			112.1			112.1	23.3
182		01:45:41.42	-04:39:42.0	4.8			65.5	111.7		111.7	21.0
183		01:45:59.09	-04:46:15.9	4.2			111.6			111.6	26.9
184		01:45:36.06	-04:35:05.9	6.2			72.7	111.0		111.0	19.0
185		01:44:55.46	-04:35:36.8	7.3			110.6			110.6	16.4
186		01:44:41.26	-04:33:59.9	5.5			110.3			110.3	20.9
187		01:44:45.45	-04:42:05.1	4.8			110.1			110.1	23.4
188		01:44:44.58	-04:26:17.4	4.4			109.7			109.7	25.4
189		01:44:30.39	-04:35:26.6	4.1			109.5			109.5	27.1
190		01:45:19.96	-04:21:25.7	4.4			109.0			109.0	25.0
191		01:46:08.1	-04:43:08.2	4.4			108.6			108.6	24.8
192		01:44:45.52	-04:43:31.1	4.3			108.6			108.6	25.5
193		01:46:05.0	-04:42:33.2	4.9			108.1			108.1	22.6
194	T	01:45:53.26	-04:34:10.7	4.9				107.6		107.6	21.9
195		01:45:23.25	-04:23:41.8	5.5			107.2			107.2	20.2
196		01:45:26.19	-04:47:33.1	4.6			107.0			107.0	23.3
197	T	01:44:59.93	-04:31:44.2	4.6				106.8		106.8	22.8
198	T	01:45:51.4	-04:39:28.1	4.5				106.8		106.8	22.5
199		01:44:35.39	-04:28:35.7	4.0			106.5			106.5	27.3
200		01:44:40.22	-04:41:28.4	4.2			105.6			105.6	24.3
201		01:46:01.6	-04:25:16.8	4.6			105.5			105.5	23.5
202		01:44:55.79	-04:28:38.9	6.0			104.7			104.7	18.4
203		01:45:44.06	-04:30:50.1	5.5			73.6	103.9		103.9	21.0
204		01:45:20.12	-04:42:03.8	4.2			61.6	103.6		103.6	22.8
205		01:46:09.0	-04:27:12.4	4.4			103.4			103.4	23.7
206		01:44:41.52	-04:37:23.4	5.0			102.6			102.6	21.2
207		01:46:13.75	-04:39:31.2	4.5			101.6			101.6	22.8
208		01:44:57.99	-04:24:27.3	4.4			100.0			100.0	22.9
209		01:46:11.57	-04:28:23.1	4.3			99.7			99.7	23.4
210	T	01:45:08.8	-04:38:23.4	4.7				99.7		99.7	20.1
211		01:45:46.7	-04:31:19.3	7.4			99.5			99.5	14.7
212		01:45:43.45	-04:46:15.6	4.5			99.2			99.2	22.3
213		01:44:38.66	-04:31:25.3	4.4			99.0			99.0	22.7
214		01:45:32.25	-04:46:37.2	4.6			98.9			98.9	21.7
215		01:46:09.9	-04:31:00.1	4.9			98.8			98.8	20.5
216		01:45:52.89	-04:31:46.2	4.4			62.9	98.7		98.7	21.3
217		01:45:03.3	-04:36:52.9	4.8			66.0	98.6		98.6	21.4
218		01:46:09.3	-04:42:04.5	4.2			98.5			98.5	23.5
219		01:44:38.17	-04:30:53.7	4.2			97.2			97.2	22.9
220		01:45:15.52	-04:35:37.8	4.6			54.9	96.5		96.5	18.0
221		01:45:58.43	-04:26:35.8	4.8			96.3			96.3	20.3
222		01:44:44.11	-04:37:59.4	4.8			95.5			95.5	20.2
223		01:44:46.4	-04:28:11.8	4.4			94.9			94.9	21.7
224		01:45:18.6	-04:29:34.6	7.2			94.5			94.5	14.3
225		01:45:57.89	-04:26:21.6	4.7			93.9			93.9	20.4
226		01:44:45.72	-04:29:44.5	4.6			93.7			93.7	20.5
227		01:44:59.41	-04:27:19.5	5.2			93.7			93.7	18.5
228		01:44:48.61	-04:42:20.6	4.3			93.4			93.4	22.1
229		01:46:07.1	-04:39:48.9	4.7			93.3			93.3	20.2
230		01:45:14.67	-04:45:58.5	4.5			92.8			92.8	21.0
231		01:45:26.94	-04:41:41.8	6.5			92.6			92.6	15.2
232		01:45:17.16	-04:46:10.7	4.4			92.4			92.4	21.1
233		01:45:44.27	-04:46:17.9	4.2			92.3			92.3	21.5
234		01:45:44.82	-04:24:08.5	4.5			92.2			92.2	20.6
235		01:45:55.81	-04:44:14.9	4.3			92.0			92.0	21.5
236		01:44:49.99	-04:28:45.7	4.7			91.8			91.8	19.4
237		01:45:55.61	-04:43:54.3	4.4			91.8			91.8	20.9
238		01:45:57.48	-04:31:07.1	5.8			91.5			91.5	16.4
239		01:44:44.91	-04:33:33.5	4.9			91.4			91.4	18.9
240		01:45:42.57	-04:23:32.4	4.3			91.1			91.1	21.2

Table 4.1 continued

Source	Flag	Right Ascension	Declination	SNR	S_p μJy b^{-1}	θ arcsec	S_{tot} μJy	S_3 μJy	S_6 μJy	S_{Best} μJy	ΔS μJy
241		01:44:45.13	-04:41:58.4	4.0			91.0			91.0	23.0
242		01:45:13.75	-04:23:47.5	4.5			91.0			91.0	20.4
243		01:45:44.92	-04:29:35.5	6.4			90.7			90.7	15.0
244		01:45:21.02	-04:41:55.9	6.2			90.7			90.7	15.5
245		01:46:08.8	-04:34:34.6	4.9			90.1			90.1	18.9
246		01:45:56.17	-04:25:09.9	4.2			89.6			89.6	21.5
247		01:45:39.58	-04:41:30.5	6.1			89.4			89.4	15.5
248		01:46:00.2	-04:37:10.2	5.6			88.6			88.6	16.5
249		01:44:47.02	-04:27:59.3	4.1			88.6			88.6	21.5
250		01:44:50.3	-04:27:34.0	4.3			88.5			88.5	20.5
251		01:44:54.46	-04:35:05.1	5.8			88.3			88.3	16.1
252		01:45:05.8	-04:33:43.3	4.0			51.6	88.0		88.0	19.7
253		01:45:28.18	-04:39:09.5	7.0			87.9			87.9	13.6
254		01:45:49.27	-04:24:28.6	4.3			87.8			87.8	20.8
255		01:46:05.1	-04:41:28.2	4.2			87.8			87.8	20.9
256		01:45:45.16	-04:26:06.3	5.1			87.7			87.7	17.7
257		01:46:03.7	-04:38:35.1	4.9			87.5			87.5	18.1
258		01:44:51.42	-04:41:42.2	4.4			87.4			87.4	20.2
259		01:46:12.1	-04:30:02.1	4.0			87.1			87.1	21.8
260		01:46:11.25	-04:32:38.0	4.4			87.0			87.0	20.1
261		01:45:28.66	-04:23:58.5	4.6			86.8			86.8	19.3
262		01:44:50.33	-04:29:17.6	4.6			86.8			86.8	19.1
263		01:45:33.35	-04:44:32.8	4.8			85.2			85.2	18.1
264		01:45:32.87	-04:24:52.1	4.8			85.1			85.1	17.6
265		01:45:04.5	-04:44:36.5	4.2			85.1			85.1	20.3
266		01:46:06.9	-04:31:56.7	4.6			85.0			85.0	18.6
267		01:44:59.46	-04:29:4.0	5.2			84.9			84.9	16.8
268		01:45:06.3	-04:43:54.6	4.5			84.9			84.9	18.9
269		01:46:04.2	-04:38:44.5	4.7			84.7			84.7	18.3
270		01:46:00.7	-04:37:16.0	5.2			84.5			84.5	16.6
271		01:44:46.35	-04:37:54.3	4.4			83.5			83.5	19.0
272		01:45:32.5	-04:27:53.3	5.8			82.9			82.9	14.8
273		01:44:56.75	-04:40:52.6	4.7			82.6			82.6	17.7
274		01:45:16.92	-04:41:00.4	5.9			82.6			82.6	14.8
275		01:46:11.09	-04:30:43.0	4.0			81.3			81.3	20.8
276		01:44:49.16	-04:34:37.5	4.8			81.2			81.2	17.3
277		01:44:50.75	-04:29:21.5	4.4			80.9			80.9	18.5
278		01:45:58.98	-04:42:16.3	4.2			80.8			80.8	19.5
279		01:45:46.95	-04:31:15.6	6.0			80.6			80.6	13.9
280		01:45:12.62	-04:25:08.7	4.5			80.6			80.6	18.3
281		01:46:02.1	-04:27:59.7	4.1			80.3			80.3	19.4
282		01:45:54.34	-04:42:35.2	4.3			80.2			80.2	18.6
283		01:45:22.71	-04:39:32.8	6.2			80.1			80.1	13.6
284		01:44:50.14	-04:39:02.9	4.4			79.7			79.7	18.3
285		01:46:01.5	-04:37:17.0	4.9			79.6			79.6	16.8
286		01:45:55.01	-04:38:48.8	5.2			79.5			79.5	15.8
287		01:45:41.0	-04:34:58.5	4.3			52.3	79.5		79.5	18.0
288		01:44:51.39	-04:29:54.2	4.4			78.9			78.9	17.6
289		01:45:24.46	-04:45:52.6	4.0			78.9			78.9	19.8
290		01:45:58.29	-04:32:15.1	5.1			78.0			78.0	15.9
291		01:45:04.4	-04:42:29.4	4.5			78.0			78.0	17.5
292		01:45:37.8	-04:35:33.3	6.5			77.5			77.5	12.7
293		01:46:04.1	-04:34:08.7	4.6			77.5			77.5	17.0
294		01:46:05.3	-04:33:2.0	4.5			77.4			77.4	16.8
295		01:45:54.67	-04:42:32.1	4.2			77.4			77.4	18.5
296		01:45:44.06	-04:32:54.5	6.1			76.8			76.8	13.3
297		01:46:00.6	-04:34:10.0	4.9			76.5			76.5	16.0
298		01:45:04.1	-04:27:04.2	4.5			76.3			76.3	17.2
299		01:45:04.7	-04:27:27.5	4.6			76.0			76.0	16.8
300		01:45:27.15	-04:43:44.4	4.6			75.9			75.9	16.7
301		01:45:03.2	-04:33:45.9	5.6			75.0			75.0	13.8
302		01:44:48.66	-04:34:08.7	4.4			75.0			75.0	17.4

Table 4.1 continued

Source	Flag	Right Ascension	Declination	SNR	S_p μJy b^{-1}	θ arcsec	S_{tot} μJy	S_3 μJy	S_6 μJy	S_{Best} μJy	ΔS μJy
303		01:44:59.76	-04:28:02.8	4.4			74.9			74.9	17.3
304		01:45:37.66	-04:44:06.7	4.3			74.8			74.8	17.6
305		01:44:52.46	-04:30:13.5	4.3			74.8			74.8	17.5
306		01:45:44.5	-04:32:35.4	5.8			74.6			74.6	13.4
307		01:44:48.27	-04:34:49.7	4.3			74.5			74.5	17.3
308		01:45:18.59	-04:32:44.5	6.2			74.3			74.3	12.6
309		01:45:14.26	-04:42:15.1	4.8			74.1			74.1	15.8
310		01:45:38.9	-04:41:25.9	5.0			73.6			73.6	15.0
311		01:45:54.46	-04:37:54.9	5.0			73.4			73.4	15.2
312		01:46:03.5	-04:31:47.7	4.3			73.2			73.2	17.3
313		01:45:56.55	-04:39:09.8	4.6			73.1			73.1	16.2
314		01:45:38.06	-04:25:36.8	4.3			72.6			72.6	17.2
315		01:45:33.47	-04:31:08.2	5.9			72.1			72.1	12.9
316		01:45:33.27	-04:43:12.3	4.5			72.1			72.1	16.2
317		01:44:48.66	-04:34:58.9	4.2			71.6			71.6	17.3
318		01:45:45.5	-04:39:45.2	5.1			71.6			71.6	14.5
319		01:45:43.96	-04:43:22.2	4.1			71.4			71.4	17.4
320		01:45:50.84	-04:40:45.8	4.5			71.2			71.2	16.0
321		01:44:53.65	-04:36:25.6	4.5			71.2			71.2	16.0
322		01:45:26.67	-04:29:05.5	5.4			71.1			71.1	13.7
323		01:45:31.73	-04:31:29.9	5.9			70.9			70.9	12.7
324		01:45:57.74	-04:29:51.8	4.3			70.8			70.8	16.6
325		01:45:19.07	-04:34:17.6	6.0			70.8			70.8	12.3
326		01:45:45.3	-04:43:30.0	4.0			70.7			70.7	17.7
327		01:45:21.04	-04:26:23.1	4.5			70.7			70.7	16.0
328		01:45:36.24	-04:42:57.8	4.4			70.5			70.5	16.1
329		01:45:43.43	-04:38:59.3	5.2			70.3			70.3	13.9
330		01:46:03.9	-04:33:58.8	4.2			70.3			70.3	16.6
331		01:45:45.79	-04:31:16.0	5.2			70.1			70.1	13.8
332		01:45:43.18	-04:43:55.5	4.0			70.1			70.1	17.9
333		01:44:48.94	-04:36:57.5	4.0			70.1			70.1	17.2
334		01:45:23.82	-04:35:44.0	6.0			69.6			69.6	12.2
335		01:45:33.12	-04:43:40.8	4.2			69.5			69.5	16.7
336		01:45:12.73	-04:38:26.6	5.4			69.5			69.5	13.4
337		01:45:15.65	-04:42:58.2	4.3			69.5			69.5	16.2
338		01:45:37.93	-04:41:19.7	4.8			69.3			69.3	14.7
339		01:44:54.38	-04:30:50.8	4.2			69.3			69.3	16.5
340		01:45:25.47	-04:26:57.8	4.6			69.3			69.3	15.2
341		01:45:03.7	-04:40:13.1	4.5			69.2			69.2	15.5
342		01:45:51.32	-04:37:22.0	4.9			69.0			69.0	14.3
343		01:45:07.8	-04:32:59.2	5.3			69.0			69.0	13.3
344		01:45:21.19	-04:27:15.5	4.6			68.7			68.7	15.1
345		01:45:02.6	-04:41:50.0	4.0			68.2			68.2	16.9
346		01:45:26.82	-04:36:02.7	5.9			68.1			68.1	12.1
347		01:45:54.53	-04:36:34.2	4.7			68.1			68.1	14.7
348		01:45:48.04	-04:41:49.8	4.2			68.1			68.1	16.3
349		01:45:34.87	-04:28:51.1	5.0			68.1			68.1	14.0
350		01:45:30.34	-04:26:57.0	4.5			67.8			67.8	15.2
351		01:45:54.43	-04:29:28.4	4.2			67.5			67.5	16.0
352		01:45:55.99	-04:30:48.4	4.3			67.4			67.4	15.6
353		01:45:02.0	-04:41:27.5	4.0			67.3			67.3	16.4
354		01:45:06.1	-04:34:28.7	5.2			67.2			67.2	13.4
355		01:45:02.7	-04:30:02.1	4.5			66.9			66.9	15.1
356		01:45:47.61	-04:40:59.5	4.3			66.9			66.9	15.6
357		01:45:07.7	-04:27:23.5	4.1			66.8			66.8	16.2
358		01:45:27.64	-04:39:15.1	5.3			66.8			66.8	13.0
359		01:44:56.23	-04:36:01.6	4.4			66.7			66.7	15.1
360		01:45:45.3	-04:30:08.3	4.8			66.5			66.5	14.1
361		01:44:53.9	-04:31:57.6	4.1			66.1			66.1	16.1
362		01:45:16.07	-04:42:55.3	4.1			65.7			65.7	16.1
363		01:45:53.28	-04:39:54.7	4.2			65.6			65.6	15.4
364		01:45:11.24	-04:28:55.5	4.6			65.3			65.3	14.5

Table 4.1 continued

Source	Flag	Right Ascension	Declination	SNR	S_p μJy b^{-1}	θ arcsec	S_{tot} μJy	S_3 μJy	S_6 μJy	S_{Best} μJy	ΔS μJy
365		01:45:03.7	-04:33:33.8	4.9			65.3			65.3	13.7
366		01:45:32.22	-04:30:39.0	5.2			65.1			65.1	12.7
367		01:45:04.4	-04:33:24.4	4.8			64.7			64.7	13.6
368		01:45:54.31	-04:37:34.4	4.4			64.2			64.2	14.8
369		01:45:20.35	-04:36:59.4	5.4			63.9			63.9	12.0
370		01:44:56.31	-04:37:23.8	4.2			63.9			63.9	15.1
371		01:45:44.81	-04:31:41.0	4.9			63.8			63.8	13.0
372		01:45:54.05	-04:36:43.1	4.4			63.8			63.8	14.5
373		01:45:05.4	-04:35:16.6	4.8			63.4			63.4	12.9
374		01:45:33.06	-04:27:05.2	4.2			63.2			63.2	15.1
375		01:45:43.68	-04:32:47.0	5.0			63.0			63.0	13.0
376		01:45:35.88	-04:34:05.9	5.3			62.7			62.7	12.2
377		01:45:35.13	-04:34:8.0	5.3			62.3			62.3	12.1
378		01:45:23.32	-04:35:39.6	5.4			62.2			62.2	12.0
379		01:45:47.72	-04:37:53.1	4.5			61.4			61.4	13.8
380		01:45:36.08	-04:35:22.0	5.2			61.3			61.3	12.1
381		01:45:22.11	-04:27:08.5	4.1			60.9			60.9	15.0
382		01:45:31.0	-04:37:08.5	5.1			60.2			60.2	12.2
383		01:45:06.4	-04:39:21.7	4.2			59.9			59.9	14.3
384		01:45:09.6	-04:37:6.0	4.6			59.6			59.6	13.1
385		01:45:19.02	-04:40:39.4	4.3			59.5			59.5	13.9
386		01:45:37.15	-04:39:59.9	4.4			59.0			59.0	13.6
387		01:45:28.98	-04:31:31.9	4.9			58.9			58.9	12.3
388		01:45:45.15	-04:31:48.1	4.5			58.4			58.4	13.2
389		01:45:04.9	-04:38:33.0	4.1			58.3			58.3	14.1
390		01:45:33.01	-04:38:22.5	4.7			58.3			58.3	12.6
391		01:45:12.28	-04:35:59.6	4.7			58.2			58.2	12.5
392		01:45:49.6	-04:35:45.7	4.4			58.1			58.1	13.5
393		01:45:10.64	-04:31:46.0	4.5			58.0			58.0	13.0
394		01:45:36.71	-04:33:23.6	4.9			57.9			57.9	12.2
395		01:45:00.1	-04:34:13.5	4.1			57.8			57.8	14.0
396		01:45:53.73	-04:33:35.8	4.1			57.6			57.6	14.2
397		01:45:36.74	-04:35:41.0	4.9			57.6			57.6	12.1
398		01:45:44.44	-04:36:01.6	4.5			57.3			57.3	12.8
399		01:45:04.7	-04:34:18.9	4.3			56.9			56.9	13.3
400		01:45:24.99	-04:39:19.4	4.5			56.7			56.7	12.8
401		01:45:31.67	-04:29:56.2	4.4			56.6			56.6	13.0
402		01:45:07.2	-04:38:12.0	4.2			56.3			56.3	13.3
403		01:45:32.75	-04:33:09.1	4.8			56.1			56.1	12.0
404		01:45:39.67	-04:34:24.1	4.6			55.7			55.7	12.2
405		01:45:29.12	-04:32:07.1	4.7			55.7			55.7	12.1
406		01:45:17.81	-04:38:25.7	4.4			55.4			55.4	12.7
407		01:45:29.16	-04:27:53.4	4.0			55.4			55.4	14.2
408		01:45:35.38	-04:37:13.8	4.6			55.3			55.3	12.3
409		01:45:32.24	-04:29:48.8	4.3			55.1			55.1	12.6
410		01:45:33.84	-04:28:25.0	4.0			54.9			54.9	13.5
411		01:45:26.61	-04:33:13.7	4.7			54.5			54.5	11.8
412		01:45:34.97	-04:39:14.9	4.2			54.3			54.3	13.0
413		01:45:03.0	-04:37:15.4	4.0			54.3			54.3	13.6
414		01:45:50.73	-04:35:24.1	4.0			54.2			54.2	13.5
415		01:45:10.87	-04:35:03.9	4.4			54.2			54.2	12.5
416		01:45:42.8	-04:36:08.8	4.3			54.1			54.1	12.6
417		01:45:21.33	-04:35:11.9	4.6			53.3			53.3	11.8
418		01:45:07.9	-04:38:22.7	4.0			53.1			53.1	13.5
419		01:45:30.53	-04:38:37.2	4.2			52.5			52.5	12.5
420		01:45:23.48	-04:39:19.3	4.1			52.5			52.5	12.5
421		01:45:29.63	-04:34:41.1	4.5			52.2			52.2	11.7
422		01:45:05.0	-04:33:41.7	4.0			52.0			52.0	13.2
423		01:45:33.59	-04:33:56.0	4.3			50.8			50.8	11.8
424		01:45:36.75	-04:33:14.8	4.2			50.8			50.8	12.0
425		01:45:46.09	-04:33:49.0	4.0			50.7			50.7	12.5
426		01:45:33.07	-04:31:26.5	4.1			50.6			50.6	12.3

Table 4.1 continued

Source	Flag	Right Ascension	Declination	SNR	S_p μJy b^{-1}	θ arcsec	S_{tot} μJy	S_3 μJy	S_6 μJy	S_{Best} μJy	ΔS μJy
427		01:45:21.33	-04:37:50.3	4.2			50.5			50.5	12.2
428		01:45:39.22	-04:37:04.4	4.1			50.4			50.4	12.4
429		01:45:17.45	-04:36:1.0	4.1			48.9			48.9	12.0
430		01:45:29.43	-04:35:25.0	4.2			48.0			48.0	11.4
431		01:45:33.79	-04:37:33.0	4.0			47.9			47.9	11.9
432		01:45:18.49	-04:33:09.3	4.0			46.7			46.7	11.9

4.7.1 Completeness

4.7.1.1 Resolution Bias

As discussed in Chapter 3, when total flux source counts are calculated from a peak flux based survey, extended sources can drop beneath the peak flux detection limit. The higher resolution of these VLA A-array 1.4 GHz maps compared to those discussed in Chapter 3 means that resolution bias is more of a concern. Also unlike the case in Chapter 3, no imaging of a higher resolution is available to provide estimates of the likely resolution bias. As in Chapter 3, the maps of varying resolution provide sensitivity to different sizes of sources. In the flux range between 45 and 72μJy, (the detection limits in the full resolution and the 3×3 arcsec maps respectively) sources more extended that $\sim$1.5 arcsec fall below the peak detection threshold. Between 72 and 180μJy, sources more extended than $\sim$3.6 arcsec are missed. Between 180 and 300μJy, the 6×6 map provides sensitivity to all sources smaller than 6 arcsecs.

Oncé again, the parameterisation of the distribution of source sizes of Bondi et al. (2003) was used to estimate the number of sources which exist, but have been missed by this survey. It should be noted that this was determined using a sample of brighter sources, but still provides a useful estimate. Their formulation gives 49 percent of sources being larger than 1.5 arcsec, 16 percent being larger than 3.6 arcsec, 7 percent larger than 6 arsec, and less than 1 percent being larger than the 10 arsec size which the 6×6 map is sensitive to at $\sim$300 μJy.

It is therefore assumed that the survey is 51 percent complete between 45 and 72 μJy, 84 percent complete 72 and 180 μJy, 93 percent complete above 180 μJy, and complete above 300 μJy. This incompleteness was accounted for in the weighting.

4.7.1.2 Bandwidth Smearing

As discussed in Section 4.5.3.2, bandwidth smearing reduces the peak flux of sources far from the phase tracking centre, while conserving total flux. In a peak flux selected survey this affects the completeness, and requires an additional correction

in computation of the source counts. Taking the function given in Section 4.5.3.2, and the detection limit flux (5σ for the source counts) the area over which a source could still be detected, given the affect of bandwidth smearing, can be calculated. This affect was included the areas used in the weighting of each source during binning.

4.7.1.3 Primary Beam degradation

The loss of sensitivity away from the phase centre due to the primary beam shape is the most significant source of incompleteness. The known shape of the primary beam allows the calculation of the area over which each source could have been detected.

4.7.2 Construction of the Source Counts

The gain of the instrumental setup as a function of radius from the phase centre was taken to be the product of the bandwidth smearing function and the primary beam shape. This was used to define an area over which a source of any particular flux could be detected. Sources of 5σ and above were separated into bins of width $0.18log(S_{Best})$. Each source was weighted by the inverse of the area over which it could be detected, and by the resolution bias at its flux. The weights were summed, divided by the bin width, and divided by $S_{Mid}^{-2.5}$ to normalise to a static, Euclidean cosmological scenario, where S_{Mid} is the log centre of the bin. The errors on the bins are taken as the Poissonian counting errors, $\sqrt{N}$.

Since these counts do not occupy any new parameter space, large amounts of time were not invested in extensive simulations to estimate and correct for Eddington Bias and further incompleteness.

The corrected source counts are given in Table 4.2 and plotted in Fig. 4.11, together with a compilation of results from other surveys. The compilation includes the 1.4 GHz source counts from Huynh et al. (2005), Formalont et al. (2006), Biggs and Ivison (2006), Simpson et al. (2006), and the compilation of Seymour et al. (2004), which includes results from Windhorst et al. (1990), White et al. (1997), Gruppioni et al. (1997), Prandoni et al. (2001), Bondi et al. (2003), and Hopkins et al. (2003). The results of Richards et al. (2000) and Grupponi et al. (1999) have been removed to account for the more recent analyses of these fields. The results from the 1^H field clearly follow the well known up turn in Euclidean normalised differential source counts. The large field to field scatter in the points justifies, at

Bin (μJy)	S_{mid} (μJy)	N_s	$S^{2.5}dN/dS$ (Jy$^{1.5}$sr^{-1})
56– 85	70	42	3.8 ± 0.6
85– 128	105	44	3.1 ± 0.5
128–194	158	43	4.6 ± 0.7
194–295	240	31	4.8 ± 0.8
295–446	363	18	5.0 ± 1.2
446–676	550	12	6.2 ± 1.8
676–1020	832	11	8.6 ± 2.6
1020–3550	1905	12	14.7 ± 4.2
3505–28180	10000	10	67.9 ± 21.5

Table 4.2: The 1.4 GHz Euclidean normalised differential source counts in the 1^H field. Columns are bin boundaries (μJy), S_{Mid} (μJy), bin population, and Euclidean normalise differential source counts

least from the point of modelling all the counts, not making extensive Eddington bias corrections to the counts from the 1^H field when any such corrections are likely to be insignificant compared to the scatter.

4.7.3 Modelling of the Source counts

As discussed in Chapter 3, the modelling of source counts has long been a method of constraining the cosmological evolution of radio source populations. Seymour et al. (2004) fit a model, by eye, to a compilation of the known 1.4 GHz source counts. More sophisticated fitting was not used as the choice of which field from which data were used was the dominant effect. In the intervening years, the sub-mJy population has been explored by several further works (Hunyth et al. 2005; Fomalont et al. 2006; Biggs and Ivison 2006; Simpson et al. 2006), including several re-analysis of archival data. With these extra data, fitting is more viable. The field to field variations are still the dominant contribution to the scatter of points, but a fit to the average sub-mJy bump is possible.

A model similar to that fitted in Chapter 3 was used. The shifting of the Rowan-Robinson et al. (1993) and Sadler et al. (2002) luminosity functions to 610 MHz was ignored, and P once again held at zero. The source counts from the FIRST survey (White et al. 1997) were not used, as the FIRST survey is not complete at faint fluxes (see fig. 11 of White et al. 1997). Fitting Q to the remaining data points shown in Fig 4.11 yields a best fitting value of 2.5. This best fitting model is shown in Fig. 4.12. It should be noted that, as indicated in Seymour et al. (2004) this model

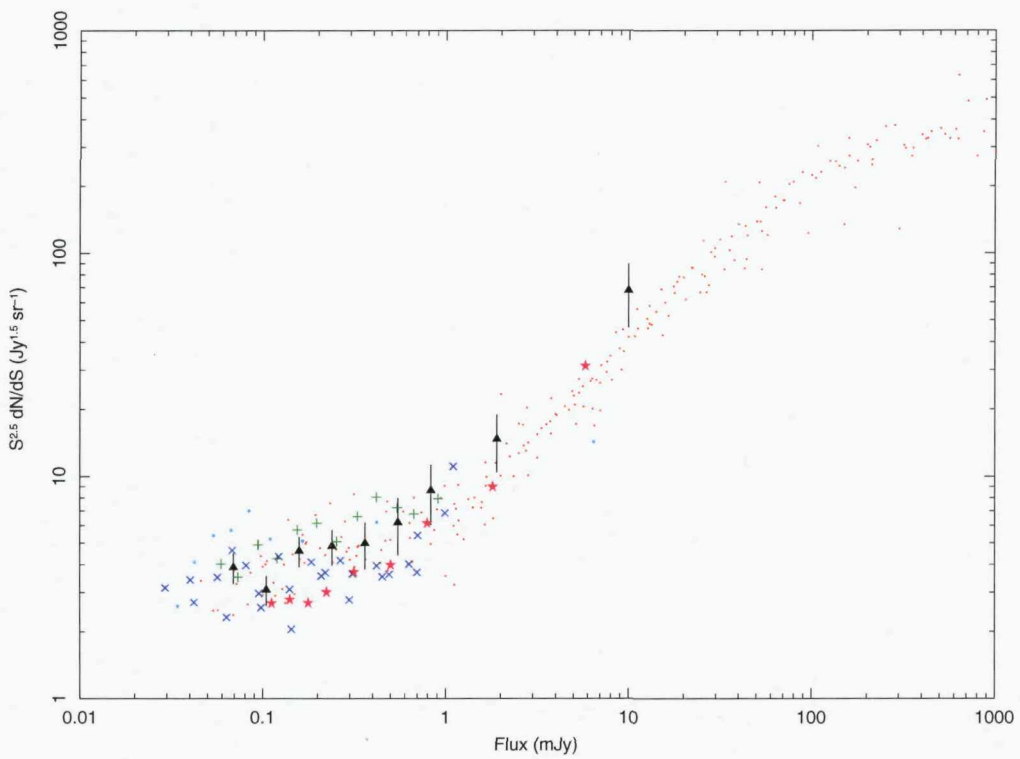

Figure 4.11: The 1.4 GHz Euclidean normalised differential source counts of this study (filled triangles), along with those from Huynh et al. (2006, stars), Formalont et al. (2006, crosses), Simpson et al. (2006, filled circles), Biggs and Ivison (2006, targets), and those of the compilation of Seymour et al. (2004, small dots). Note that the newer HDF and ELAIS source counts from Biggs and Ivison (2006) have replaced those of these fields from Seymour et al. (2004).

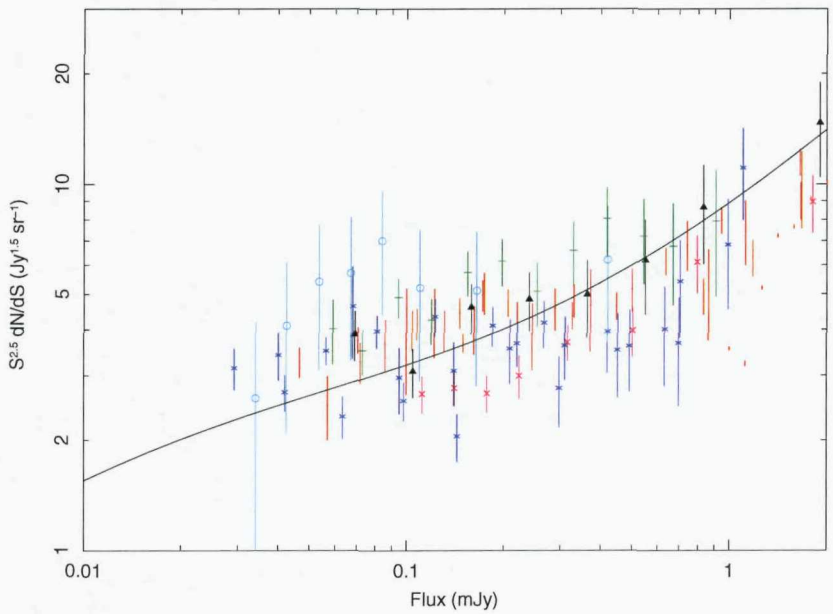

Figure 4.12: The 1.4 GHz Euclidean normalised differential source counts below $\sim$ 1 mJy. Symbols are the same as those in Fig 4.11. The solid line shown is the best fitting source counts model.

does slightly over predict the counts between 1 and 10mJy, which is a limitation in the accuracy of the AGN component. Other populations may also have some effect. For example, Jarvis & Rawlings (2004) suggest that some of the sub-mJy bump may be due to the detection of the radio signatures of the central engines of radio quiet AGN. This supposition originates from measuring radio fluxes in the FIRST survey of X-ray detected AGN and evolving their luminosity function in a manner similar to that shown in Ueda et al. (2003). However, their *total* AGN counts still underestimate the total counts below 1 mJy, and a further, starburst population is required. Any such extra AGN population would decrease the luminosity evolution of the starburst population required to account for the sub-mJy bump – decreasing Q. Such models can be tested once the sources which constitute the sub-mJy bump have been separated into AGN and starburst – the eventual culmination of this work once it is combined with others based on radio morphology, radio to MIR ratios, radio luminosity and other discriminants.

This value of 2.5 agrees with that determined in Chapter 3, and is consistent with other determinations at 1.4 GHz such as $Q = 2.5 \pm 0.5$ (Rowan-Robinson et al. 1993), $Q = 3.1 \pm 0.8$ (Hopkins et al. 1998), $Q = 3.0 \pm 1$ (Condon et al. 2002), $Q = 2.5 \pm 0.5$ (Seymour et al. 2004) and $Q = 2.7$ (Huynh et al. (2005).

4.8 Radio Morphology

The majority of the 13^H field is covered by high resolution MERLIN imaging (Zoghbi et al. in prep) to provide good morphological discrimination between AGN and galaxies whose radio emission is due to star formation. For the areas of the 13^H field not covered by MERLIN, the areas of the 13^H field where the MERLIN observations suffer from bandwidth smearing, and the whole of the 1^H field, the best morphological information is provided by the VLA 1.4 GHz images. Unresolved point sources can be either AGN or starburst. Slightly extended sources may also be either. But at the $\sim$1 arcsec resolution of the 1^H field 1.4 GHz survey map, several sources can be reliably identified, by eye, as the double lobes of an AGN. Sources 1, 4, 8, 13, 14, and 17 in the 1^H field 1.4 GHz catalogue display such double lobes, and can therefore be categorised as AGN. Fig. 4.13 shows contour plots of the emission from these sources. Also, although the majority of the flux from source 9 is point like, it does show extended structure to the East and North West. These structures extend beyond the extent of the optical object co-incident with source 9, and so it has also been classified as an AGN based on its morphology and is included in Fig. 4.13. The sinc-like sidelobes discussed in Section 4.4.1 can be seen affecting sources 1, 9 and 13.

4.9 Conclusions

In a VLA A-array 1.4 GHz observation of the 1^H XMM-*Newton* / *Chandra* survey area, 432 sources are detected down to a 4σ detection limit of 45 μJy within a 15 arcmin radius. The source counts derived from the resulting catalogue agree with those determined in other deep 1.4 GHz surveys. A compilation of these multi–field source counts can be modelled with AGN and the local 1.4 GHz starburst population undergoing a power law evolution with index of 2.5.

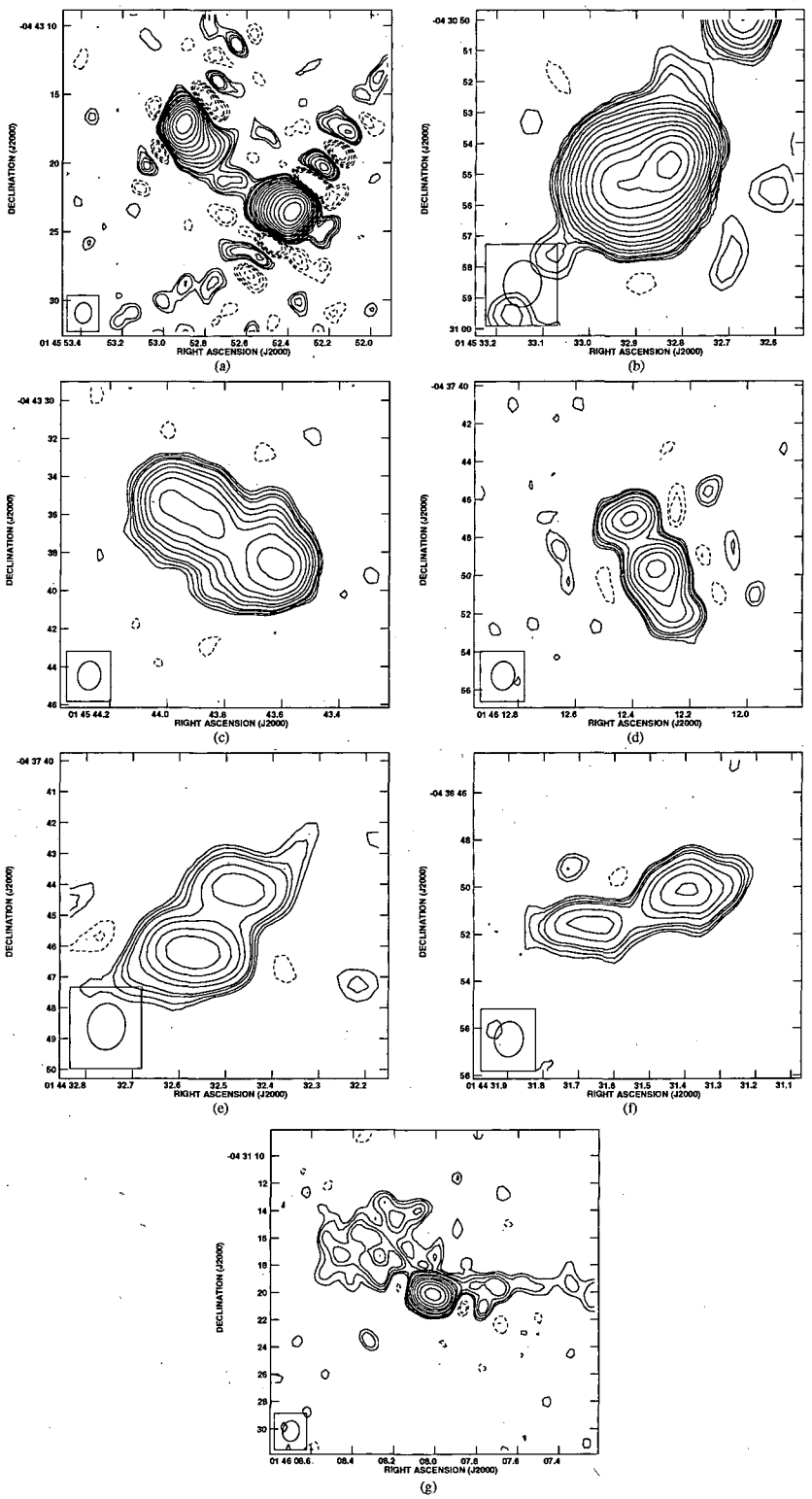

Figure 4.13: Contours of the 1.4 GHz emission of the 7 sources identified as the AGN. Panels a, b, c, d, e, and f, show the emission from sources 1, 4, 8, 13, 14 and 17 respectively. Source 9 is also shown in panel g. Note the effect of the sinc-like sidelobes are visible around sources 1, 9 and 13.

Chapter 5

Radio Spectra of Faint Sources

In this chapter, the individual radio spectral indices are presented. The two field, two frequency survey is completed with the 610 MHz survey of the 13^H field, in which 206 sources are discovered, and the multi–field 610 MHz source counts modelled. Tapered maps of the 1.4 GHz observation of the 13^H field are examined, and radio spectral indices calculated for 76 sources detected at two frequencies in the 13^H field. The 1^H field yields a further 76 spectra. An additional 14 and 8 sources have useful limits on their spectra in the 13 and 1^H fields respectively. These spectral properties are briefly compared to the radio morphological information available from the VLA imaging.

5.1 Introduction

As introduced in Chapter 1, radio spectra are key diagnostics of the nature of the *radio* emission from sources discovered in deep radio surveys, and a clean sample of radio flux density measurements of star forming galaxies can provide an independent and unbiased view of the cosmic star formation history.

The expected synchrotron nature of the radio emission detected from distant objects in deep radio surveys predicts simple power-law spectra over centimetre wavelengths. As shown in Chapters 3 and 4, modelling of the source counts at different frequencies can provide information about the average spectral index of a population. However, flux density measurements at two frequencies can provide good estimates of the radio spectra of individual objects, and so a sensible strategy is to perform deep surveys of the same region of sky at differing frequencies. The survey of the 13^H field at 1.4 GHz is presented in Seymour (2002) and Seymour et al. (2004), and briefly discussed in Section 5.5. Observations of the 1^H field at

both 1.4 GHz and 610 MHz have been presented in previous chapters. For radio spectra to be calculated for both fields, measurements of the 610 MHz flux densities of sources in the 13^H field are required. Section 5.2 deals with such an observation.

Since the 610 MHz survey images include the entire 1.4 GHz survey areas, flux densities or upper limits are available at both frequencies for all sources detected at 1.4 GHz. These fluxes, along with the assumption of a simple power-law spectrum of the form $S \propto \nu^{\alpha}$ allow the calculation of two point radio spectral indices for each source - aiding AGN/starburst discrimination on a source by source basis.

5.2 610 MHz Observations of the 13^H Field

5.2.1 Observations and Data Reduction

The 13^H was observed for ~ 4.5 hours in August of 2004, during the same observing run that provided the data presented and analysed in Chapter 3. The observational details were identical to those presented therein. A total bandwidth of 32 MHz was split into 128 channels in each of two sidebands, with 17 second averaging. Regular observations of 3C286 provided flux, phase, and bandpass calibration. Initial calibration and careful flagging were performed on a single channel at 601 and 620 MHz in the LSB and USB respectively. After bandpass calibration, each sideband carefully inspected for RFI, and was compressed into 11 channels. A further round of phase and bandpass calibration was performed on channels at 603 and 618 in the LSB and USB respectively. Each sideband of this data was self calibrated separately, with solutions found for phase only in intervals of 20, 6 and 2 minutes. A further round of phase and amplitude self calibration was also performed.

The two side bands were then combined into one *uv* database of 23 channels using UVFLP (provided by Dave Green – http://www.mrao.cam.ac.uk/~dag/UVFLP) and DBCON.

5.2.1.1 Attempts to Remove the Brightest Source

Initial imaging showed that the dominant source of noise in the images was the side lobes surrounding the brightest source in the field, caused by small residual phase errors and/or imperfect deconvolution of its extended structure.

The removal of a model of the source from the *uv* database can help with such deconvolution problems. The Clean algorithm performs a similar task, removing a model based on the results of initial imaging – the dirty map. This method has

therefore already been shown to perform less than ideally, since this Cleaned map is dominated by sidelobes. A more accurate model, free of imaging artifacts, can be used to remove the source in the *uv* plane – helping to remove the noise that results from deconvolution errors. Since the 13^H field has already been covered at higher resolution with the VLA, such information does exist. A model was constructed from the Clean Components (CC) of a map of the source at 1.4 GHz made with the A-array only data of Seymour et al. (2004). The frequency difference between the two observations, combined with the steep spectrum of the extended radio emission, mean that the flux of the model required modification before subtraction from the 610 MHz *uv* database. Each CC was widened to a Gaussian, and various schemes of flux adaption were tried. Simple multiplication of the flux of each 1.4 GHz CC by factors ranging from 1.5, to 3 were attempted, as well as more sophisticated strategies, such as multiplication factors varying over the source. Various numbers of CCs were also used.

The best result was achieved with multiplication factors ranging from 3 to 7 being applied to the measured flux (i.e. no primary beam correction applied at either 1.4 GHz or 610 MHz, so these are not indicative of actual spectra indices). This was removed from the *uv* database, reducing the flux density of the bright source in the map from 289 mJy to 57 mJy. However, the noise surrounding the source was not significantly reduced. This implies that the primary reason for the high noise are small remaining phase calibration errors rather than deconvolution problems. These calibration errors are discernible above the background noise of the image due to the extremely bright flux of this source, which is detected at 289 mJy. Unlike the HDF, the location of which was selected to avoid bright radio sources, this field was selected based purely on the IRAS 100μm cirus maps to provide low absorption in the X-ray, and so the effects of this source were not considered. Future observations of the 13^H field will utilise much shorter intervals between calibrator scans to help improve phase calibration and mitigate the effects of the source on the extended map.

5.2.1.2 Imaging

Imaging was performed on a 5×5 grid of facets (similar to that used in Chapter 3), to account for 3D smearing. Also included were 26 external fields to Clean the sidelobes of sources outside the main lobe of the primary beam. One such source, located 1.25 deg from the phase centre, which has a flux of 3 Jy in the NVSS, appears as the region of emission of 123 mJy.

Figure 5.1: The entire 610 MHz map of the 13^H field before any correction for primary beam degradation.

A pixel scale of 1×1 arcsec was used to fully sample the dirty beam. The highest sensitivity image was achieved with Robust=0 weighting, and gave a restoring beam of 6×5 arcsec.

The 25 facets covering the primary beam were combined into a single mosaic, shown in Fig. 5.1 using the AIPS task FLATN, with no correction being made for the reduction in sensitivity of the primary beam with distance from the pointing centre. A zoom in to the centre of the image is shown in Fig. 5.2.

5.2.2 Analysis

As can be seen in Fig. 5.1, the noise is not uniform across the field. The bright sources are surrounded by areas of noise higher than that seen in the rest of the map. These are due to small remaining calibration errors, and imperfect deconvolution

Figure 5.2: A central region ($\sim 17 \times 17$ arcmin) of the 610 MHz map of the 13^H field before any correction for primary beam degradation.

of the dirty beam from the extended structure of the associated source. SExtractor (Bertin & Arnouts 1996) was used to create a rms noise map of mesh size 24 by 24 pixels. Noise values varied from 55μJy beam^{-1} in the most sensitive regions to 130 μJy beam^{-1} in the noisiest, with the peak of the distribution at 60 μJy beam^{-1}. The centre of the map, which benefits from the highest sensitivity region of the primary beam, is slightly effected by the higher noise caused by the bright extended sources, so even though on a non-primary beam corrected map the modal noise is 60μJy beam^{-1}, the most sensitive region, in terms of absolute sensitivity, suffers slightly higher noise $\sim$ 68μJy beam^{-1}.

The noise level achieved here, with a slightly differing reduction to that discussed in Chapter 3, is a similar factor above the thermal noise as the 610 MHz image of the 1^H field. Both observations were conducted in August of 2004, suggesting that, as discussed in Chapter 3, the system temperatures in the summer of 2004 may have been higher than thought, though such large scale and uniform variation of many electronic components seems unlikely to be responsible for such a large increase in the noise above the theoretical level. The presence of a very bright source near the centre of the field suggests that, once again, dynamic range limitations may well also play a part in increasing the noise above the theoretically possible level.

The noise map was used to generate a signal to noise ratio map, upon which source detection was performed. To ensure consistency with previous chapters, the AIPS task SAD was used to find all sources with a signal to (*local*) noise of over 5, corresponding to a most sensitive detection limit of 275 μJy. Each source was examined by eye to eliminate obvious sidelobes. The residual maps produced by SAD were also examined to discover any cases of SAD failing to sufficiently well model a source with a Gaussian. Inside the 32 arcmin radius, 20 percent sensitivity level of the GMRT 610 MHz primary beam, 201 sources were significantly detected. SAD was then used to measure the properties of the detected sources from the map of total flux density. Of the 201 sources, 183 were suitably fitted by Gaussians. The remaining 18 sources, poorly fitted by SAD, were extracted by hand using TVSTAT, and are flagged with a T in Table 5.1.

To check for the effect of Clean Bias on the measured source properties, simulations similar to those of Chapter 3 were performed. Sources of known flux were inserted into the full *uv* data and the imaging and source extraction repeated. Comparison of the average inserted measured flux density to the known model flux gave offsets of 17.5, 16.2, 18.4 and 19.3 at 1, 2, 3, and 5 mJy respectively. A simple constant was fitted to these values, giving an estimate of the Clean bias of 17.5μJy. This is less that the estimate made in Chapter 3, for the effect of the same number of Clean iterations on an image of similar dimensions. The difference may be explained by the differing noise characteristics of the two maps. The detected fluxes of the real sources were corrected accordingly, before being corrected for the degradation in sensitivity of the primary beam.

5.2.3 Catalogue

In cases where two nearby sources appeared to constitute the double lobes of an AGN, the higher sensitivity and resolution 1.4 GHz catalogue of Seymour et al. (2004) was consulted. Outside the area covered at 1.4 GHz, overlays of the radio emission on i' band imaging from MegaCam were examined, and a decision based on the relative radio/optical morphology and/or displacement.

A resolution criterion, based upon detected S_{tot}/S_p similar to those employed in Chapters 3 and 4, was used to define the best measurement of the flux of each source.

A tapered map was made to search for sources of low surface brightness, the flux of which may have been resolved out of the full resolution map. Four new

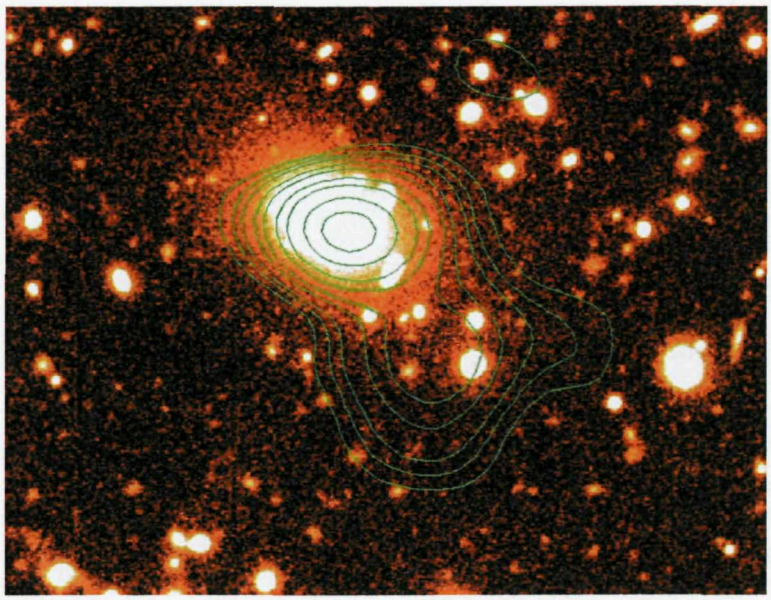

Figure 5.3: The contours of 610 MHz radio emission (from the tapered map) of source 20 overlaid on the i' band image of the region. Source 20 was initially identified in the full resolution map as the region of 610 MHz emission in the upper left of this image. The region of emission in the lower right part of the figure is ~3 times brighter in the tapered map than in the map made at full resolution. Contours are shown at levels of 300, 450, 600, 900, 1200, 1800 and 2400 μJy beam^{-1}.

isolated sources were discovered and added to the catalogue. One further detection was made, 18 arcsec to the South East of source 20. In the full resolution map, a slight over density was apparent at this location, but considered a sidelobe. Also, although source 20 aligned with an optical object, this dimmer emission did not. In the tapered map, this region of emission is very significantly detected, with a peak flux $\sim$ 11 times the local noise, and appears to be an extension of source 20, though the exact nature of the complex is not clear. An overlay of the emission from the tapered map on the i' band image of the region is shown in Fig. 5.3. The flux of the region of emission in the lower right of Fig. 5.3, as measured from the tapered map, was included with that of source 20.

The final catalogue is given in Table 5.1. Columns are: Number; flag (T means detected first in the tapered map, H means extracted by hand using TVSTAT); RA; Dec; SNR; size (SAD deconvolved size for reliably resolved Gaussian sources, longest distance between 2σ contours for non-Gaussians); peak flux density, S_p, in μJy beam^{-1} (for reliably resolved sources); total flux density, S_{tot}, in μJy; error in μJy.

Table 5.1: The complete catalogue of 610 MHz sources in the 13^H field. Source Number, flag,RA, Dec, detection signal to noise ratio (SNR), peak flux density S_p in μJy beam^{-1}, angular size in arcsec (see Section 5.2.3), integrated flux density S_{tot} in μJy, both for sources considered reliably resolved, and Δ_S, the error on the best determination of the flux density, in μJy.

Source	Flag	Right Ascension	Declination	SNR	peak (μJy b^{-1})	θ ($''$)	S_{tot} (μJy)	ΔS (μJy)
1	h	13:32:49.9	37:45:05.7	913.4	20664.4	150.0	425715.1	274.1
2	h	13:33:29.0	37:56:1.0	873.8	62282.0	35.0	365839.8	164.9
3	h	13:34:25.1	38:17:53.9	683.4	53338.6	18.0	289952.3	275.7
4	h	13:36:56.7	37:44:07.7	160.7	99348.4	15.0	115043.9	464.8
5	h	13:33:49.0	38:21:37.6	284.3	8924.6	50.0	81287.2	422.0
6	h	13:35:00.8	37:38:36.3	503.2	19057.4	30.0	71760.3	189.1
7	h	13:33:21.3	37:54:15.9	180.7	2447.1	90.0	27416.2	174.3
8	h	13:34:02.9	37:59:48.6	176.1	23351.4	14.0	25110.0	142.4
9		13:35:16.6	38:00:07.2	173.3	19570.4	4.21	24795.2	153.9
10		13:32:07.6	37:43:20.5	33.9	10570.9	4.53	14822.0	646.8
11		13:35:47.9	38:01:49.3	121.2			13916.9	83.0
12		13:32:59.3	38:13:38.4	54.6	11374.4	2.91	13866.1	379.1
13	h	13:33:07.9	37:51:40.9	98.4	4862.9	48.0	13283.1	198.9
14		13:36:26.4	37:31:12.3	37.8	11114.5	3.84	12999.8	603.0
15	h	13:36:8.0	38:12:15.1	74.2	5414.5	16.0	12453.2	314.7
16		13:36:45.4	37:46:40.9	45.1			12368.1	163.9
17		13:34:38.4	38:06:26.3	124.4			11978.4	71.7
18		13:33:19.6	37:29:28.1	34.8	7696.2	4.63	10942.8	524.9
19		13:34:14.2	37:24:14.4	37.2	9439.1	2.48	10457.4	518.0
20	h	13:35:44.1	37:45:04.7	88.5	6172.7	20.0	10258.2	185.5
21		13:34:28.6	37:27:35.7	33.8	6458.3	4.01	9361.0	428.6
22		13:34:44.7	37:33:50.6	67.1	8514.5	2.08	9095.8	225.4
23	h	13:36:40.6	37:50:22.9	48.5	4159.9	20.0	8416.2	307.0
24		13:33:25.0	38:20:49.4	31.4	7090.2	2.39	8109.7	469.1
25	h	13:34:57.5	37:50:29.8	100.9	1443.1	15.0	7504.1	135.8
26		13:37:10.8	37:48:21.4	21.7	6355.1	4.88	7437.0	545.2
27		13:32:27.5	37:44:37.0	31.2	6622.6	3.17	7359.3	374.4
28		13:32:46.4	37:42:23.5	6.0	1312.6	12.26	7058.1	963.4
29	t	13:32:37.9	37:57:18.3	5.1	1904.3	20.35	7044.9	1252.0
30		13:33:04.6	38:18:53.4	28.6			6884.1	230.8
31	t	13:33:29.8	37:34:01.8	5.1	1434.6	27.38	6659.2	1620.0
32		13:34:02.6	38:14:54.3	33.7	5641.0	2.23	6235.4	235.6
33		13:32:43.3	37:43:40.7	14.4	2755.4	7.05	5757.8	454.1
34		13:32:59.4	37:56:10.6	28.8	4259.4	3.83	5498.9	229.7
35	h	13:35:41.6	37:41:56.7	51.7	1375.1	25.0	5232.1	201.0
36		13:33:59.9	37:49:11.2	50.9	4065.6	3.16	4790.2	146.0
37		13:33:02.7	38:05:25.5	29.3	3991.2	2.73	4704.2	247.5
38		13:34:38.0	37:41:32.5	54.6			4653.0	75.3
39	t	13:33:34.1	37:39:47.6	5.4	1229.3	20.11	4583.6	966.9
40	h	13:35:58.8	37:55:08.3	42.8	1939.5	20.0	4568.5	183.7
41		13:35:06.5	38:03:47.8	57.7			4415.9	69.7
42		13:36:47.2	37:58:26.7	27.7			4220.7	155.6
43		13:36:47.6	38:13:23.1	13.7			4024.0	310.4
44		13:36:49.7	37:40:32.7	8.9	2600.7	5.13	3998.2	568.8
45	h	13:34:49.2	38:05:52.0	42.6	1597.8	30.0	3910.8	153.9

Table 5.1 continued

Source	Flag	Right Ascension	Declination	SNR	peak (μJy b^{-1})	θ ($''$)	S_{tot} (μJy)	ΔS (μJy)
46		13:35:49.0	37:29:58.5	10.6	1887.9	8.09	3792.9	604.6
47		13:36:03.1	38:18:10.2	18.7			3744.0	202.6
48		13:33:02.1	37:56:36.2	29.6			3550.8	96.5
49		13:34:33.0	38:22:03.8	14.2			3349.4	174.9
50	h	13:34:38.1	37:57:6.0	43.4	1761.0	18.0	3302.2	130.9
51		13:32:18.3	37:44:18.1	14.1			3261.8	238.2
52		13:35:35.6	37:26:22.4	13.0			3231.1	270.9
53		13:35:25.3	38:05:35.5	20.0	1720.9	5.61	3169.1	228.9
54		13:32:48.9	37:47:11.1	13.6	2279.0	4.46	3128.2	291.2
55		13:33:48.6	37:42:02.1	6.8	595.5	20.55	3062.7	539.6
56		13:34:05.3	38:18:31.9	20.2			3005.1	139.9
57		13:32:38.5	37:51:17.5	5.1	738.7	13.6	2853.3	666.5
58	t	13:34:9.0	38:01:30.6	5.6	1155.6	14.38	2788.9	458.9
59		13:32:33.1	37:52:41.5	5.2	888.0	8.79	2726.4	591.8
60		13:32:30.4	38:03:18.4	10.5	1778.7	4.92	2704.4	414.4
61		13:33:03.5	37:57:11.9	5.2	656.2	14.3	2591.8	495.4
62		13:34:42.6	38:22:14.0	11.5			2564.7	202.5
63		13:34:05.4	38:07:37.6	21.9	2053.2	3.49	2537.9	176.7
64		13:36:29.0	37:39:28.0	6.4	1290.0	5.64	2501.3	508.9
65		13:35:44.5	37:57:41.7	24.9	2140.8	3.57	2498.2	167.1
66		13:35:35.3	37:53:13.2	31.8			2451.7	71.5
67		13:33:51.5	37:42:17.7	29.4			2450.5	81.8
68		13:33:10.2	37:55:28.2	22.6			2389.8	88.6
69		13:35:41.6	38:15:59.8	8.6	1275.8	5.16	2365.2	416.4
70		13:32:53.7	37:48:47.5	5.0	702.9	11.07	2346.8	504.4
71		13:32:47.5	37:51:25.6	5.0	697.2	12.74	2322.3	524.5
72		13:36:46.1	37:51:46.2	13.4			2248.1	171.2
73		13:32:36.2	37:49:35.6	12.2			2057.5	154.1
74		13:32:40.8	37:41:20.2	9.6			2033.9	183.6
75		13:34:13.5	37:45:38.7	17.5	1358.0	4.84	1987.1	171.6
76		13:36:10.3	37:35:00.6	11.8			1981.0	193.2
77		13:32:22.6	37:50:48.6	10.6			1962.8	190.0
78		13:34:01.1	38:23:50.6	8.5			1957.6	246.8
79		13:36:25.1	38:02:46.0	14.2			1820.7	139.9
80		13:36:55.3	37:40:47.0	6.0			1811.4	273.6
81		13:33:25.6	38:21:05.7	7.4			1797.5	244.7
82		13:32:20.3	37:54:51.7	8.9			1790.2	189.5
83		13:33:35.1	38:09:34.4	5.0	511.7	13.39	1789.6	468.2
84		13:34:58.3	38:04:29.1	21.6			1745.3	69.4
85		13:32:41.1	37:52:22.3	11.9			1745.1	141.7
86		13:33:07.4	37:36:12.3	10.3			1694.8	172.1
87		13:34:44.7	37:28:15.3	9.8			1627.3	185.7
88		13:35:53.5	37:41:27.5	15.9			1550.0	117.4
89		13:36:14.7	38:20:13.7	5.0			1503.4	301.9
90		13:35:49.0	37:51:34.1	18.3			1476.8	79.3
91		13:32:39.4	37:51:57.4	9.4			1461.3	145.6
92		13:32:48.8	38:11:54.8	8.1			1426.9	200.2
93		13:37:06.3	37:59:58.7	5.7			1424.1	254.0
94		13:32:37.4	38:10:06.1	7.1			1361.7	214.2

Table 5.1 continued

Source	Flag	Right Ascension	Declination	SNR	peak (μJy b^{-1})	θ ($''$)	S_{tot} (μJy)	ΔS (μJy)
95		13:32:49.3	38:15:17.6	6.2			1347.1	239.9
96		13:33:36.5	38:23:53.7	5.0			1343.1	300.1
97		13:34:13.5	37:57:31.4	10.2	757.4	6.45	1307.3	173.7
98		13:35:55.9	38:13:44.4	8.6			1297.5	159.0
99		13:36:28.5	37:39:04.3	6.5			1276.2	193.5
100		13:33:49.8	38:03:33.7	13.7			1273.8	74.3
101		13:35:16.1	37:56:20.0	6.3	451.4	12.03	1240.7	254.0
102		13:33:48.4	37:54:56.3	5.9	527.4	7.78	1205.2	229.9
103		13:36:57.0	37:49:51.0	5.7			1181.1	212.3
104		13:36:09.6	38:02:22.8	11.2			1157.5	116.2
105		13:33:46.5	38:00:21.7	9.6			1155.8	81.0
106		13:35:50.9	37:29:36.2	5.7			1154.4	233.2
107		13:36:58.5	38:03:11.9	5.7			1153.7	235.9
108		13:33:13.5	37:31:31.9	6.1			1145.3	220.2
109		13:32:54.5	37:34:00.5	5.5			1126.7	225.9
110		13:34:01.5	37:49:09.4	9.5	745.3	4.95	1123.2	169.9
111		13:35:51.0	37:44:01.6	5.0	474.6	11.24	1123.1	327.8
112		13:32:33.5	37:43:44.4	6.2			1122.3	188.7
113		13:33:58.3	38:08:10.5	7.0	702.2	4.23	1116.9	218.0
114		13:33:24.0	38:07:14.3	10.0			1110.1	111.4
115		13:34:42.7	37:57:33.2	14.7			1100.2	60.7
116		13:36:44.1	37:55:22.0	7.1			1089.3	165.3
117		13:36:10.6	38:17:19.3	5.2			1072.2	236.0
118		13:32:31.1	37:54:48.1	7.0			1062.1	162.0
119		13:35:11.7	38:20:00.3	5.1			1045.1	176.0
120		13:32:56.8	38:06:27.1	7.1			1037.5	141.7
121		13:34:27.4	38:08:31.4	10.9			1035.0	88.1
122		13:32:36.8	38:02:09.5	6.2			1030.4	158.9
123		13:36:21.0	38:02:07.1	7.7			1020.5	130.6
124		13:36:32.6	37:40:40.6	5.4			1002.0	190.0
125		13:33:48.1	37:53:52.9	7.7	577.6	5.43	985.6	187.9
126		13:36:03.2	38:10:30.4	7.4			977.5	143.9
127		13:34:53.7	37:48:15.3	14.9			951.0	73.1
128		13:34:28.6	37:46:46.2	6.7	619.3	5.29	949.0	168.8
129		13:32:57.5	37:59:35.9	7.8			948.2	118.9
130		13:36:00.1	37:53:46.1	11.1			936.9	97.8
131		13:32:33.2	37:48:36.6	6.0			932.0	166.3
132		13:36:38.7	37:57:51.1	6.5			919.1	154.9
133		13:35:36.5	38:11:39.2	8.1			916.7	121.5
134		13:33:38.0	37:43:24.9	11.2			914.9	96.9
135		13:35:03.7	38:08:41.3	5.1	415.6	7.17	914.5	268.5
136		13:34:46.3	37:42:46.4	12.6			911.0	82.7
137		13:35:19.5	38:11:08.3	9.2			900.6	107.8
138		13:34:53.0	37:50:43.4	13.4			873.2	70.5
139		13:36:0.0	37:40:38.4	7.0			865.2	129.5
140		13:34:19.8	37:28:49.7	5.1			852.3	179.7
141		13:32:40.8	37:54:04.2	5.6			845.0	141.2
142		13:33:48.6	38:07:01.4	6.9			844.2	91.8
143		13:34:02.7	38:11:02.3	7.6			825.7	102.3

Table 5.1 continued

Source	Flag	Right Ascension	Declination	SNR	peak (μJy b^{-1})	θ ($''$)	S_{tot} (μJy)	ΔS (μJy)
144		13:32:37.8	37:54:37.8	5.9			809.4	141.7
145		13:35:00.6	37:44:07.7	11.6			806.6	81.3
146		13:33:44.6	38:13:47.6	6.5			801.3	125.5
147		13:33:08.2	37:48:18.9	6.1			770.4	108.2
148		13:36:07.1	38:11:10.7	5.3			768.9	154.9
149		13:34:25.6	37:36:53.6	7.7			768.7	104.1
150		13:33:04.4	37:39:11.0	5.3			759.4	152.3
151		13:32:49.7	37:57:11.0	6.1			741.8	126.0
152		13:35:13.2	37:48:56.5	11.4			736.6	76.2
153		13:33:58.4	37:56:08.4	8.4			728.9	73.8
154	h	13:34:39.9	37:57:02.9	5.4	372.9	14.0	724.5	130.9
155		13:35:45.4	37:37:07.7	5.8			712.1	132.9
156		13:35:48.2	37:58:51.0	8.1			707.5	89.3
157		13:34:06.9	37:40:06.3	7.6			706.3	95.0
158		13:33:18.6	38:02:23.8	6.7			697.7	101.6
159		13:34:15.0	37:35:43.3	6.4			690.8	114.2
160		13:34:57.2	37:47:57.9	10.2			674.5	74.0
161		13:34:02.4	37:36:6.0	5.5			666.9	114.8
162		13:35:48.0	37:38:20.2	5.6			656.1	128.2
163		13:33:58.7	37:43:21.1	8.5			651.8	87.2
164		13:35:20.3	37:36:13.3	5.8			645.6	115.7
165		13:33:08.7	38:05:48.9	5.2			630.0	116.9
166		13:33:32.1	37:36:58.9	5.7			627.0	130.7
167		13:35:56.3	38:02:37.5	5.9			621.8	103.0
168		13:36:02.6	38:04:46.4	5.9			620.3	114.6
169		13:34:20.8	37:59:29.9	9.1			612.1	70.0
170		13:35:01.5	37:47:25.0	8.9			610.5	75.3
171		13:33:53.7	37:35:49.0	5.5			610.0	122.8
172		13:33:25.1	38:05:10.6	5.7			607.4	103.4
173		13:36:02.8	38:05:05.7	5.7			602.7	116.5
174		13:36:06.2	38:04:04.5	5.7			599.6	116.9
175		13:33:56.4	38:04:05.5	6.7			598.8	83.3
176		13:35:50.7	38:09:26.2	5.6			595.4	122.2
177		13:35:30.0	37:37:26.9	5.8			589.8	118.4
178		13:34:02.2	38:10:36.6	5.5			576.3	101.8
179		13:33:44.4	38:02:07.6	5.4			563.1	82.7
180		13:33:40.7	38:02:44.7	5.1			533.6	87.4
181		13:34:58.9	37:40:46.0	5.7			528.9	90.5
182		13:35:04.8	37:49:01.9	7.3			528.3	74.0
183		13:35:14.8	38:01:08.8	5.6			527.2	77.4
184		13:35:00.2	37:56:32.3	7.7			520.8	70.5
185		13:34:51.9	37:57:42.3	7.4			514.8	69.9
186		13:34:36.4	38:08:42.3	5.6			514.1	87.4
187		13:34:17.5	37:44:32.0	6.5			511.2	79.7
188		13:34:22.8	37:37:32.8	5.2			504.4	99.9
189		13:35:42.0	37:41:9.0	5.2			492.0	109.2
190		13:33:38.3	37:44:56.4	5.5			490.8	88.6
191	h	13:33:07.7	37:52:0.0	4.5	659.4	6.0	488.1	198.8
192		13:34:13.9	37:57:12.0	6.6			486.6	70.7

Table 5.1 continued

Source	Flag	Right Ascension	Declination	SNR	peak (μJy b^{-1})	θ ($''$)	S_{tot} (μJy)	ΔS (μJy)
193		13:33:56.9	37:51:24.8	6.4			476.1	75.1
194		13:34:58.2	38:06:35.6	5.5			464.5	84.0
195		13:36:05.1	37:58:44.5	5.2			462.9	104.6
196		13:34:32.5	37:58:01.7	6.4			461.2	69.3
197		13:34:52.3	37:42:45.3	6.0			454.7	83.4
198		13:34:24.8	37:40:06.8	5.3			449.6	91.2
199		13:33:39.4	37:45:53.8	5.1			449.2	85.3
200		13:34:09.7	37:54:30.1	5.8			433.6	70.9
201		13:34:19.4	37:40:15.4	5.1			426.2	91.5
202		13:35:02.3	37:51:25.2	5.9			424.5	70.0
203		13:35:40.0	37:46:24.4	5.0			393.5	89.9
204		13:35:12.3	37:51:31.7	5.3			389.2	70.1
205		13:34:33.1	37:52:20.4	5.1			365.1	68.9
206		13:33:50.9	37:47:53.8	5.3			361.9	79.6

5.2.4 Source Counts

Sources were binned on total flux, and weighted in a manner similar to that in Chapter 3. Corrections for incompleteness caused by primary beam degradation, high noise regions and resolution bias were applied as in Chapter 3. The area over which a source could have been detected was calculated by examining the distribution of pixels values in a SExtractor noise map derived from a primary beam corrected version of Fig. 5.1. Eddington bias simulations were performed as in Chapter 3, and used the best fitting population from the 1^H field (i.e. $Q = 2.45$) as an estimate of the true underlying population. They implied that the effect of the noise on lowest flux bin was a 26 percent overestimation, along with a 21 percent overestimation in the second lowest flux bin. This bias at higher fluxes compared to those affected in the 1^H field is likely to be due to the differing noise characteristics of the two maps.

Fig. 5.4 shows the resulting counts, plotted along with the those from the 1^H field. The two fields exhibit similar source counts, with the bin values agreeing to within the Poissonian counting errors. The 13^H field shows slightly lower source density than the 1^H field below 1 mJy. This is also the case at 1.4 GHz, where the Euclidean normalised differential source counts of the 1^H field are $\sim$15 percent higher that those of the 13^H field for comparable low flux bins.

See Section 5.4 for the modelling of the multi-field 610 MHz source counts.

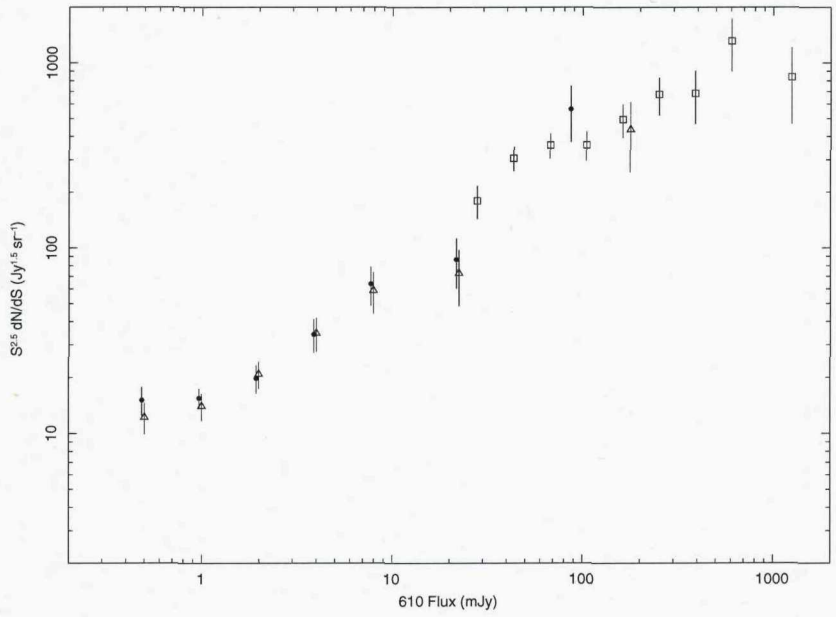

Figure 5.4: The Euclidean normalised differential 610 MHz source counts from the 13^H field (empty triangles), plotted along with those from the 1^H field (filled circles), and empty squares denoting the results of Katgert (1979).

5.3 Deeper 610 MHz Observations of Both Fields

Both the 13^H and 1^H fields were observed with the GMRT at 610 MHz for a further 20 hours each in February of 2006, with the intention of more closely matching the detection limits of the 610 MHz and 1.4 GHz images. Observations were performed identically to those in 2004 with the exception that the averaging time of each visibility was reduced to from 17 to 8 seconds. Reduction was performed in a manner similar to that discussed in Chapter 3. Similar numbers of baselines were lost to power outages and electronics glitches, and an initial calibration solution of a 'channel 0' for the 13^H field appeared adequate. Bandpass calibration also appeared successful. Upon examining the variation of the visibilities with frequency and time using the AIPS task SPFLG (which effectively plots trailed spectra), ripples across the bandpass became apparent in many (>70 percent) of the baselines, including all those contained entirely within the central square of the GMRT. The purpose of bandpass calibration is to remove any structure in the frequency response of the antennas, so such a pattern is not expected. However, the ripples move across the band with time, inhibiting their removal by calibration. Also, the speed of this motion changes, and in some case the direction of motion reverses. Fig. 5.5 shows the trailed spectra (time on the y axis, frequency on the x), for the baselines between

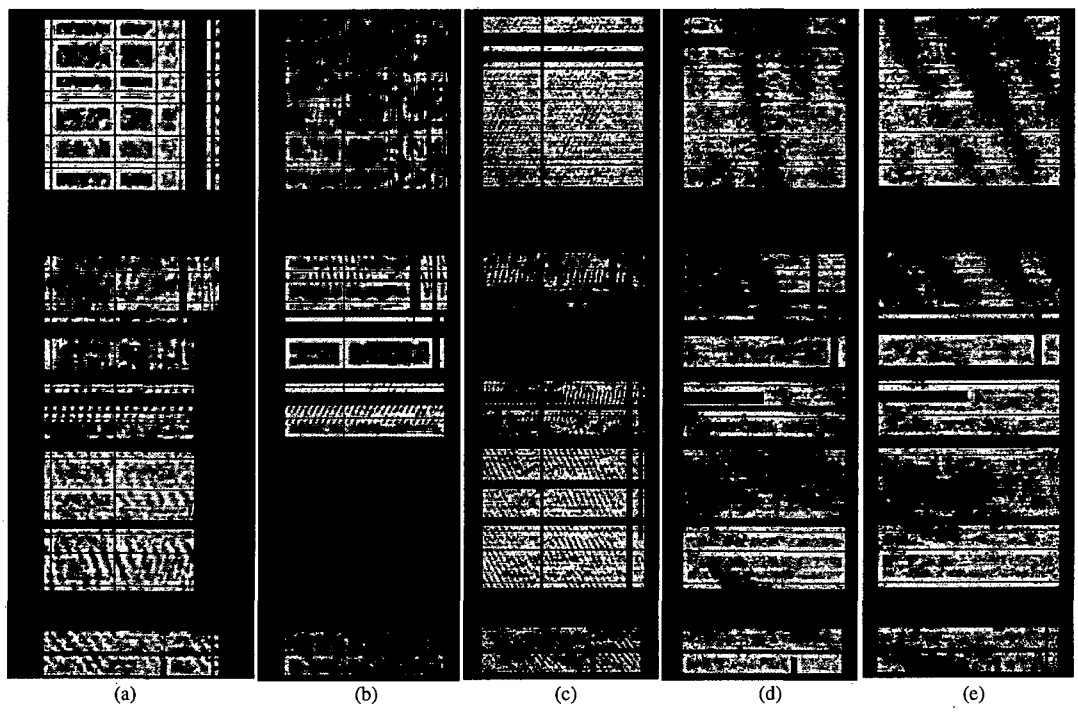

Figure 5.5: The amplitude (greyscale) of the visibilities against frequency (x-axis) and time (y-axis) for baselines between antennas 2 and 8, 2 and 12, 4 and 14, 4 and 25, and 8 and 12 in panels a, b, c, d, e, and f respectively.. Each pixel represents one 8 second averaged visibility in one channel.

antennas 2 and 8, 2 and 12, 4 and 14, 4 and 25, and 8 and 12 during observations of 3C286 in the USB. As can be seen in Fig. 5.5, the ripples do not share a common wavelength (in frequency-time space).

The amplitude of the ripples in visibility amplitude is ~10 percent. They are present in the uncalibrated data, and therefore not a result of poor bandpass calibration. Staff at the GMRT could provide no explanation for these effects, though the instrument was experiencing intermittent correlator problems at the time of the observations.

Data reduction was continued to investigate the effect of these bandpass ripples on the sensitivity of the final maps. An image made using the *uv* data of the USB from all 20 hrs of the observation of the 13^H field achieved a rms noise of 160μJy beam^{-1}, much worse than achieved with the 4.5 hr observation in 2004. A reduction of the LSB of 8hr worth of observations of the 1^H field achieved a noise level of 140μJy, when a noise level at least comparable to that in the maps made with the 2004 data was expected.

After many attempts to improve the calibration of the data, it was agreed that

the observations should be repeated. Make-up observations were scheduled, but not completed within the time frame of this work.

5.4 Modelling of 610 MHz Source Counts

As was shown in Chapter 3, the modelling of source counts can provide information about the average spectral index of a population. In that study, models were fitted to the counts from one field. As has been seen in Chapter 4, radio source counts can vary significantly from field to field. The availability of counts from several fields greatly increases the robustness of any model fits

Models were fitted to the source counts from the 13^H and 1^H fields. Published 610 MHz source counts are also available for the VVDS survey (Bondi et al. 2007). The resolution bias corrections suggested in table 2 of Bondi et al. (2007) have been applied.

The starburst evolution power law index, Q, was fitted as in Chapter 3. The best fitting model, with $Q = 2.6 \pm 0.1$ is plotted in Fig. 5.6. Within the 1σ errors on the various fitted values, this is consistent with the determination in both Chapters 3 and 4, confirming that the population that constitute the sub-mJy bump have, on average, a spectrum of $\alpha = -0.7$.

As mentioned in Chapter 3, this two population model may over simplify the situation. It is not impossible for the same galaxy to possess both a radio loud AGN and a starburst, a contingency which the models do not account for. Also, the overestimation of the source counts by the AGN component of the model between 1 and 10mJy is a limit upon the accuracy of the fitted starburst evolution, and does not take account of the possible contribution from radio quiet quasars (Jarvis & Rawlings 2004). However, since the same model has been fitted at both 1.4 GHz and 610 MHz, the determination of the average spectral index of -0.7 is a reasonable one.

5.5 1.4 GHz Observations of the 13^H Field

Radio observations covering the 13^H field were presented in Seymour (2002) and Seymour et al. (2004). Their importance in the context of this study justifies a short summary here. The 13^H Field was observed with the VLA in B-array for 10 hours in 1995. A further 14 hours of useful data were obtained from the VLA in A-array in 1998. All observations were conducted in 4-IF pseudo-continuum mode, with

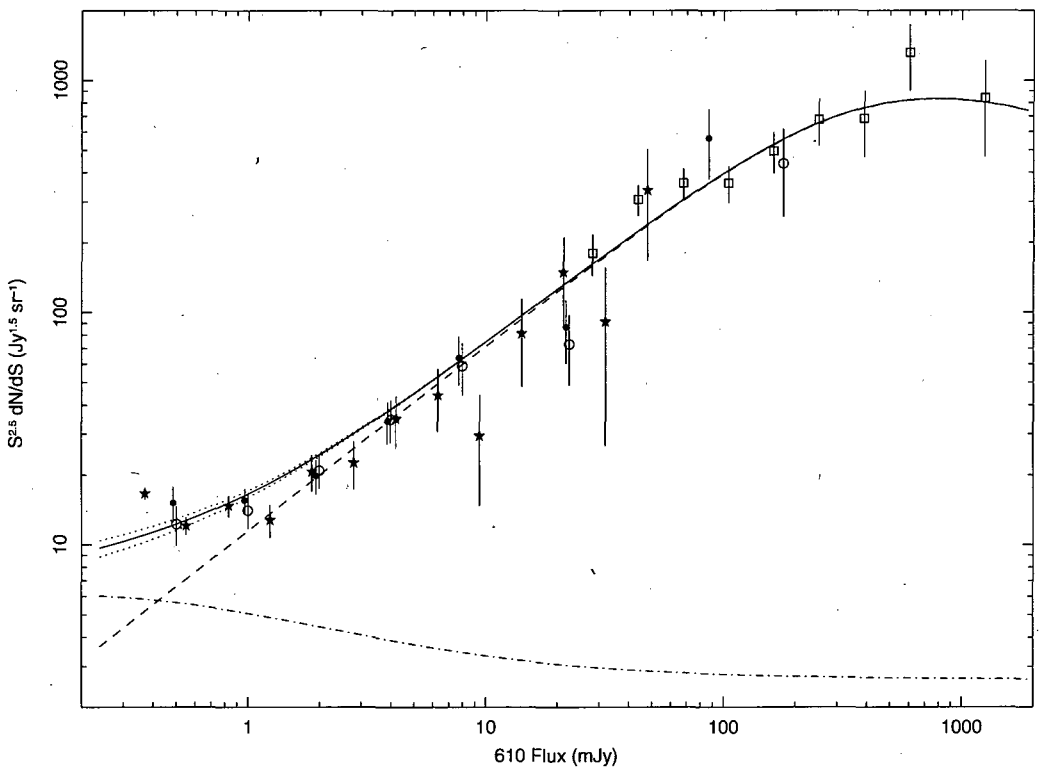

Figure 5.6: The best fitting model of the 610 MHz, that of $Q = 2.6$, together with the source counts from the 1^H field (filled circles), the 13^H field (empty circles), the VVDS (stars, Bondi et al. 2007), and Katgert (1979, empty squares).

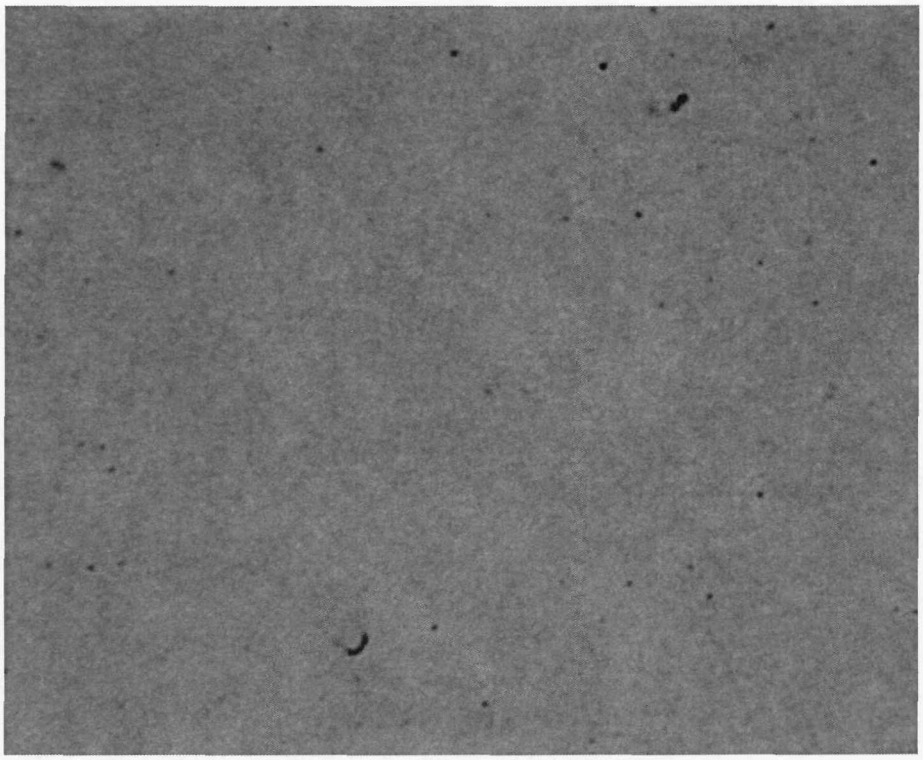

Figure 5.7: A central portion ($\sim 10 \times 10$ arcmin) of the 1.4 GHz image of the 13^H Field, as presented by Seymour et al. (2004). This image has had no correction for for primary beam degradation applied.

both polarisations of each Intermediate Frequency (IF) being split into 8 channels of 3.25 MHz each, as in the observation presented in Chapter 4. The observations were bandpass, flux and phase calibrated in the standard manner using 3C286, 3C286 and 1310+323 respectively. The data from the two array configurations were combined in the *uv* plane. Three iterations of self-calibration were conducted, and total intensity maps were made using a mosaic of 9 central, and four smaller external facets to adequately cover confusing sources. After CLEANing, the image, made with natural weighting, had a central rms noise of 7.5μJy beam^{-1}, and a restoring beam of 3.4 arcsec. A central portion of this image can be seen in Fig. 5.7.

To a 4σ detection limit of 30μJy, 449 sources were found. The source counts computed from this catalogue can be seen as the filled triangles in Fig. 1.5.

5.5.1 Resolution degraded 1.4 GHz Maps of the 13^H Field

As discussed in previous chapters, the calculation of accurate spectral indices requires that the flux measurements in the two bands be made from images of similar resolution. This ensures that no flux is resolved out of the higher resolution image, artificially steepening the spectra.

The restoring beam used to generate the map shown in Fig. 5.7 was ~3 arcsec, while the restoring beam of the deepest 610 MHz maps of the 13^H field is ~ 6 arcsec. Since nothing can be done to increase the resolution of the 610 MHz maps, the higher resolution VLA maps require degrading to gain comparable resolution.

During the construction of the 1.4 GHz catalogue presented by Seymour et al. (2004), a map was made from *uv* data tapered to provide greater sensitivity to extended structure. A resolution of 6×6 arcsec was achieved by tapering the *uv* data with a Gaussian of width (to 30% amplitude) of 35 and 35 kλ. Except this tapering, imaging was conducted in a manner identical to that used to generate the image shown in Fig. 5.7, as reported in Section 5.5 and in Seymour (2002) and Seymour et al. (2004). The resulting image has a central rms noise of 12.9μJy beam^{-1}.

In the course of this work, this map was used to measure 1.4 GHz fluxes directly comparable to those at 610 MHz. Source extraction was performed using AIPS task SAD. The measured fluxes were added to the catalogue of Seymour et al. (2004) for any source which was seen as having a significantly brighter flux than that taken from the full resolution map. See Section 5.6 for details on the use of this map to calculate spectral indices of the sources therein.

5.5.2 13^H Field Radio Morphology

Although the resolution of the deep imaging of the 13^H field is lower than that of the 1^H field maps, enough morphological information is preserved to positively identify several AGN. Sources 1, 2, 7, 8, and 10 in the catalogue presented in Seymour et al. (2004) are obviously AGN. However, this resolution does not allow any sources to be identified as starburst with any confidence, although source 21 in that catalogue does show some extension in both dimensions across a large optical galaxy. See Section 5.7 for further discussion of the use of the radio-only diagnostics.

5.6 Radio Spectra of Faint Radio Sources

The potential of spectral indices to assist in the characterisation of faint radio sources has lead to several studies attempting acquire large numbers radio spectra of radio faint sources. Seymour (2002) presented, along with the 1.4 GHz catalogue of the 13^H field, a VLA D-array mosaic observation of the same area of sky at 4.8 GHz. 105 sources were discovered to 100μJy, giving 51 radio spectra. The original study of the radio properties of the HDF-N (Richards 2000) also considered a previous 8.4 GHz observation which provided 30 spectra. The HDF-S has been the subject of radio observations with the Australian Telescope Compact Array (ATCA) which reached 10μJy at 1.4, 2.5, 5.2 and 8.7 GHz. The combined catalogue contains 4 point radio spectra, or limits thereon, for 473 sources (Huynh et al. 2007). The 1.4 GHz surveys of both the Lockman Hole and the ATESP survey are complimented by 4.8 GHz observations (Ciliegi et al. 2003, and Prandoni et al. 2006 respectively).

In all of the studies mentioned above, the surveys were originally conducted at 1.4 GHz, and spectral information acquired by observing at higher frequencies. Since the size of the primary beam (and hence the field of view) of radio dishes is inversely proportional with frequency, higher frequencies require mosaics of pointings to cover 1.4 GHz survey areas. The advent of the GMRT has provided the opportunity to conduct sensitive, high resolution surveys with the large fields of view associated with lower frequencies, and hence to efficiently cover the areas of surveys at higher frequencies with few pointings. The shape of the typical spectra of extragalactic radio sources (flux decreasing with frequency) also means that lower sensitivity (i.e. higher noise, and therefore shorter integration times) is required to detect most radio sources at lower frequencies.

The 13^H and 1^H field are not the only deep survey fields to exploit this combination of VLA 1.4 GHz and GMRT 610 MHz surveys. The VLA VLT Deep Survey (VVDS, Bondi et al. 2003) was also among the first wave of fields to be covered with the GMRT at 610 MHz. To a detection limit of 260μJy 514 sources were found within 1 sq. deg. mosaic (Bondi et al. 2007). The Spitzer First Look Survey (SFLS, Lacy et al. 2005; Fadda et al. 2006; Frayer et al. 2006), was the first deep pointing with the Spitzer space telescope. Covered at 1.4 GHz by the VLA in B-array (Condon et al. 2003), a mosaic of 610 MHz pointings with the GMRT reached 27 to 30μJy rms and provided 610 MHz fluxes for 3944 sources (Garn et al. 2007). The Lockman Hole has also been covered at 610 MHz, in an attempt to, among others goals, acquire radio spectra for a sample of sub-millimetre galaxies discovered within

it.

5.6.1 Sample

For the purposes of the calculation of spectral indices, the full catalogue of Seymour et al. (2004) was used for the 1.4 GHz source list of the 13^H field. The sources in Table 4.1 were taken as the equivalent for the 1^H field. The basic sample therefore consists of 449 sources in the 13^H field and 432 in the 1^H field.

Inside the 15 arcmin radius of the areas covered at both frequencies, the 610 MHz catalogues in Tables 3.2 and 5.1 provide flux measurements for 66 and 84 sources above $\sim 300\mu$Jy and 300μJy in the 13 and 1^H fields respectively. Sources outside of these areas, though useful for the calculation of source counts and therefore, via modelling, the average spectral index, are not useful for the calculation of the individual source spectra, since reliable 1.4 GHz fluxes are not available.

5.6.2 Matching

An initial cross matching between the full catalogues at 1.4 GHz and 610 MHz was performed based on spatial proximity. A large initial search radius of 10 arcsec was used to account for the large sizes, and therefore possible inaccuracies in position measurement, of some of the sources. Each source was then inspected by eye, viewing the contours of radio emission at both frequencies overlaid on an optical image. See Appendix A for the thumbnail images used. In 9 cases, sources identified at 1.4 GHz were confused in the lower resolution 610 MHz imaging. In the 13^H field, 60 sources where seen to clearly match. In the 1^H field, the equivalent number was 76. The slightly higher number of matches in the 1^H field can be put down to the areas of high noise in the 13^H and the smaller number of sources therefore discovered therein.

Many sources detected at 1.4 GHz are not detected at 610 MHz, as expected from the relative sensitivities of the maps at the two frequencies. The 6 sources detected at 610 MHz within the 15 arcmin radius area of the 1.4 GHz coverage of the 13^H field without a match have no positionally coincident partner in the catalogue of Seymour et al. (2004) to beyond 20 arcsec. In the 1^H field, 12 sources detected at 610 MHz are similarly without 1.4 GHz counterparts These non-detections at 1.4 GHz are surprising, given that the relative sensitivities of the images mean that the 1.4 GHz maps should pick up all sources detected at 610 MHz with spectra flatter than $\alpha \sim -2.4$. These sources will be discussed at more length in the following sections.

5.6.3 Calculation of Spectral Index

A spectral index was calculated,

$$\alpha = 2.77 log \left(\frac{S_{1.4}}{S_{610}} \right) \tag{5.1}$$

(where 2.77 is the reciprocal of the logarithm of $1.4 \times 10^9 / 6.1 \times 10^8$) for each source detected at either frequency within the 15 arcmin radius areas covered at both frequencies. Where available, the flux densities used in the calculation are those determined from the maps made with closest matching resolutions. In the cases of sources faint at 1.4 GHz and therefore not significantly detected in the lower sensitivity tapered maps, the flux density from the full resolution 1.4 GHz map has been used. In the 13^H field, 45 of the 60 matches exploited tapered fluxes. In the 1^H field, 27 of the 76 matches used fluxes from the 6×6 arcsec map, and a further 14 used fluxes from the 3×3 arcsec map. In cases where a source was detected at one frequency, but not the other, an upper limit of 4 times the local rms noise was taken, and an upper/lower limit on α calculated. For sources detected at 610 MHz more that 15 arcmin from the pointing centre of either survey area, no reliable 1.4 GHz flux is available, and no spectral index has been calculated.

The 13^H field is also covered at 4.8 GHz with VLA D-array observations dating from 1991 (Seymour 2002). Of the 449 sources detected at 1.4 GHz in the 13^H field, 51 have 4.8 GHz flux measurements. Of these, 32 also have 610 MHz detections, and a power law can be fitted to the three point spectra. In the remainder of the cases, the 1.4 to 4.8 GHz spectral index can be calculated in a manner similar to that expressed in Eq. 5.1.

5.6.4 Discussion

All the measured spectra are plotted against 1.4 GHz flux in Figs. 5.8 and 5.9 for the 13 and 1^H fields respectively. Sources not detected at 610 MHz are represented by lower limits on α. The relative detection limits of the survey images are illustrated by the linear features which these limits follow. In Fig. 5.8, the sources detected at 4.8 GHz but not at 610 MHz fall beyond this line. Upper limits are given for the sources not detected at 1.4 GHz which are, for clarity, plotted at the flux of the 610 MHz detection, not the limiting 1.4 GHz flux.

As discussed in Chapter 1, radio spectra are potential AGN/starburst discriminants. The optically thin synchrotron emission expected from starburst sources is

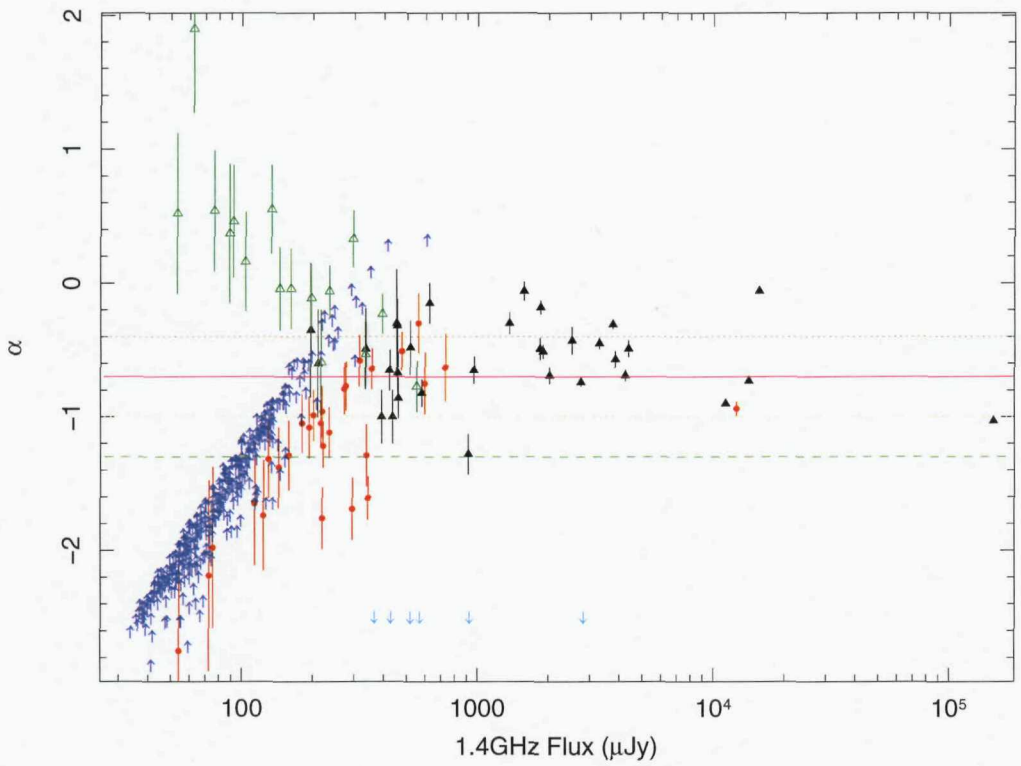

Figure 5.8: The variation of radio spectral index with 1.4 GHz flux for sources in the 13^H field. Solid triangles represent sources detected at 610 MHz, 1.4 GHz and 4.8 GHz, the spectra of which have therefore been calculated by fitting to flux measurements in those 3 bands. Empty triangles represent those sources detected at 1.4 and 4.8 GHz, but not at 610 MHz. Filled circles represent sources detected at 610 MHz and 1.4 GHz only. The arrows denote limits on α from non-detections at either frequency. For clarity, sources not detected at 1.4 GHz are plotted at their 610 MHz flux, and at $\alpha = -2.5$. The solid line indicates the canonical spectral index for optically thin synchrotron emission, $\alpha = -0.7$. The dotted lines illustrate the upper and lower bounds of range of spectral indices expected for such optically thin emission. The dashed horizontal line indicates $\alpha = -1.3$, that taken as an upper limit for a source to be considered a USS.

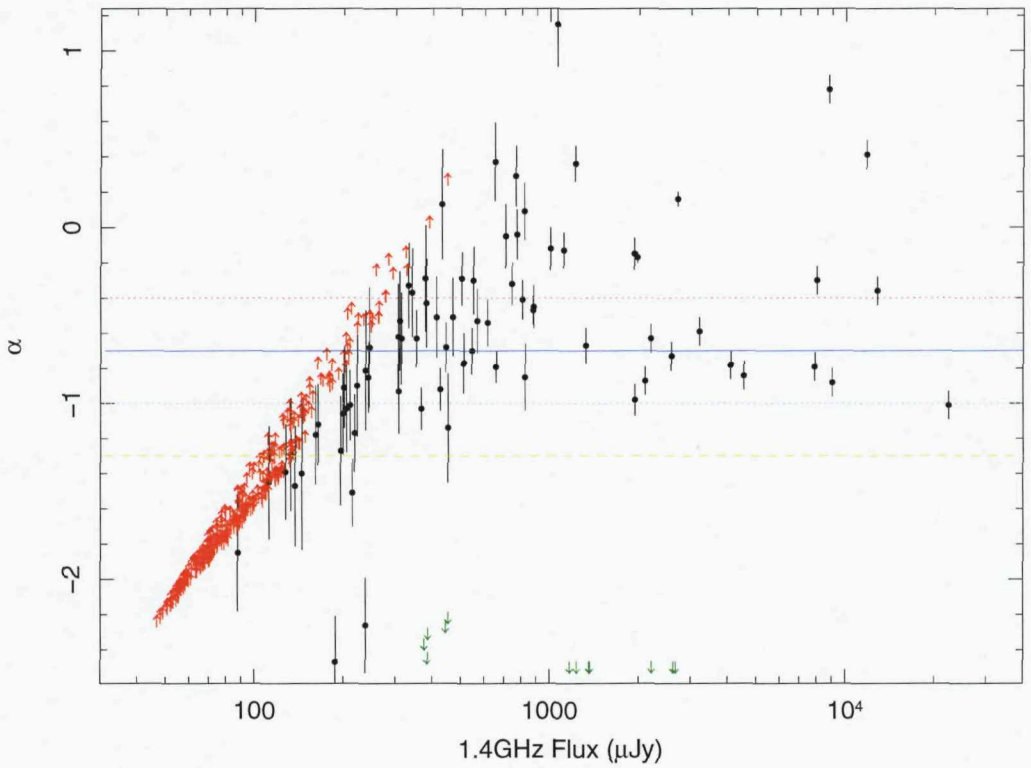

Figure 5.9: The variation of radio spectral index with 1.4 GHz flux for sources in the 1^H field. Filled circles represent sources detected at 610 MHz and 1.4 GHz. The arrows denote limits on α from non-detections at either frequency. For clarity, sources not detected at 1.4 GHz, and with limits on α steeper than -2.5, are plotted at their 610 MHz flux, and at $\alpha = -2.5$. The solid line indicates the canonical spectral index for optically thin synchrotron emission, $\alpha = -0.7$. The dotted lines illustrate the upper and lower bounds of range of spectral indices expected for such optically thin emission. The dashed horizontal line indicates $\alpha = -1.3$, that taken as an upper limit for a source to be considered a USS.

expected to have an average radio spectral index of $\alpha = -0.7$, and a fairly narrow spread in values. AGN can have a wide spread from inverted spectra ($\alpha > 0$) to very steep ($\alpha < -1.3$). Also therefore indicated in Figs. 5.8 and 5.9 are the canonical $\alpha = -0.7$ value (solid line), and the limits outside of which a source is unlikely to be a starburst ($-1 < \alpha < -0.4$, dotted lines). These lines help illustrate that some of the lower limits on α from non-detections at 610 MHz are still useful. Sources with 1.4 GHz fluxes of greater than ~ 200 mJy not detected at 610 MHz must either have spectral indices flatter than $\alpha = -0.4$, or have varied in their flux between the epoch of the 1.4 GHz observations ($\sim$1998) and that of the 610 MHz observations (2004). Both possibilities suggest an AGN as the source of the radio emission.

Perhaps unsurprisingly, the majority of the measured spectra do indeed lie near the $\alpha = -0.7$ line. Figs. 5.8 and 5.9 show no clear trend of changing spectral index with flux, and neither is there any clear segmentation into separate populations. In the 13^H field, just under 50 percent of the sources with fluxes measured at two frequencies lie within the $-1 < \alpha < -0.4$ envelope of expected optically thin spectra, and could therefore be either starburst or AGN. In the 1^H field, once again, just under 50 percent of the spectra lie near $\alpha = -0.7$. However, in both fields several sources lay outside this region, and can therefore reasonably be considered to be AGN.

Of these sources, those of flat spectrum will be considered first. In the 13^H field, the measurements undertaken in this and previous chapters show that 34 sources have spectra flatter than -0.4. A further 5 sources have measured spectral indices flatter than -0.4, but errors on the measurement do not preclude $\alpha \leq -0.4$. Of the 34 flat spectrum sources, which are therefore likely to be AGN , 14 are those with spectra measured using flux measurements at 1.4 GHz and 4.8 GHz alone, with no detection at 610 MHz. As can be seen in Fig. 5.8 (where they are marked as hollow triangles), these 14 sources consititute the majority (81%) of the sample of sources whose spectrum has been determined in this way. The high noise of the 610 MHz map relative to those at higher frequencies means that this sample of sources all having flat spectra is not surprising. A note of caution should be taken about these 14 spectra. Firstly, the 4.8 GHz map was made in the D-array of the VLA and therefore has a resolution of 14 arcsec, which does not match the resolution of the 1.4 GHz A+B array observations ($\sim$ 3 arcsec). Although there does not appear to be any extended emission or potentially confusing sources near these objects in the 1.4 GHz image, it should be noted that any such emission may be picked up at 4.8 GHz and artificially flatten the spectrum. Also, the eight years between the

dates of the 4.8 GHz and 1.4 GHz observations may allow temporal variability of the sources to alter the measured fluxes.

In the 1^H field, 26 sources can be said to flatter than $\alpha = -0.4$ with a degree of confidence. A further 7 have measured spectra flatter than $\alpha = -0.4$, but errors on the measurements allow $\alpha \leq -0.4$.

The steep sources in both fields will now be addressed. The vast majority of the sources detected at 1.4 GHz but not at 610 MHz fall below $\alpha = -1$. Unlike the limits in the flat spectrum region of Figs 5.8 and 5.9, these lower limits are not useful as the they cannot be used to rule out star formation being the source of the radio emission. However, several sources detected at both frequencies do have spectra steeper than $\alpha < -1$. In the 13^H field, 21 sources are steeper than $\alpha = -1$, with another 6 steeper than $\alpha = -1$, but with errors that include $\alpha \geq -1$. Of the 21 sources with spectra definitely steeper than $\alpha = -1$, 6 are the objects detected at 610 MHz but not at 1.4 GHz mentioned in Section 5.6.2. These are puzzling objects. Of the 20 (with another 10 likely) steep (i.e. $\alpha < -1$) sources in 1^H field, 12 are also non-detections at 1.4 GHz. The spectra calculated from the upper limits at the positions of these sources vary from -2.2 – which is very steep, but believable considering 4 sources detected at both frequencies are measured to be this steep – to more negative than -5, which is rather harder to credit. The possible causes of these extremely steep measured spectra – including source variability – will be discussed further in Sections 5.6.4.1 and 5.6.6.

5.6.4.1 Sources Not Detected At 1.4 GHz

Possibilities to explain the calculation of such extreme spectra as those exhibited by the sources not detected at 1.4 GHz include false detections at 610 MHz, source variability and truly very steep spectra.

Of the six sources detected at 610 MHz but not at 1.4 GHz in the 13^H field (610 MHz sources 58, 135, 179, 186, 202 and 206 in Table 5.1), none have a low significance detection (i.e. $< 4\sigma$) coincident with them in the 1.4 GHz map, and all were detected at a signal to noise ratio of less than 6 at 610 MHz – making them some of the least significant detections. It is interesting to note that source 135 is detected at 5.13σ, and would not have been accepted by Garn et al. (2007) who use a detection limit of 5.25σ. Source 58 has a peak flux of over 1mJy in the tapered map, and is therefore very unlikely to be a noise spike. It is possible that it is a highly extended source, the flux of which is resolved out by the VLA at 1.4 GHz. There is a small possibility that source 179 may be a distant sidelode of source 2,

but the distance between them (~7 arcmin) makes this seem unlikely.

Of these 6 sources, 3 have no optical counterpart within 10 arcsec. There is a very faint source in the B band image ($B \sim 26.4$) within 2 arcsec of the position of source 135, which dims to a magnitude in the g band of 26.4 and is not detected in any image of longer wavelengths. This would suggest that source 135 may be a high redshift AGN whose steep measured spectrum may be due to variability or energy loss steepening. Of course, with such deep optical imaging, chance coincidence cannot be ruled out. The remaining 2 sources are near (3 and 6 arcsec) optical sources, but do not appear to lie within them.

Source variability may explain several of these sources. Given that sources detected at both frequencies have spectra measured to be as steep as $\alpha = -2.5$ (though these may themselves have undergone variation), flux variations of only a few percent between 1998 and 2004 would be enough to drop source 206 out of the 1.4 GHz catalogue. However, for the spectrum of source 58 to have at one point been $\alpha > -2.5$, it needs to have increased in flux by a factor of 10 in the 6 years between the two observations, which is unlikely.

The possibility exists that these sources are genuine. They would have to be very high redshift AGN to not be detectable in the deep optical data, and to have either the spectral of temporal characteristics required to explain their observed properties.

In the 1^H field, 12 sources detected at 610 MHz are not detected at 1.4 GHz (sources 66, 67, 76, 102, 103, 115, 123, 206, 207, 220, 221, and 223 in Table 3.2). Of these, 5 are detections of very low significance ($< 5.2\sigma$). Another 3 have detections of 5.3σ. Two of these faint detections fall within the boundaries of large optical galaxies, though neither is coincident with centre of the optical galaxy. Another two have very faint optical emission near their centres.

Four of the 12 610 MHz-only detections are, however, much more significant. Sources 66, 67, 76 and 102 in Table 3.2 are detected at signal to noise ratios of 6.8, 6.4, 11 and 9 respectively. Source 66 is detected in the tapered 610 MHz map only – implying large extension of low surface brightness emission – and is the location of 3σ 1.4 GHz emission as well as a very faint optical source. Source 67 was also first detected in the tapered 610 MHz map, though a wide patch of 2σ emission is present in the full resolution map at this frequency. It does not share its location with any emission at 1.4 GHz or in the optical. The 1.4 GHz may have resolved out much of the extended emission from these two sources.

Sources 76 and 102 are located near a bright source (number 21 in Table 3.2, and 7 in Table 4.1), but do not appear to follow the pattern of sidelobes (as expected

from examining other sources), and are the locations of very faint optical emission.

Should any of these sources have been at the location of low significance 1.4 GHz emission and an optical source, it would seem reasonable to consider that they are real. As it stands, either they are spurious detections, sources of high variability, or objects with truly remarkable characteristics. Spurious detections seems the most likely, but a combination of these factors may explain the population of 1.4 GHz non-detections. The deeper observations which failed in 2006, and are in the process of being repeated, will shed further light on this matter.

5.6.5 Flux Limited Sample

Fig. 5.10 shows the distribution of radio spectral indices for a 1.4 GHz flux limited sample across both fields. The spectra included are those for all sources with a flux density of greater than 200μJy at 1.4 GHz and, for consistency, are calculated using only the 1.4 GHz and 610 MHz data. Limits from non-detections at 610 MHz are also shown as the dotted lines. The break down by field is shown in Figs. 5.11 and 5.12 for the 13^H and 1^H fields respectively.

The average spectral index, across both fields, of the sources detected at both frequencies, and with $S_{1.4} > 200\mu$Jy, is -0.57 with a standard deviation of 0.5. For the individual fields, the averages are -0.64 ± 0.50 and -0.51 ± 0.50 in the 13^H and 1^H fields respectively. These averages are flatter than the canonical value of -0.7, though as can be seen by inspecting the distribution in Fig. 5.10, the modal value for the measured spectral index is -0.7. The mean is affected by the asymmetry of the distribution shown in Fig. 5.10, where there is a tail on the distribution on the flatter side of its peak. This tail is due to the flat sources being detected, while their counterparts steeper than -1 have been missed by the 610 MHz map – i.e. this $S_{1.4} > 200\mu$Jy sample was selected to show all sources with spectra usefully limited to being flat.

5.6.6 Ultra Steep Spectrum Sources

As presented in Chapter 1, sources with ultra steep spectra ($\alpha < -1.3$), are a good sample from which to discover high redshift radio galaxies, which are often among the largest galaxies at their redshift, and therefore provide information about early structure formation (e.g. De Breuck et al. 2004). As can be seen from Figs. 5.8 and 5.9, 36 sources fit this criterion. Of these, 18 are the non detections at 1.4 GHz which

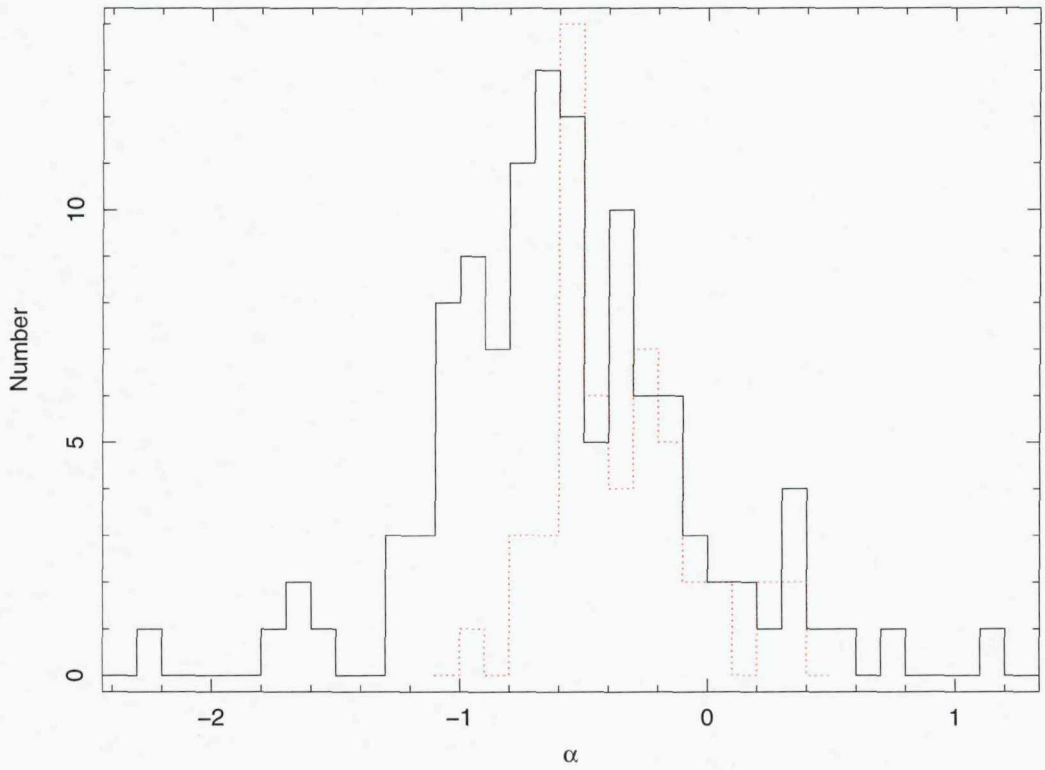

Figure 5.10: The distribution of spectral indices of a flux limited sample ($S_{1.4} > 200\mu$Jy) across both fields. The dotted line illustrates the distribution of the limits upon the spectra calculated when a 1.4 GHz source is not detected at 610 MHz.

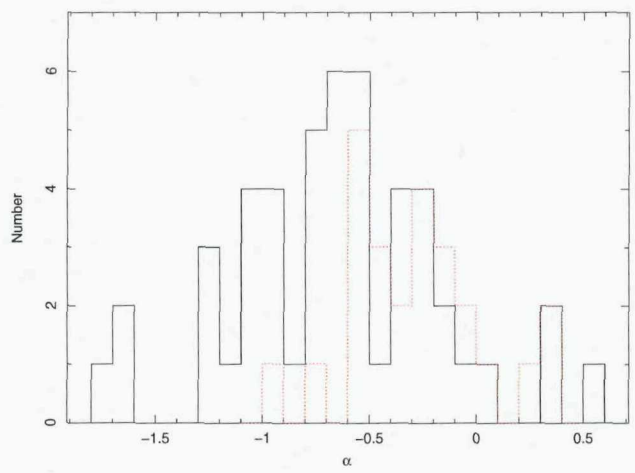

Figure 5.11: The distribution of spectral indices of a flux limited sample ($S_{1.4} > 200\mu$Jy) from the 13^H field. The dotted line illustrates the distribution of the limits upon the spectra calculated when a 1.4 GHz source is not detected at 610 MHz.

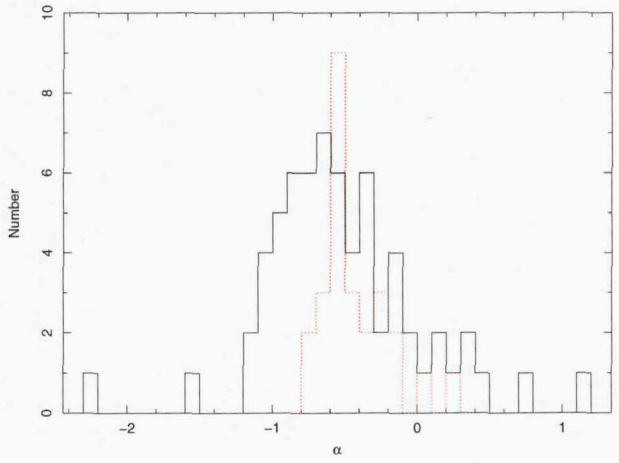

Figure 5.12: The distribution of spectral indices of a flux limited sample ($S_{1.4} > 200\mu$Jy) from the 1^H field. The dotted line illustrates the distribution of the limits upon the spectra calculated when a 1.4 GHz source is not detected at 610 MHz.

may be spurious. This leaves 6 and 4 sources in the 13^H and 1^H fields respectively with spectra definitely measured as being steeper than $\alpha = -1.3$. The inclusion of sources likely to be steeper than $\alpha = -1.3$, but whose errors still allow $\alpha \geq 1.3$ increases the respective numbers to 10 and 8.

The flux of the majority of these 18 sources are below 300μJy at 1.4 GHz. Since the accuracy with which a source's parameters can be measured decreases with decreasing flux, due to the effect of noise, the measurement of these spectra are less certain that those above 1 mJy. However, estimates of the errors on the flux measurements have been used to provide errors on the determination of the spectral index in each case, and 10 can be said to be ultra steep, within the limitations of this data, with a fair degree of confidence. A further 8 are likely to have spectral indices steeper than $\alpha = -1.3$.

While source variability may account for the excessive steepness of some of these sources, they provide a tantalising possibility of a population of faint USS sources. Should any of them prove to be high redshift AGN, the low fluxes imply that either they are further down the luminosity function at those redshifts, or that they are more distant than the currently well studied samples.

The optical properties of these sources will be dealt with in the next chapter. The coordinates and fluxes of these sources are given in Table 5.2. Also included are those sources not detected at 1.4 GHz, which have been flagged with a "ND", and whose number is augmented with a "G" to indicate that it is from the 610 MHz catalogue of its respective field.

Field	1.4 GHz Num	RA	DEC	$S_{1.4}$ (μJy)	S_{610} (μJy)	α	$\Delta\alpha$	Flag
13^H	31	13:34:13.64	37:57:32.89	342.88	1307.36	-1.61	0.16	D
	51	13:33:48.39	37:54:57.52	295.12	1205.29	-1.69	0.23	D
	101	13:34:52.41	37:42:45.41	143.6	454.73	-1.38	0.3	P
	112	13:34:58.95	37:40:47.57	123.9	528.96	-1.74	0.41	P
	115	13:35:12.26	37:51:31.16	130	389.25	-1.32	0.29	P
	125	13:34:28.69	37:46:47.35	219.77	949.07	-1.76	0.23	D
	164	13:34:24.98	37:40:7.09	113.7	449.65	-1.65	0.46	P
	259	13:33:39.64	37:45:53.96	72.7	449.24	-2.19	0.71	D
	324	13:35:40.12	37:46:25.26	75.4	393.51	-1.98	0.6	D
	438	13:33:40.76	38:2:46.05	54.2	533.65	-2.75	0.7	D
	G58	13:34:09.08	38:01:30.62	<36.87	2788.99	-5.2		ND
	G135	13:35:03.72	38:08:41.33	<56.65	914.56	-3.34		ND
	G179	13:33:44.48	38:02:07.66	<47.16	563.15	-2.98		ND
	G186	13:34:36.40	38:08:42.30	<52.1	514.16	-2.75		ND
	G202	13:35:02.32	37:51:25.26	<33.01	424.56	-3.07		ND
	G206	13:33:50.97	37:47:53.84	<42.84	361.98	-2.56		ND
1^H	79	01:44:48.19	-04:23:15.58	237.26	1557.4	-2.26	0.27	D
	85	01:45:26.92	-04:47:25.78	214.39	752.5	-1.51	0.19	D
	100	01:46:00.09	-04:44:59.09	187.76	1467.1	-2.47	0.26	D
	125	01:45:12.29	-04:45:11.18	144.45	463.3	-1.4	0.43	P
	134	01:46:20.58	-04:28:20.50	137.33	468.7	-1.47	0.34	P
	151	01:45:58.51	-04:37:13.99	127.42	407	-1.39	0.27	P
	182	01:45:41.42	-04:39:42.08	111.76	374.9	-1.45	0.32	P
	256	01:45:45.16	-04:26:06.32	87.702	409.6	-1.85	0.33	D
	G66	01:45:27.68	-04:37:41.3	<45.87	2663	-4.88		ND
	G67	01:46:02.8	-04:37:18.6	<56.64	2614.1	-4.61		ND
	G76	01:46:15.59	-04:40:15.4	<73.75	2210.5	-4.09		ND
	G102	01:46:16.36	-04:39:58.9	<74.13	1363.5	-3.5		ND
	G103	01:45:01.9	-04:44:55.3	<66.72	1355.6	-3.62		ND
	G115	01:45:38.31	-04:20:28.7	<81.44	1232.09	-3.26		ND
	G123	01:45:35.85	-04:37:49.2	<46.56	1165.7	-3.87		ND
	G206	01:44:45.25	-04:42:18.4	<71.29	451	-2.22		ND
	G207	01:45:52.05	-04:44:55.0	<66.66	441.4	-2.27		ND
	G220	01:45:40.73	-04:43:16.6	<56.46	385	-2.31		ND
	G221	01:45:48.18	-04:38:09.8	<49.83	383.8	-2.45		ND
	G223	01:44:58.01	-04:36:03.1	<51.78	373.8	-2.37		ND

Table 5.2: The positions, fluxes and spectral indices of the sources, detected at both 1.4 GHz or 610 MHz, measured to have ultra-steep spectra (α steeper than -1.3). A flag of D means that, even allowing for the errors on the measurement of α, the source has a spectrum steeper that $\alpha = -1.3$. A flag of P means that though the spectrum is measured as steeper than $\alpha = -1.3$, errors on the measurement allow $\alpha \geq -1.3$. A flag of ND means that the source is a non-detection at 1.4 GHz and the source number is that in the 610 MHz catalogue of its respective field.

5.7 Radio Diagnostics

The radio spectral index is not a truly reliable discriminant between AGN and starbursts when considered alone. As discussed previously, temporal variability and resolution effects can mean that that an accurate measurement of the true spectral index of a source is not easy. However, it is the combination of discriminants that provides the most useful tool. The use of radio/IR ratios, radio luminosities, SED fitting, and radio/optical ratios are outside the scope of this work. The optical magnitude and size distribution of the radio sources will be discussed in Chapter 6. However, it is illustrative to give a simple example of how the combination of solely radio diagnostics can be useful for some sources.

The 13^H field is the subject of a deep MERLIN survey to provide detailed morphological information at a resolution of 0.2 arcsec (Zoghbi et al, in prep.). Though the use of these very high resolution data is also outside the scope of this work, the 1.4 GHz VLA A and A+B array observations can provide some useful morphological information for the brighter sources, as discussed in Sections 4.8 and 5.5.2, which can be compared to radio spectra.

Conservatively defining the starburst excluded range as $\alpha > -0.4$ and $\alpha < -1$, the number of sources in the 1.4 GHz samples that can be considered AGN is 49 and 34 in the 13^H and 1^H fields respectively. This leaves 400 and 398 sources in the two fields that, based on radio spectral arguments, can either be AGN or starburst. The deeper, corrupted, 610 MHz observations undertaken in 2006 would have more closely matched the sensitivity of the 610 MHz imaging to that at 1.4 GHz and produced many more spectra. The observations have been retaken, and will provide a deeper insight into the low frequency radio spectral properties of the sub-mJy population.

In the 13^H field, 5 sources where designated AGN based on morphology. These sources have spectral indices of -1, -0.9, -0.7, -0.4, and -0.5, as expected for the optically thin emission from the lobes of an AGN viewed side on. The 6 morphologically identified AGN in the 1^H field have spectra of -1, -0.8, -0.7, -0.6, and -1 (with one being confused in the 610 MHz maps), again consistent with that expected for side-on AGN.

The ~ 3 arcsec resolution of the 1.4 GHz image of the 13^H field is not sufficient to resolve radio emission from starbursts. The higher resolution offered by the VLA, A-array only, 1.4 GHz image of the 1^H field can begin to resolve brighter systems. As shown in Fig. 5.13, this image does resolve several sources in both dimensions

across the expanse of an optical counterpart. These 6 sources have spectral indices of −0.88, −0.78, −0.59, −0.85, −0.7, and −1.14. The first 5 are all consistent with a starburst galaxy, but the last shows that it is more likely to be an AGN.

The comparison of radio spectra and morphology with other diagnostics (radio luminosity, optical morphology and various colour information) will be discussed in Chapter 6.

5.8 Conclusions

The 610 MHz-1.4 GHz radio spectra of the radio sources in the 13^H and 1^H fields have been presented. At 610 MHz, 206 sources were discovered to $\sim 300\mu$Jy within a 32 arcmin radius of the 13^H field centre. Along with the catalogues presented in Chapters 3 and 4, and in Seymour et al. (2004), this provides 2 point spectral measurements for the radio sources in the 13^H and 1^H fields. Additional fluxes at 4.8 GHz provide 3 point spectra for 32 of the sources in the 1^H field and 2 point spectra for a further 14 not detected at 610 MHz. Across the two fields, 152 sources have spectra computed from detections in at least 2 bands, with another 40 useful limits being placed on spectral index. If starburst galaxies are assumed to be limited to the range $-1 < \alpha - 0.4, (S \propto \nu^{\alpha})$, 83 sources can be said to be AGN. A further 11 sources can be identified as AGN from radio morphology. The combination of radio morphology and spectral index suggests that 5 of the 1.4 GHz sources in the 1^H field could be said to be starburst galaxies rather than AGN. The multi-field 610 MHz sources can be reasonably well fit with a model that includes AGN and a population of starburst galaxies undergoing luminosity evolution with a power law index of 2.6. When taken into comparison with the value of 2.5 for the same index at 1.4 GHz from Chapter 4, this confirms that the population responsible for the sub-mJy bump has, on average, a spectral index of $\alpha = -0.7$.

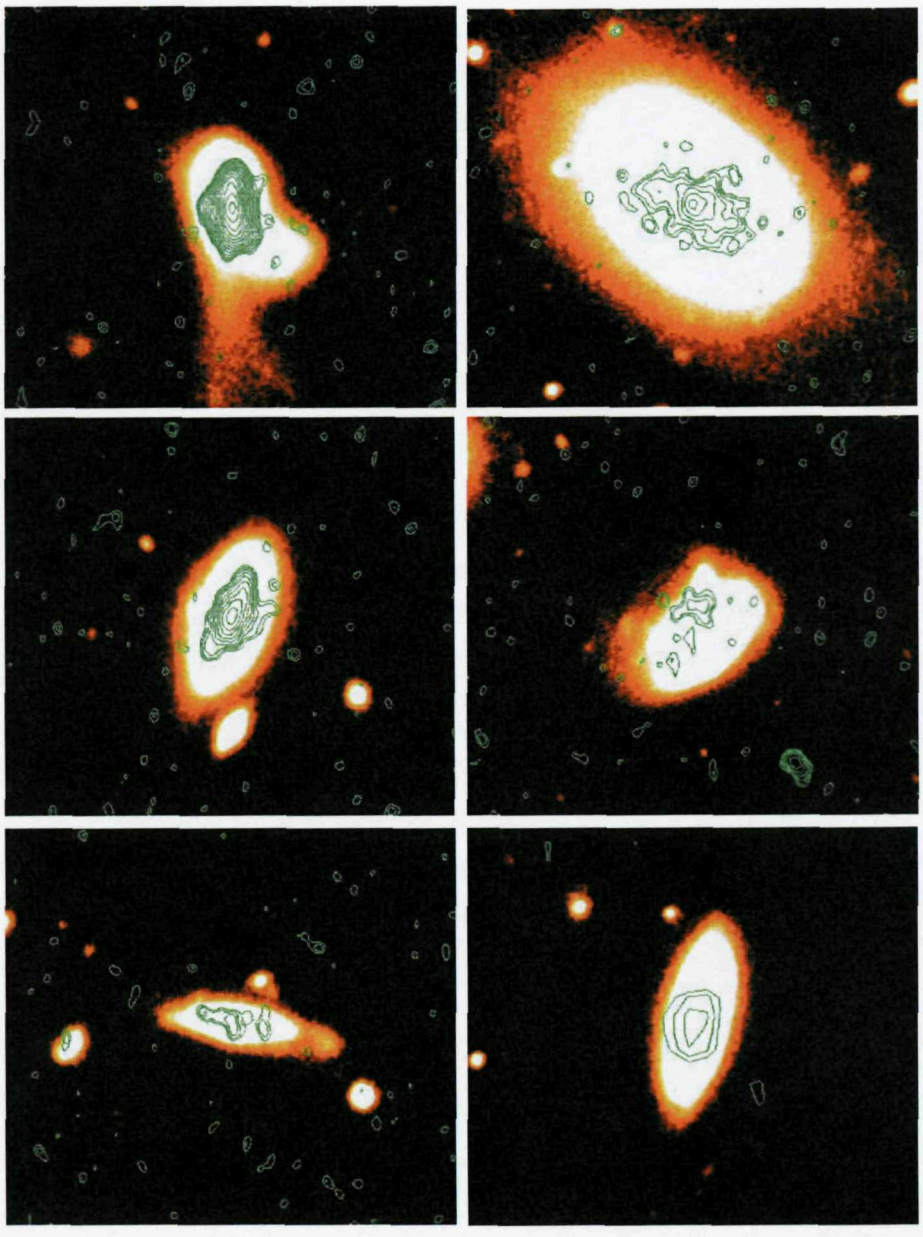

Figure 5.13: The 1.4 GHz contours of several sources seen to be slightly resolved across the expanse of an optical galaxy, and may therefore be due to star formation. The optical images are from the Subaru i' band coverage.

Chapter 6

Optical Properties of the Faint Radio Source Population

In this chapter, some basic optical properties of the 1.4 GHz radio samples undergo a preliminary investigation. The optical magnitude distribution of the radio sources is presented. The variation of optical magnitude and colour with radio flux and radio spectral characteristics is discussed.

6.1 Introduction

Previous chapters have dealt with radio only diagnostics. Both the 13^H and 1^H fields are covered in many other wavebands, ranging from the MIR to the X-ray. Optical observations provide information on host galaxy morphology and colours, and redshift (and hence, radio luminosity). X-rays detections are good indicators of AGN activity.

The detailed analysis of optical spectra, optical morphology, photometric redshifts, IR photometry and SED fitting, and the combination thereof, are outside of the scope of this work. Instead, this chapter will attempt to provide a brief overview of the optical properties (magnitudes and colours) of the radio samples. When combined with simple arguments about the nature of AGN and starbursts, such basic optical analysis has the potential to be quite illuminating. If one assumes that the sub-mJy bump is caused by a population of star burst galaxies, differing bulk optical properties might be expected. Given the lower luminosities of starburst compared to AGN, starburst galaxies detected in the radio in a flux limited survey are likely to be, on average, closer than AGN. This would hint at larger, brighter optical objects being detected coincident with them.

The optical properties of faint radio samples have been recently discussed in far more depth by, for example, Muxlow et al. (2005), Afonso et al. (2006), and Simpson et al. (2006).

6.2 Optical Observations

Deep optical observations of both fields in various bands have been conducted with SuprimeCam on the Subaru telescope, the PFC on the WHT, and MEGACAM on the CFHT. Near IR coverage of both fields has been provided by observations with WFCAM on UKIRT, WIRC on the Palomar 200inch and WIRCam on the CFHT. Additionally, the 13^H field has been covered with both MIPS and IRAC on board *Spitzer*. See Chapter 1 for details.

The central 15 arcmin radius areas of each field are covered in all the ground-based imaging mentioned above. Beyond these regions, where the only radio sources are those detected solely at 610 MHz, limited optical coverage is available. Hence, the investigation of the optical properties of the radio sources will concentrate on the 1.4 GHz selected samples, the constituents of which all fall within these areas of good multi-band coverage.

The optical properties of the 1.4 GHz sources in the 13^H field have been discussed by Seymour et al. (2002). However, these can now be examined in combination with some radio spectral information.

6.3 Radio to Optical Matching – the 1^H Field

The 1^H field has been the subject of observations at K, H, J, z', i', R, and B bands. The degree to which the data are reduced is significantly less than the 13^H field.

Source lists supplied with the pipeline-reduced Subaru B i' and z' band data, and created with SExtractor were searched for counterparts to the 1.4 GHz sources based on spatially proximity. Thumbnail images of the radio contours of each source overlaid on the Subaru i' band image were eyeballed to check the quality of any match. See Appendix A for these thumbnail images. In cases of no i' band counterpart, images at other bands were inspected at the location of the radio emission. Fig. 6.1 shows the distribution of spatial offsets between the radio and optical sources. Of the 432 1.4 GHz sources, 279 have plausible optical counterparts within $\sim$2 arcsec within the pipeline SExtractor catalogue from the Subaru observations. It should be

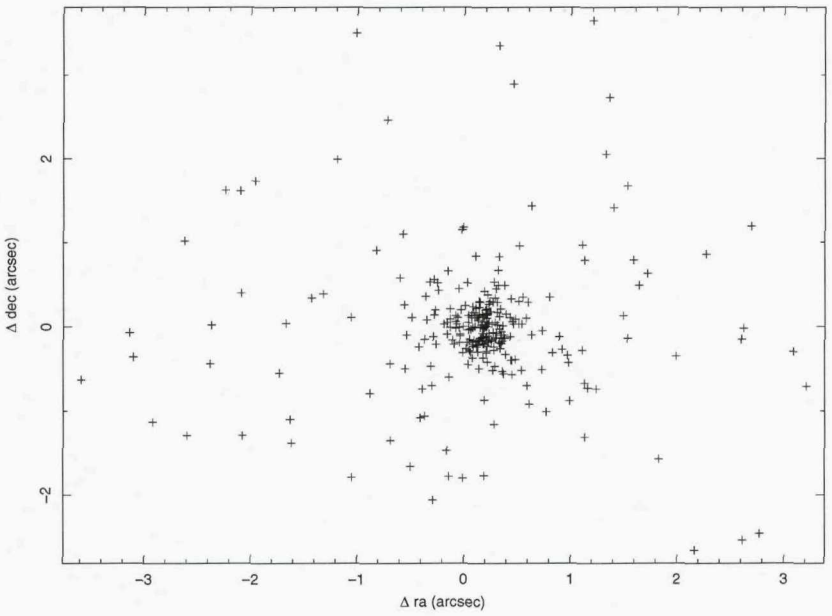

Figure 6.1: The spatial offsets between the radio sources discovered at 1.4 GHz in the 1^H field and their likely optical counterparts

noted that pipeline reduction is not ideal, and the catalogue is not complete beyond $i' \sim 25.5$.

The extended nature of some sources in either the radio band, the optical band, or both means that the position recorded for a source in different bands may be different by slightly more than 2 arcsec, hence the outliers seen in Fig. 6.1. Of the 152 radio sources without an obvious optical counterpart, 14 are in regions of the optical images confused by bright emission from other sources. A further 14 radio sources appear to lie on regions of faint optical emission which have not been catalogued as sources by the automated SExtractor analysis. Approximately another 50 radio sources have optical objects between 2 and 4 arcsec away from there radio coordinates, which do not appear associated in images and catalogues made with the current reduction of the optical data. Distortions in the coordinate systems of the Subaru images have been found in detailed analysis of the 13^H field images, which, if present here, may account for some of the large number of optically blank radio positions, although the small magnitude (< 1 arcsec) of this effect means this is unlikely. Note also that the centroid of the points in Fig. 6.1 is offset slightly from zero, implying non-perfect coordinate alignment. Future improved reduction of the optical and IR imaging of the 1^H field, and improved source detection analysis will probably therefore produce a larger number of optical/IR counterparts to the 1^H radio sources.

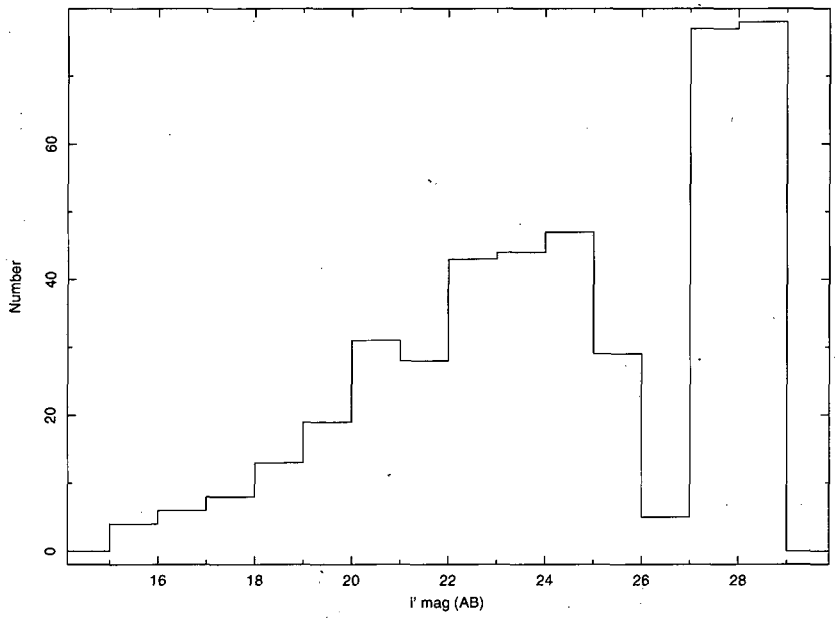

Figure 6.2: The distribution of i' band magnitudes of the optical counterparts of sources detected at 1.4 GHz in the 1^H field. Radio sources with no optical counterpart are arbitrarily given an i' band magnitude of 28 or 29.

The distribution of i' band magnitudes of the counterparts of the sources detected at 1.4 GHz in the 1^H field is shown in Fig. 6.2

6.4 Variation of Optical Properties With Radio Flux

The variation of bulk optical properties with radio flux has the potential to provide a simplistic guide to the make-up of the sub-mJy radio population. If the optical properties show some trend with radio flux below $\sim$1 mJy, it is further indication that a separate population is indeed responsible for the sub-mJy bump. Also, on a case by case basis, optical properties can provide further simple diagnostics. For example, the radio emission from a source which is red in the optical is unlikely to due to star formation, as the massive stars which give rise to the SNR responsible for the radio emission are young, hot, and therefore blue.

6.4.1 Optical Magnitude

Figs. 6.3 and 6.4 show the variation of optical magnitude with 1.4 GHz flux density for sources in the 13^H and 1^H fields respectively. The first thing of note is that

there are no clear trends of optical magnitude with radio flux. Neither are there any clear-cut segregation between two populations. Naive expectation may have lead one to expect that, if the sub-mJy radio population was dominated by star forming galaxies located closer to us than AGN with similar observed radio fluxes, some sign of brighter optical objects at low fluxes may have been seen. Actually, the only obvious feature shared by Figs. 6.3 and 6.4 is the lack of bright optical sources at low radio fluxes. A similar lack of high optical/radio ratio sources is also suggested by fig. 9 of Simpson et al. (2006), though the radio sample used therein is limited to brighter fluxes. A running average across both fields is shown as the stars in Figs. 6.3 and 6.4, and the associated errors bars are the standard deviation about the mean. The bins used are those exploited for the source counts in Chapter 4. This shows that the average magnitude of the optical sources identified as radio emitting increases with decreasing radio flux.

6.4.2 Optical Colour

Figs. 6.5 and 6.6 show the variation of optical colour $(B - i')$ for sources in the 13^H and 1^H fields respectively. Once again, the most noteworthy feature is the lack of any clear trend or segregation. A naive expectation would be that, if sources whose radio emission was primarily due to star formation do indeed dominate the sub-mJy population, a progressively higher proportion of blue objects would be seen as one descends to low radio fluxes. However, no such trend is apparent to a simple visual inspection of Figs. 6.5 and 6.6. This is confirmed buy the running average, as indicated by the empty stars.

Figs. 6.5 and 6.6 do show that in most cases, the optical galaxy associated with radio emission has a $b - i'$ colour of around 1.7. This is roughly that expected for normal galaxies, and so indicated that in the majority of cases, whatever mechanism is responsible for the radio emission is largely outshone by the stellar population of the galaxy at optical wavelengths.

6.4.3 Optical Size

The variation of the size of an optical source with its radio flux is another relation that could potentially differentiate between AGN and starbursts in a quick and simple manner. Star bursts are expected to be generally of lower luminosity than AGN, and therefore those detected in a flux limited radio sample are likely to be, on average closer. The optical counterparts identified with radio sources might

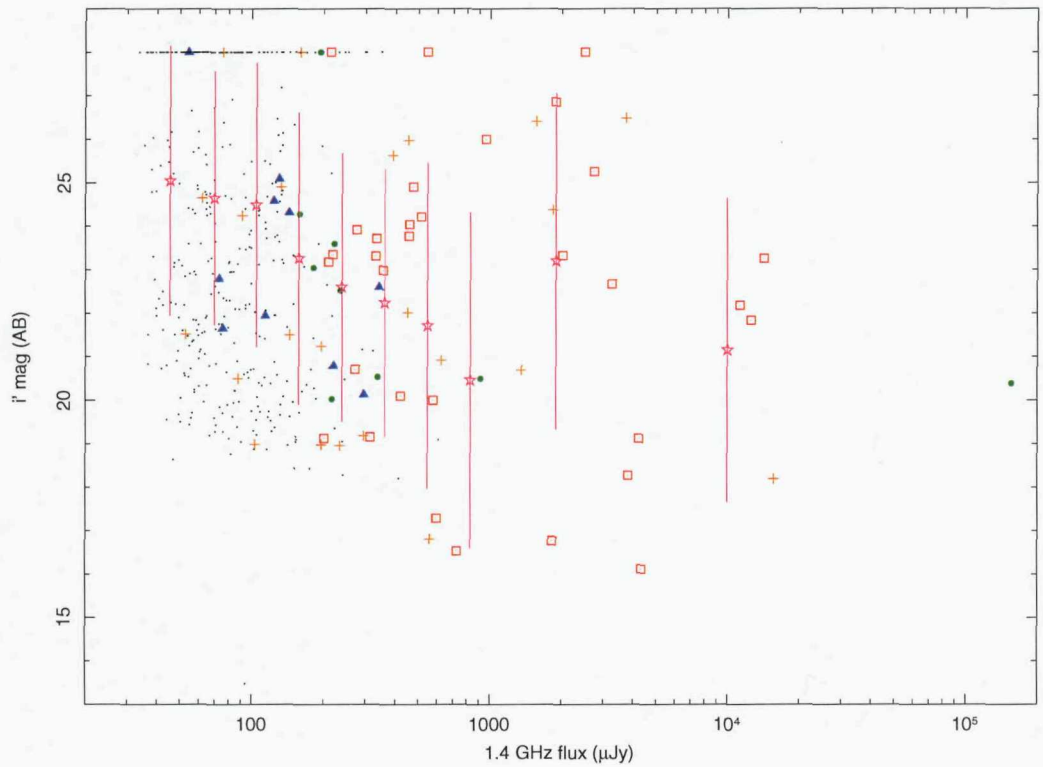

Figure 6.3: The variation of i' band magnitude with 1.4 GHz flux for all sources detected at 1.4 GHz in the 13^H field. Radio sources with no optical counterpart are arbitrarily given an i' band magnitude of 28. The differing symbols indicate differing radio spectral properties. Crosses indicate sources with flat radio spectral indices ($\alpha > -0.4$), open squares indicate sources with spectra consistent with optically thin synchrotron emission ($-1 < \alpha < -0.4$), solid circles represent sources with spectra considered too steep to be due to star formation ($-1.3 < \alpha < -1$) and filled triangles represent USS sources ($\alpha < -1.3$). Sources with only limits to their radio spectra available are indicated with small dots. The stars and error bars show the binned average i' magnitude and standard deviations upon them. The averages are across both fields, and the bin ranges those used for the source counts.

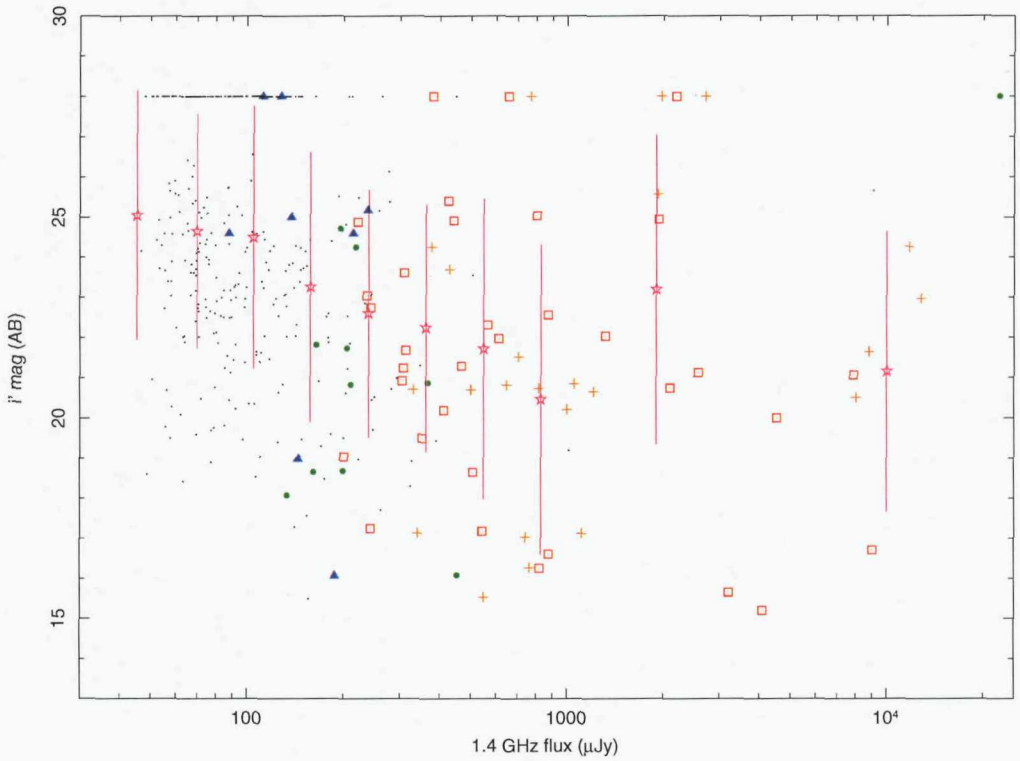

Figure 6.4: The variation of i' band magnitude with 1.4 GHz flux for all sources detected at 1.4 GHz in the 1^H field. Radio sources with no optical counterpart are arbitrarily given an i' band magnitude of 28.The differing symbols indicate differing radio spectral properties. Crosses indicate sources with flat radio spectral indices ($\alpha > -0.4$), open squares indicate sources with spectra consistent with optically thin synchrotron emission ($-1 < \alpha < -0.4$), solid circles represent sources with spectra considered too steep to be due to star formation ($-1.3 < \alpha < -1$) and filled triangles represent USS sources ($\alpha < -1.3$). Sources with only limits to their radio spectra available are indicated with small dots. The stars and error bars show the binned average i' magnitude and standard deviations upon them. The averages are across both fields, and the bin ranges those used for the source counts.

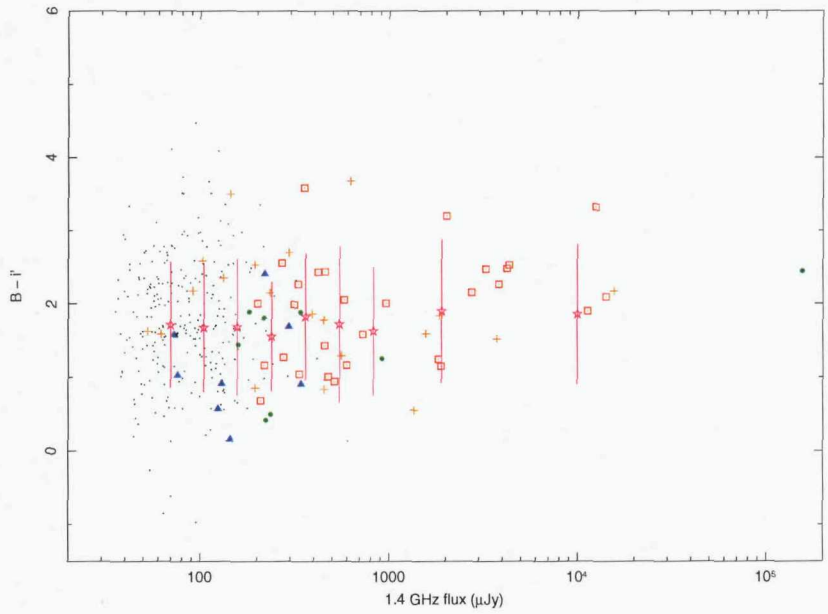

Figure 6.5: The variation of $B - i'$ colour with 1.4 GHz flux for all sources detected at 1.4 GHz in the 13^H field and seen to have optical counterparts. If a source is detected at only one of the B or i' bands, a value of 28th magnitude is used for the second, and limit upon the colour is shown. The symbols are as in Figs. 6.3 and 6.4.

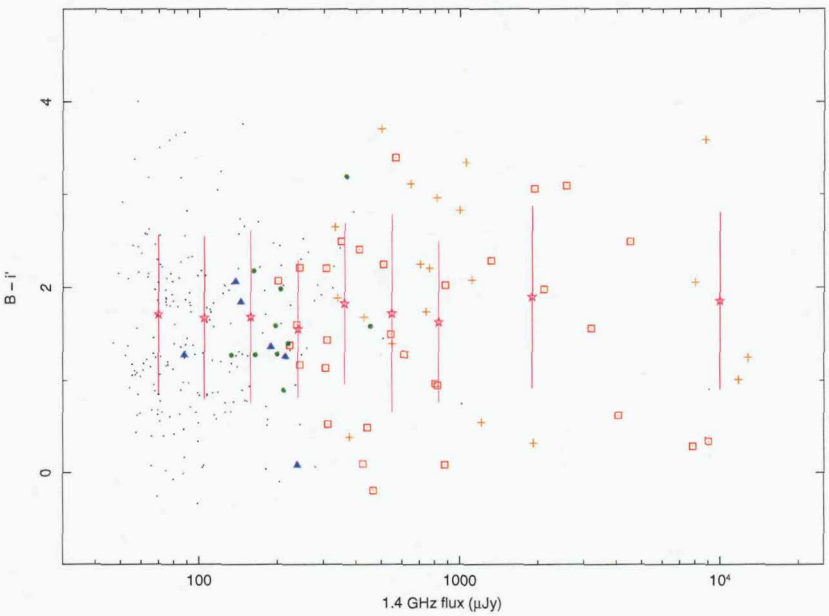

Figure 6.6: The variation of $B - i'$ colour with 1.4 GHz flux for all sources detected at 1.4 GHz in the 1^H field and seen to have optical counterparts. If a source is detected at only one of the B or i' bands, a value of 28th magnitude is used for the second, and limit upon the colour is shown. The symbols are as in Figs. 6.3 and 6.4.

therefore be expected to increase in size as one descends in radio flux to below 1 mJy levels. The pipeline reduced optical catalogue of the 1^H field does not include any information upon size. The detailed multi wavelength optical/IR analysis of the 13^H field is focused on obtaining photometric redshifts for sources too dim for optical spectroscopy. Since these are all dim and small, the analysis of the optical images, and the set up of the SExtractor software used for object detection, is focused on the smaller scale emission. The reliability of the size of sources measured by SExtractor is a sensitive function of the deblending levels used during the analysis, and since these parameters have been optimised for small objects, the sizes reported for larger objects are unreliable. However, the analysis of the R-band image of the 13^H field (M^{c}Hardy et al. 2003) extracted source properties in a manner more suited to investigating the size distribution of source.

The R-band catalogue from this study was searched for the sizes of the optical objects identified as the sources of radio emission. The SExtractor *Stellarity* parameter was used as an indication of the size of an optical object. *Stellarity* is a measure of a source's similarity to the morphology of a star, and the values range from 0 (bares no resemblance to the point spread function – and therefore is extended) to 1 (entirely point-like). This parameter therefore measures extension or non-extension, and therefore will not show how optical size varies with radio flux. However, it can indicate any change in the number of extended sources with radio flux.

The *Stellarity* of the sources detected as radio emitters at 1.4 GHz in the 13^H field are shown in Figs.6.7 and 6.8. The accuracy of the measurement of *Stellarity* decreases with dimmer optical sources, being reasonably accurate to $R \sim 25$, but being unreliable at fainter magnitudes, as can be seen in Fig. 6.7, where the spread of values increases with R-band magnitude. With this information as a caveat, the variation of *Stellarity* with radio flux seen in Fig. 6.8 can be viewed with caution. Once again, no clear trend can be seen with radio flux, though an over density of extended optical sources at faint radio fluxes is apparent. Twenty two sources have *Stellarities* close to 1 - implying quasar-like optical morphology (although one is actually a star - as determined by optical spectroscopy) and therefore increasing the likelihood that the radio emission is due to an AGN.

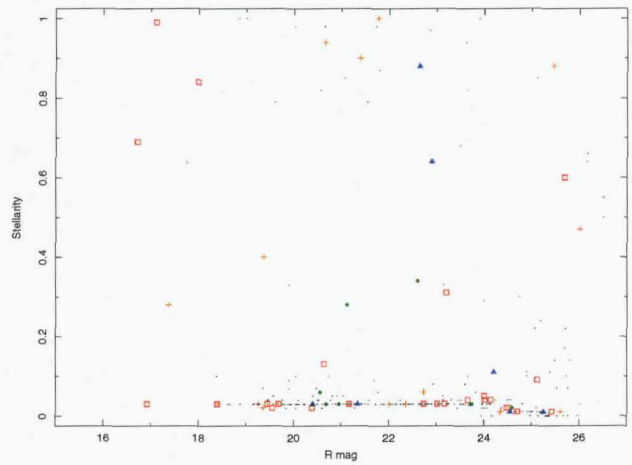

Figure 6.7: The variation of *stellarity*, as measured by SExtractor, with R-band magnitude for all radio sources detected at 1.4 GHz in the 13^H field and seen to have optical counterparts. The symbols are as in Figs. 6.3 and 6.4.

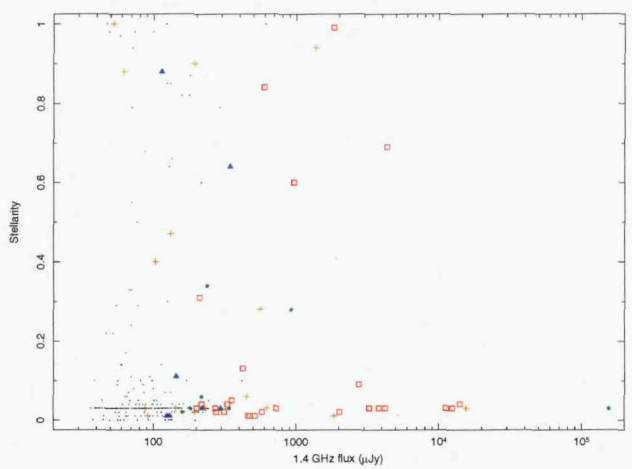

Figure 6.8: The variation of *stellarity*, as measured by SExtractor, with 1.4 GHz flux for all radio sources detected at 1.4 GHz in the 13^H field and seen to have optical counterparts. The symbols are as in Figs. 6.3 and 6.4.

6.5 Variation of Optical properties with Radio Spectral Index

Along with the variation of optical properties with radio flux, Figs. 6.3 to 6.6 also show radio spectral information. The differing symbols used within these figures indicate differing radio spectral properties. Crosses indicate sources with flat radio spectral indices ($\alpha > -0.4$), open squares indicate sources with spectra consistent with optically thin synchrotron emission ($-1 < \alpha < -0.4$), solid circles represent sources with spectra considered too steep to be due to star formation ($-1.3 < \alpha < -1$) and filled triangles represent USS sources ($\alpha < -1.3$). Sources with only limits to their radio spectra available are indicated with small dots. Once again, no clear trend of optical properties with radio spectral index is immediately obvious.

The flat spectrum objects will be considered first. The i'-band magnitudes of these sources are fairly evenly distributed at all radio fluxes. Neither is there any apparent trend in optical colour. The small numbers involved in each radio spectral class do however mean that any trend is unlikely to be readily apparent. Individual cases, though, can be commented upon. Two of the flat spectrum objects in the 1^H field have very red colours - possibly suggesting a high redshift AGN as the source. Three others have no detection in the i' band – also suggesting a distant origin. The sample in the 13^H field shows fewer cases of interest in the flat spectral class. All the flat sources are discovered to have counterparts in the i' band, and their colours are unremarkable, though 4 are associated with point-like objects, and therefore can be said to be AGN with some confidence.

The objects with spectral indices in the range $-1 < \alpha < -0.4$ are expected to be a mixture of AGN and starbursts – indeed, most sources of optically thin synchrotron emission should lie within these bounds. Perhaps unsurprisingly, the distributions of magnitude, colour and *stellarity* of these sources encompass the spreads shown by the entire population, though 3 sources appear point like in Fig. 6.8, effectively ruling out starbursts. Sources with this radio spectral type lying in the upper regions of Figs. 6.5 and 6.6 are unlikely to be starburst.

Objects with spectra steeper than $\alpha = -1$ are expected to be AGN. The brightest source in the 1^H is such an object, and has no coincident optical counterpart. Only one other source of similar spectral index is not detected in the optical, while the remaining sources are evenly distributed about the average colour.

The USS sources ($\alpha < -1.3$) show properties more worthy of remark. One (in the 1^H field) appears to be associated with a bright, 16th magnitude optical object.

Ten objects follow more expected behaviour, being measured as being dimmer than i'=24 (of which 3 are not detected). This is more akin to the properties expected from the high redshift radio galaxies, which are expected to make up at around 30 percent of the USS population.

Chapter 7

Conclusions

In this final chapter, the results achieved are reviewed and conclusions drawn. The short term strategy adopted for continuation of the radio spectral part of the wider project is discussed, along with the longer term future of deep radio surveys.

7.1 Introduction

This thesis has presented 3 radio surveys. The 1^H XMM-*Newton* / *Chandra* / *Spitzer* has been covered at 1.4 GHz and 610 MHz, while its sister field (at 13^H) has been covered at 610 MHz. These surveys aim to increase the known sample of the sub-mJy population, and acquire radio spectra for as many of its constituents as possible, with an aim to aiding the discrimination between AGN and starbursts.

7.2 610 MHz Observations of the 1^H Field

The 1^H field is one of the first extragalactic deep survey fields to be the subject of a deep pointing with the GMRT at 610 MHz. With 4.5 hours on source, a 5σ detection limit of 300 μJy was achieved. Within the 32 arcmin, 20 percent power radius of the GMRT antennas at 610 MHz, 223 sources were discovered. The properties of these sources were corrected for clean bias, and the degradation in sensitivity of the primary beam. Bandwidth, time delay and 3D smearing were seen to be unimportant. The sources in the resulting catalogue, when corrected for resolution bias, Eddington bias and incompleteness, were used to compute the 610 MHz source counts, where the sub-mJy bump is seen for the first time at this frequency. These counts can be reasonably well fitted with a simple two population model involving

AGN and an evolving starburst population. The best fitting power-law index of the evolution, in $(1+z)$, is 2.45, comparable to determinations of 2.5 to 3 from similar fitting at 1.4 GHz.

7.3 1.4 MHz Observations of the 1^H Field

The 1^H field is also the target of one of the deepest 1.4 GHz observations with the VLA. A-array observations reach a noise limit of 11.2 μJy beam^{-1}, with 432 sources detected out to the 50 percent power level of the primary beam (15 arcmin radius). Source properties were corrected for bandwidth and time delay smearing, and primary beam degradation. After completeness corrections have been applied, the source counts computed from this sample are consistent with those from other 1.4 GHz deep fields, though a reasonably large field to field scatter is seen. Fitting a compilation of these counts with the same simple model as used in Chapter 3 gives a best fitting value of the power law index of luminosity evolution of 2.5.

7.4 610 MHz Observations of the 13^H Field

The 13^H field, which is covered to noise limit of 7.5 μJy beam^{-1} with VLA A+B array observations at 1.4 GHz (Seymour et al. 2004), is also the subject of a 610 MHz survey. Reaching a detection limit $\sim$300 μJy, 206 sources were discovered within 32 arcmin of the centre of the 13^H field. The source counts, once corrected for incompleteness and Eddington bias, and combined with those from the 1^H and VVDS fields (Bondi et al. 2007), can be modelled with AGN and a starburst population undergoing luminosity evolution with a power law index of 2.6. Comparing this with a similar determination at 1.4 GHz confirms that the population that constitutes the sub-mJy bump has an average spectral index of -0.7.

7.5 Radio Spectra

The catalogues compiled in Chapters 3, 4 and 5, when combined with the catalogue of Seymour et al. (2004), provide measurements, or limits thereon, of fluxes at 610 MHz and 1.4 GHz in both the 13^H and 1^H fields. Within the 15 arcmin radius of the 1.4 GHz surveys, 152 sources have spectra measurable with the combination of these 4 images, and a further 40 useful limits can be determined. Of these 192 sources, 83 can be said to AGN with reasonable confidence from radio spectral

arguments (i.e. $\alpha < -1$ or $\alpha > -0.4, S \propto \nu^{\alpha}$). A further 11 sources can be identified as AGN based on their arcsec scale radio morphology.

7.6 Conclusions

The advent of the GMRT has allowed the 610 MHz sky to be probed to sensitivities and resolutions far in excess of those available before, an opportunity which is being exploited by many of the deep radio fields. The 13^H and 1^H fields are among the first to sample the 610 MHz sky at such sub-mJy sensitivity.

The shape of the 610 MHz source counts, in combination with those at higher frequencies, confirm that the population responsible for the upturn in the Euclidean normalised differential radio source counts below ~1 mJy have, on average, a spectrum of optically thin synchrotron radiation, and are likely to be the higher redshift counterparts of local sources whose radio emission is dominated by star formation. It is therefore unlikely that this population includes a large proportion of flat spectrum AGN. However, a very basic analysis of the optical properties of these sub-mJy radio sources does not show any trend of a greater proportion of brighter or bluer galaxies with decreasing radio flux, as might naively be expected.

Multi band radio observations have provided spectra for some of these sub-mJy sources, and future observations will collect an unprecedentedly large sample of low frequency radio spectra for members of the sub-mJy population. This data, when combined with other observations, will provide a much clearer picture of the nature of the faint radio population in the near future.

7.7 Future Work

Any study performed during the preparation for a thesis such as this is merely a snap shot of the state of both the project within which it is placed, and the wider state of knowledge and techniques. Understanding of the scientific principles involved, and the instrumentation used to study them, are in a constant state of flux, and so the future development of any work should be considered. In the case of this project, short term progress with be facilitated by a large influx of new data. Longer term goals, as well as this data, will now be discussed.

7.7.1 Short Range

Over the next year, a larger 610 MHz dataset will become available, and the many disparate sub-projects to provide AGN/starburst discrimination will coalesce.

7.7.1.1 New Data

As mentioned in Chapter 5, both the 13^H and 1^H fields were observed for a further 20 hours each in February of 2006, but the observations failed to achieve noise levels remotely near those expected due to some technical issues which are not well understood. The observations of the 1^H field have since been repeated, and the expected thermal noise is $\sim$ 10 μJy beam^{-1}, though as discussed in Chapter 3, it remains to be seen how consistently the GMRT achieves the thermal limit in deep observations at 610 MHz. Repeat observations of the 13^H field will be scheduled in the Autumn of 2007, while the intervening time has seen a new set of observations targeting this field undertaken. Totalling 50 hours on source at 610 MHz, this new set of observations, when combined with the retaken 2006 observations, has an expected thermal noise of $\sim$ 7 μJy beam^{-1}, low enough to detect the majority of the sources seen in the 1.4 GHz survey of the field, and place useful limits on the remainder.

As noted in Chapter 5, a bright source ($\sim$360 mJy) lies within 14 arcmin of the centre of the 13^H field. This source is responsible for a considerable amount of noise in the 610 MHz maps of Chapter 3, as any errors in the phase calibration of the *uv* data are amplified above the thermal noise by it large detected flux. As such, more attention has been paid to very careful phase calibration in the new observations. Instead of intervals of 40 minutes, the phase calibrator was observed every 15 to 20 minutes to keep a more accurate track of any phase instabilities in the instrument and atmosphere. Special care will be taken during the self calibration procedure to ensure the best possible model is used to fit the antenna gains to, and with the highest possible time resolution.

Once these two later generations of 610 MHz imaging are completed, the 610 MHz survey of the 13^H field will rival that at 1.4 GHz. Useful spectral information will be available for nearly all the radio sources in the XMM-*Newton* / *Chandra* / *Spitzer* survey area, The large number of new sources that will be discovered in the extended area of the 610 MHz images will provide a better constraint on the 610 MHz source counts, and the potential availability of more sophisticated AGN source count models will allow the evolution of the starburst population to be more

accurately constrained.

7.7.1.2 Combination of Data

The spectra gathered here, and in the newer 610 MHz imaging of the two fields are part of a concerted effort to discriminate between AGN and starbursts in the population discovered at sub-mJy 1.4 GHz fluxes. This effort involves deep MERLIN imaging, and its combination with the VLA 1.4 GHz data, deep multi-band optical and IR imaging to provide photometric redshifts for the radio sources, optical spectroscopy, and MIR photometry. The majority of these facets are nearing completion, and their culmination will provide a view of the sub-mJy population of unprecedented detail. Preliminary results of such analysis show that the upturn in the radio source counts below 1 mJy may be partially due to an upturn the counts of AGN. However, the majority of the sub-mJy population as detected in deep, narrow surveys does appear to be due to star formation.

7.7.1.3 Follow Up Observations of the USS Sources

As noted in Chapter 5, 18 sources were detected in both radio bands and seen to have radio spectra steeper than $\alpha = -1.3$, a value used to classify USS sources – a population which is a good sample to select from to identify high redshift radio galaxies. As seen in Chapter 6, several of these are faint at optical wavelengths, and may well be distant AGN. Very high redshift galaxies can place strong constraints upon early galaxy formation. Follow up observations are planned to further investigate these sources, including proposed Keck optical spectroscopy. The deeper 610 MHz observations will confirm or deny the validity of the detections of those sources detected at 610 MHz but not at 1.4 GHz.

7.7.2 Mid Range

The mid range future of the project within which this work is a part, and radio astronomy in general, is dominated by the imminent instigation of vastly improved observational facilities. Both the VLA and MERLIN are currently undergoing intensive upgrade procedures, with the new instrument configurations to be known as the eVLA and eMERLIN respectively. The electronics and receivers of the VLA are being over-hauled to provide greater sensitivity. Plans to extend the array to cover a wider portion of the state of New Mexico will also provide greater resolution - both key attributes in the detection and classification of the sub-mJy radio population.

The upgrades to eMERLIN also involve a large improvement in sensitivity. With such an increase, mosaics of pointings will be able to cover reasonable areas with sub-arcsec resolution, both detecting and morphologically classifying members of the sub-mJy population.

The next 3 to 4 years will therefore see a huge leap in the sensitivity of radio telescopes, and an associated leap in the depths of radio surveys. The larger project discussed herein will provide a solid grounding for the techniques and strategies required to extend the study of the faint radio population to the greater depths soon to become available. This improvement in depth will allow radio studies of the star formation history to more closely match those at optical wavelengths in terms of redshift coverage.

7.7.3 Long Range

The longer term future of radio astronomy – and therefore of deep radio surveys – is dominated by similar considerations as its medium term future. The planned improvements in radio astronomy instrumentation do not stop with the upgrades to the current telescopes. Two large projects are under way to construct entirely new arrays – the LOw Frequency ARray (LOFAR) and the Square Kilometre Array (SKA).

LOFAR is in the initial construction stage. It will consist of an array of small omni-directional antennas spread around North West Europe, and operate at low radio frequencies (between 10 and 240 MHz). The final interferometer is projected to contain 15,000 array elements, with a maximum baseline of $\sim$100 km.Once complete, this instrument will provide another step forward in sensitivity, allowing deep surveys to probe out to greater depths, and better sample the sub-mJy population. The numbers of sources likely to be detected will help provide star formation history measurements out to far higher redshifts.

The SKA is still in the preliminary planning stage. Its is hoped to be a continent-spanning array of unprecedented sensitivity, and should reach sub-μJy noise levels at sub-arcsec resolution in the centimetre bands. If such ambitions are realised, radio observations may provide the state of the art star formation measures.

The future of deep radio surveys is therefore bright. The upgrades of the existing arrays, and the development of new instruments, ensures that radio surveys will continue to form a vital role in our understanding of the extragalactic populations. The next generation of optical instruments will also give new understanding about

early star formation.

As is being experimented with by this project among others, the combination of the new ultra-deep radio data with next generation observations at shorter wavelengths will provide a deep and rich data set with which to answer questions about the nature of the cosmos – and find new ones to ask.

Appendix A

Radio – Optical Overlays

This Appendix shows the contours of radio emission at both frequencies overlaid on deep optical imaging of the survey areas. In both cases, the contours of 1.4 GHz emission in in red, and the contours of 610 MHz emission in blue. Sources are shown in 1.4 GHz, then 610 MHz, flux order, with contours at 2, $2\sqrt{2}$, 4, $4\sqrt{2}$ ... times the local rms noise.

The following pages show contours of radio emission at both radio frequencies overlaid on the optical imaging of the 13^H field. The Subaru I band image is used if available, and the Megacam i' band image elsewhere. The numbers below each image are: 1.4 GHz catalogue number (left); spectral index (middle); 610 MHz catalogue number (right). If no 610 MHz catalogue number is given, the spectrum given is a limit. Sources detected at only 1.4 GHz, with no formal match at 610 MHz, are shown in images of 20×20 arcsec. Any source detected at 610 MHz are shown in images with 40 arcsec on a side.

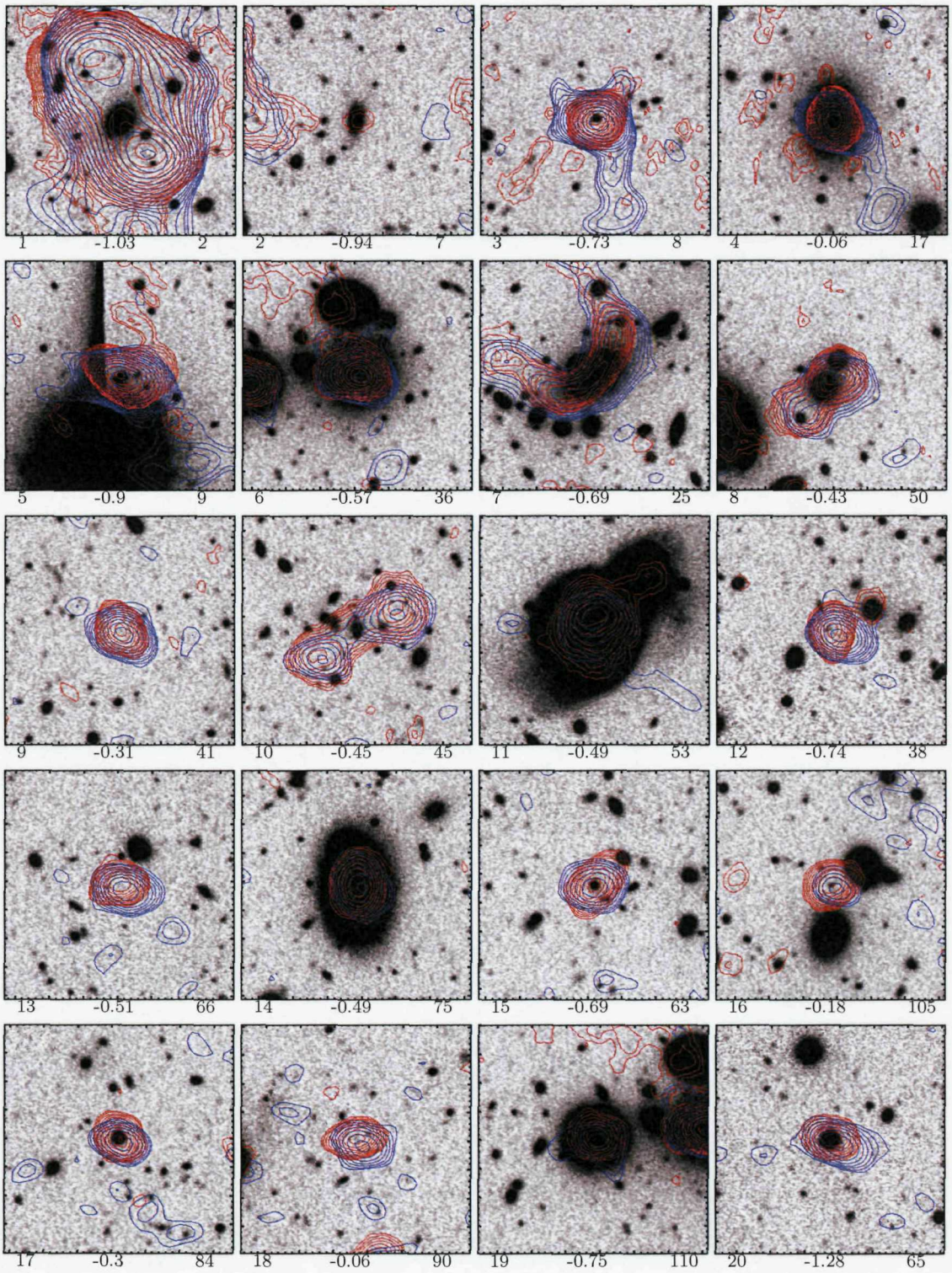
1 -1.03 2
2 -0.94 7
3 -0.73 8
4 -0.06 17
5 -0.9 9
6 -0.57 36
7 -0.69 25
8 -0.43 50
9 -0.31 41
10 -0.45 45
11 -0.49 53
12 -0.74 38
13 -0.51 66
14 -0.49 75
15 -0.69 63
16 -0.18 105
17 -0.3 84
18 -0.06 90
19 -0.75 110
20 -1.28 65

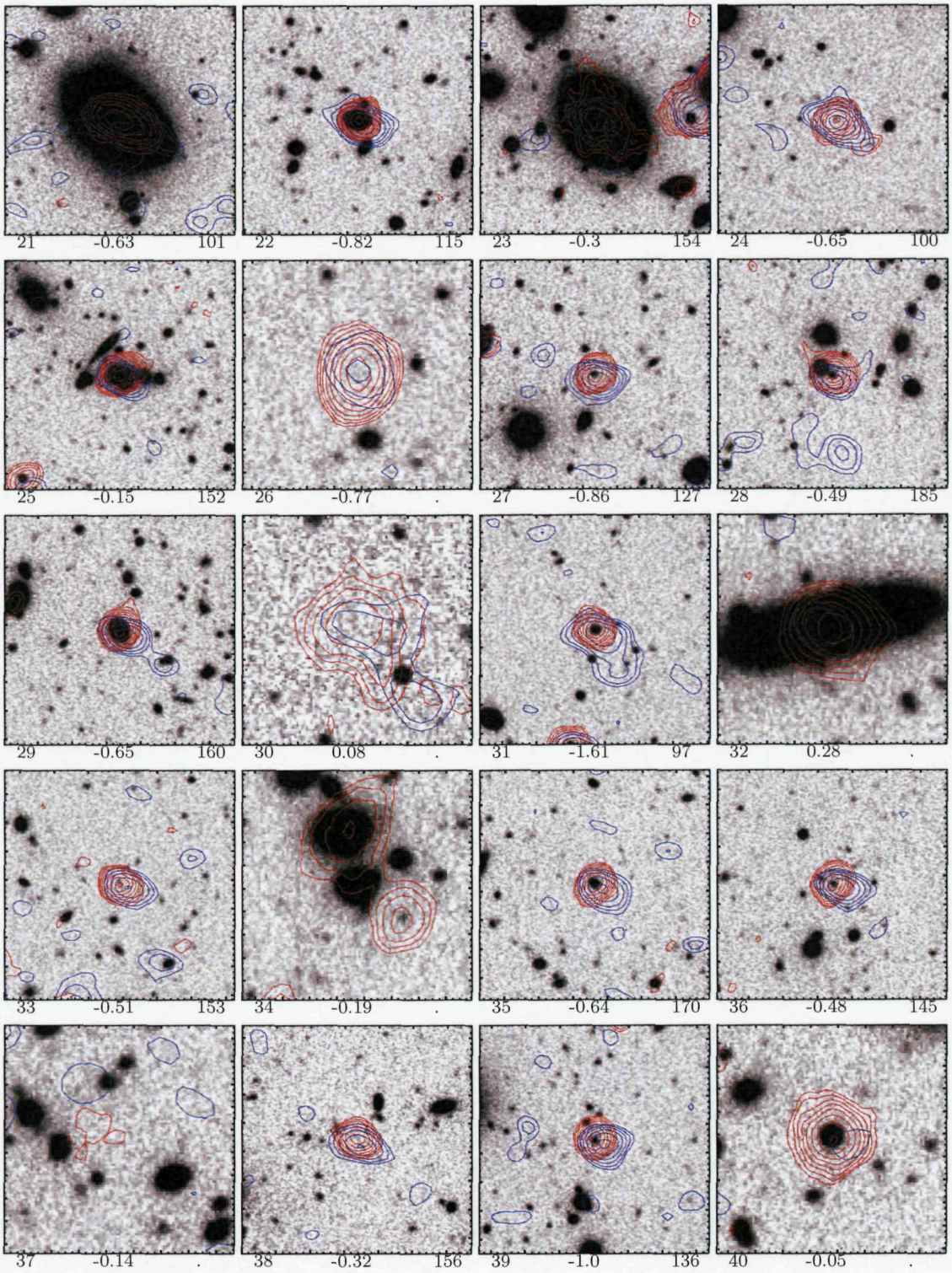
21 -0.63 101
22 -0.82 115
23 -0.3 154
24 -0.65 100
25 -0.15 152
26 -0.77 .
27 -0.86 127
28 -0.49 185
29 -0.65 160
30 0.08 .
31 -1.61 97
32 0.28 .
33 -0.51 153
34 -0.19 .
35 -0.64 170
36 -0.48 145
37 -0.14 .
38 -0.32 156
39 -1.0 136
40 -0.05 .

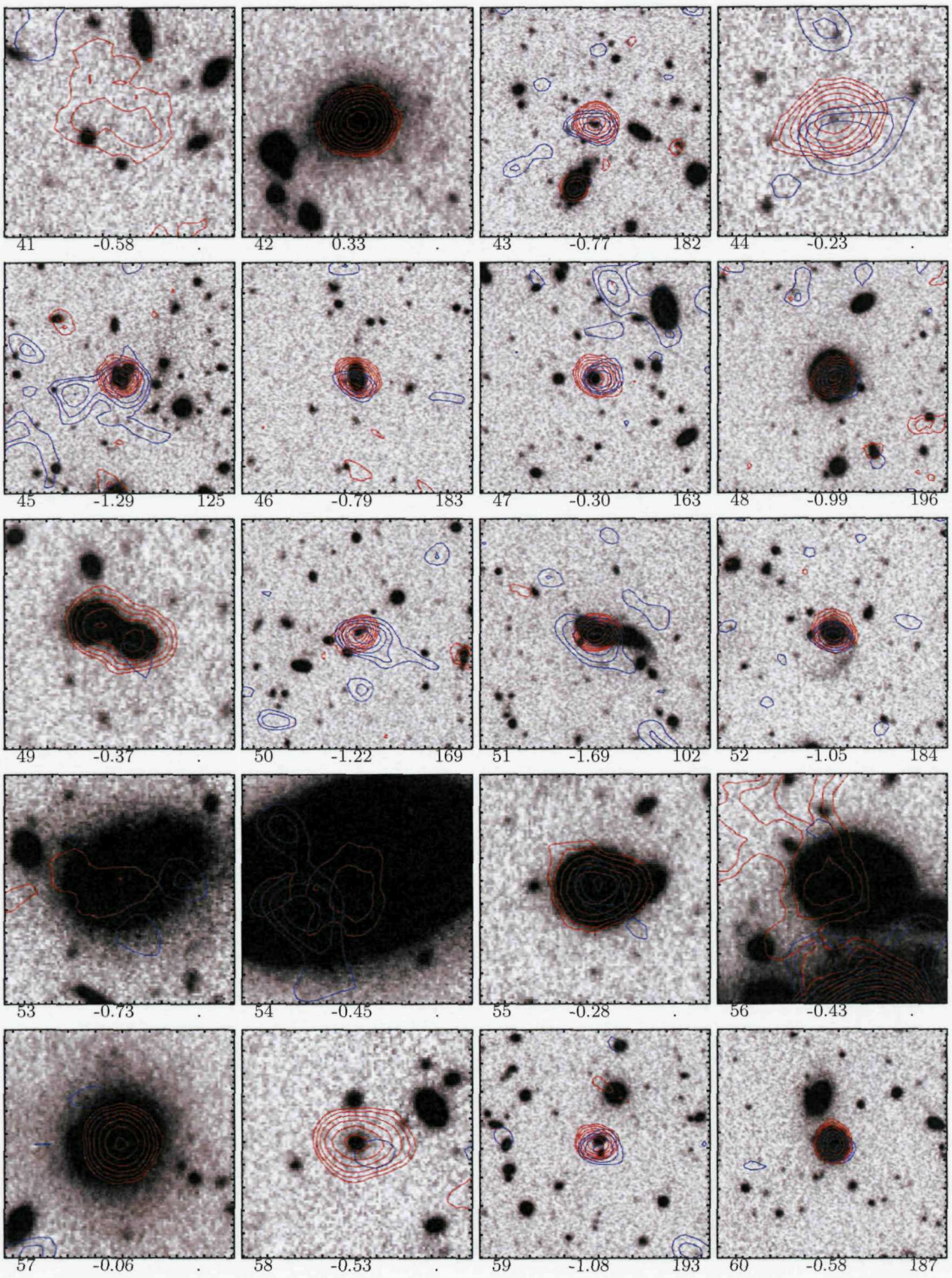
41 -0.58 .
42 0.33 .
43 -0.77 182
44 -0.23 .
45 -1.29 125
46 -0.79 183
47 -0.30 163
48 -0.99 196
49 -0.37 .
50 -1.22 169
51 -1.69 102
52 -1.05 184
53 -0.73 .
54 -0.45 .
55 -0.28 .
56 -0.43 .
57 -0.06 .
58 -0.53 .
59 -1.08 193
60 -0.58 187

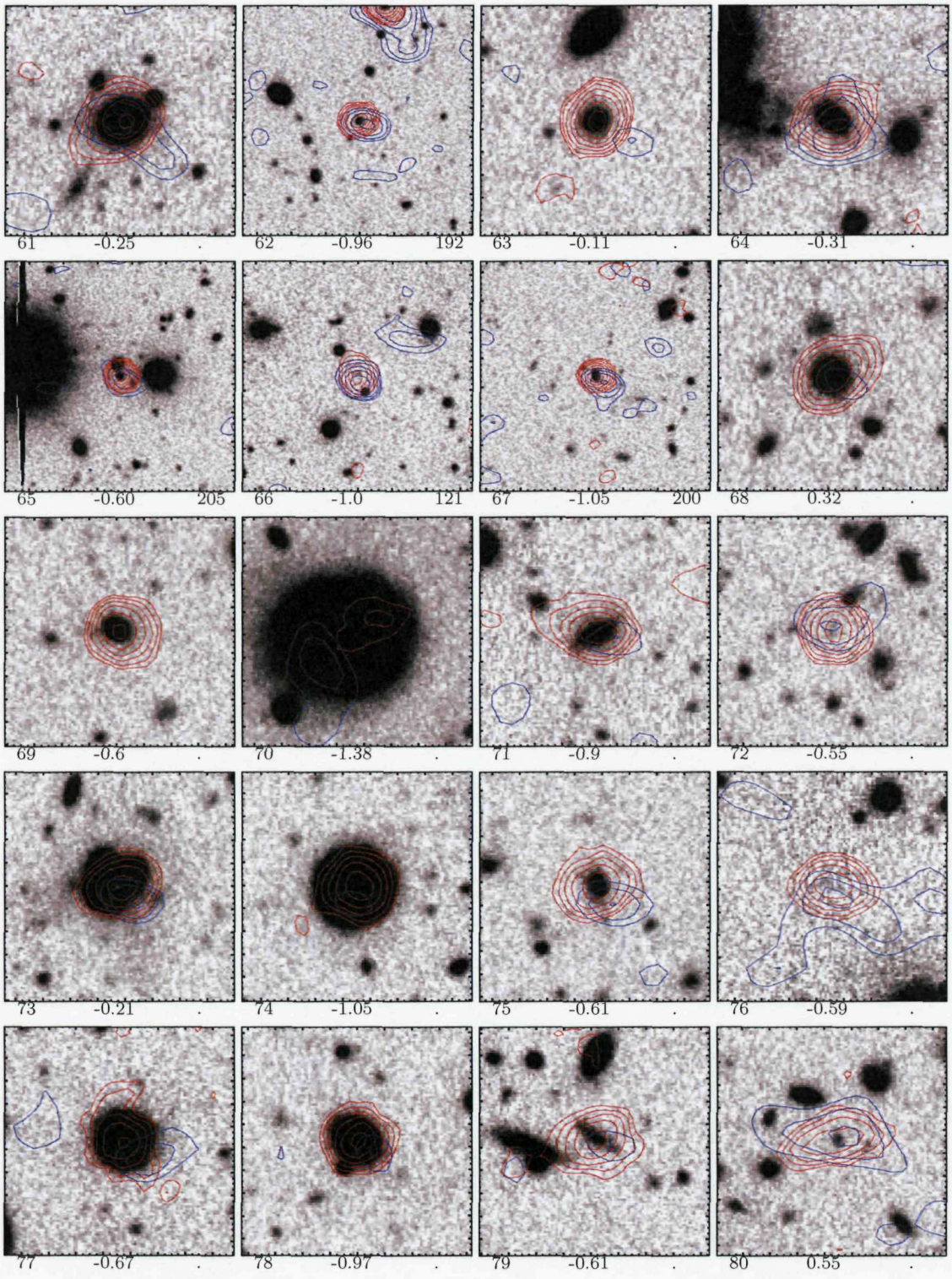
61 -0.25 .
62 -0.96 192
63 -0.11 .
64 -0.31 .
65 -0.60 205
66 -1.0 121
67 -1.05 200
68 0.32 .
69 -0.6 .
70 -1.38 .
71 -0.9 .
72 -0.55 .
73 -0.21 .
74 -1.05 .
75 -0.61 .
76 -0.59 .
77 -0.67 .
78 -0.97 .
79 -0.61 .
80 0.55 .

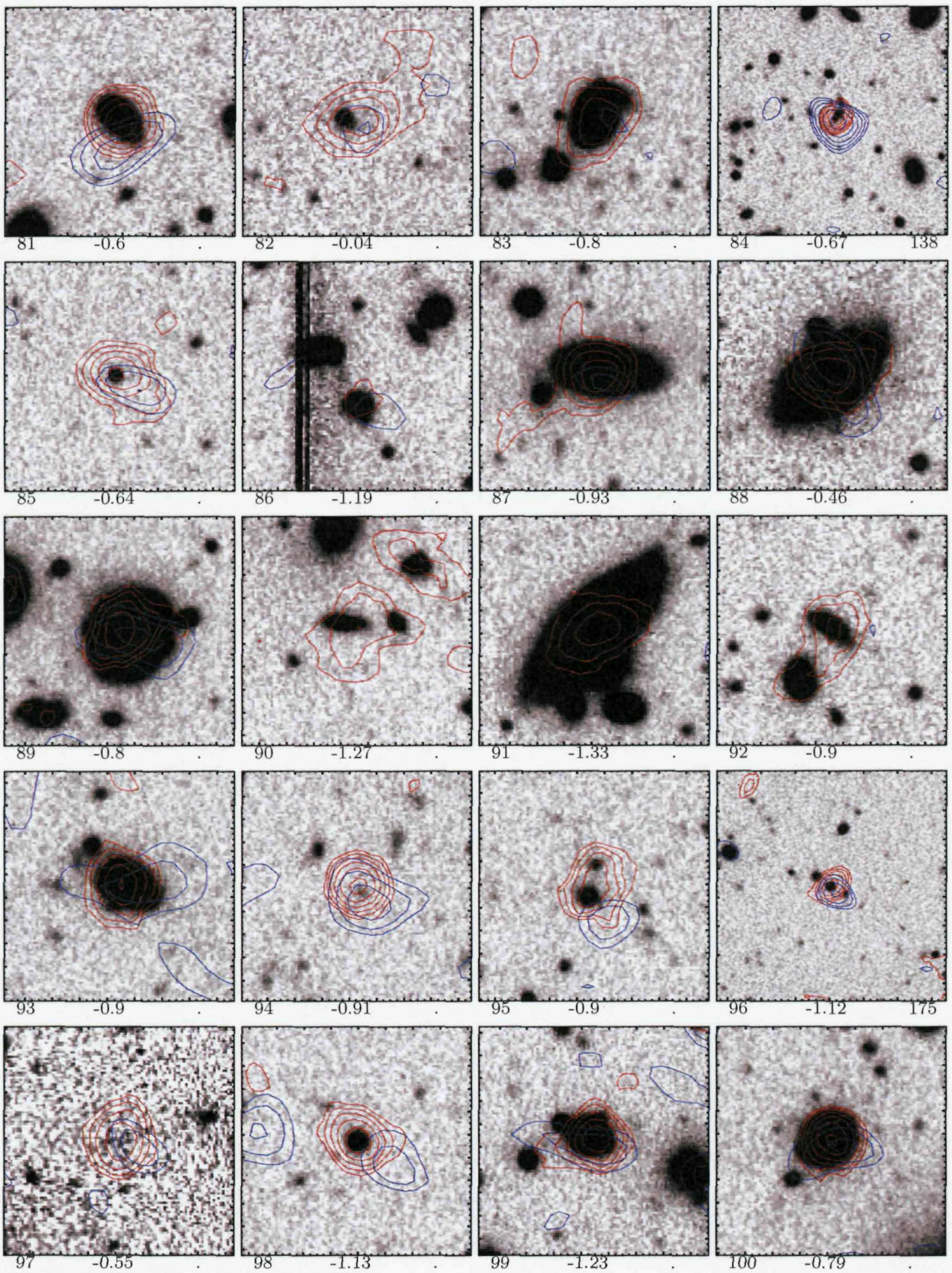
81 -0.6 .
82 -0.04 .
83 -0.8 .
84 -0.67 138
85 -0.64 .
86 -1.19 .
87 -0.93 .
88 -0.46 .
89 -0.8 .
90 -1.27 .
91 -1.33 .
92 -0.9 .
93 -0.9 .
94 -0.91 .
95 -0.9 .
96 -1.12 175
97 -0.55 .
98 -1.13 .
99 -1.23 .
100 -0.79 .

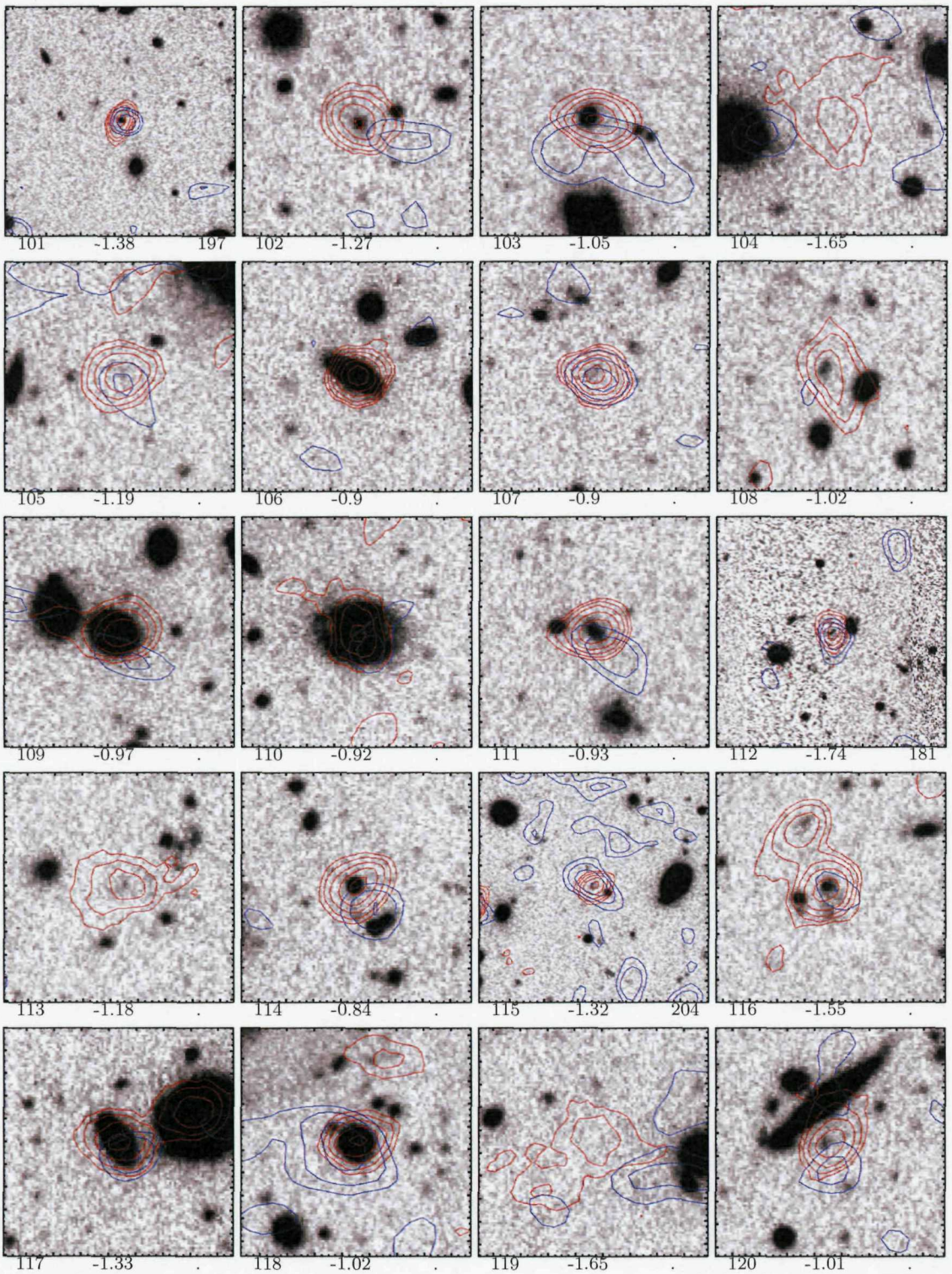
101 -1.38 197
102 -1.27 .
103 -1.05 .
104 -1.65 .
105 -1.19 .
106 -0.9 .
107 -0.9 .
108 -1.02 .
109 -0.97 .
110 -0.92 .
111 -0.93 .
112 -1.74 181
113 -1.18 .
114 -0.84 .
115 -1.32 204
116 -1.55 .
117 -1.33 .
118 -1.02 .
119 -1.65 .
120 -1.01 .

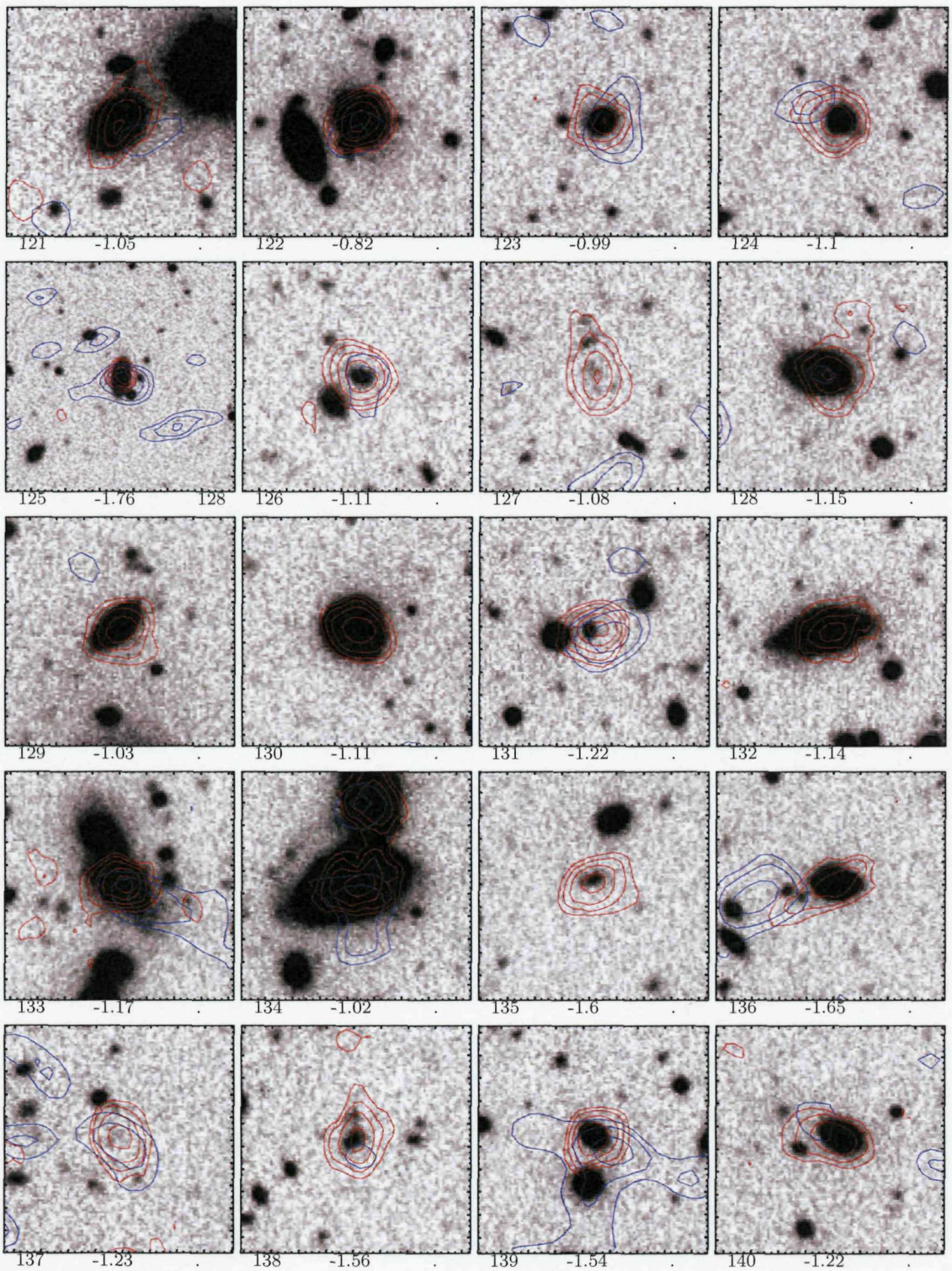
121 -1.05 .
122 -0.82 .
123 -0.99 .
124 -1.1 .
125 -1.76 128
126 -1.11 .
127 -1.08 .
128 -1.15 .
129 -1.03 .
130 -1.11 .
131 -1.22 .
132 -1.14 .
133 -1.17 .
134 -1.02 .
135 -1.6 .
136 -1.65 .
137 -1.23 .
138 -1.56 .
139 -1.54 .
140 -1.22 .

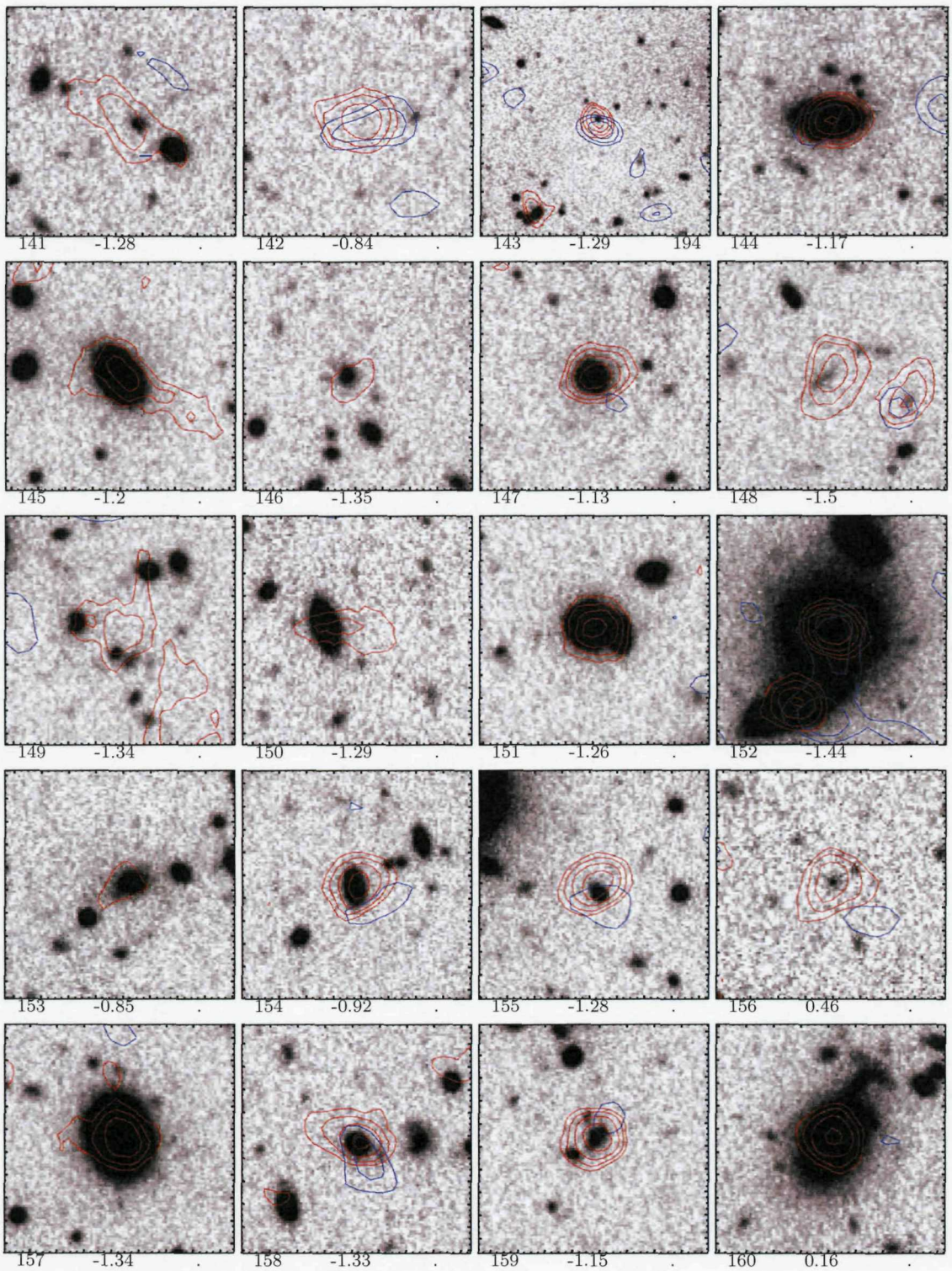
141 -1.28 .
142 -0.84 .
143 -1.29 194
144 -1.17 .
145 -1.2 .
146 -1.35 .
147 -1.13 .
148 -1.5 .
149 -1.34 .
150 -1.29 .
151 -1.26 .
152 -1.44 .
153 -0.85 .
154 -0.92 .
155 -1.28 .
156 0.46 .
157 -1.34 .
158 -1.33 .
159 -1.15 .
160 0.16 .

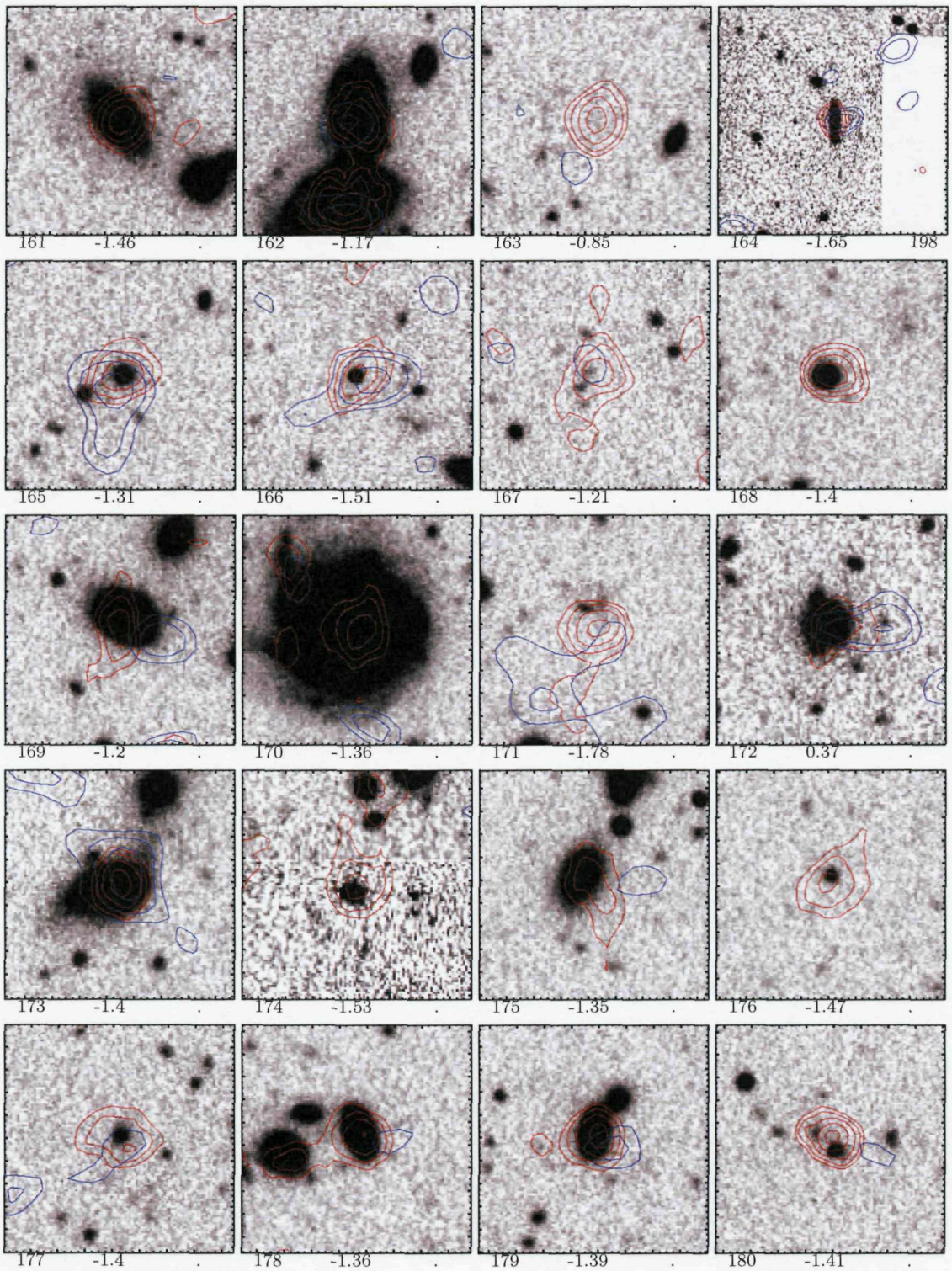
161 -1.46 .
162 -1.17 .
163 -0.85 .
164 -1.65 198
165 -1.31 .
166 -1.51 .
167 -1.21 .
168 -1.4 .
169 -1.2 .
170 -1.36 .
171 -1.78 .
172 0.37 .
173 -1.4 .
174 -1.53 .
175 -1.35 .
176 -1.47 .
177 -1.4 .
178 -1.36 .
179 -1.39 .
180 -1.41 .

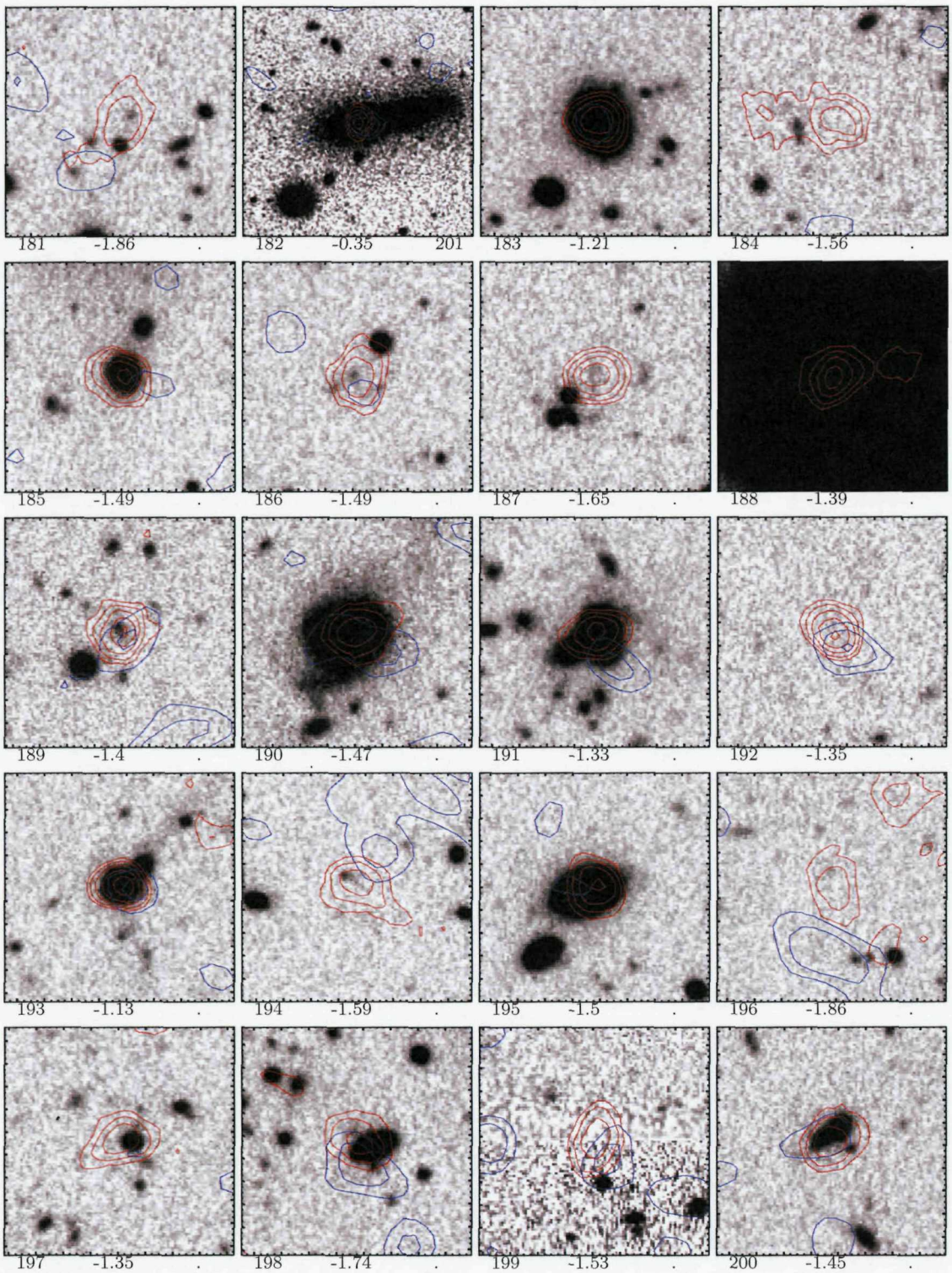
181 -1.86 .
182 -0.35 201
183 -1.21 .
184 -1.56 .
185 -1.49 .
186 -1.49 .
187 -1.65 .
188 -1.39 .
189 -1.4 .
190 -1.47 .
191 -1.33 .
192 -1.35 .
193 -1.13 .
194 -1.59 .
195 -1.5 .
196 -1.86 .
197 -1.35 .
198 -1.74 .
199 -1.53 .
200 -1.45 .

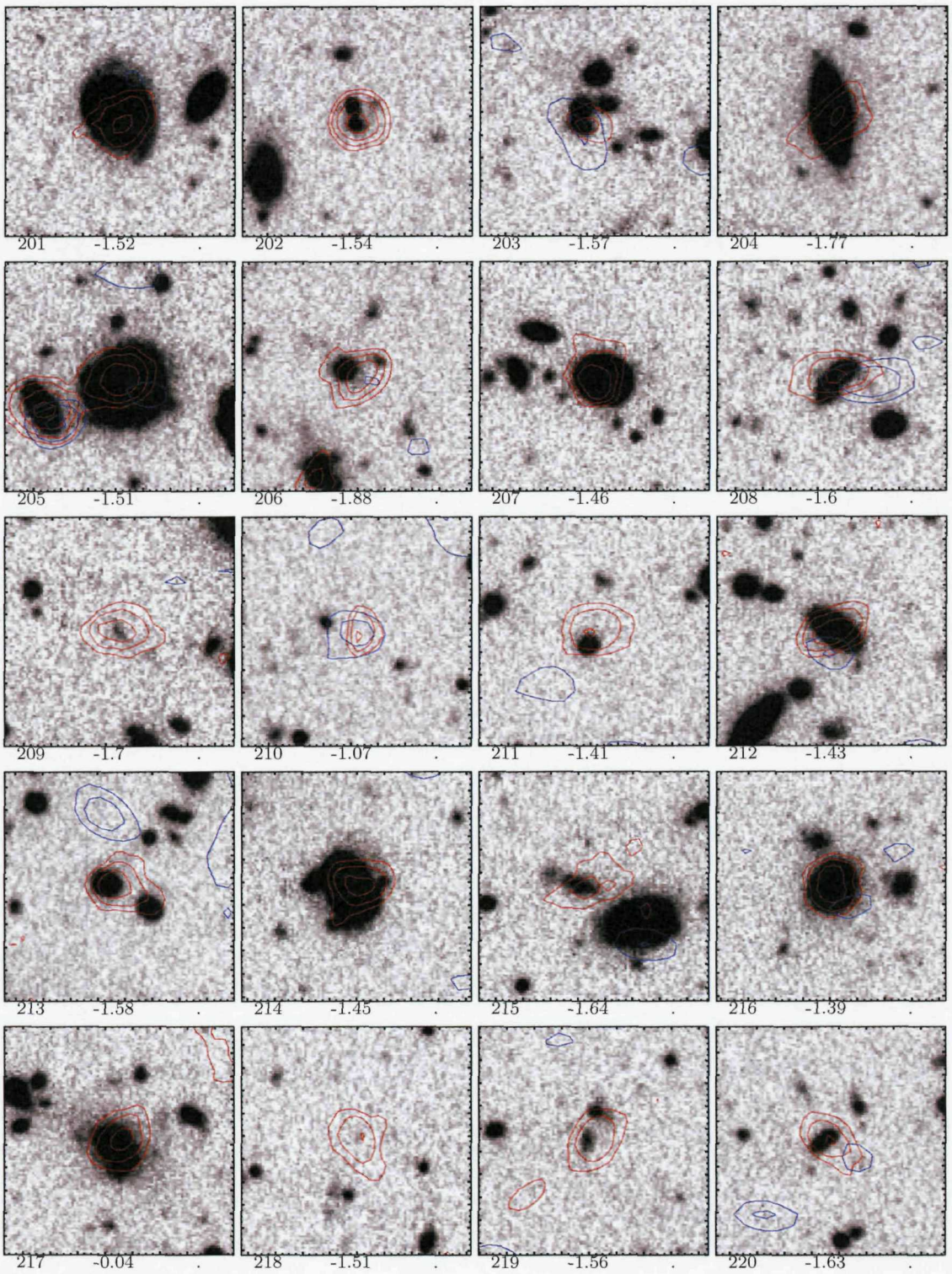
201 -1.52 .
202 -1.54 .
203 -1.57 .
204 -1.77 .
205 -1.51 .
206 -1.88 .
207 -1.46 .
208 -1.6 .
209 -1.7 .
210 -1.07 .
211 -1.41 .
212 -1.43 .
213 -1.58 .
214 -1.45 .
215 -1.64 .
216 -1.39 .
217 -0.04 .
218 -1.51 .
219 -1.56 .
220 -1.63 .

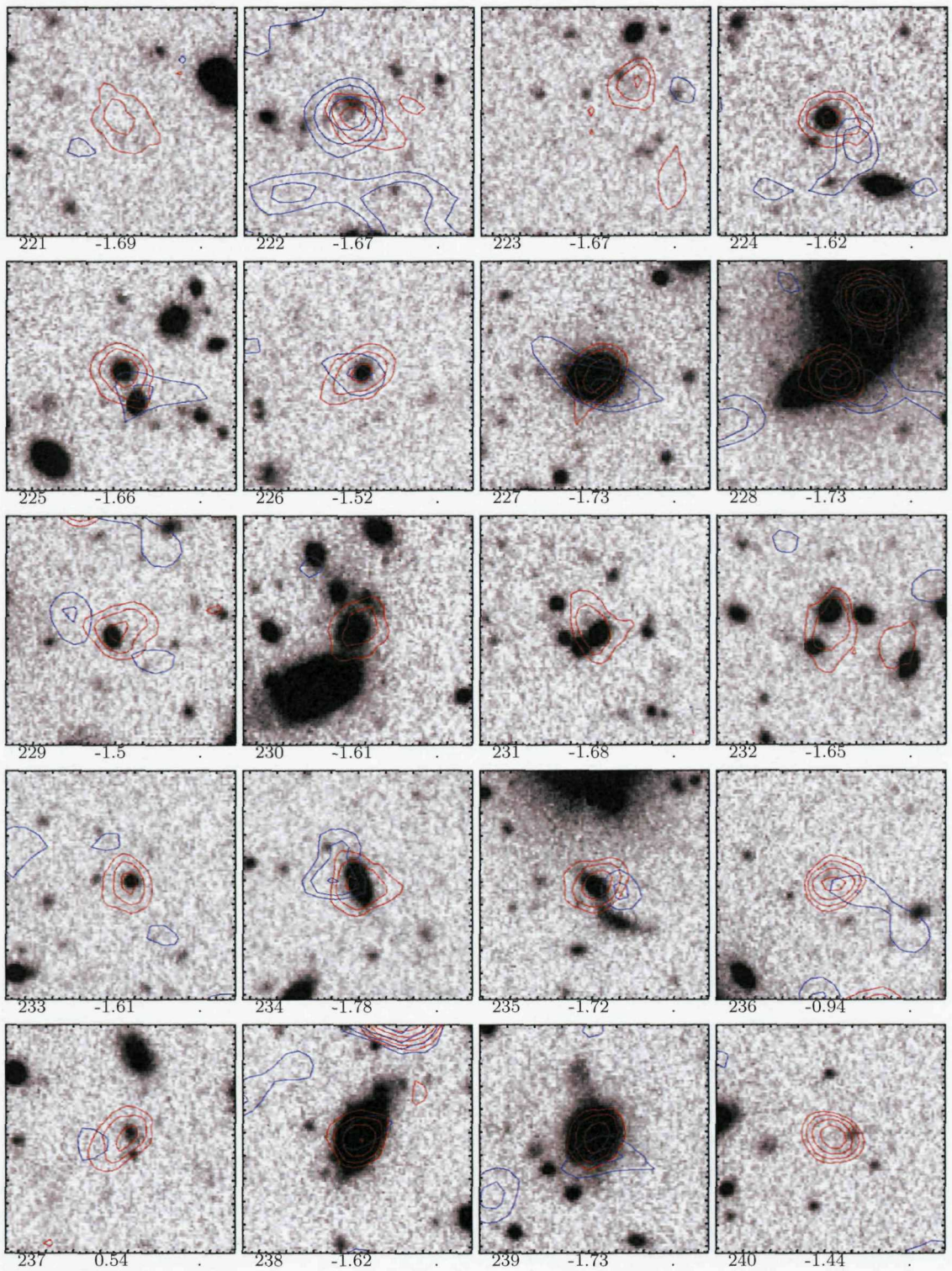
221 -1.69 .
222 -1.67 .
223 -1.67 .
224 -1.62 .
225 -1.66 .
226 -1.52 .
227 -1.73 .
228 -1.73 .
229 -1.5 .
230 -1.61 .
231 -1.68 .
232 -1.65 .
233 -1.61 .
234 -1.78 .
235 -1.72 .
236 -0.94 .
237 0.54 .
238 -1.62 .
239 -1.73 .
240 -1.44 .

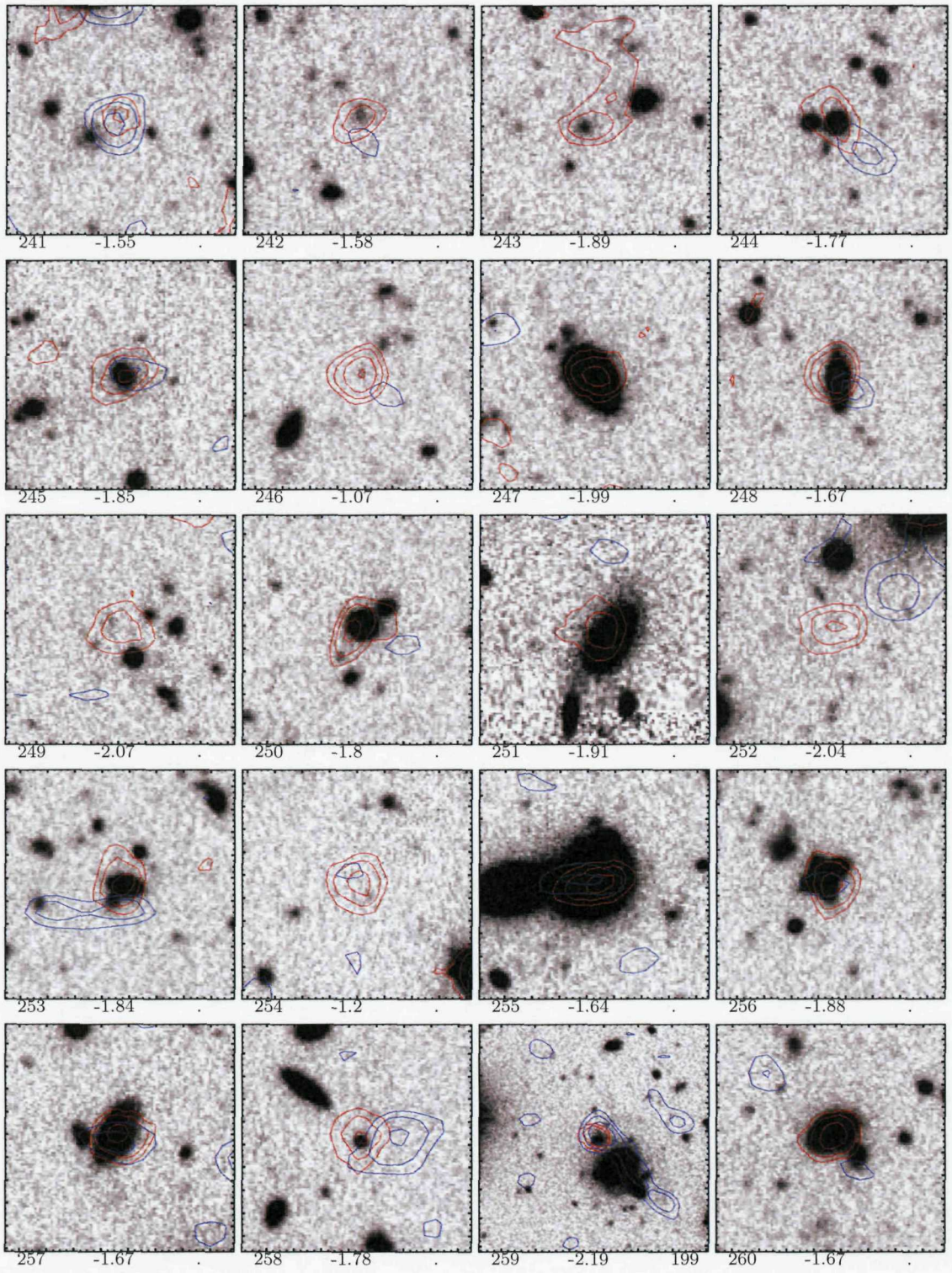
241 -1.55 .
242 -1.58 .
243 -1.89 .
244 -1.77 .
245 -1.85 .
246 -1.07 .
247 -1.99 .
248 -1.67 .
249 -2.07 .
250 -1.8 .
251 -1.91 .
252 -2.04 .
253 -1.84 .
254 -1.2 .
255 -1.64 .
256 -1.88 .
257 -1.67 .
258 -1.78 .
259 -2.19 199
260 -1.67 .

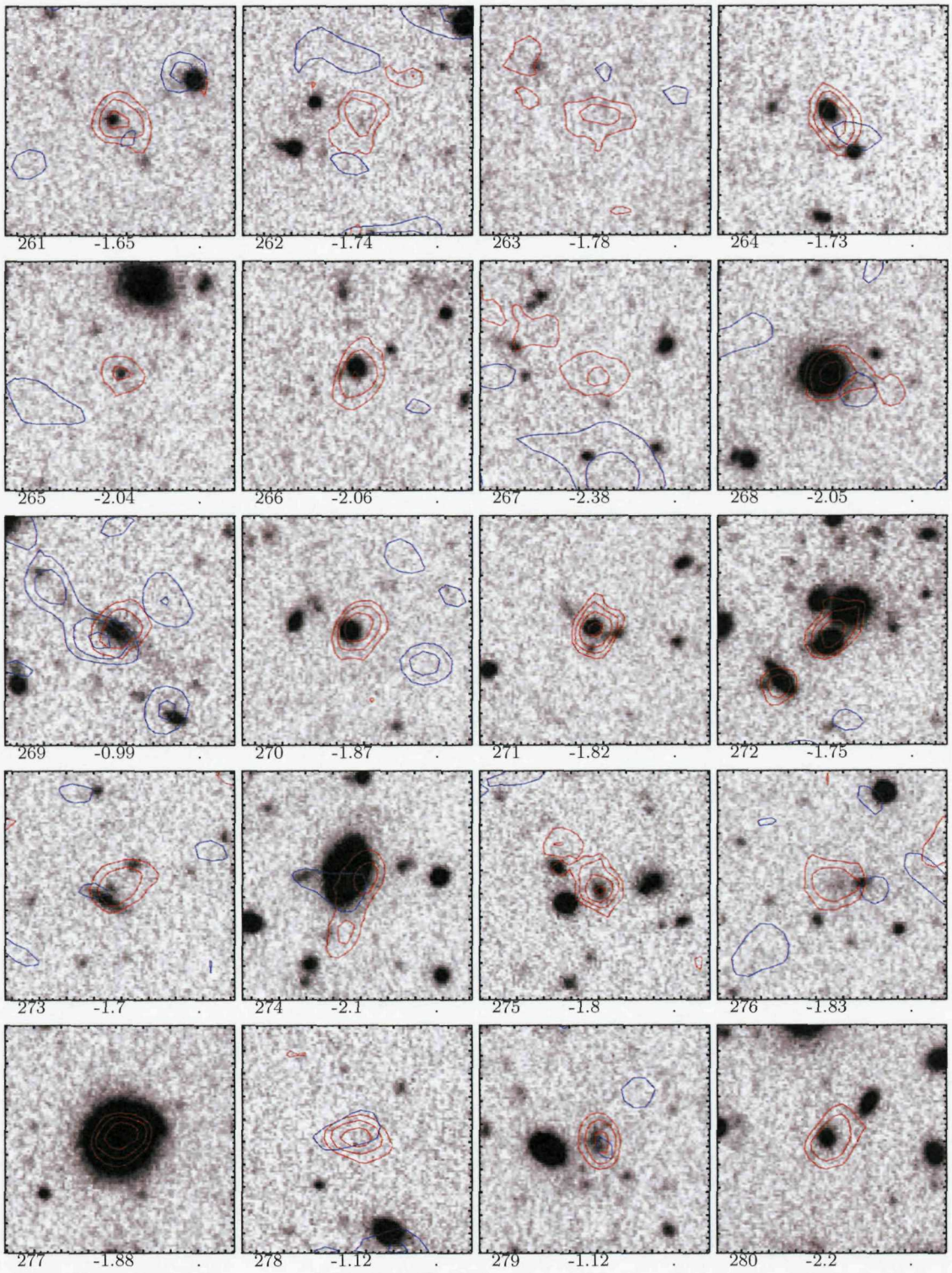
261 -1.65 .
262 -1.74 .
263 -1.78 .
264 -1.73 .
265 -2.04 .
266 -2.06 .
267 -2.38 .
268 -2.05 .
269 -0.99 .
270 -1.87 .
271 -1.82 .
272 -1.75 .
273 -1.7 .
274 -2.1 .
275 -1.8 .
276 -1.83 .
277 -1.88 .
278 -1.12 .
279 -1.12 .
280 -2.2 .

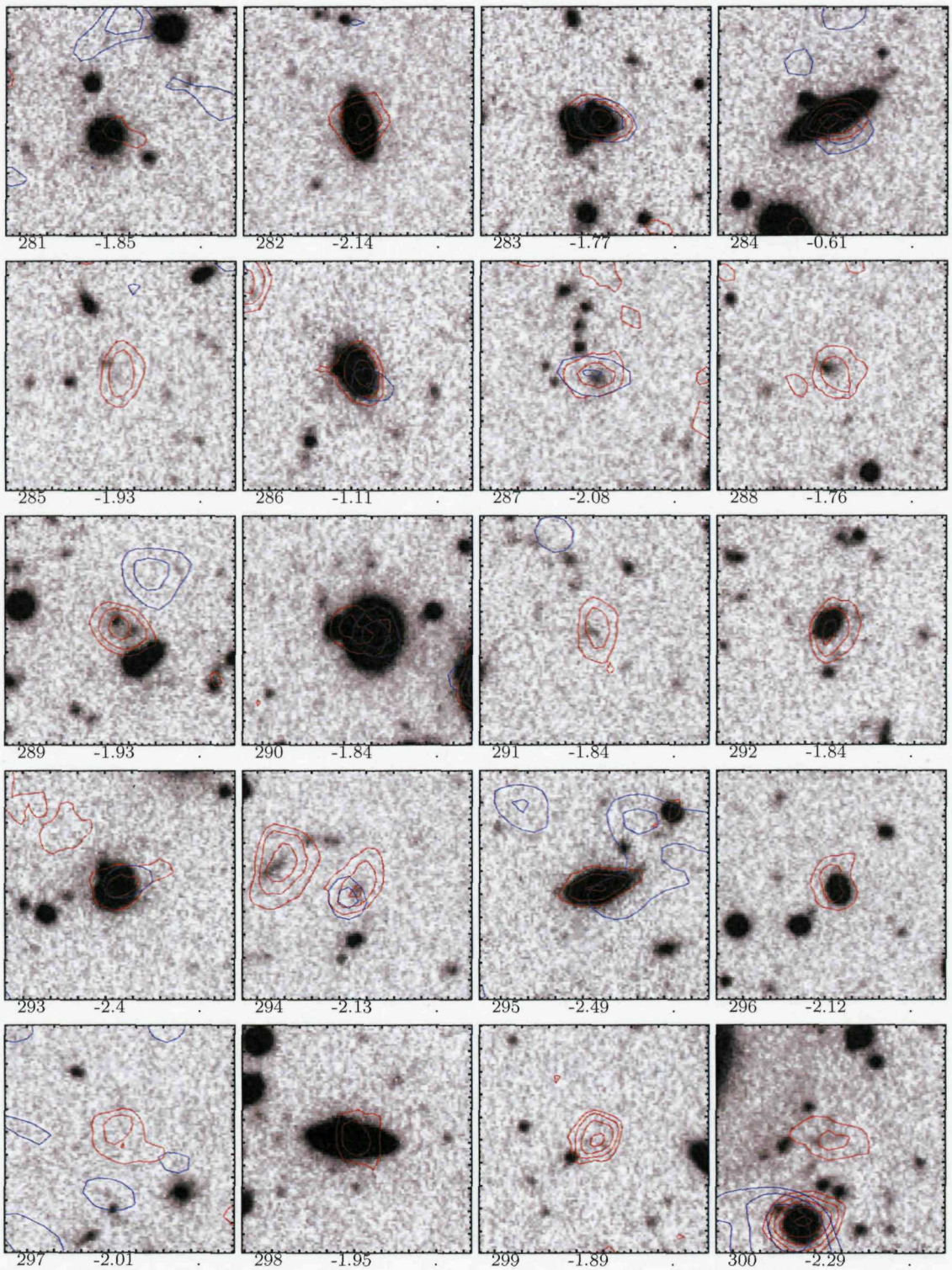
281 -1.85 .
282 -2.14 .
283 -1.77 .
284 -0.61 .
285 -1.93 .
286 -1.11 .
287 -2.08 .
288 -1.76 .
289 -1.93 .
290 -1.84 .
291 -1.84 .
292 -1.84 .
293 -2.4 .
294 -2.13 .
295 -2.49 .
296 -2.12 .
297 -2.01 .
298 -1.95 .
299 -1.89 .
300 -2.29 .

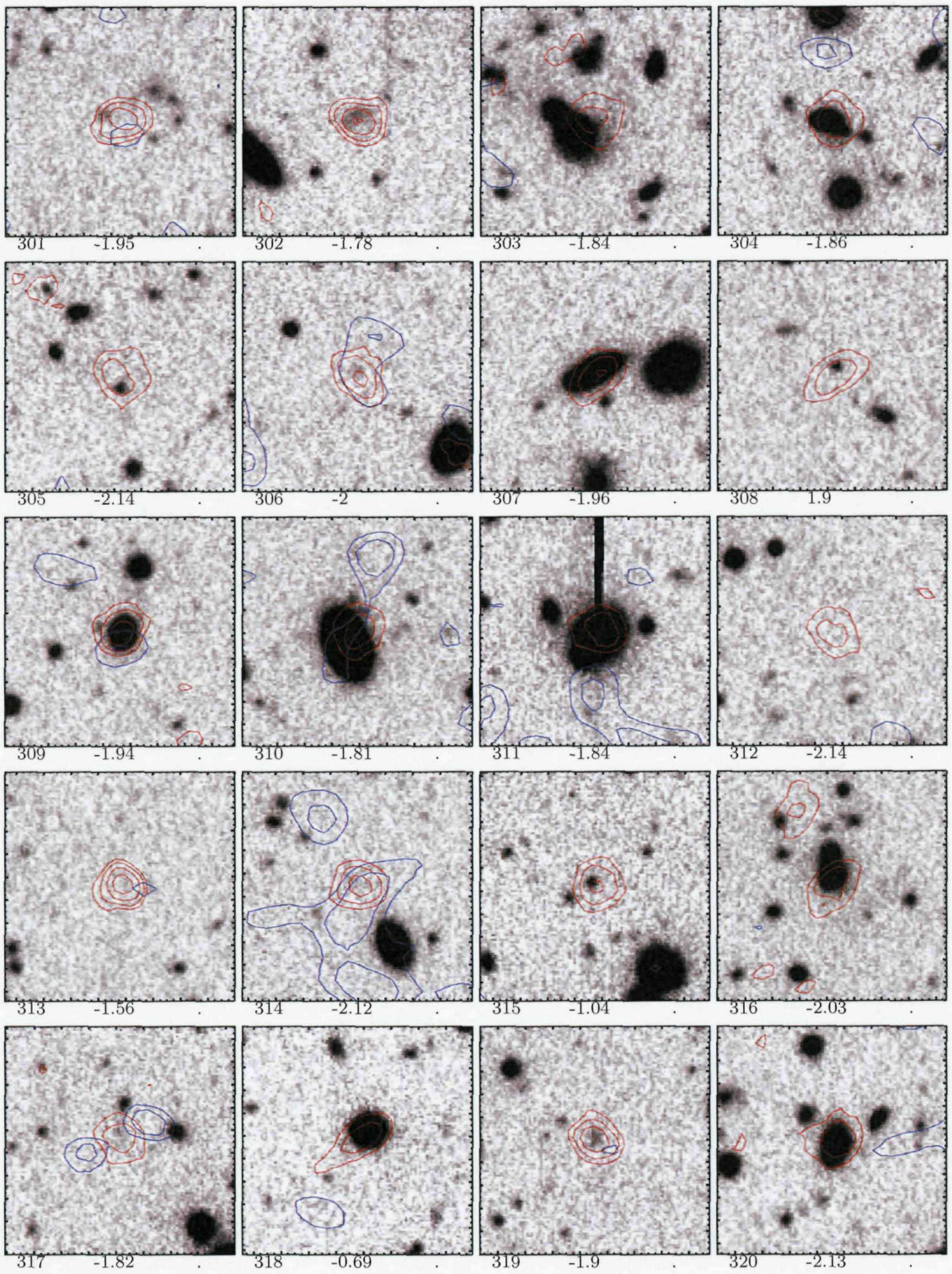
301 -1.95 .
302 -1.78 .
303 -1.84 .
304 -1.86 .
305 -2.14 .
306 -2 .
307 -1.96 .
308 1.9 .
309 -1.94 .
310 -1.81 .
311 -1.84 .
312 -2.14 .
313 -1.56 .
314 -2.12 .
315 -1.04 .
316 -2.03 .
317 -1.82 .
318 -0.69 .
319 -1.9 .
320 -2.13 .

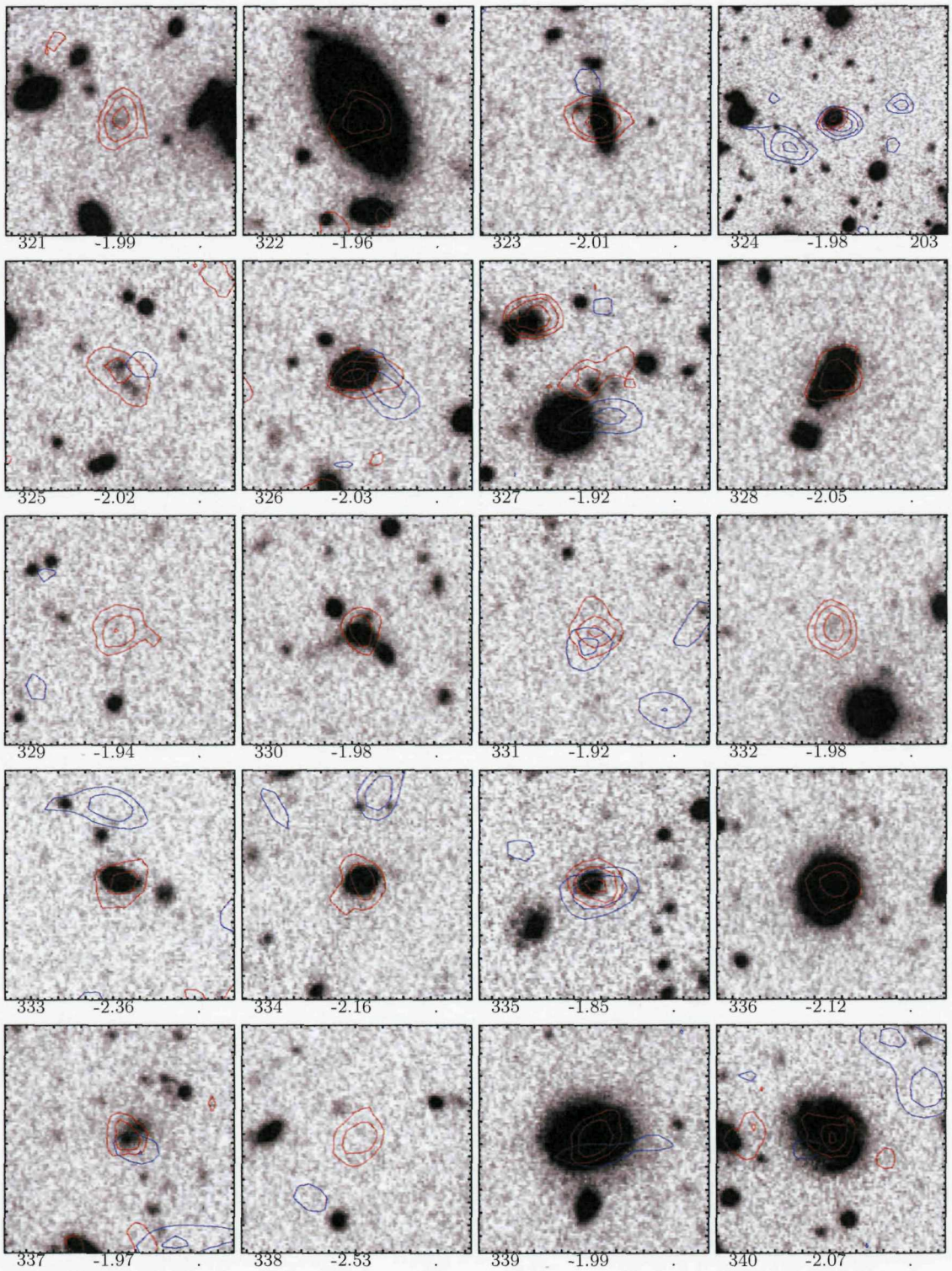
321 -1.99 .
322 -1.96 .
323 -2.01 .
324 -1.98 203
325 -2.02 .
326 -2.03 .
327 -1.92 .
328 -2.05 .
329 -1.94 .
330 -1.98 .
331 -1.92 .
332 -1.98 .
333 -2.36 .
334 -2.16 .
335 -1.85 .
336 -2.12 .
337 -1.97 .
338 -2.53 .
339 -1.99 .
340 -2.07 .

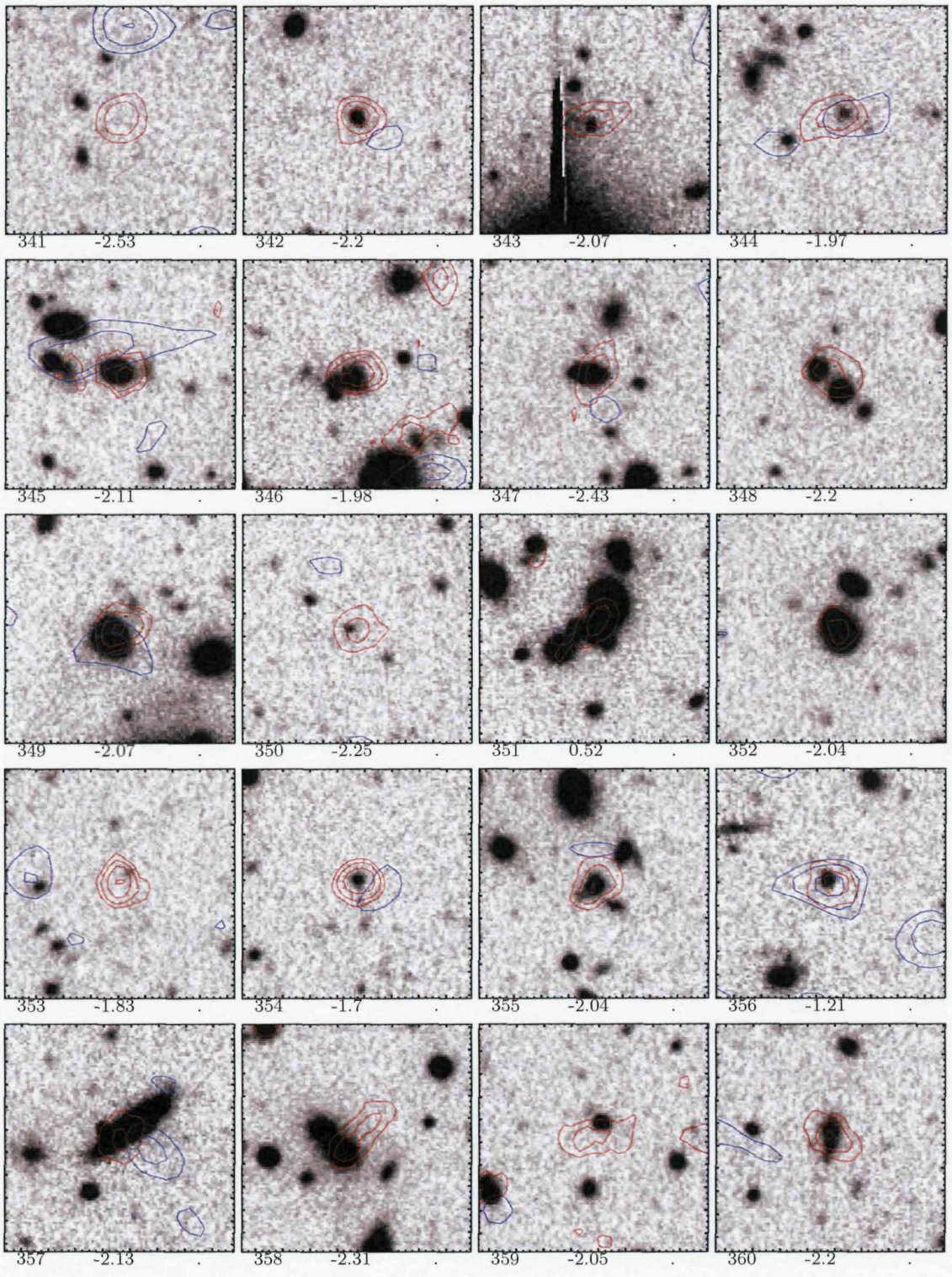
341 -2.53
342 -2.2
343 -2.07
344 -1.97
345 -2.11
346 -1.98
347 -2.43
348 -2.2
349 -2.07
350 -2.25
351 0.52
352 -2.04
353 -1.83
354 -1.7
355 -2.04
356 -1.21
357 -2.13
358 -2.31
359 -2.05
360 -2.2

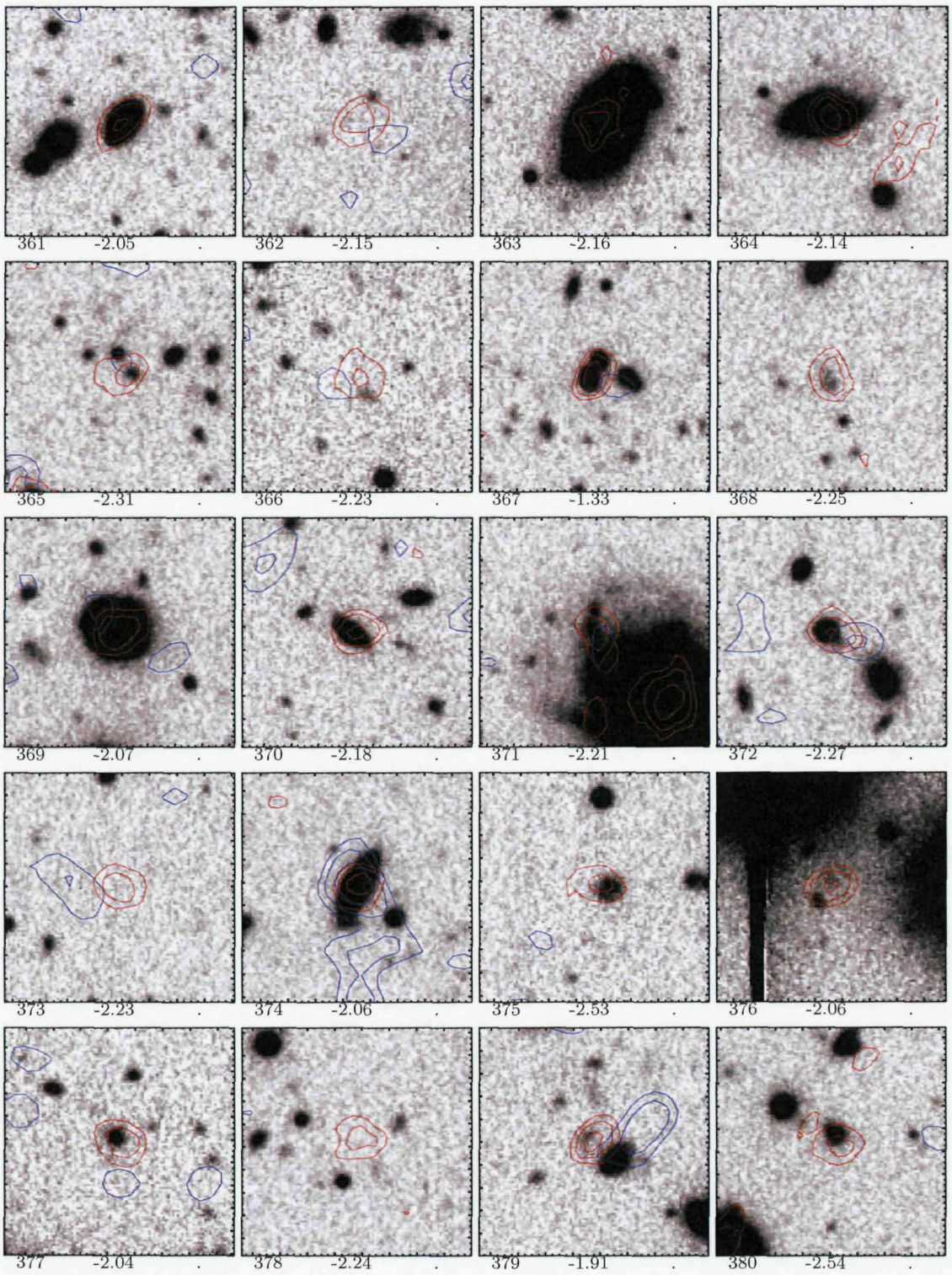
361 -2.05 .
362 -2.15 .
363 -2.16 .
364 -2.14 .
365 -2.31 .
366 -2.23 .
367 -1.33 .
368 -2.25 .
369 -2.07 .
370 -2.18 .
371 -2.21 .
372 -2.27 .
373 -2.23 .
374 -2.06 .
375 -2.53 .
376 -2.06 .
377 -2.04 .
378 -2.24 .
379 -1.91 .
380 -2.54 .

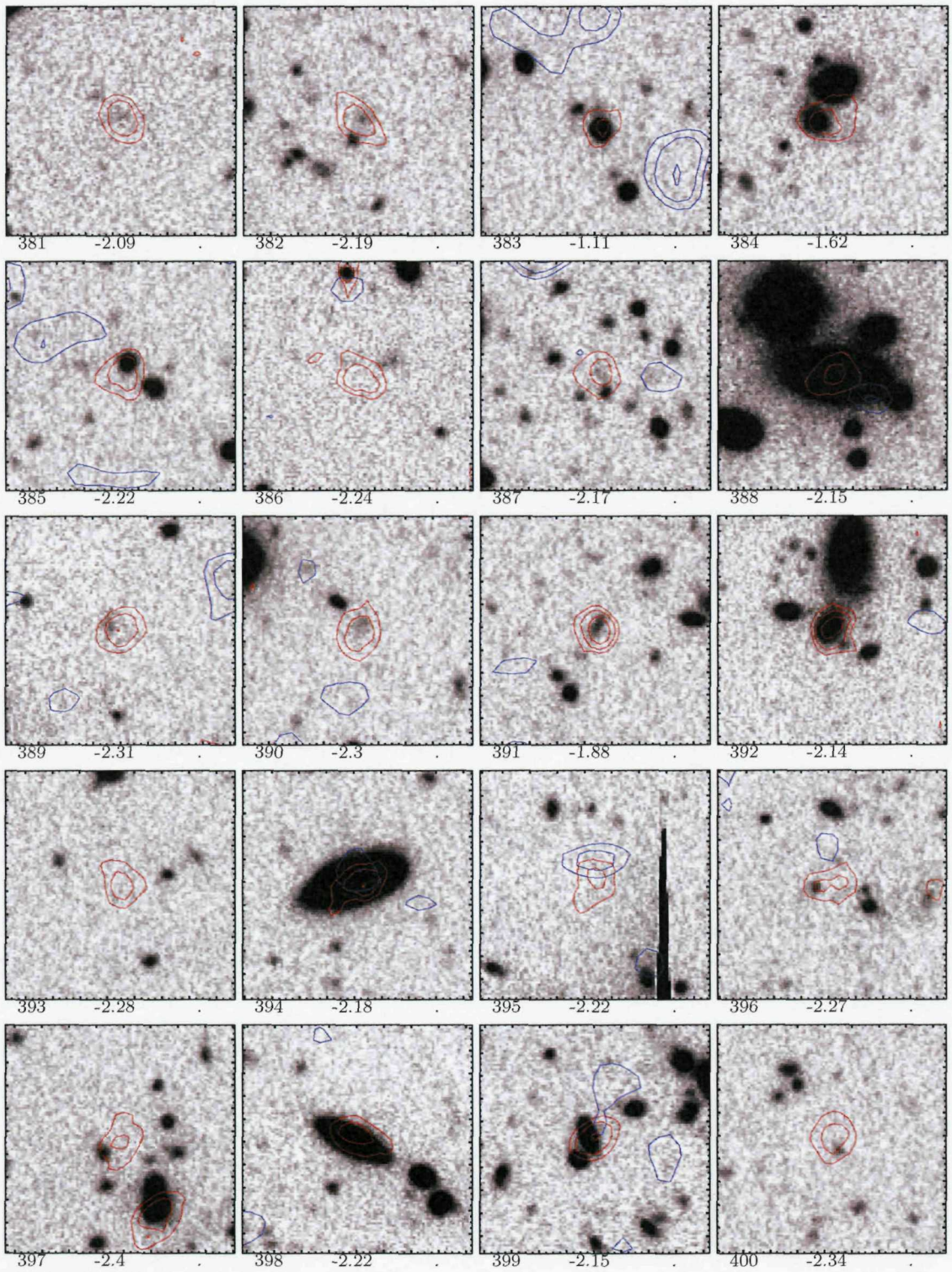
381 -2.09 .
382 -2.19 .
383 -1.11 .
384 -1.62 .
385 -2.22 .
386 -2.24 .
387 -2.17 .
388 -2.15 .
389 -2.31 .
390 -2.3 .
391 -1.88 .
392 -2.14 .
393 -2.28 .
394 -2.18 .
395 -2.22 .
396 -2.27 .
397 -2.4 .
398 -2.22 .
399 -2.15 .
400 -2.34 .

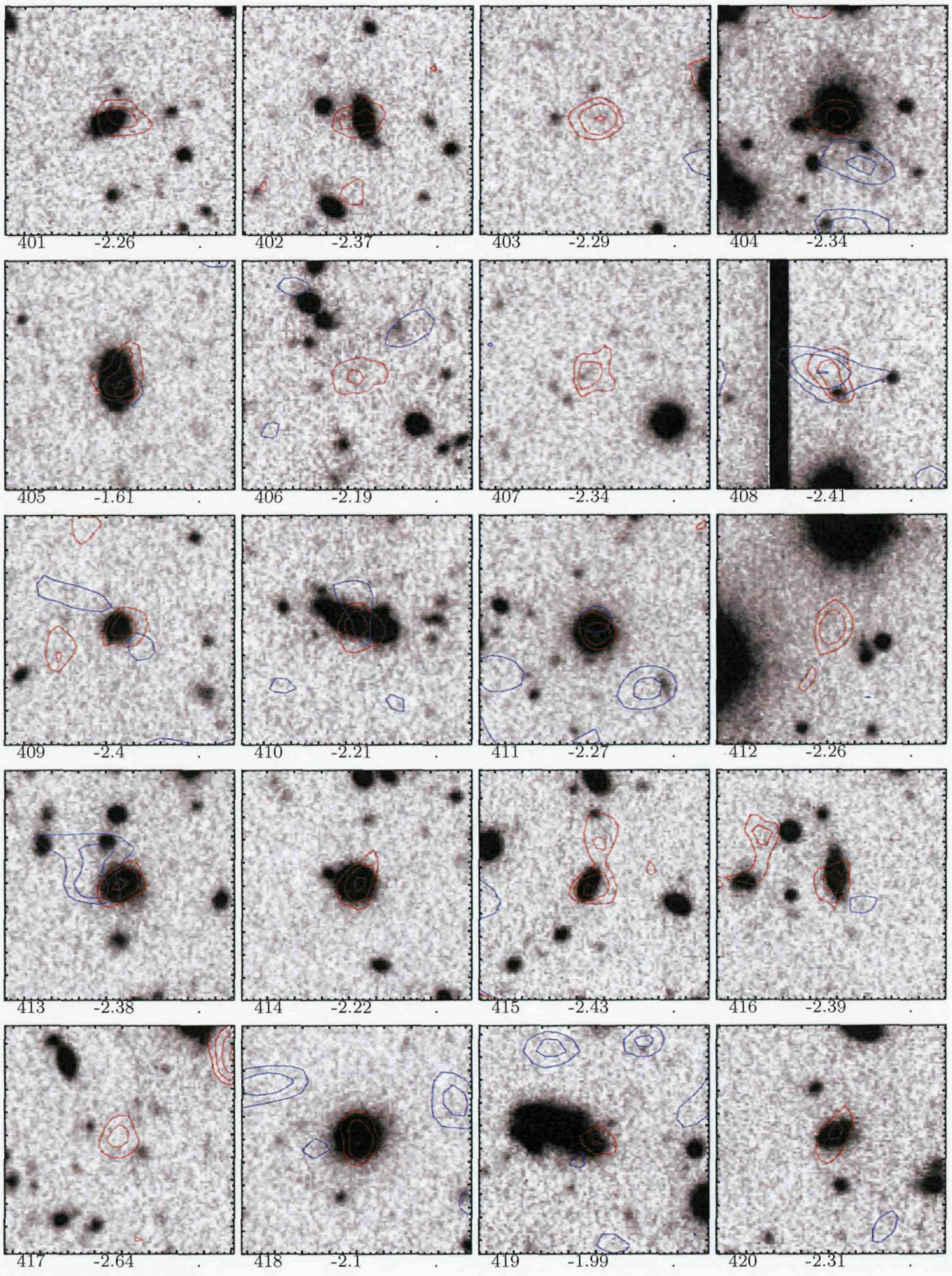
401 -2.26
402 -2.37
403 -2.29
404 -2.34
405 -1.61
406 -2.19
407 -2.34
408 -2.41
409 -2.4
410 -2.21
411 -2.27
412 -2.26
413 -2.38
414 -2.22
415 -2.43
416 -2.39
417 -2.64
418 -2.1
419 -1.99
420 -2.31

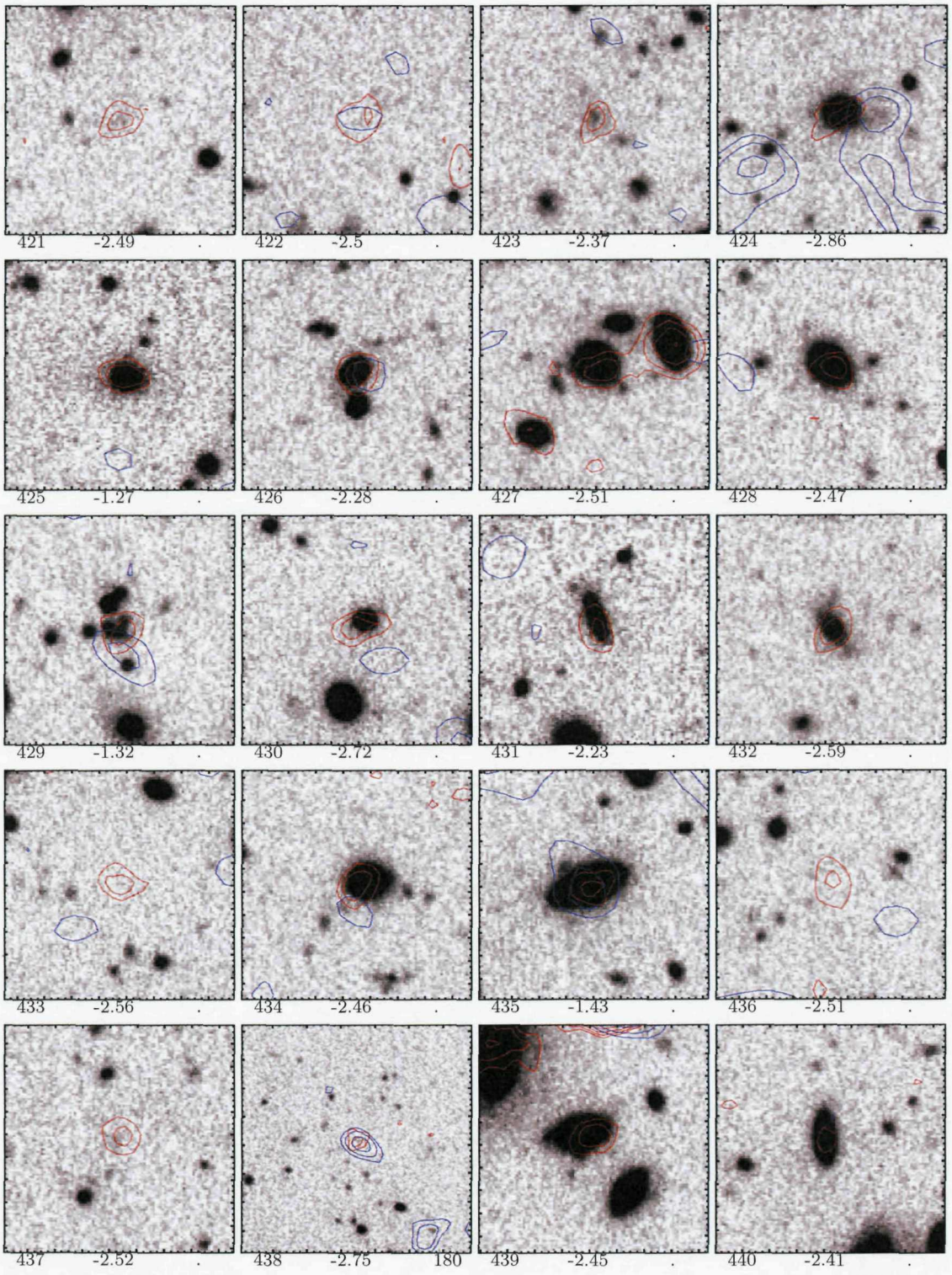
421 -2.49 .
422 -2.5 .
423 -2.37 .
424 -2.86 .
425 -1.27 .
426 -2.28 .
427 -2.51 .
428 -2.47 .
429 -1.32 .
430 -2.72 .
431 -2.23 .
432 -2.59 .
433 -2.56 .
434 -2.46 .
435 -1.43 .
436 -2.51 .
437 -2.52 .
438 -2.75 180
439 -2.45 .
440 -2.41 .

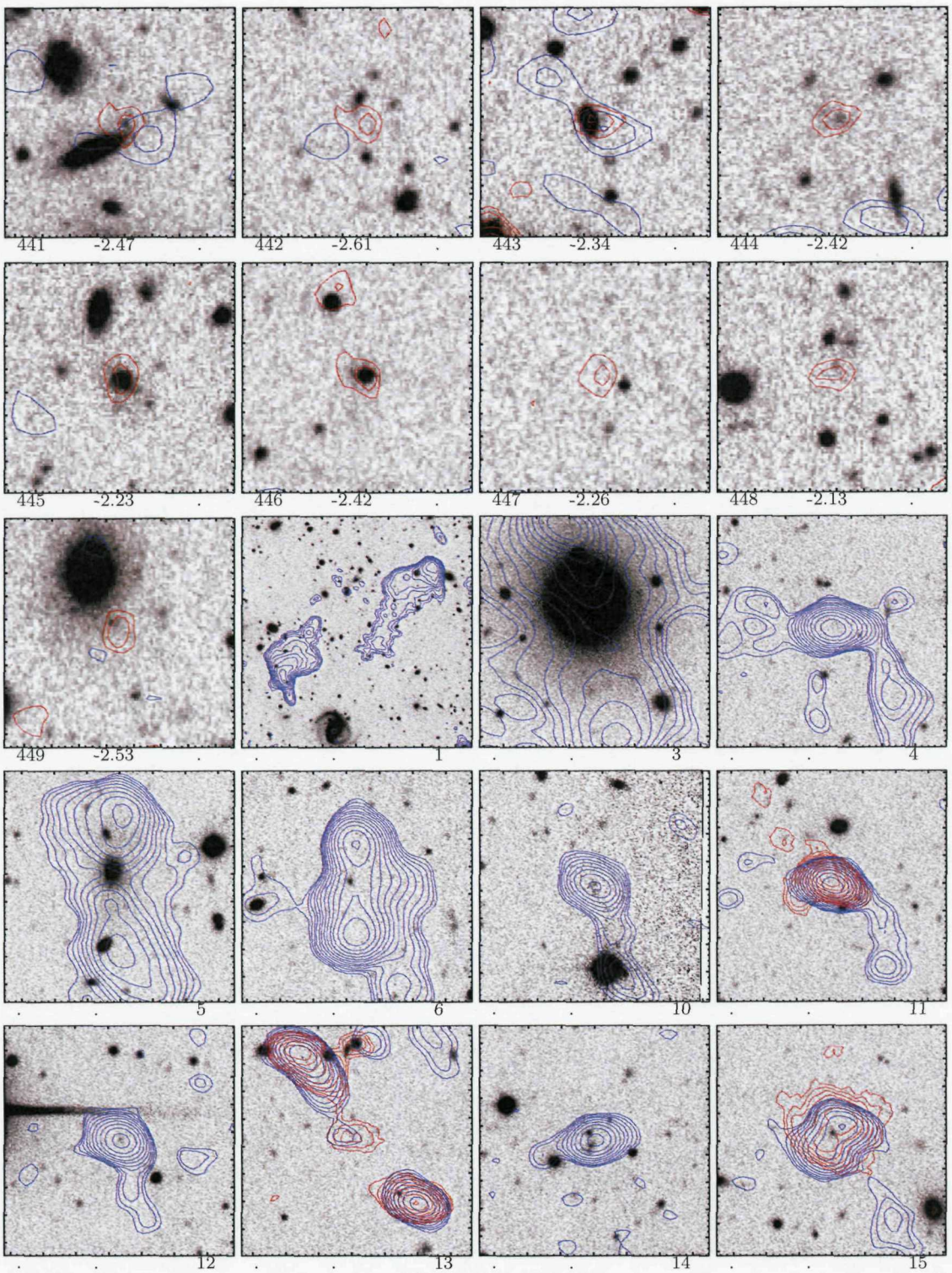
441 -2.47 .
442 -2.61 .
443 -2.34 .
444 -2.42 .
445 -2.23 .
446 -2.42 .
447 -2.26 .
448 -2.13 .
449 -2.53 .
. . 1
. . 3
. . 4
. . 5
. . 6
. . 10
. . 11
. . 12
. . 13
. . 14
. . 15

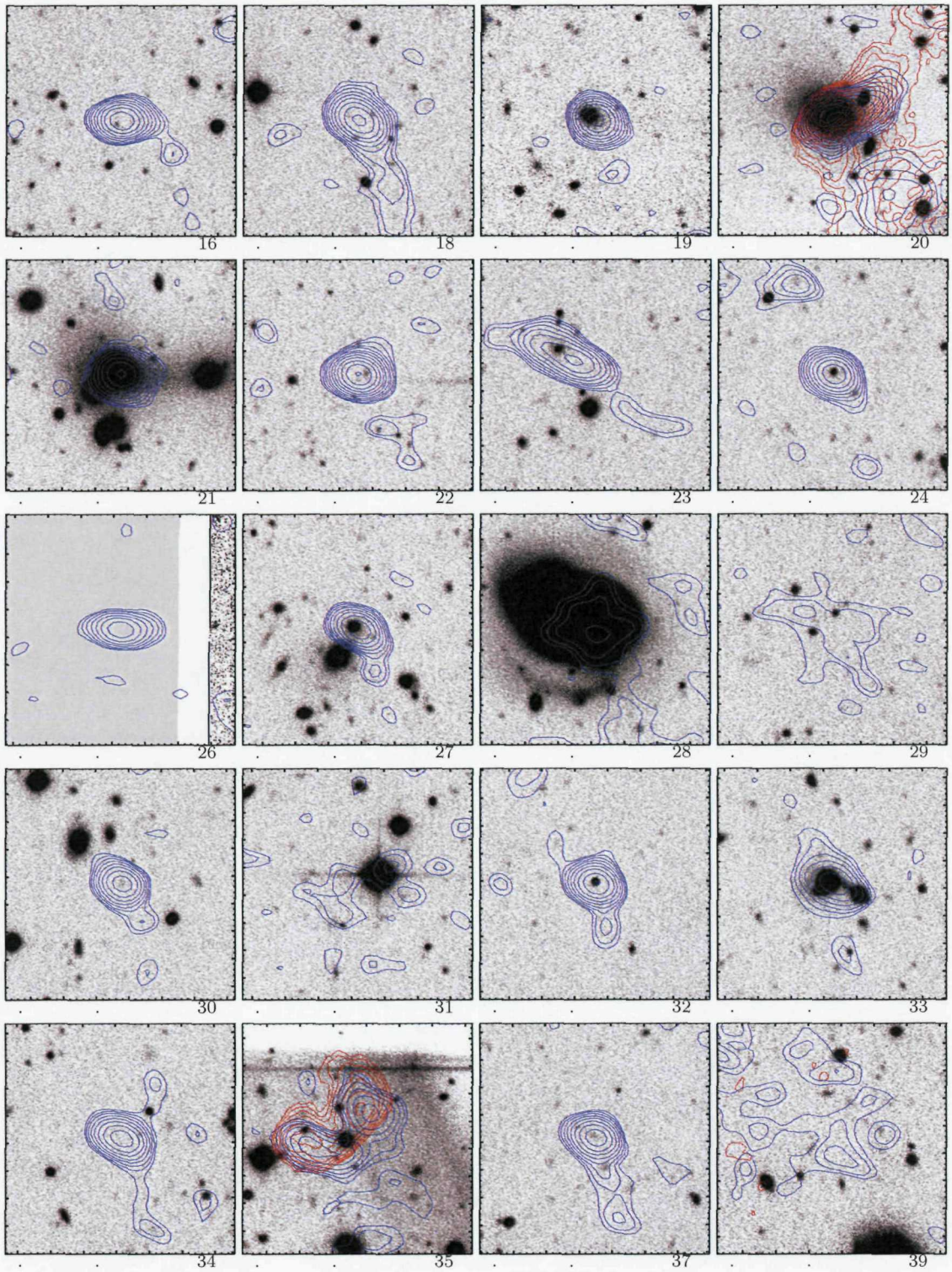
16
18
19
20
21
22
23
24
26
27
28
29
30
31
32
33
34
35
37
39

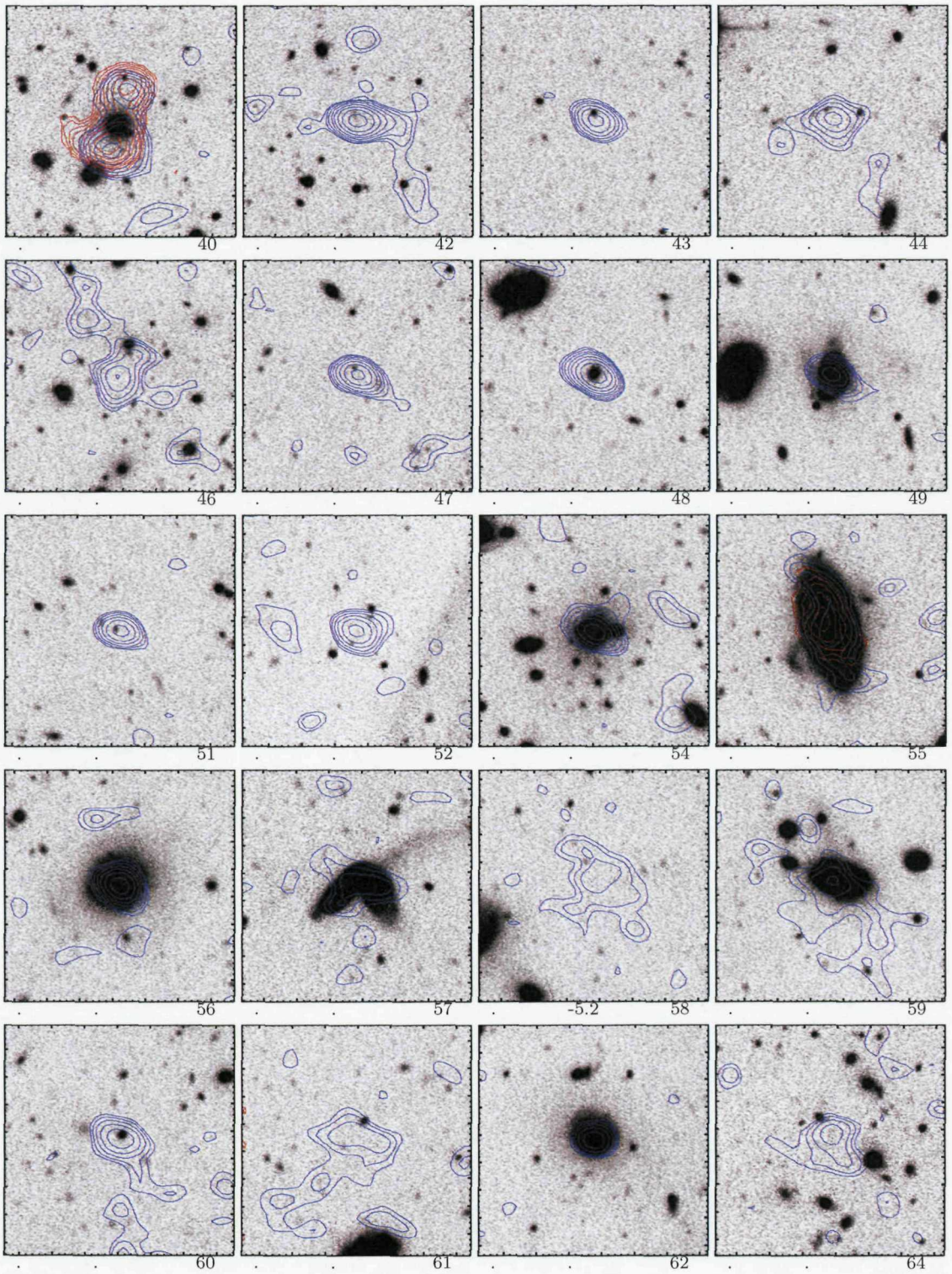
40
42
43
44
46
47
48
49
51
52
54
55
56
57
-5.2
58
59
60
61
62
64

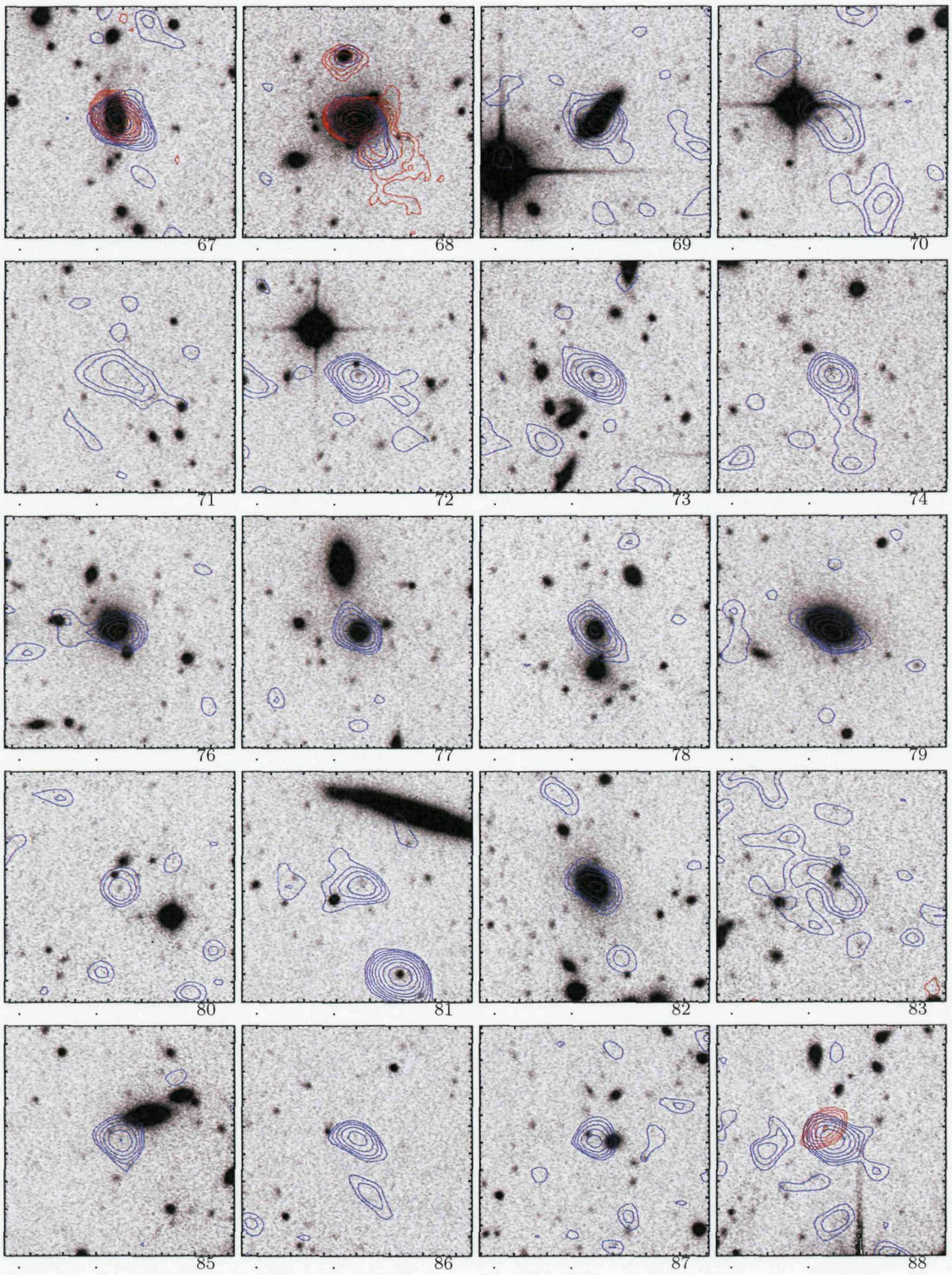
67
68
69
70
71
72
73
74
76
77
78
79
80
81
82
83
85
86
87
88

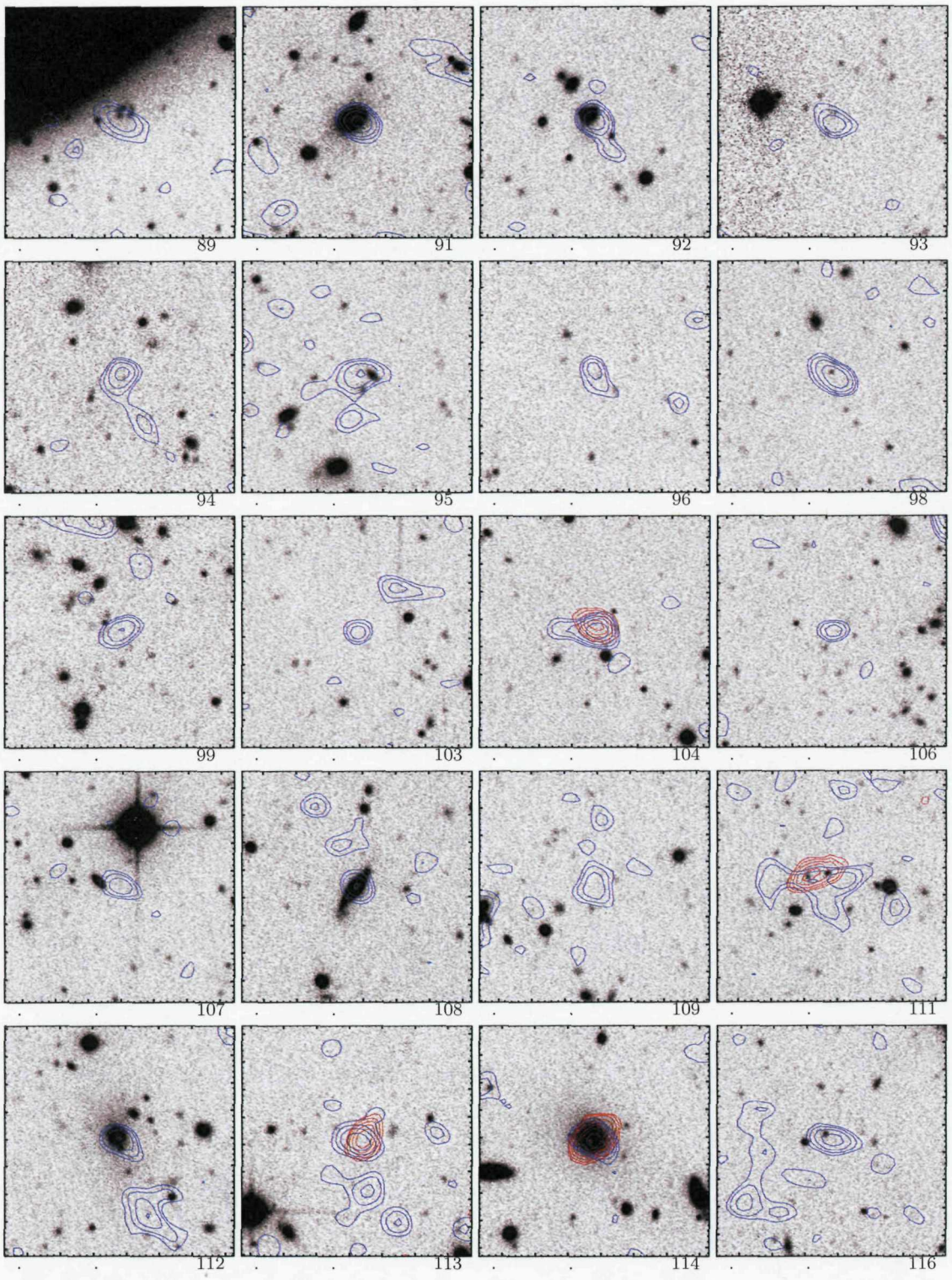
89
91
92
93
94
95
96
98
99
103
104
106
107
108
109
111
112
113
114
116

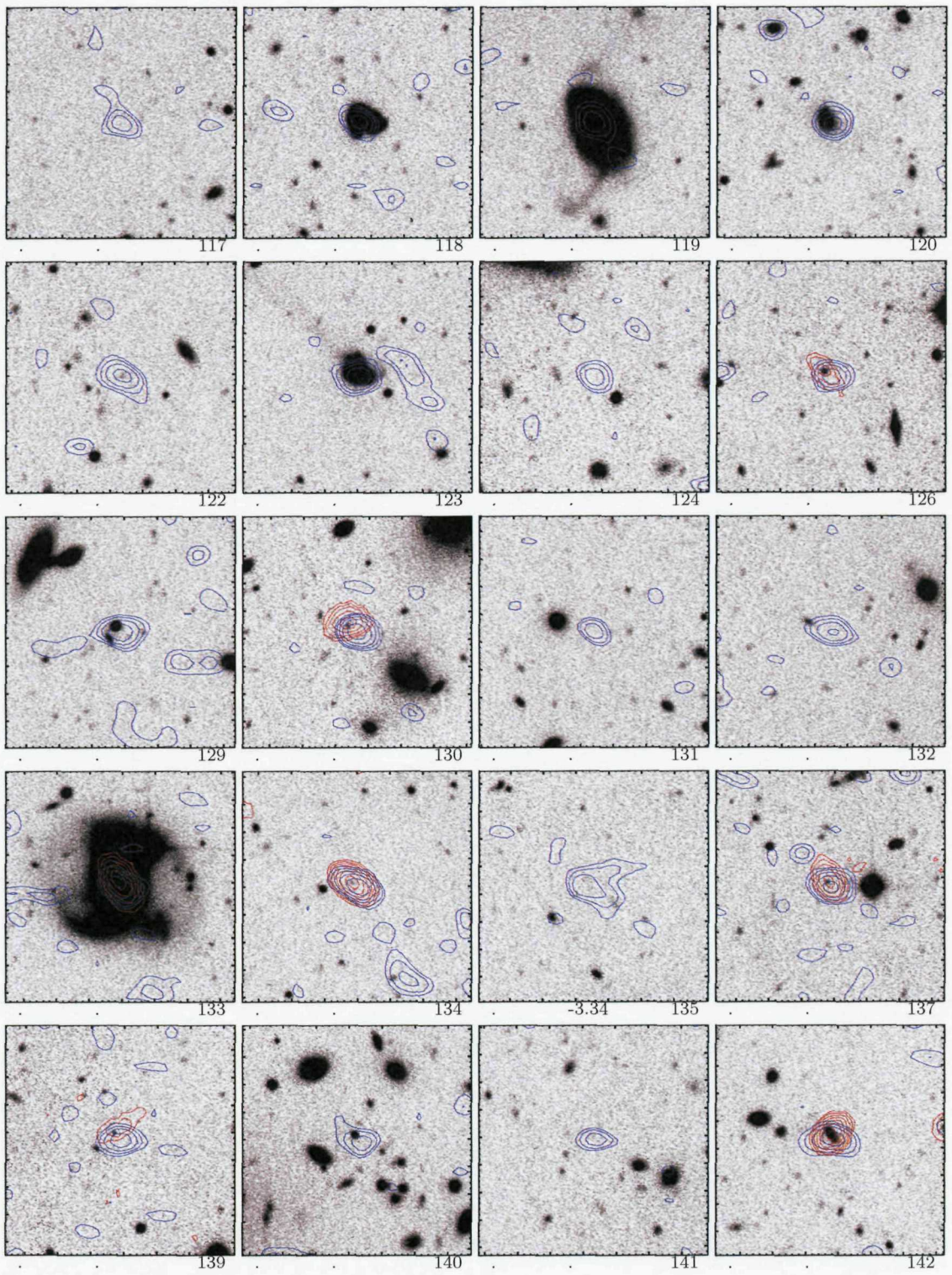
117
118
119
120
122
123
124
126
129
130
131
132
133
134
-3.34
135
137
139
140
141
142

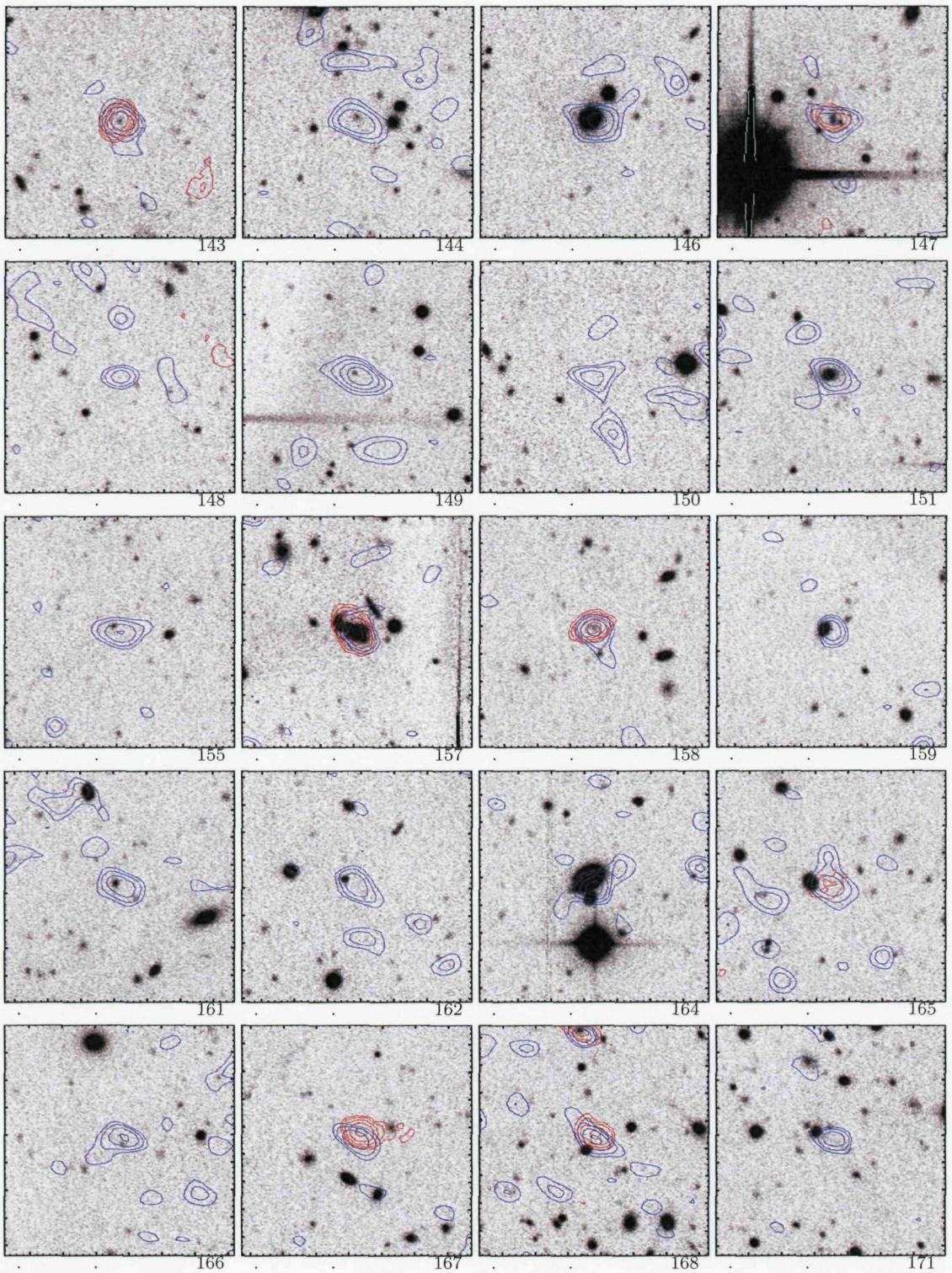
143
144
146
147
148
149
150
151
155
157
158
159
161
162
164
165
166
167
168
171

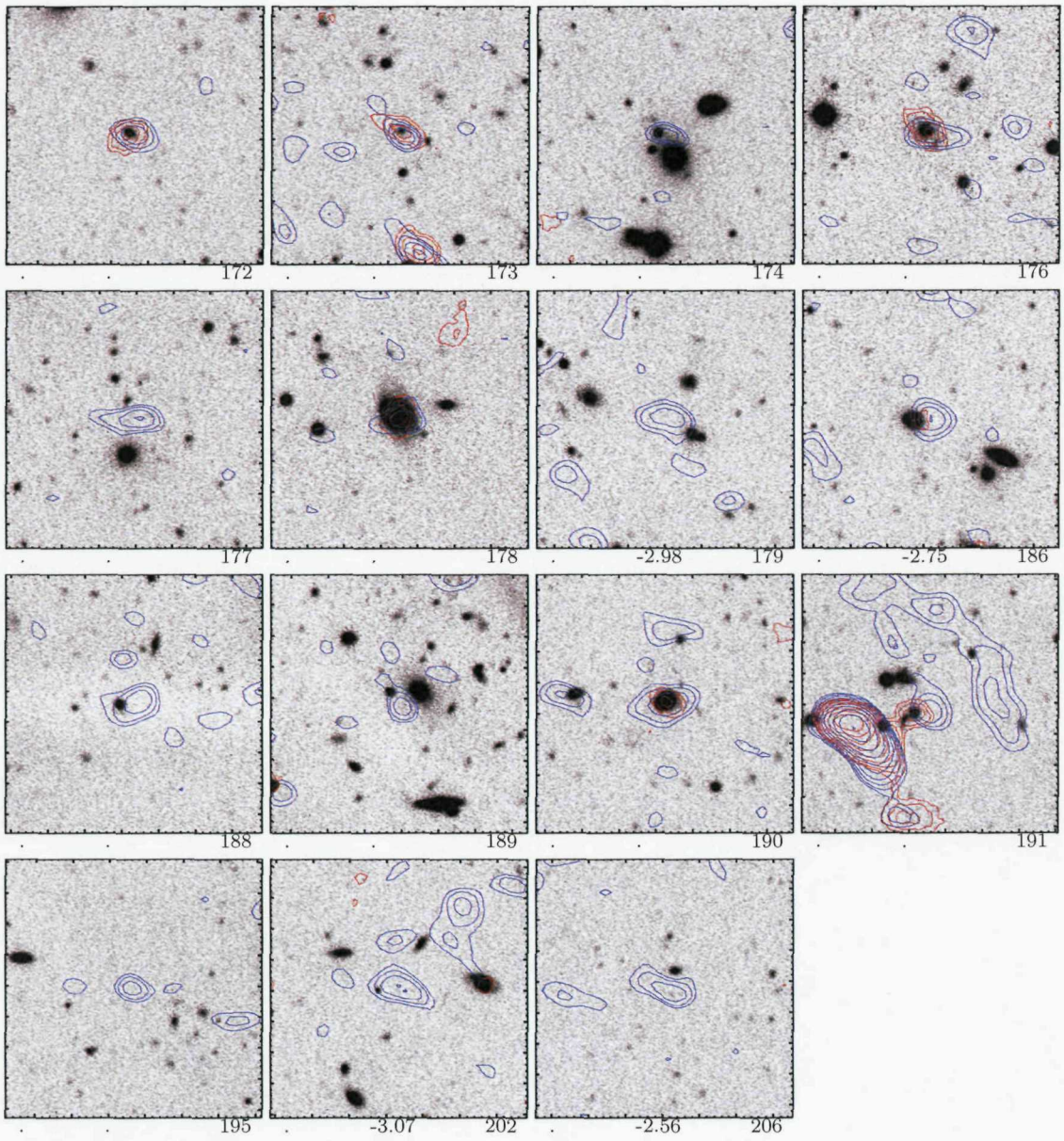
172
173
174
176
177
178
-2.98
179
-2.75
186
188
189
190
191
195
-3.07
202
-2.56
206

The following pages show contours of radio emission at both radio frequencies overlaid on the optical imaging of the 1^H field. The Subaru i' band image is used where available, and the DSS R band image outside this. The numbers below each image are: 1.4 GHz catalogue number (left); spectral index (middle); 610 MHz catalogue number (right). If no 610 MHz catalogue number is given, the spectrum given is a limit. Sources detected at only 1.4 GHz, with no formal match at 610 MHz, are shown in images of 20×20 arcsec. Any source detected at 610 MHz are shown in images with 40 arcsec on a side.

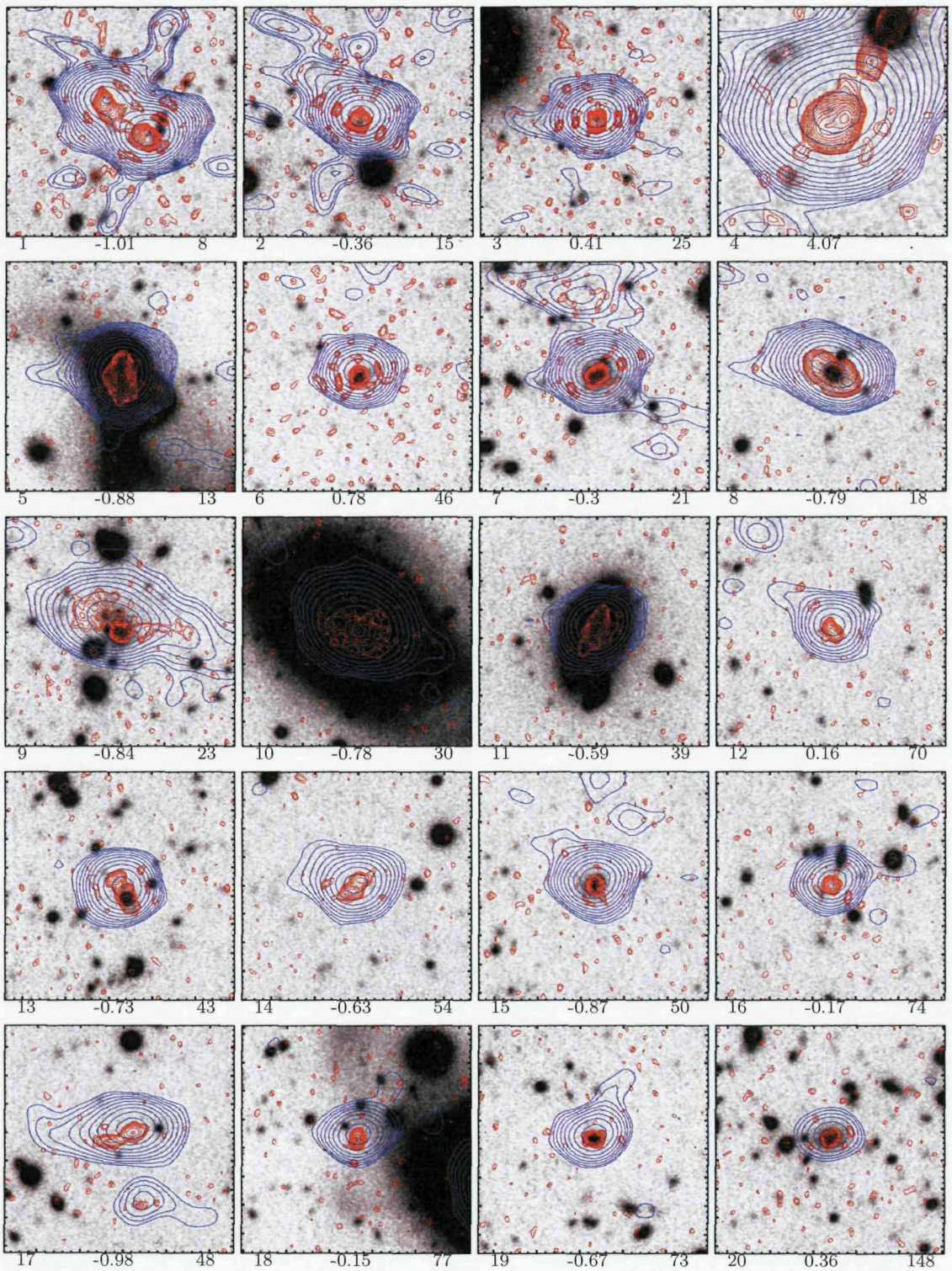
1 -1.01 8
2 -0.36 15
3 0.41 25
4 4.07
5 -0.88 13
6 0.78 46
7 -0.3 21
8 -0.79 18
9 -0.84 23
10 -0.78 30
11 -0.59 39
12 0.16 70
13 -0.73 43
14 -0.63 54
15 -0.87 50
16 -0.17 74
17 -0.98 48
18 -0.15 77
19 -0.67 73
20 0.36 148

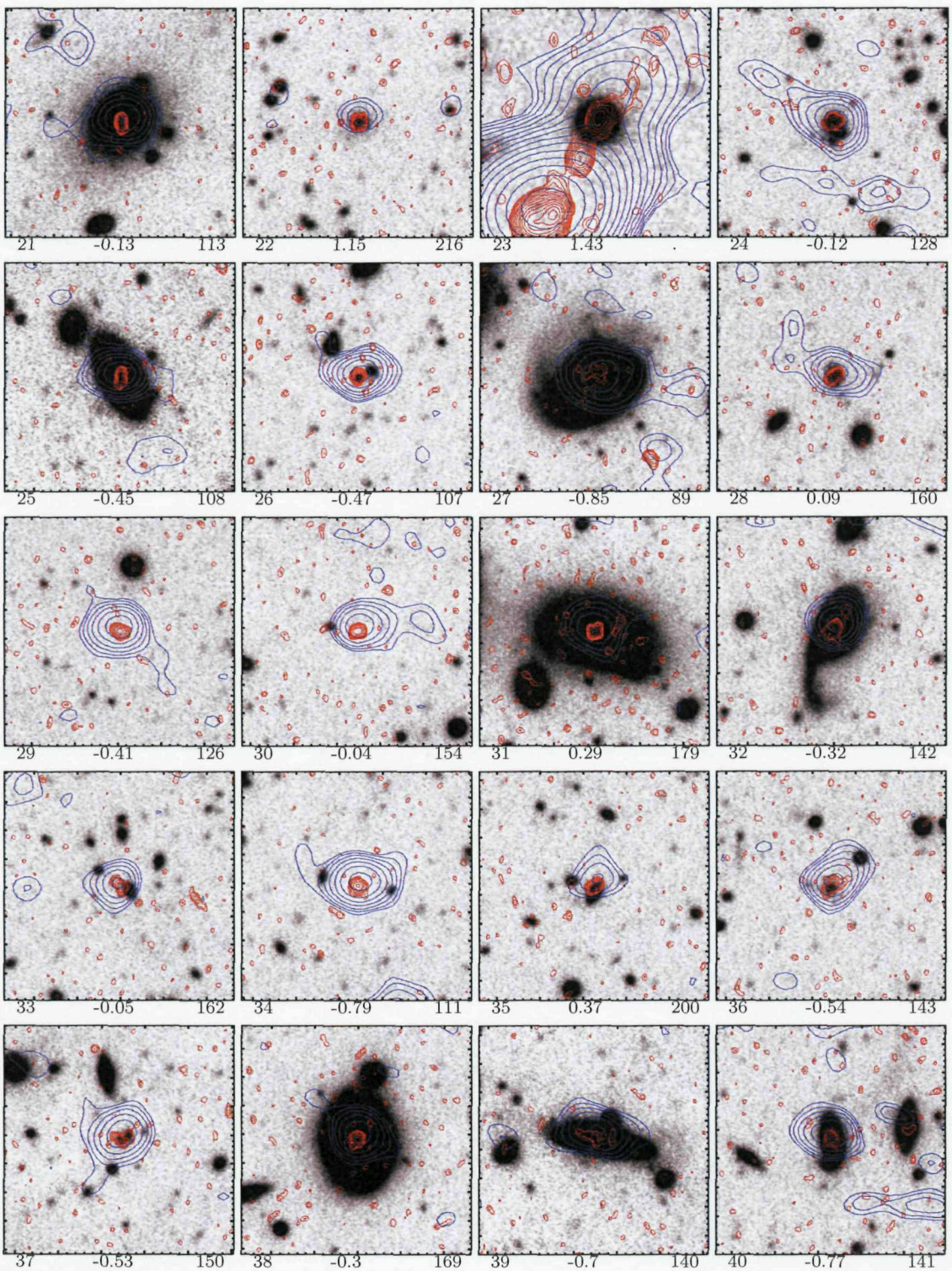
21 -0.13 113
22 1.15 216
23 1.43 .
24 -0.12 128
25 -0.45 108
26 -0.47 107
27 -0.85 89
28 0.09 160
29 -0.41 126
30 -0.04 154
31 0.29 179
32 -0.32 142
33 -0.05 162
34 -0.79 111
35 0.37 200
36 -0.54 143
37 -0.53 150
38 -0.3 169
39 -0.7 140
40 -0.77 141

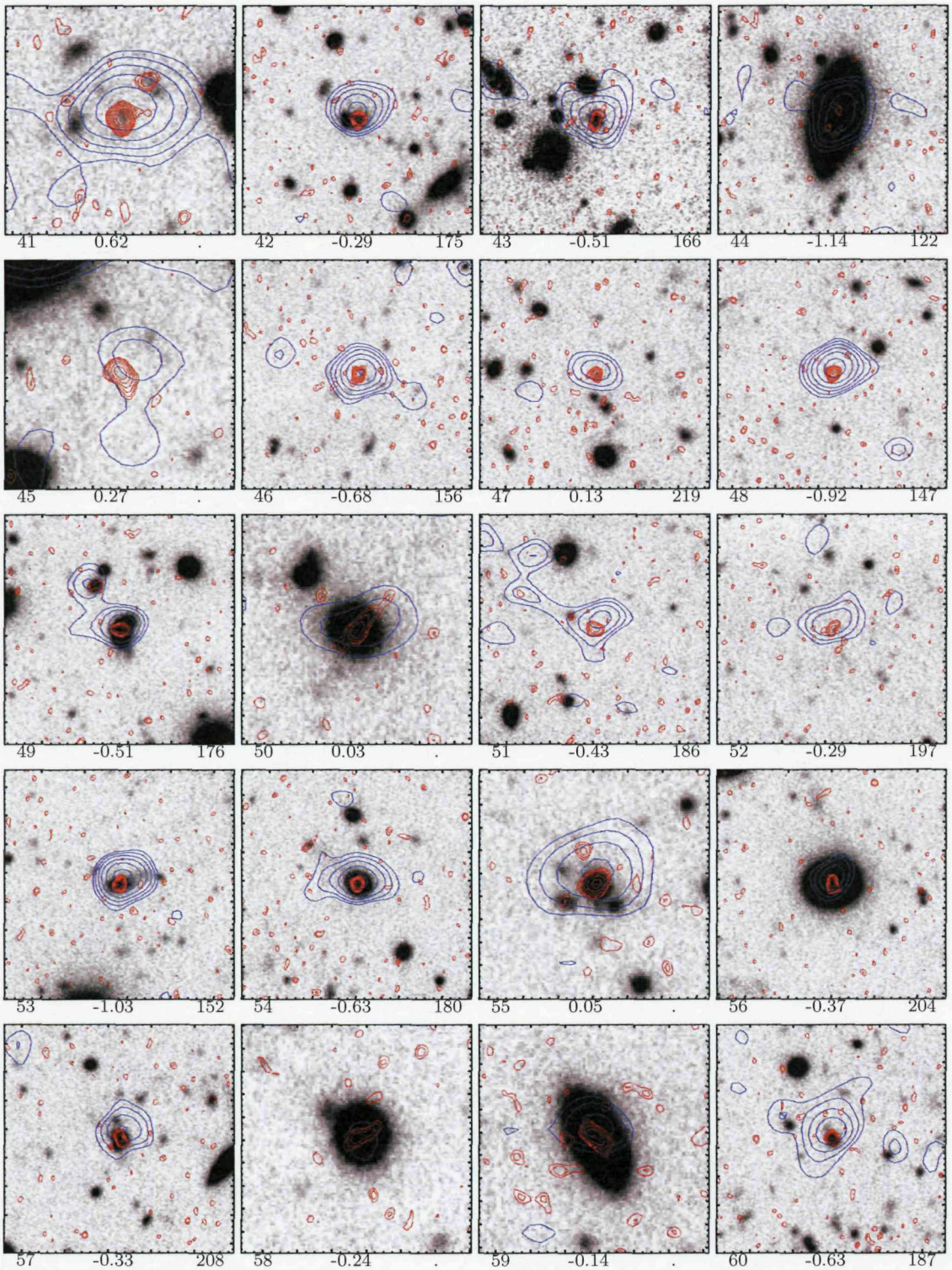
41 0.62 .
42 -0.29 175
43 -0.51 166
44 -1.14 122
45 0.27 .
46 -0.68 156
47 0.13 219
48 -0.92 147
49 -0.51 176
50 0.03 .
51 -0.43 186
52 -0.29 197
53 -1.03 152
54 -0.63 180
55 0.05 .
56 -0.37 204
57 -0.33 208
58 -0.24 .
59 -0.14 .
60 -0.63 187

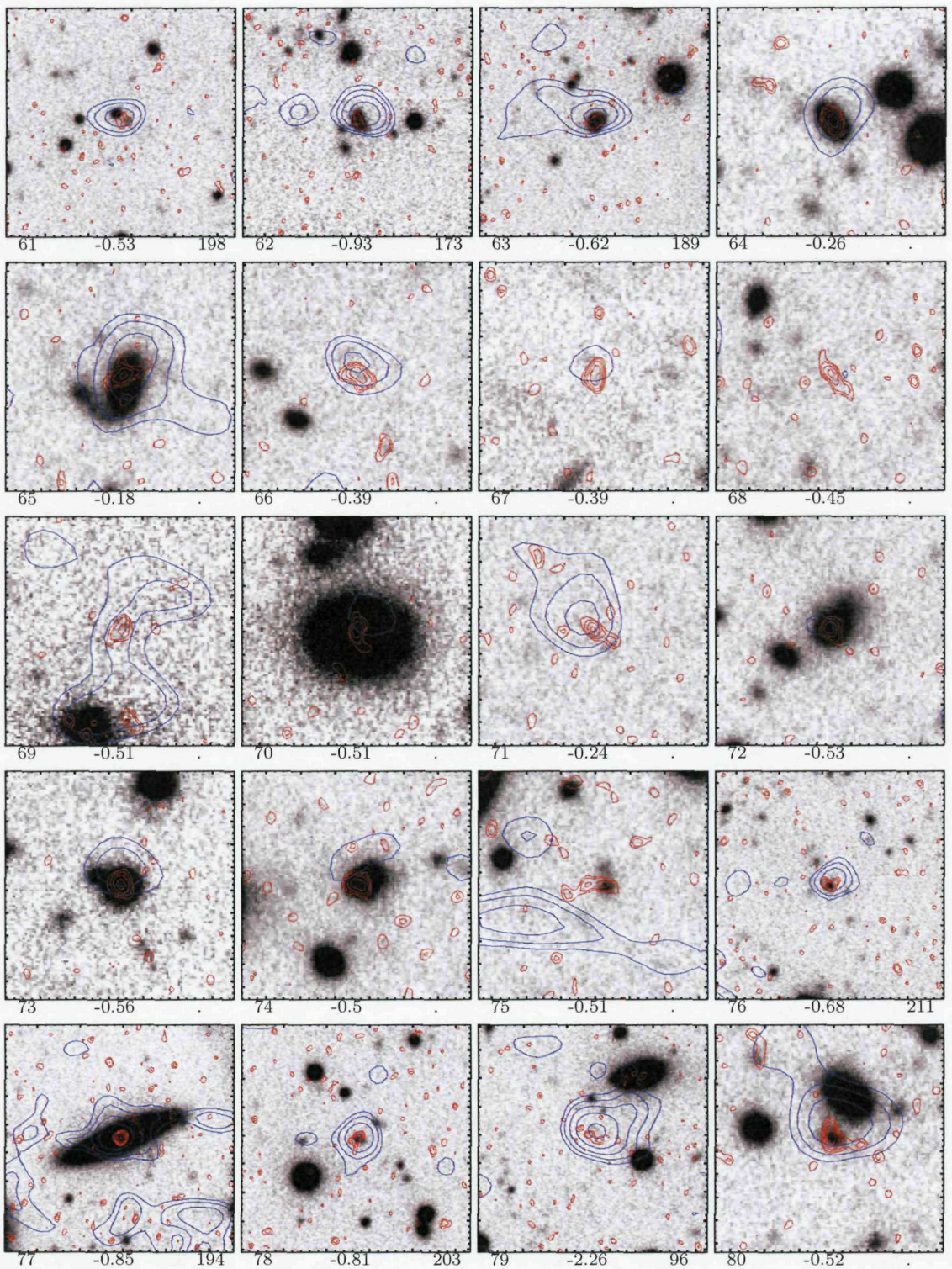
61 -0.53 198
62 -0.93 173
63 -0.62 189
64 -0.26 .
65 -0.18 .
66 -0.39 .
67 -0.39 .
68 -0.45 .
69 -0.51 .
70 -0.51 .
71 -0.24 .
72 -0.53 .
73 -0.56 .
74 -0.5 .
75 -0.51 .
76 -0.68 211
77 -0.85 194
78 -0.81 203
79 -2.26 96
80 -0.52 .

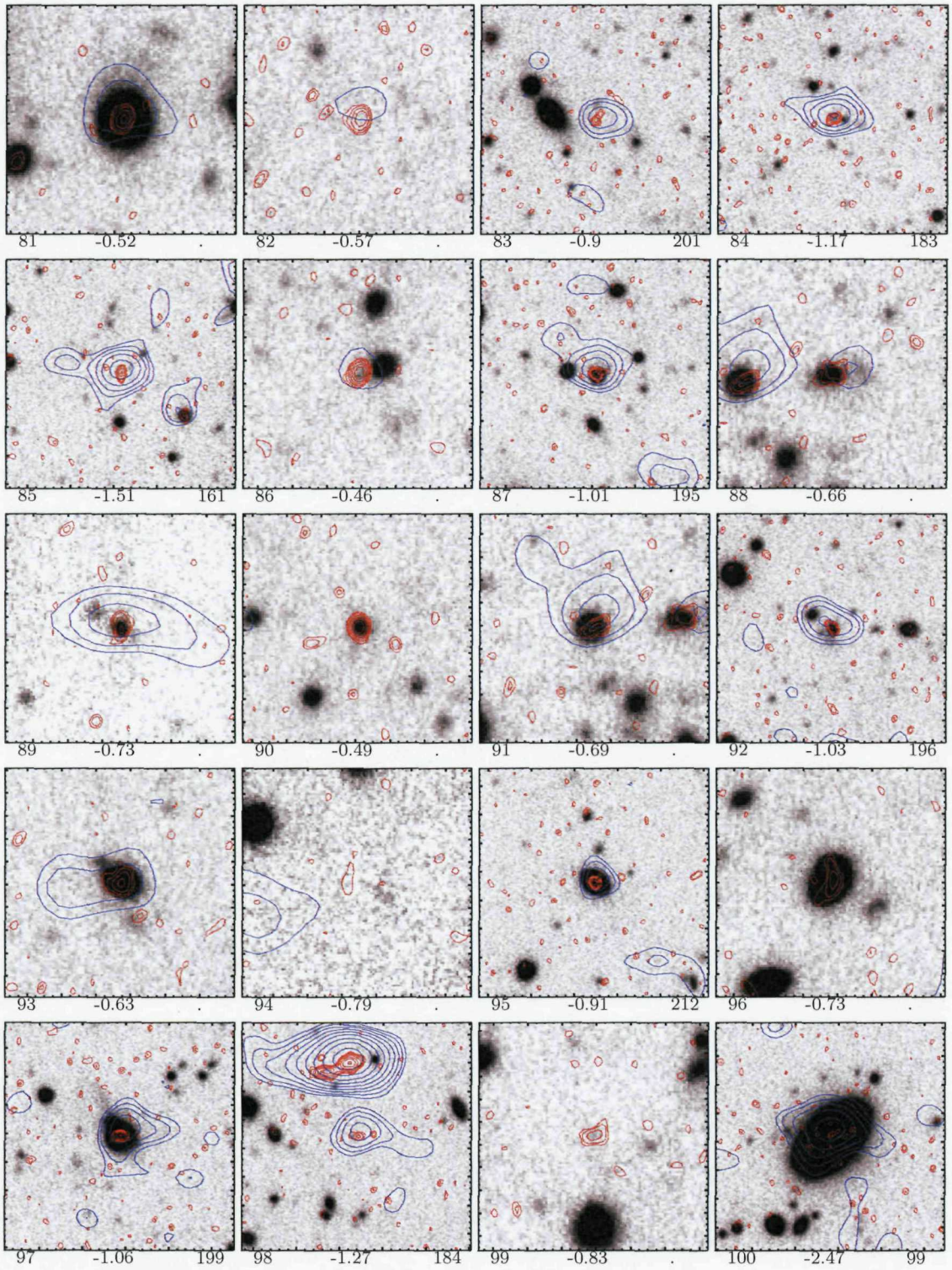
81 -0.52 .
82 -0.57 .
83 -0.9 201
84 -1.17 183
85 -1.51 161
86 -0.46 .
87 -1.01 195
88 -0.66 .
89 -0.73 .
90 -0.49 .
91 -0.69 .
92 -1.03 196
93 -0.63 .
94 -0.79 .
95 -0.91 212
96 -0.73 .
97 -1.06 199
98 -1.27 184
99 -0.83 .
100 -2.47 99

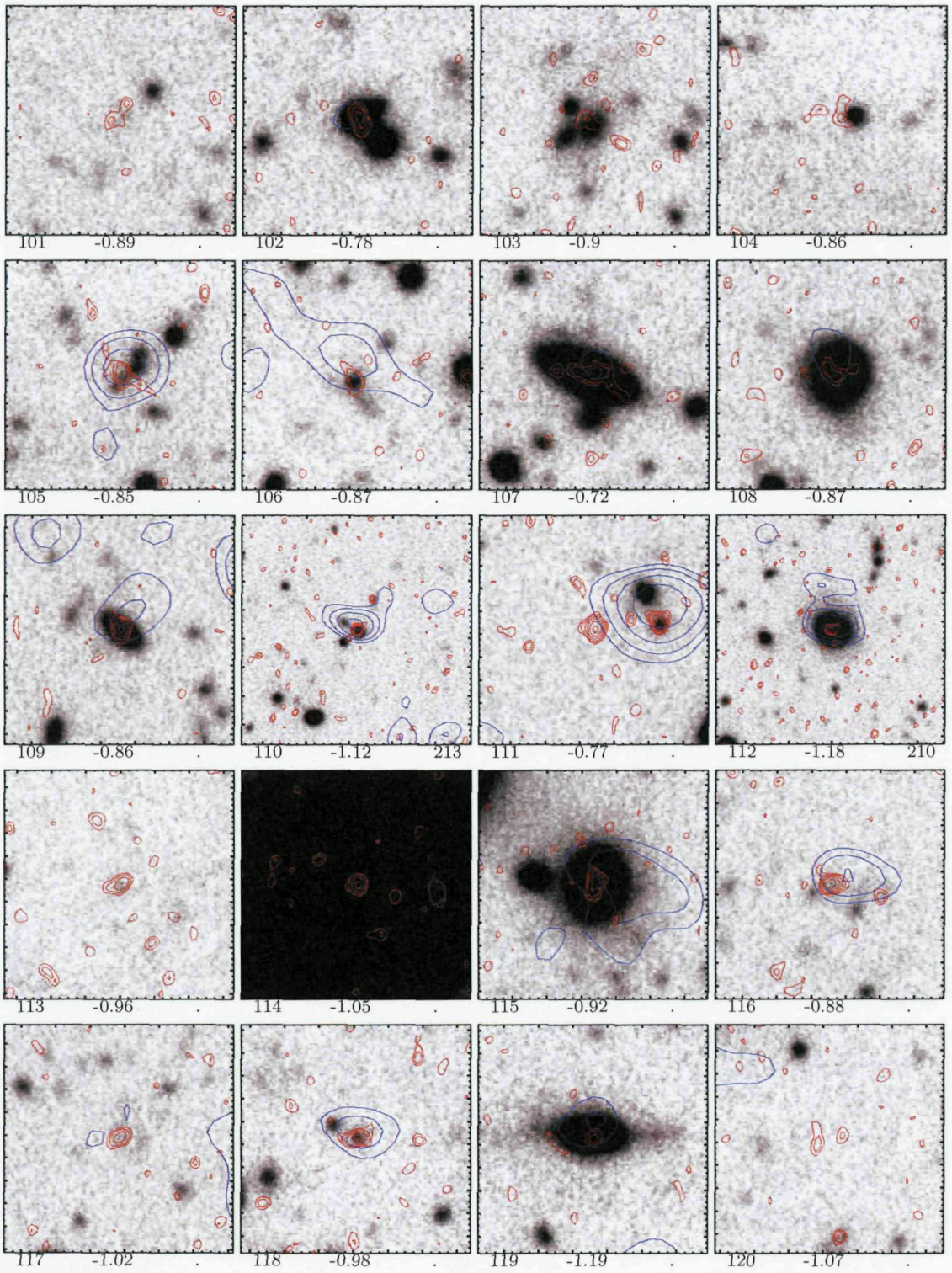
101 -0.89 .
102 -0.78 .
103 -0.9 .
104 -0.86 .
105 -0.85 .
106 -0.87 .
107 -0.72 .
108 -0.87 .
109 -0.86 .
110 -1.12 213
111 -0.77 .
112 -1.18 210
113 -0.96 .
114 -1.05 .
115 -0.92 .
116 -0.88 .
117 -1.02 .
118 -0.98 .
119 -1.19 .
120 -1.07 .

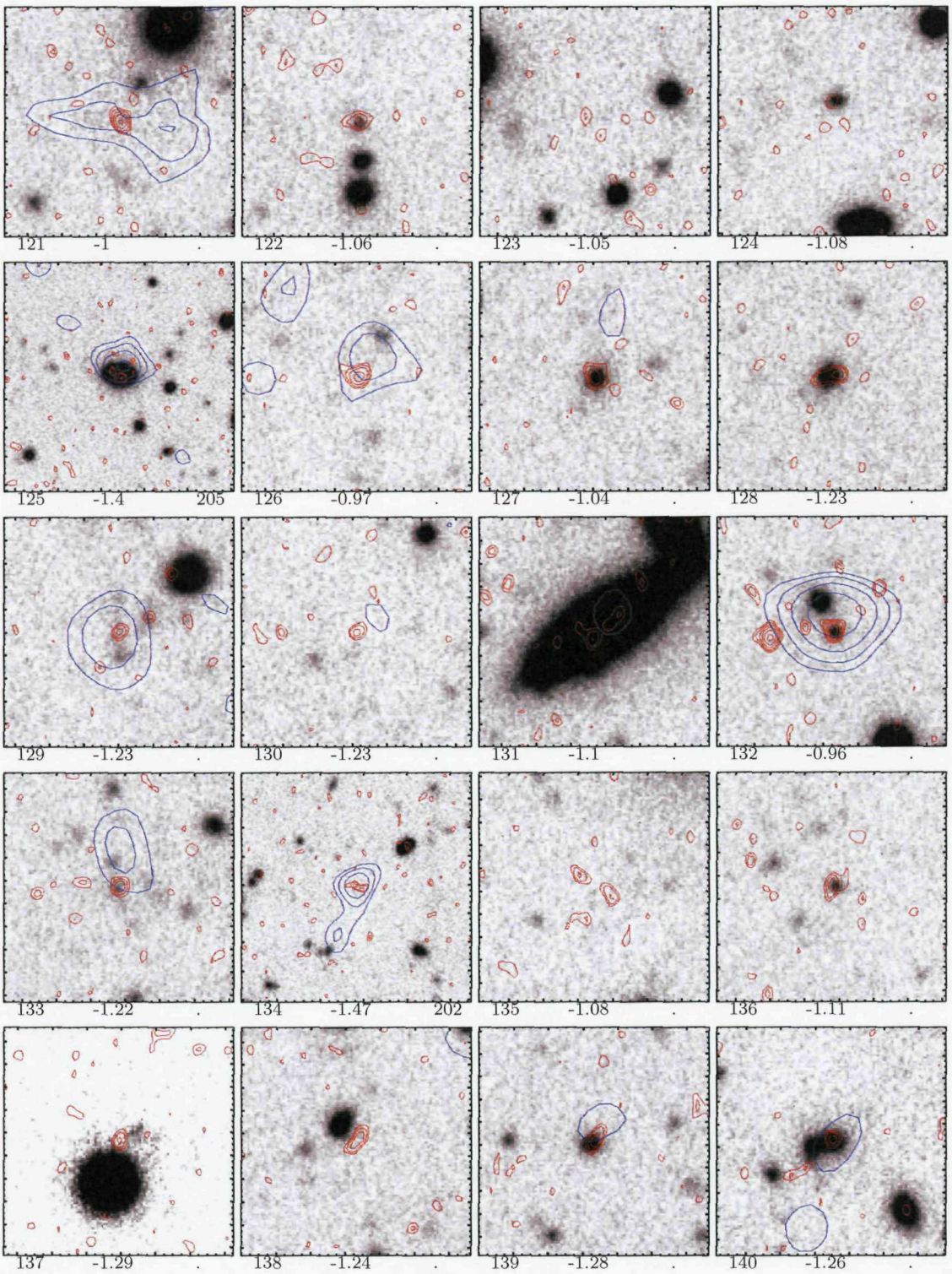
121 -1 .
122 -1.06 .
123 -1.05 .
124 -1.08 .
125 -1.4 205
126 -0.97 .
127 -1.04 .
128 -1.23 .
129 -1.23 .
130 -1.23 .
131 -1.1 .
132 -0.96 .
133 -1.22 .
134 -1.47 202
135 -1.08 .
136 -1.11 .
137 -1.29 .
138 -1.24 .
139 -1.28 .
140 -1.26 .

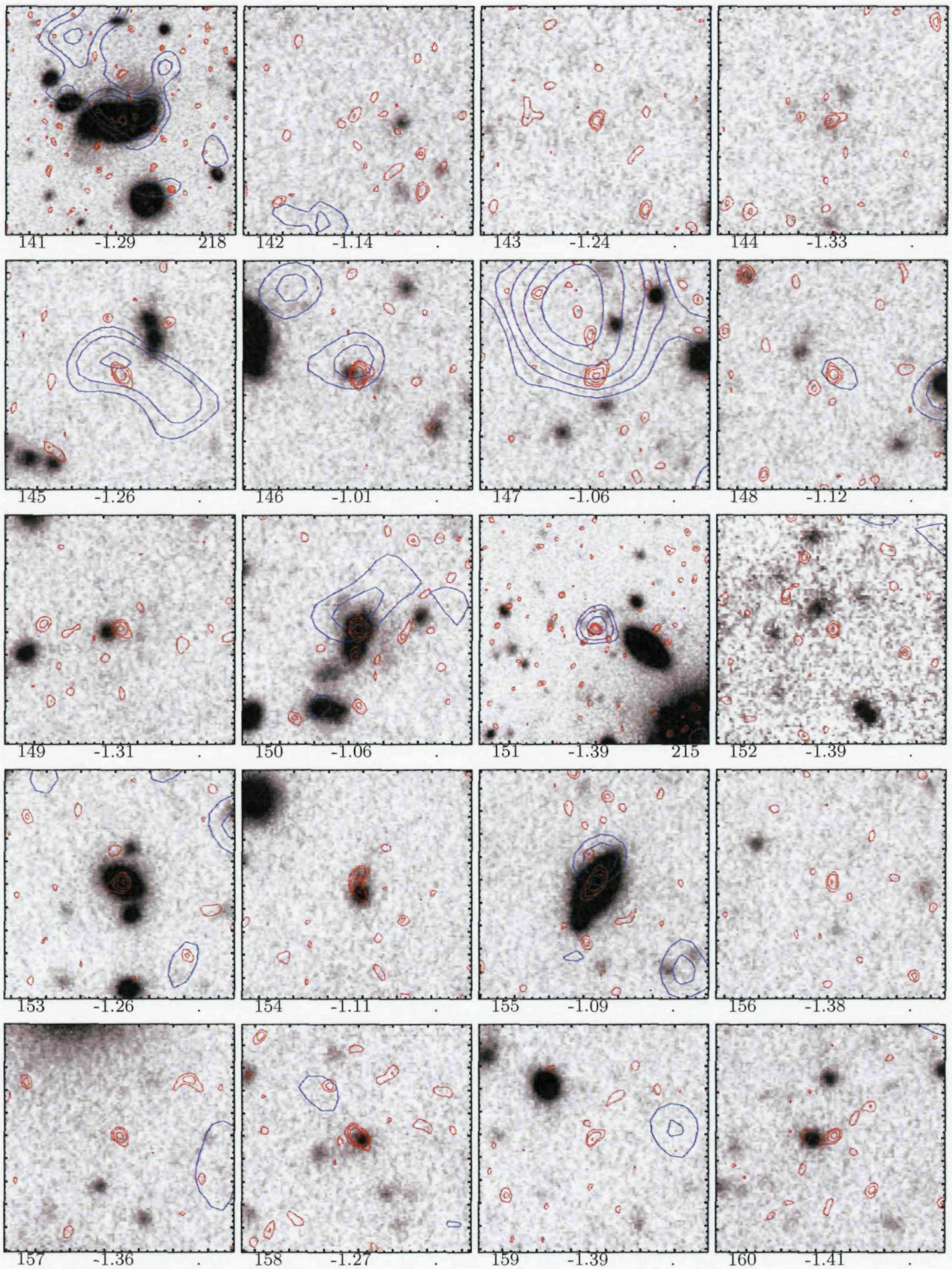
141 -1.29 218
142 -1.14 .
143 -1.24 .
144 -1.33 .
145 -1.26 .
146 -1.01 .
147 -1.06 .
148 -1.12 .
149 -1.31 .
150 -1.06 .
151 -1.39 215
152 -1.39 .
153 -1.26 .
154 -1.11 .
155 -1.09 .
156 -1.38 .
157 -1.36 .
158 -1.27 .
159 -1.39 .
160 -1.41 .

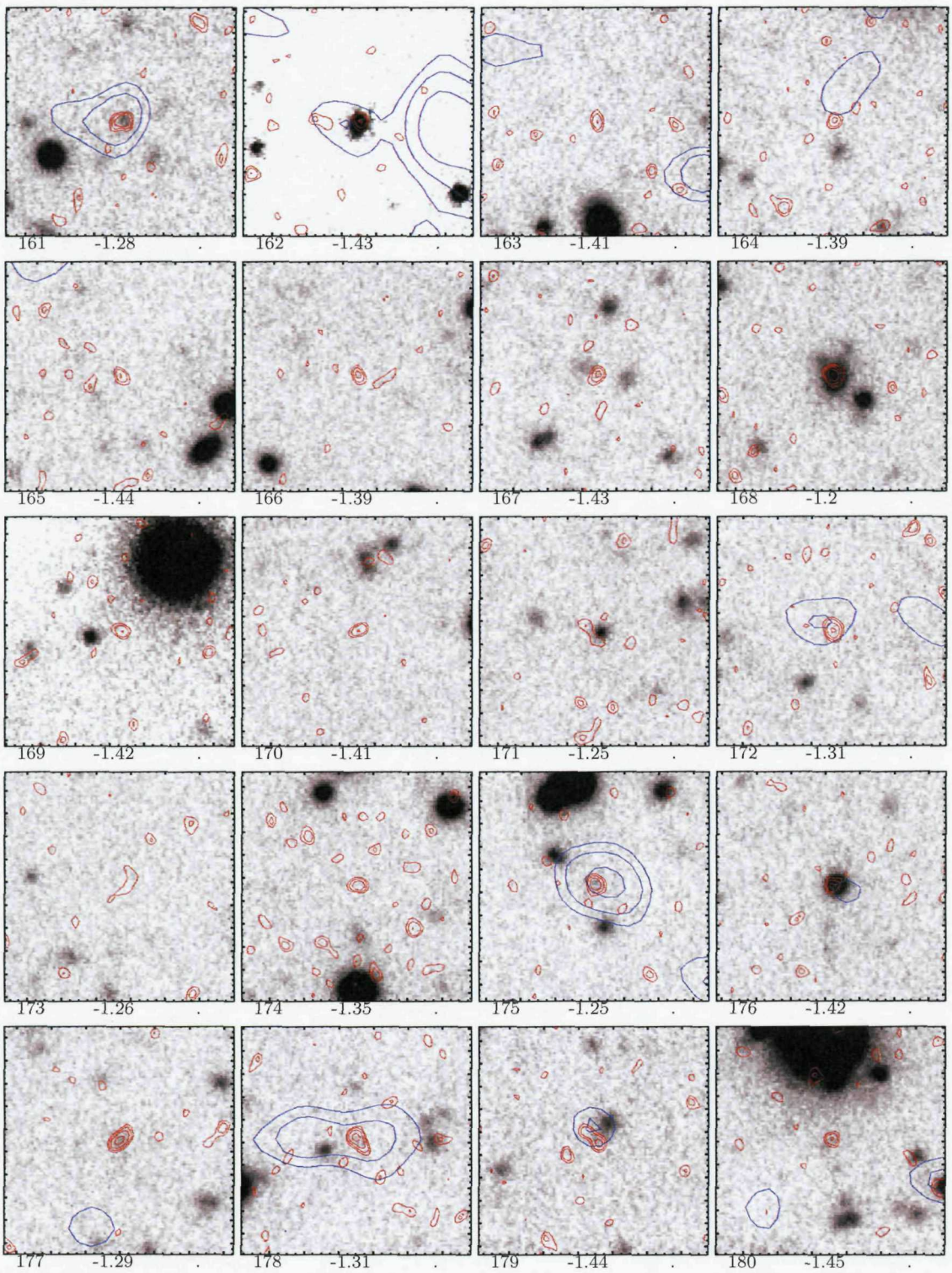
161 -1.28 .
162 -1.43 .
163 -1.41 .
164 -1.39 .
165 -1.44 .
166 -1.39 .
167 -1.43 .
168 -1.2 .
169 -1.42 .
170 -1.41 .
171 -1.25 .
172 -1.31 .
173 -1.26 .
174 -1.35 .
175 -1.25 .
176 -1.42 .
177 -1.29 .
178 -1.31 .
179 -1.44 .
180 -1.45 .

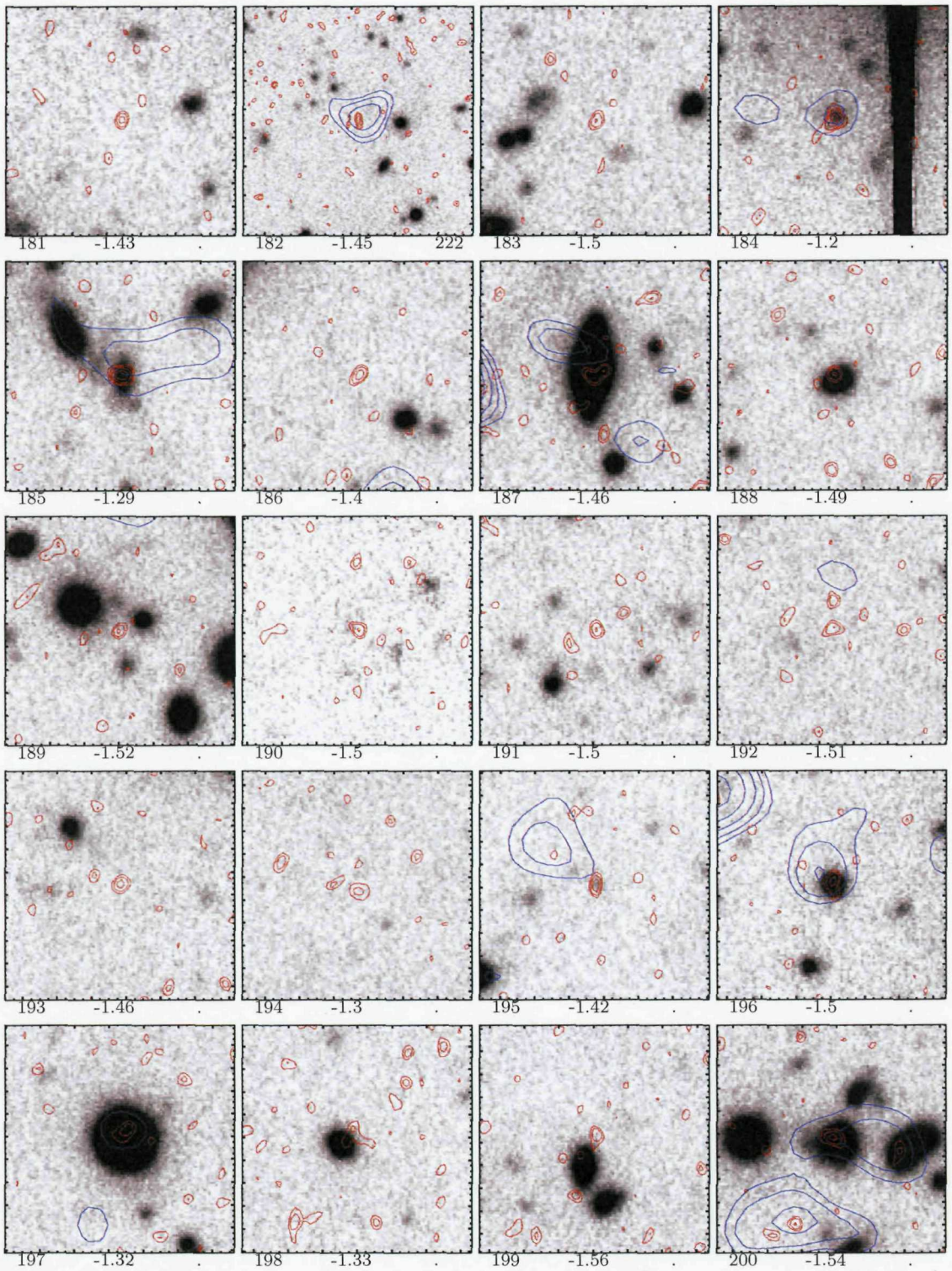
181 -1.43 .
182 -1.45 222
183 -1.5 .
184 -1.2 .
185 -1.29 .
186 -1.4 .
187 -1.46 .
188 -1.49 .
189 -1.52 .
190 -1.5 .
191 -1.5 .
192 -1.51 .
193 -1.46 .
194 -1.3 .
195 -1.42 .
196 -1.5 .
197 -1.32 .
198 -1.33 .
199 -1.56 .
200 -1.54 .

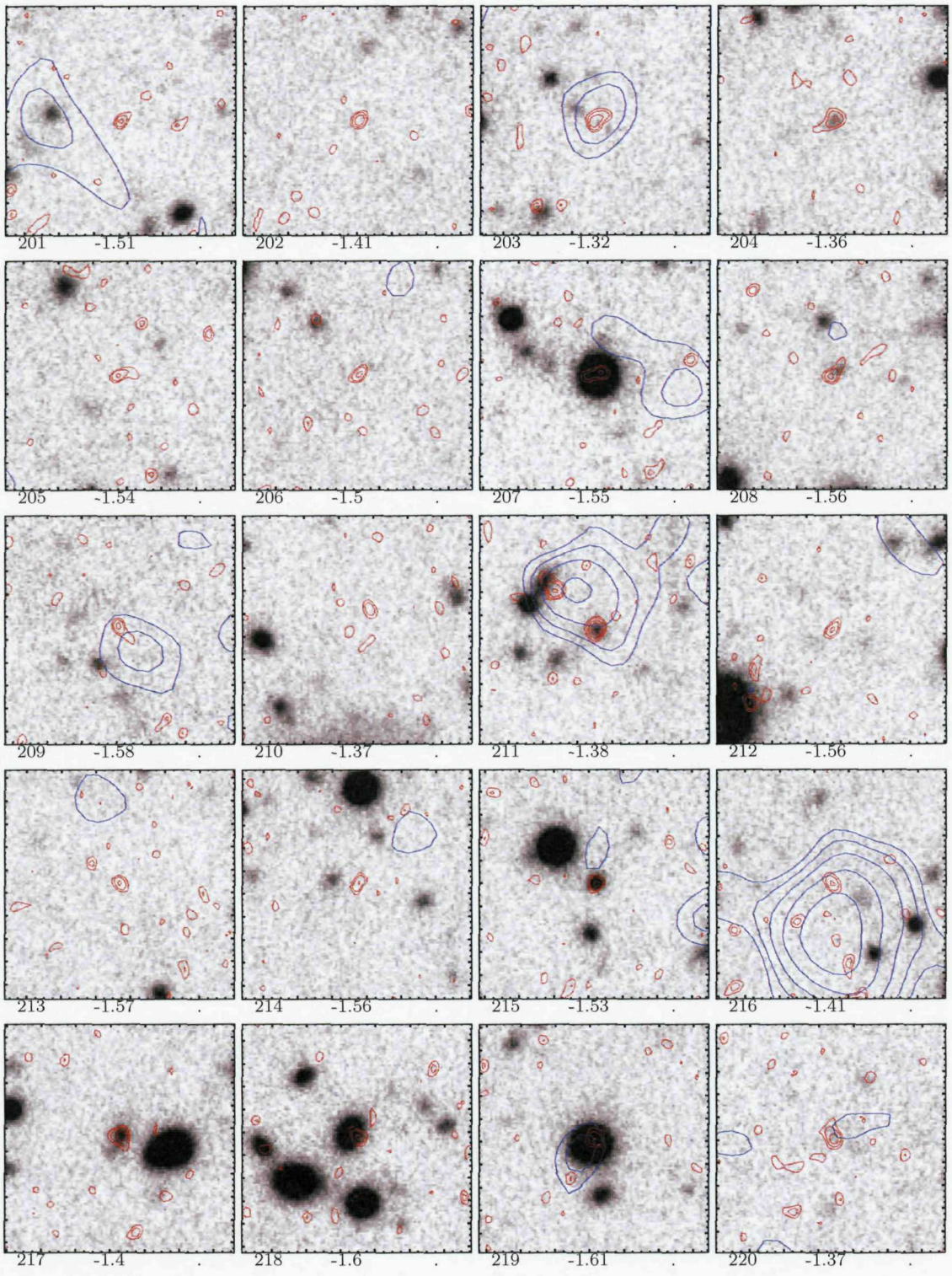
201 -1.51
202 -1.41
203 -1.32
204 -1.36
205 -1.54
206 -1.5
207 -1.55
208 -1.56
209 -1.58
210 -1.37
211 -1.38
212 -1.56
213 -1.57
214 -1.56
215 -1.53
216 -1.41
217 -1.4
218 -1.6
219 -1.61
220 -1.37

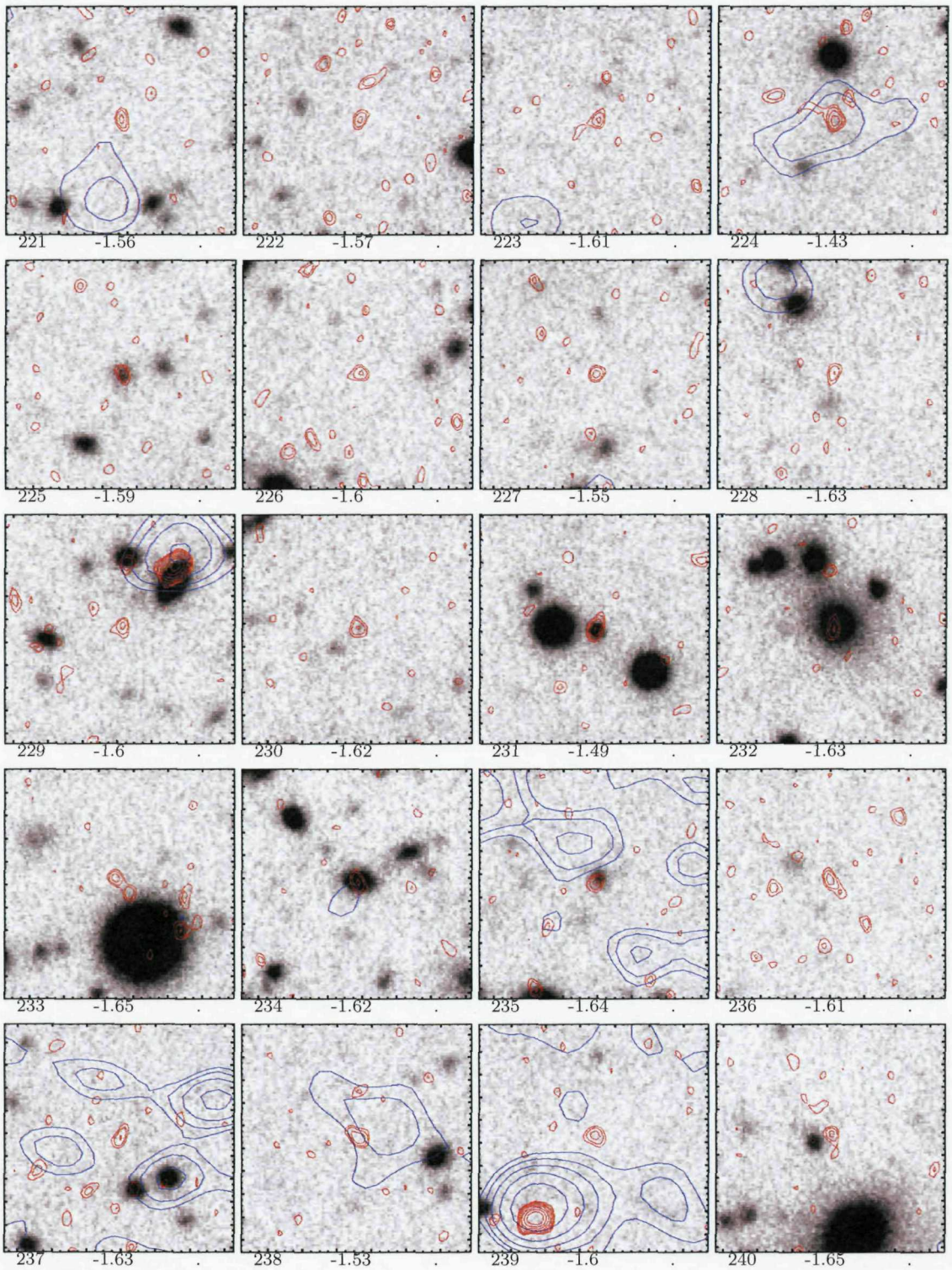
221 -1.56 .
222 -1.57 .
223 -1.61 .
224 -1.43 .
225 -1.59 .
226 -1.6 .
227 -1.55 .
228 -1.63 .
229 -1.6 .
230 -1.62 .
231 -1.49 .
232 -1.63 .
233 -1.65 .
234 -1.62 .
235 -1.64 .
236 -1.61 .
237 -1.63 .
238 -1.53 .
239 -1.6 .
240 -1.65 .

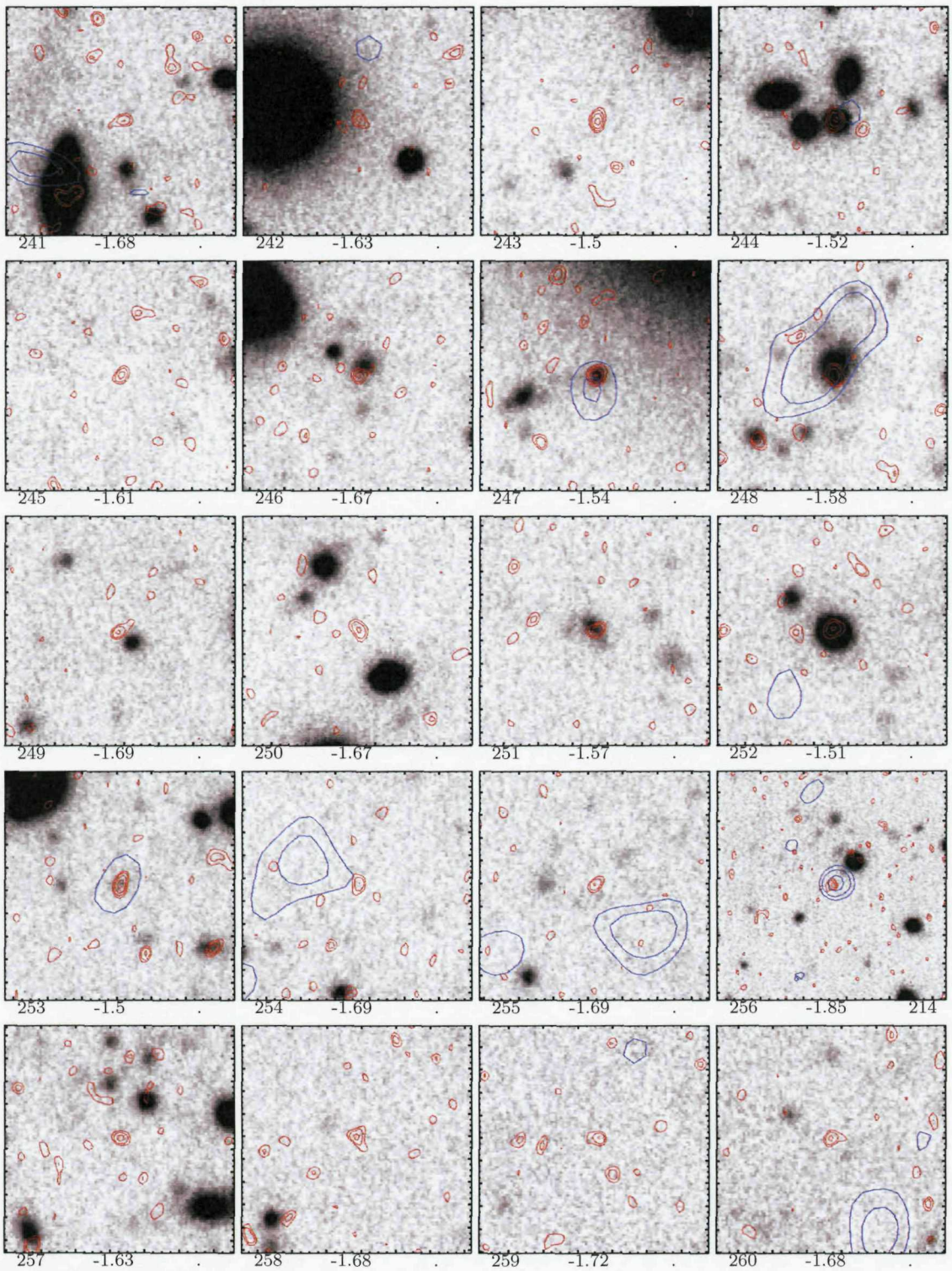
241 -1.68 .
242 -1.63 .
243 -1.5 .
244 -1.52 .
245 -1.61 .
246 -1.67 .
247 -1.54 .
248 -1.58 .
249 -1.69 .
250 -1.67 .
251 -1.57 .
252 -1.51 .
253 -1.5 .
254 -1.69 .
255 -1.69 .
256 -1.85 214
257 -1.63 .
258 -1.68 .
259 -1.72 .
260 -1.68 .

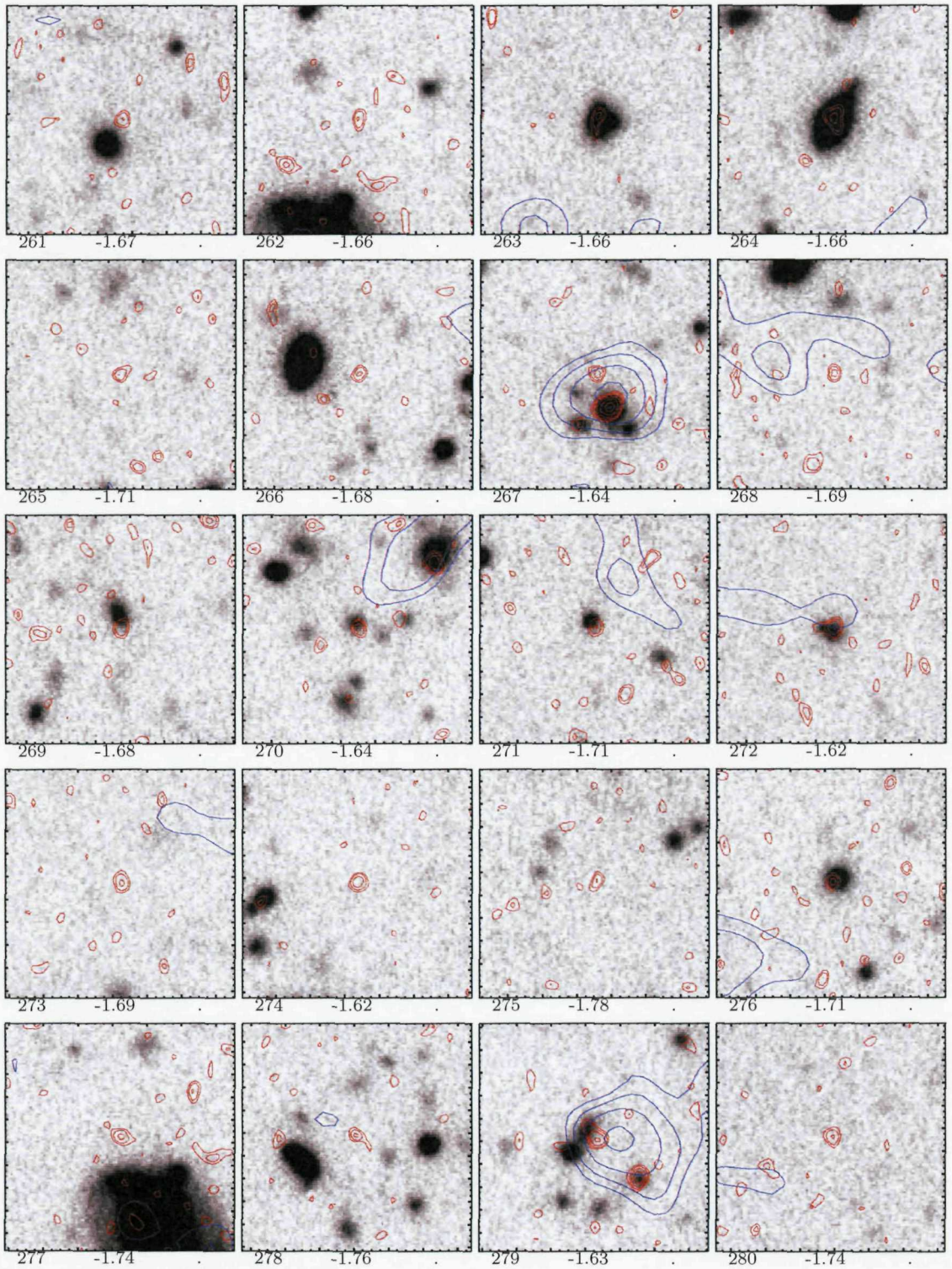
261 -1.67 .
262 -1.66 .
263 -1.66 .
264 -1.66 .
265 -1.71 .
266 -1.68 .
267 -1.64 .
268 -1.69 .
269 -1.68 .
270 -1.64 .
271 -1.71 .
272 -1.62 .
273 -1.69 .
274 -1.62 .
275 -1.78 .
276 -1.71 .
277 -1.74 .
278 -1.76 .
279 -1.63 .
280 -1.74 .

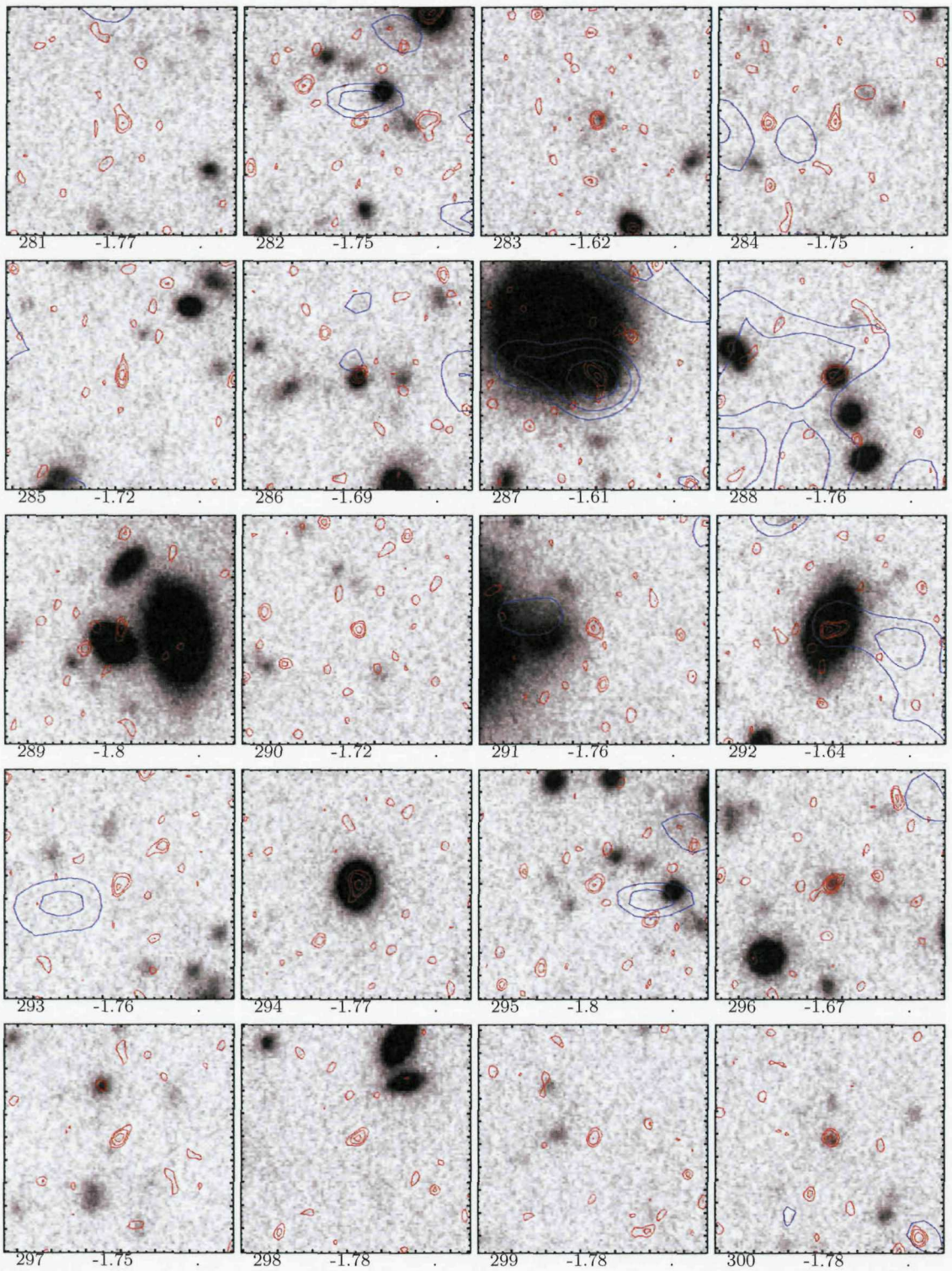
281 -1.77 .
282 -1.75 .
283 -1.62 .
284 -1.75 .
285 -1.72 .
286 -1.69 .
287 -1.61 .
288 -1.76 .
289 -1.8 .
290 -1.72 .
291 -1.76 .
292 -1.64 .
293 -1.76 .
294 -1.77 .
295 -1.8 .
296 -1.67 .
297 -1.75 .
298 -1.78 .
299 -1.78 .
300 -1.78 .

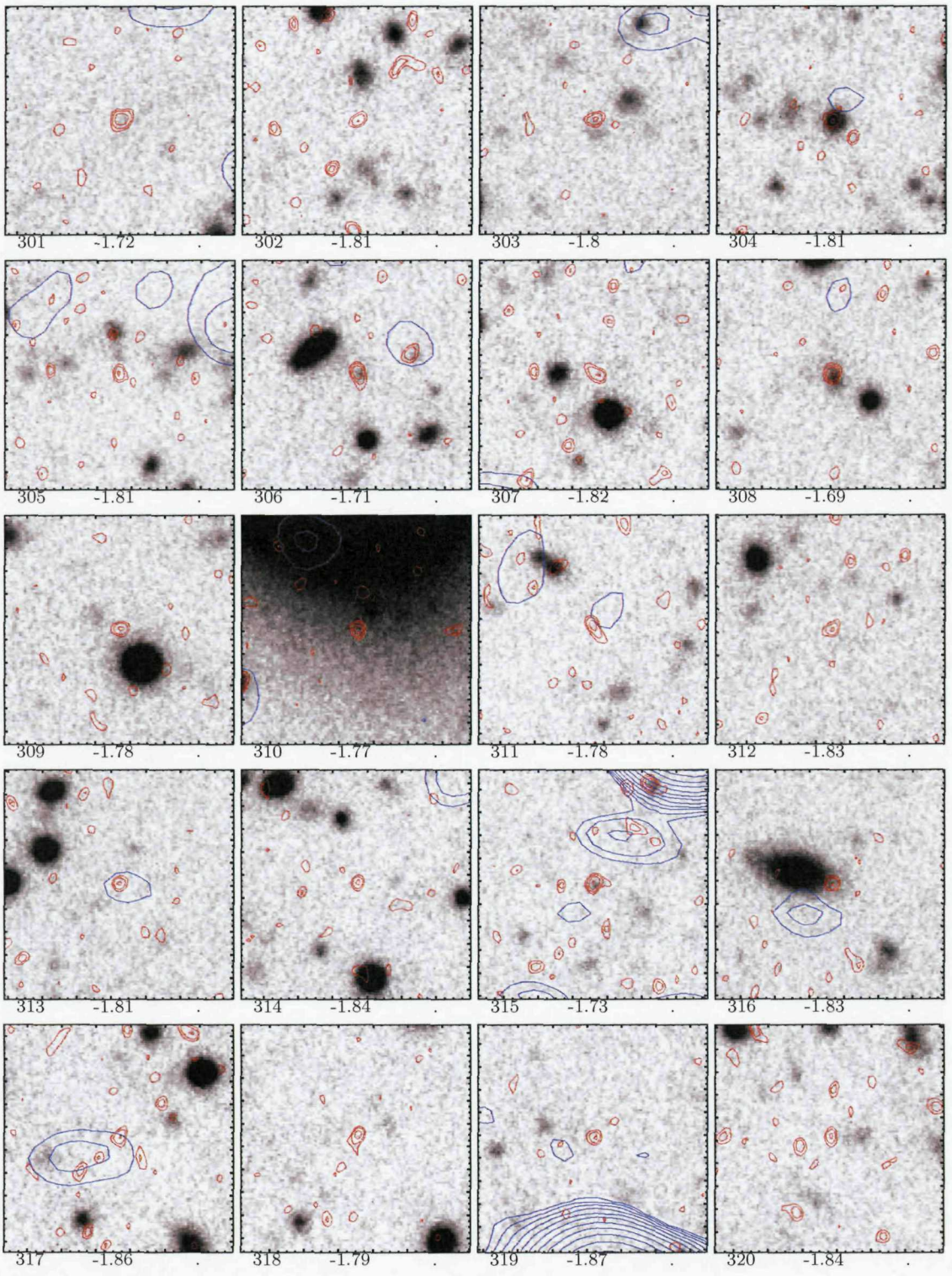
301 -1.72 .
302 -1.81 .
303 -1.8 .
304 -1.81 .
305 -1.81 .
306 -1.71 .
307 -1.82 .
308 -1.69 .
309 -1.78 .
310 -1.77 .
311 -1.78 .
312 -1.83 .
313 -1.81 .
314 -1.84 .
315 -1.73 .
316 -1.83 .
317 -1.86 .
318 -1.79 .
319 -1.87 .
320 -1.84 .

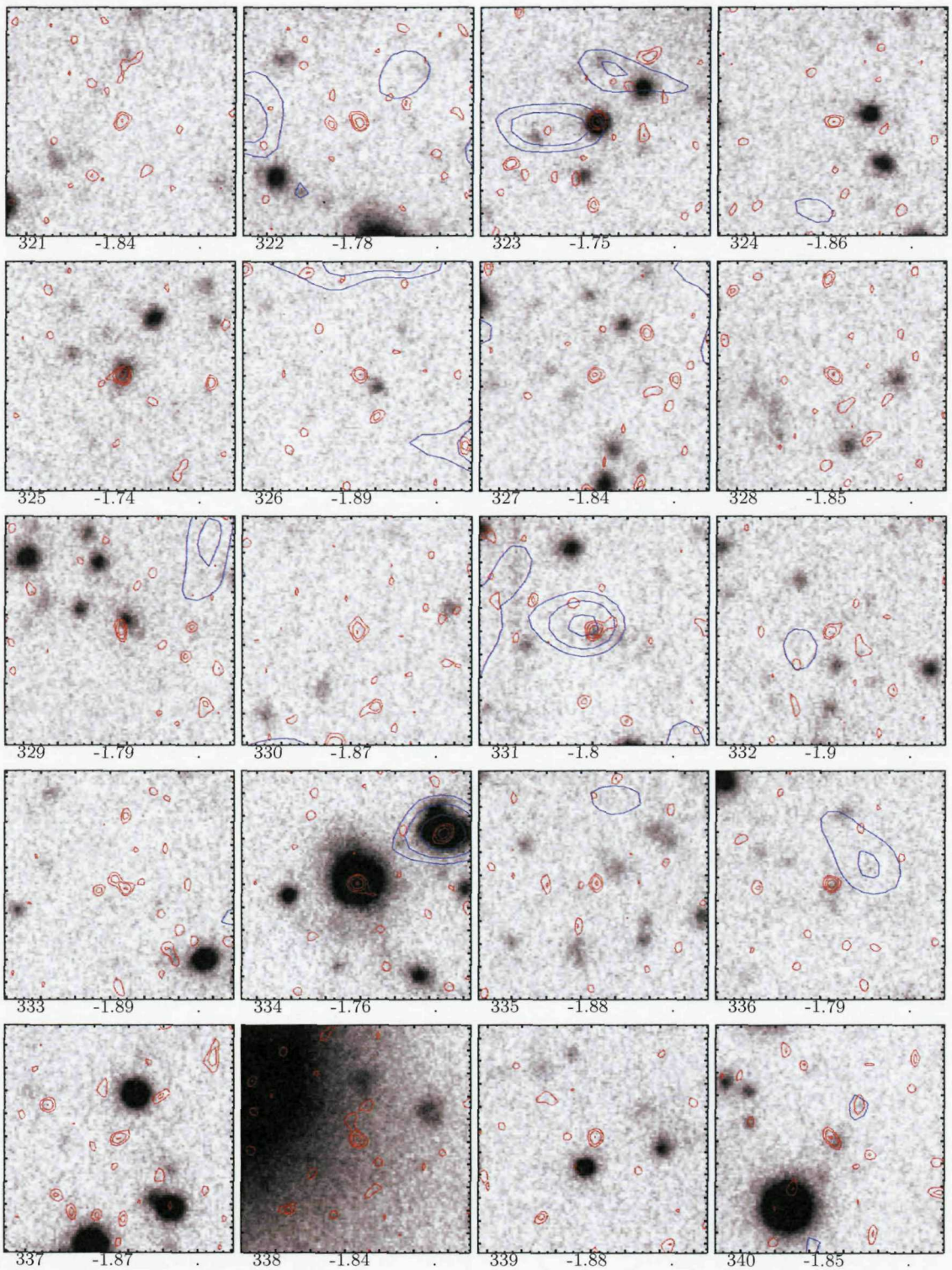
321 -1.84 .
322 -1.78 .
323 -1.75 .
324 -1.86 .
325 -1.74 .
326 -1.89 .
327 -1.84 .
328 -1.85 .
329 -1.79 .
330 -1.87 .
331 -1.8 .
332 -1.9 .
333 -1.89 .
334 -1.76 .
335 -1.88 .
336 -1.79 .
337 -1.87 .
338 -1.84 .
339 -1.88 .
340 -1.85 .

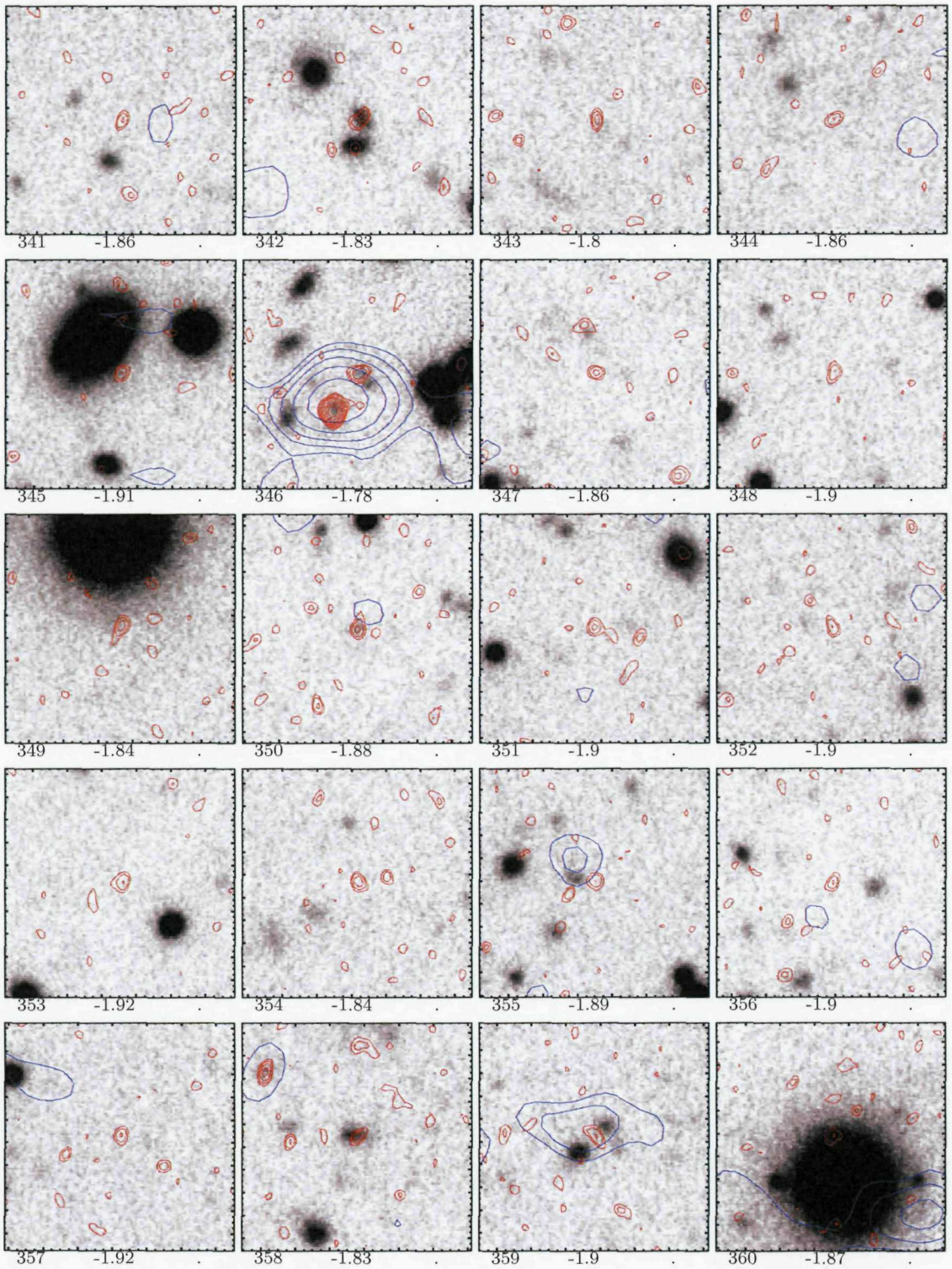
341 -1.86 .
342 -1.83 .
343 -1.8 .
344 -1.86 .
345 -1.91 .
346 -1.78 .
347 -1.86 .
348 -1.9 .
349 -1.84 .
350 -1.88 .
351 -1.9 .
352 -1.9 .
353 -1.92 .
354 -1.84 .
355 -1.89 .
356 -1.9 .
357 -1.92 .
358 -1.83 .
359 -1.9 .
360 -1.87 .

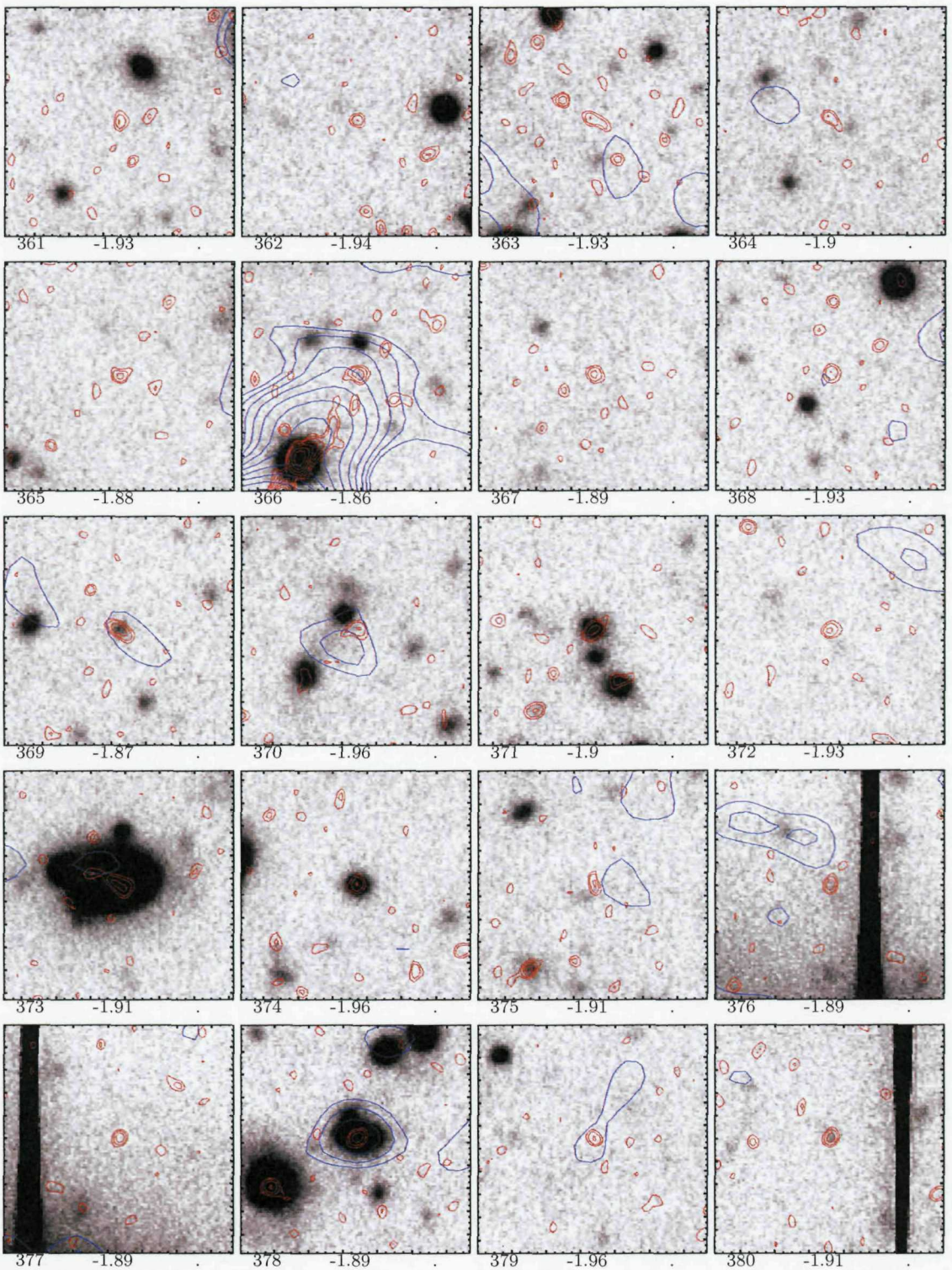
361 -1.93 .
362 -1.94 .
363 -1.93 .
364 -1.9 .
365 -1.88 .
366 -1.86 .
367 -1.89 .
368 -1.93 .
369 -1.87 .
370 -1.96 .
371 -1.9 .
372 -1.93 .
373 -1.91 .
374 -1.96 .
375 -1.91 .
376 -1.89 .
377 -1.89 .
378 -1.89 .
379 -1.96 .
380 -1.91 .

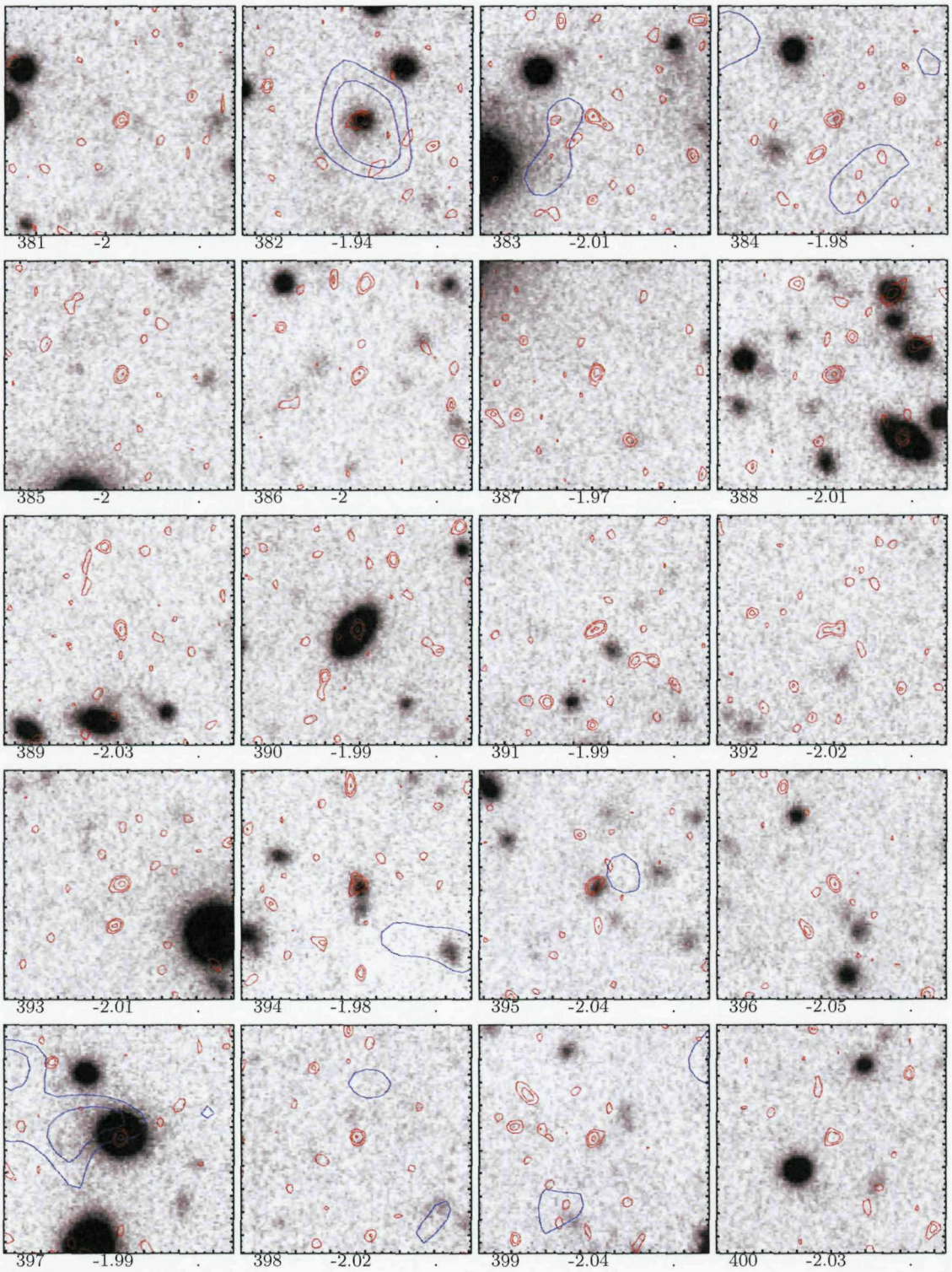
381 -2 .
382 -1.94 .
383 -2.01 .
384 -1.98 .
385 -2 .
386 -2 .
387 -1.97 .
388 -2.01 .
389 -2.03 .
390 -1.99 .
391 -1.99 .
392 -2.02 .
393 -2.01 .
394 -1.98 .
395 -2.04 .
396 -2.05 .
397 -1.99 .
398 -2.02 .
399 -2.04 .
400 -2.03 .

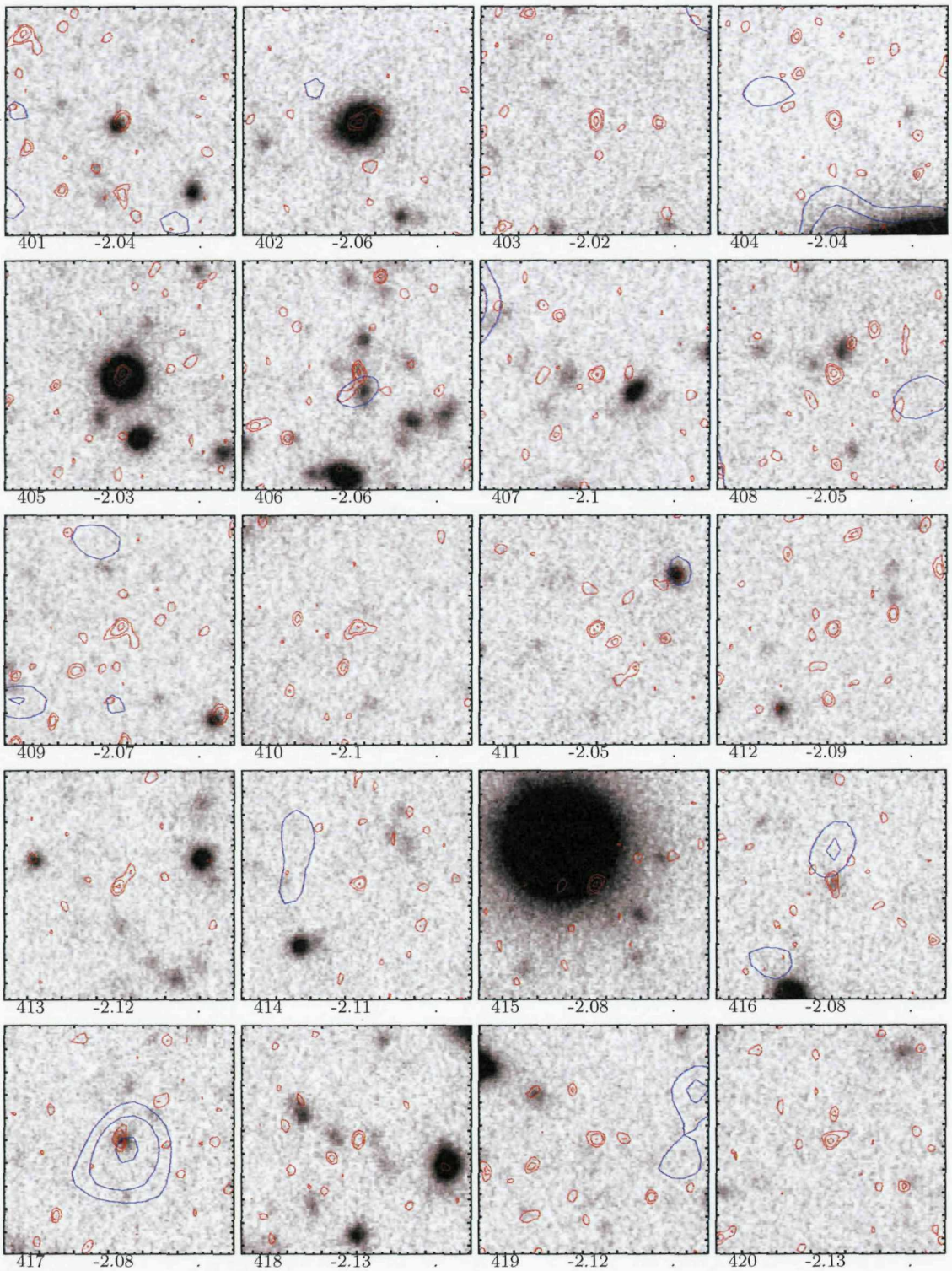
401 -2.04 .
402 -2.06 .
403 -2.02 .
404 -2.04 .
405 -2.03 .
406 -2.06 .
407 -2.1 .
408 -2.05 .
409 -2.07 .
410 -2.1 .
411 -2.05 .
412 -2.09 .
413 -2.12 .
414 -2.11 .
415 -2.08 .
416 -2.08 .
417 -2.08 .
418 -2.13 .
419 -2.12 .
420 -2.13 .

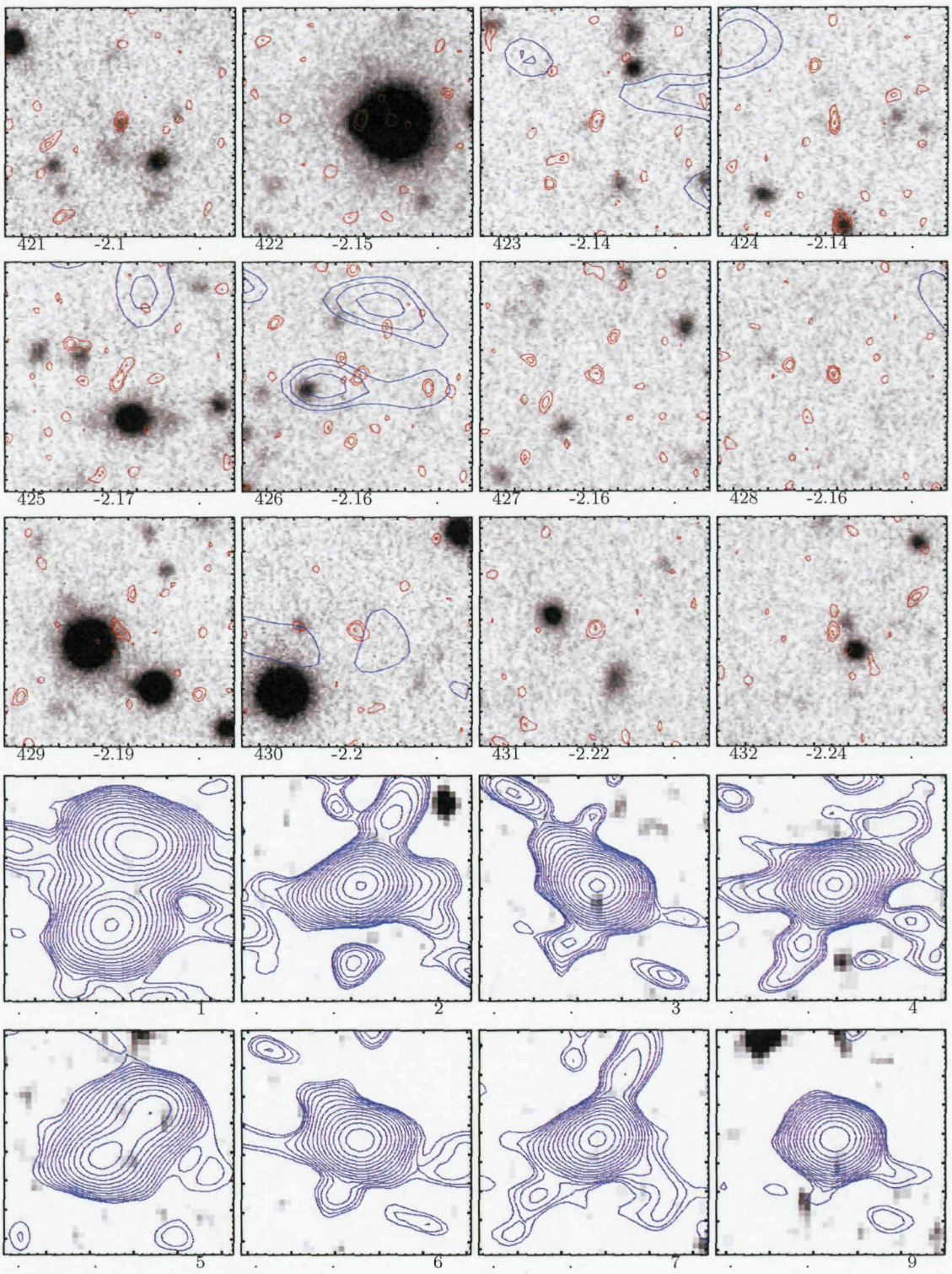
421 -2.1 .
422 -2.15 .
423 -2.14 .
424 -2.14 .
425 -2.17 .
426 -2.16 .
427 -2.16 .
428 -2.16 .
429 -2.19 .
430 -2.2 .
431 -2.22 .
432 -2.24 .
. . 1
. . 2
. . 3
. . 4
. . 5
. . 6
. . 7
. . 9

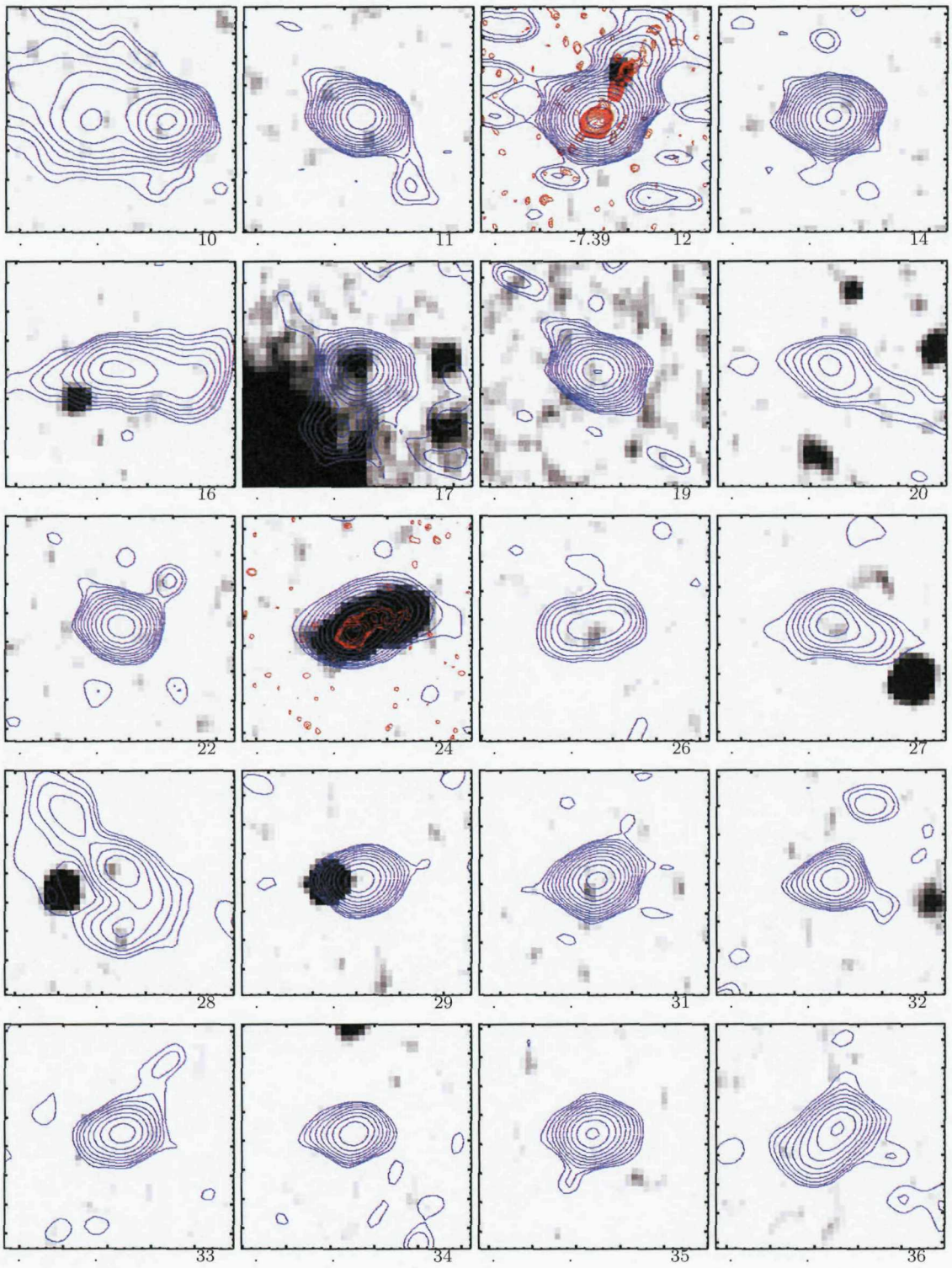
10
11
-7.39
12
14
16
17
19
20
22
24
26
27
28
29
31
32
33
34
35
36

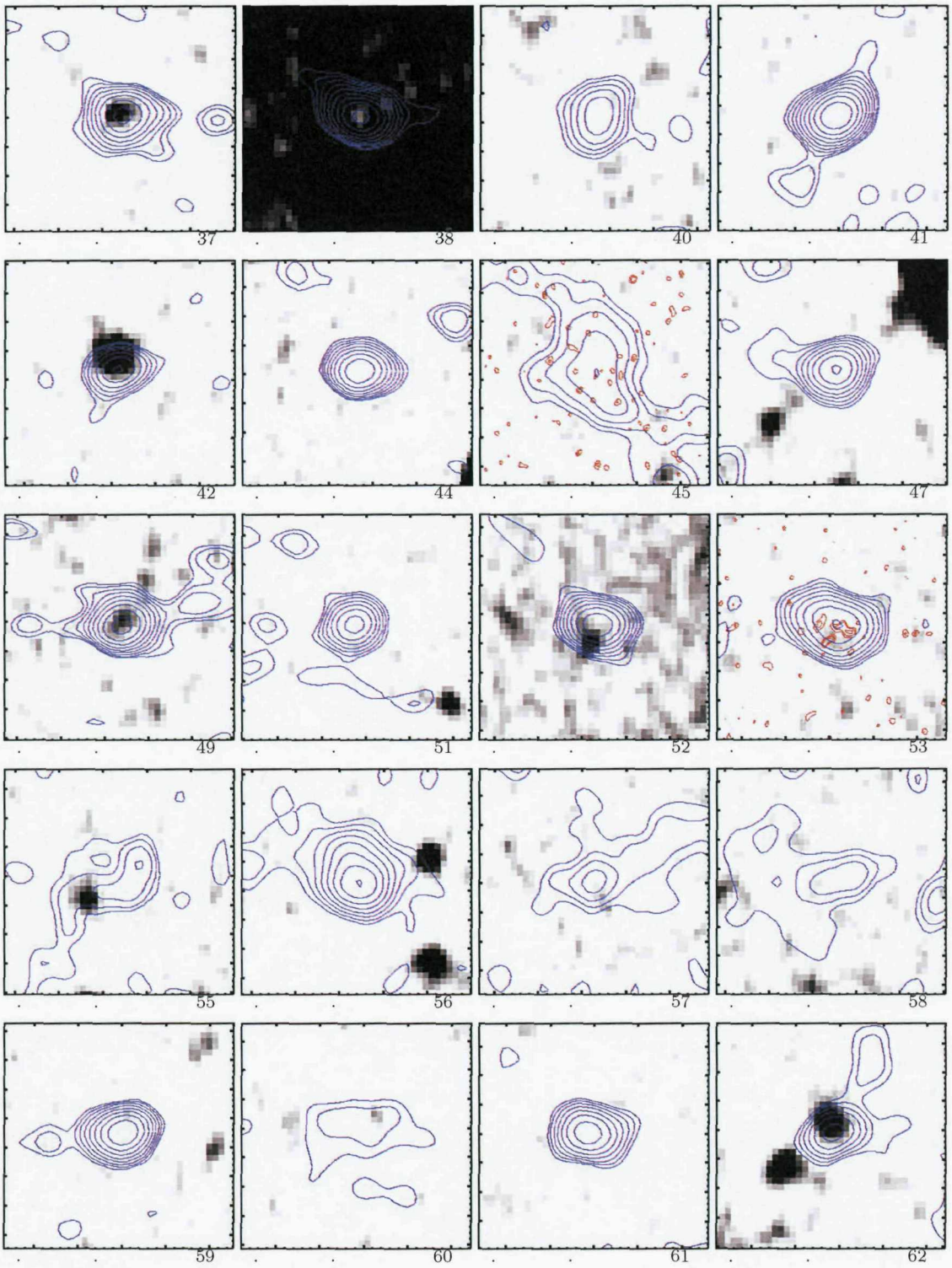
37
38
40
41
42
44
45
47
49
51
52
53
55
56
57
58
59
60
61
62

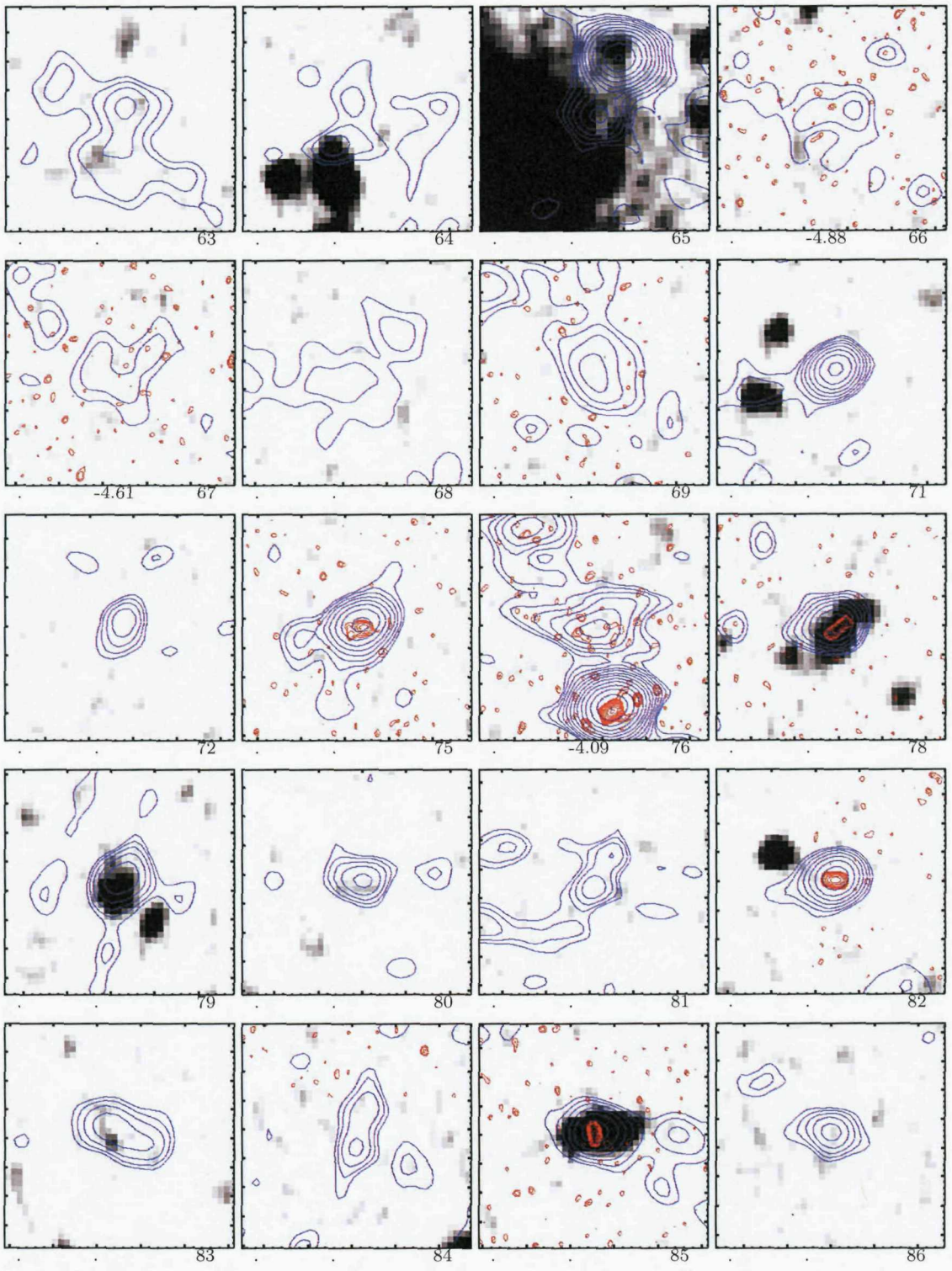
63
64
65
-4.88
66
-4.61
67
68
69
71
72
75
-4.09
76
78
79
80
81
82
83
84
85
86

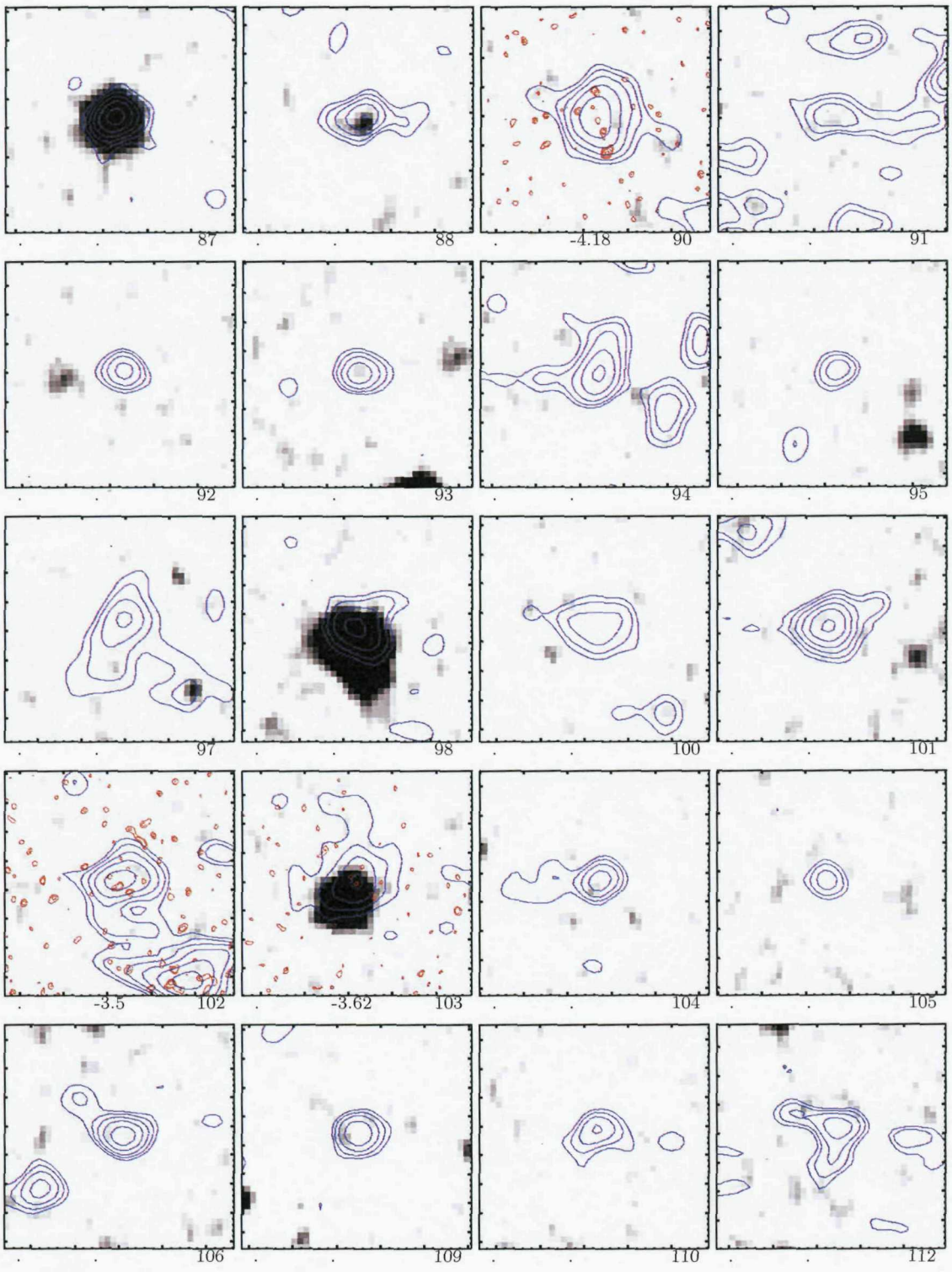
87
88
-4.18
90
91
92
93
94
95
97
98
100
101
-3.5
102
-3.62
103
104
105
106
109
110
112

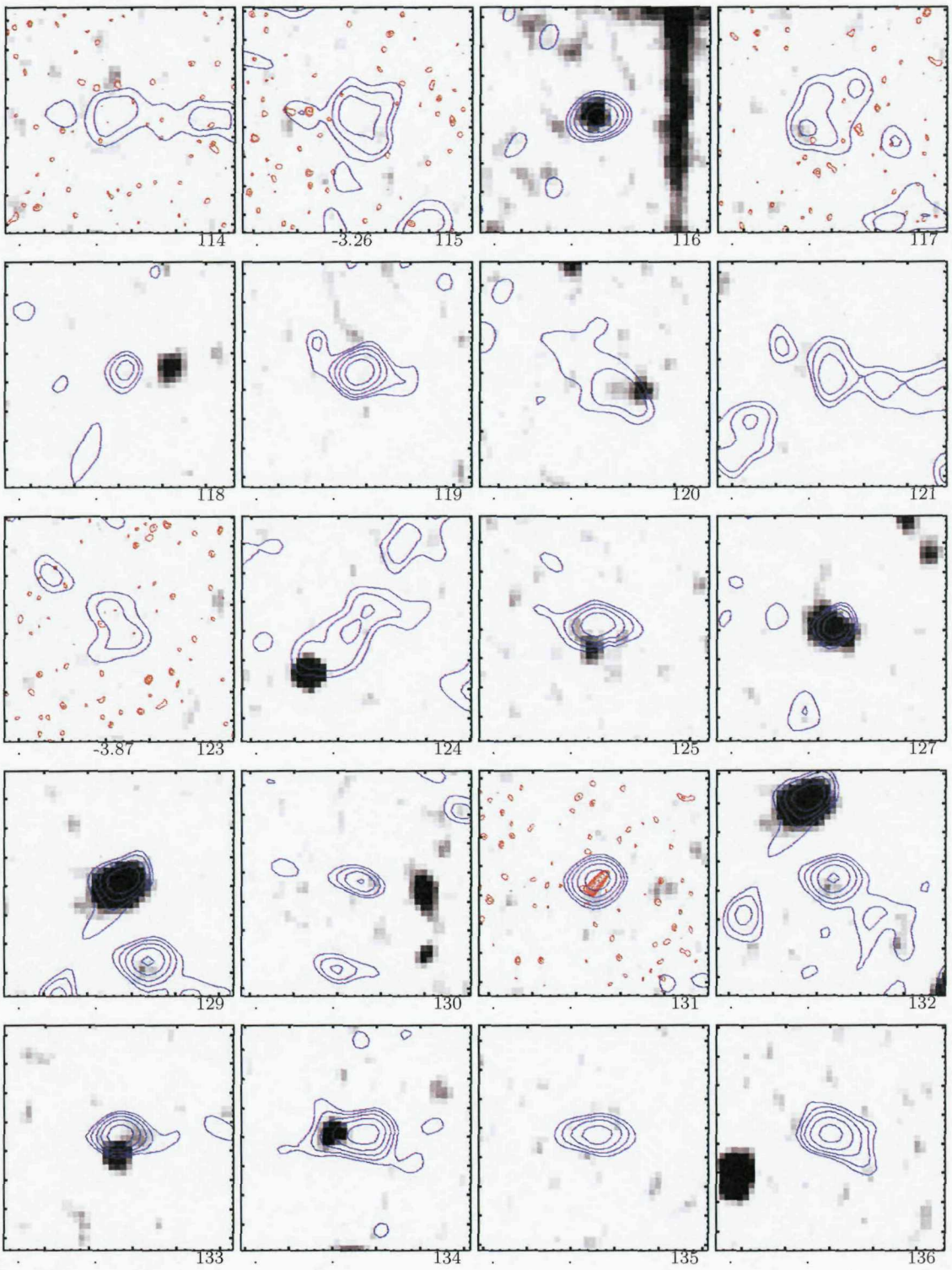
114
-3.26
115
116
117
118
119
120
121
-3.87
123
124
125
127
129
130
131
132
133
134
135
136

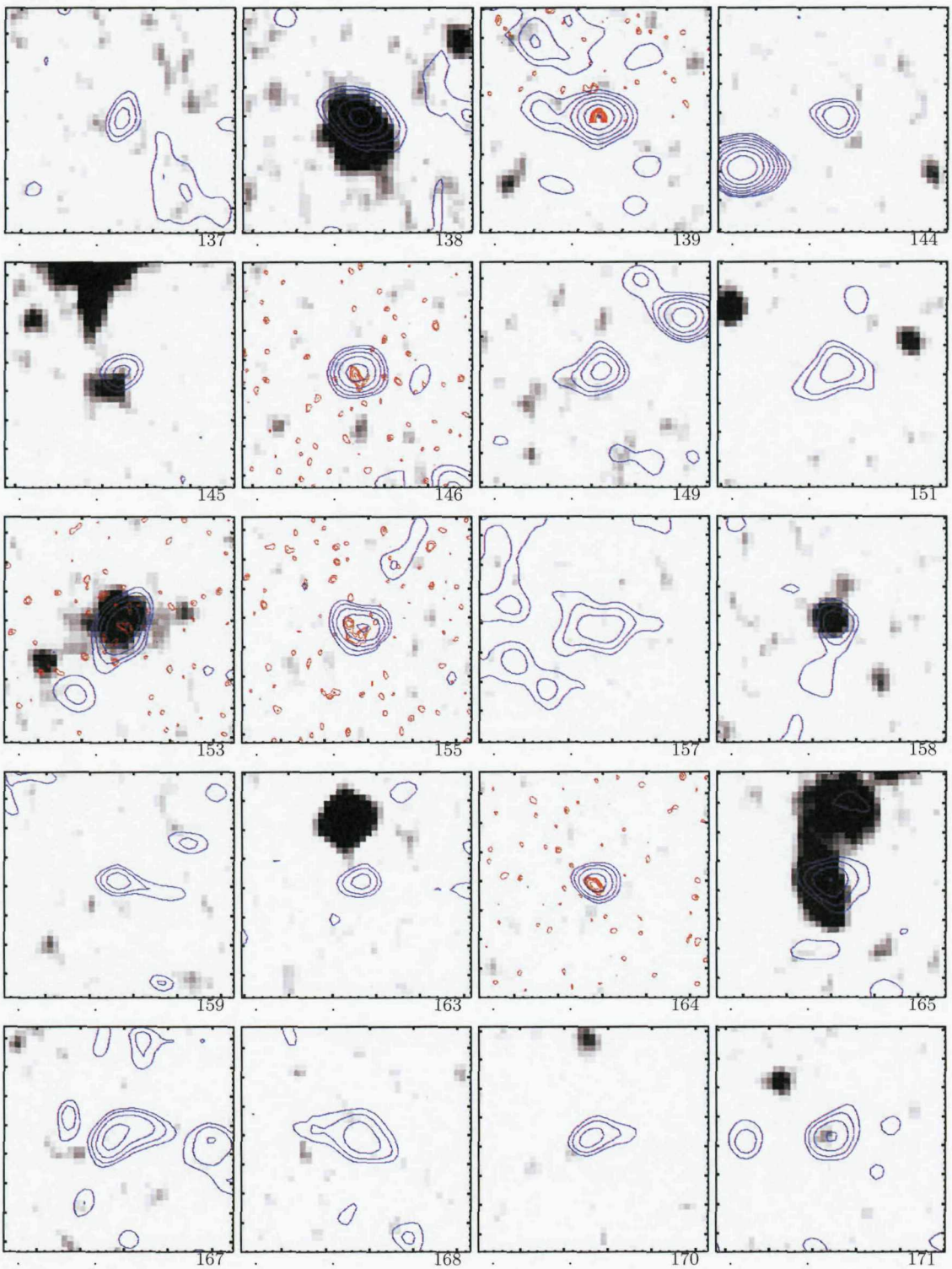
137
138
139
144
145
146
149
151
153
155
157
158
159
163
164
165
167
168
170
171

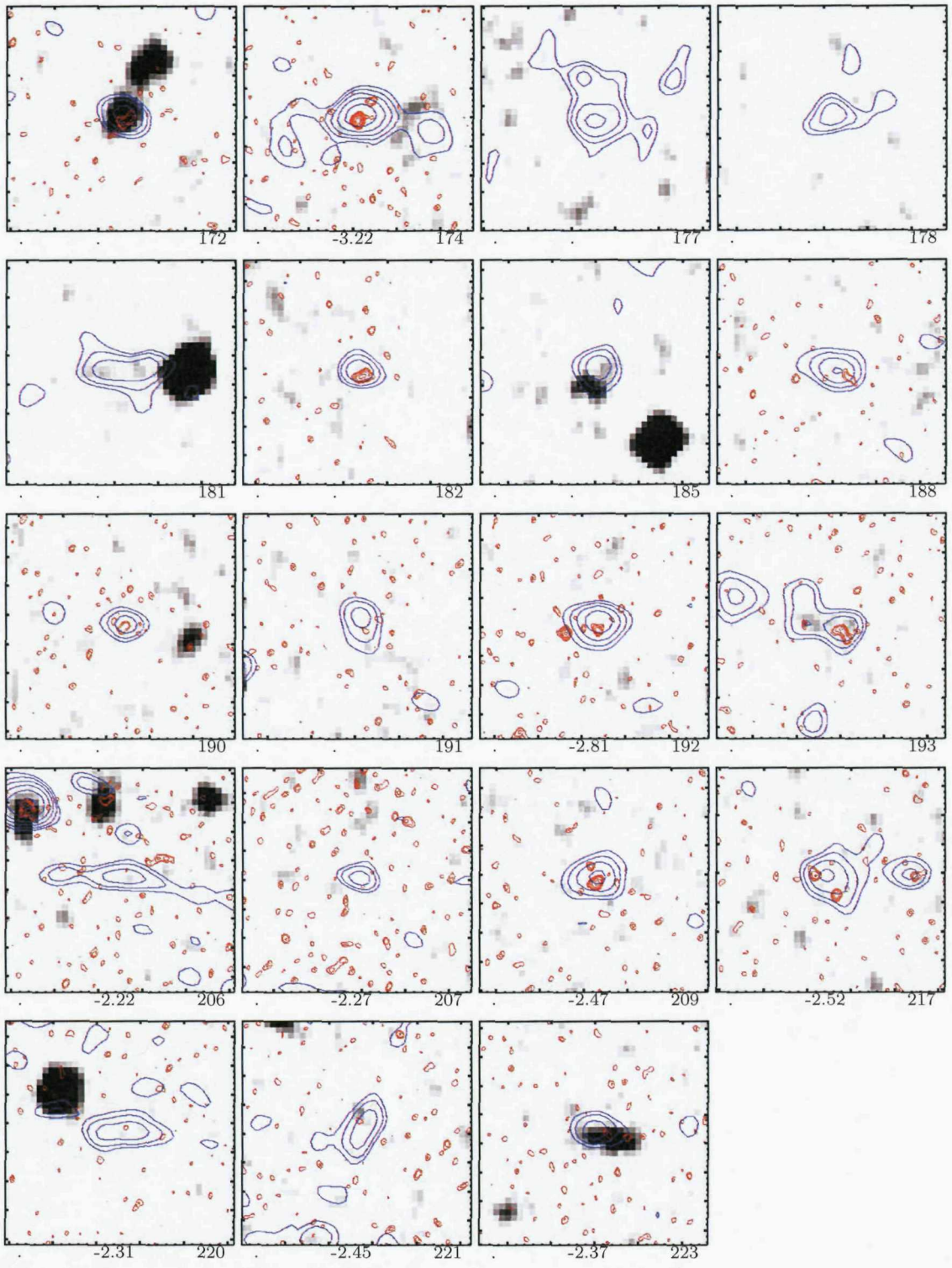
172
-3.22
174
177
178
181
182
185
188
190
191
-2.81
192
193
-2.22
206
-2.27
207
-2.47
209
-2.52
217
-2.31
220
-2.45
221
-2.37
223

Bibliography

Afonso J. et al., 2005, ApJ, 624, 135

Anton S. et al., 2004, MNRAS, 120A

Antonucci R.J., Ulvestad J.S., 1985, ApJ, 294, 158

Antonucci R., 1993, ARA&A, 31, 473

Baars J. W. M., Genzel R., Pauliny-Toth I. I. K., Witzel A., 1977, A&A, 61, 99

Becker R. H. et al., 2001, AJ, 122, 2850

Benn C.R., Rowan-Robinson M., McMahon R.G., Broadhurst T.J., Lawrence A., 1993, MNRAS, 263, 98

Bertin E., Arnouts S., 1996, A&AS, 117, 393

Biggs A. D., Ivison R. J., 2006, MNRAS, 371, 963

Blandford R., Eichler, D., 1987, Physical Reports, 154, 1

Bondi M. et al., 2003, A&A, 403, 857

Bondi M. et al., 2007, A&A, 463, 519

Bothun G., 1998, Modern Cosmological Observations and Problems. Taylor and Francis.

Bouwens R. J., Illingworth G. D., Blakeslee J. P., Franx, M., 2006, ApJ, 653, 53

Böttcher et al., 2001, ApJ, 553, 683

Bridle A. H., Perley R. A., 1984, ARA&A, 22, 319

Briggs D. S., 1995, Bulletin of the American Astronomical Society, 27, 1444

Brodie J., Bowyer S., Tennant A., 1987, ApJ, 318, 175

Caccianiga A,. Marcha M.J., Anton S., Mack K.-H., Neeser M.J., 2002, MNRAS, 329, 877

Ciliegi P., Zamorani G., Hasinger G., Lehmann I., Szokoly G., Wilson G., 2003, A&A, 398, 901

Clark B. G., 1980, A&A, 89, 377

Comastri A. et al., 2002a, ApJ, 571, 771

Comastri A., et al. 2002b, Oral contribution to "New Visions of the X-ray Universe in the XMM-Newton and Chandra Era", astro-ph 0203019v1

Condon J. J., 1984, ApJ, 284, 44

Condon J. J., 1989, ApJ, 338, 13

Condon J. J., 1992, ARA&A, 30, 575

Condon J. J., Cotton W. D., Greisen E. W., Yin Q. F., Perley R. A., Taylor G. B., Broderick J. J., 1998, AJ, 115, 1693

Condon J. J., Cotton W. D., Broderick J. J., 2002, AJ, 124, 675

Condon J. J., Cotton W. D., Yin Q. F., Shupe D. L., Storrie-Lombardi L. J., Helou G., Soifer B. T., Werner M. W., 2003, AJ, 125, 2411

De Breuck C., Hunstead R. W., Sadler E. M., Rocca-Volmerange B., Klamer I., 2004, MNRAS, 347, 837

Dickey J.M., Lockman F.J., 1990, ARA&A, 28, 215

Di Matteo et al., 1999, MNRAS, 305, 492

Dressler A., Shectman S.A., 1987, ApJ, 94, 899

Dunlop J.S., Peacock J.A., 1990, MNRAS, 247, 19

Dwelly T., Page M. J., Loaring N. S., Mason K. O., McHardy I., Gunn, K. Sasseen T., 2005, MNRAS, 360, 1426

Eddington A., 1913, MNRAS, 73, 359

Elvis M. et al., 1994, ApJS, 15, 1

Fadda D., et al., 2006, AJ, 131, 2859

Fanaroff B. L., Riley J. M., 1974, MNRAS, 167, 31P

Fazio G.G. et al., 2004, ApJS, 154, 10

Fomalont E. B., Kellermann K. I., Cowie L. L., Capak P., Barger A. J., Partridge R. B., Windhorst R. A., Richards E. A., 2006, ApJS, 167, 103

Frayer D. T. et al., 2006, AJ, 131, 250

Garn T., Green D. A., Hales S. E. G., Riley J. M., Alexander P., 2007, MNRAS, 376, 1251

Georgantopoulos I., Georgakakis A., 2005, MNRAS, 358, 131

George I.M., Warwick R.S. Bromage G.E., 1988, MNRAS, 232, 793

Gruppioni C., Zamorani G., de Ruiter H. R., Parma P., Mignoli M., Lari C., 1997, MNRAS, 286, 470

Gruppioni C. et al., 1999, MNRAS, 305, 297

Gunn J. E., Peterson B. A., 1965, ApJ, 142, 1633

Gunn K. F. et al., 2001, MNRAS, 324, 305

Helou G., Bicay M. D., 1993, ApJ, 415, 93

Hewish A., Bell S. J., Pilkington J. D., Scott P. F., Collins R. A., 1968, Nat, 217, 709

Högbom J. A., 1974, A&AS, 15, 417

Hogg D. W., 1999, ArXiv Astrophysics e-prints, arXiv:astro-ph/9905116

Hopkins A. M., Mobasher B., Cram L., Rowan-Robinson M., 1998, MNRAS, 296, 839

Hopkins A. M., Afonso J., Chan B., Cram L. E., Georgakakis A., Mobasher B., 2003, AJ, 125, 465

Hopkins A. M., 2004, ApJ, 615, 209

Hornschemeier A. E. et al., 2000, ApJ, 541, 49

Hornschemeier A. E. et al., 2001, ApJ, 554, 742

Huynh M. T., Jackson C. A., Norris R. P., Prandoni I., 2005, AJ, 130, 1373

Huynh M. T., Jackson C. A., Norris R. P., 2007, AJ, 133, 1331

Jansky K.G., 1933, Nat, 132, 66

Jarvis M. J., Rawlings S., 2004, in Carilli C. and Rawlings S., eds, New Astronomy Review, Vol. 48, Science with the Square Kilometer Array. Elsevier, Amsterdam, p.1173

Jiang L., Fan X., Ivezić Ž., Richards G. T., Schneider D. P., Strauss M. A., Kelly B. C., 2007, ApJ, 656, 680

Juneau S. et al., 2005, ApJL, 619, L135

Huynh M.T., Jackson C.A., Norris R.P., Prandoni I., 2005, AJ, 130, 1373

Katgert J.K., 1979, A&A, 73, 107

Khachikian E. Y., Weedman D. W., 1974, ApJ, 192, 581

Lacy M. et al., 2005, ApJS, 161, 41

Le Fevre O., Crampton D., Felenbok P., Monnet G., 1994, A&A, 282,325

Lilly S. J., Le Fevre O., Hammer F., Crampton D., 1996, ApJL, 460, L1

Loaring N.S. et al., 2005, MNRAS, 362, 137

Longair M. S., 1966, MNRAS, 133, 421

Madau P., Ferguson H. C., Dickinson M. E., Giavalisco M., Steidel C. C., Fruchter A., 1996, MNRAS, 283, 1388

Marcha M.J.M. and Browne I.W.A., 1995. MNRAS 275, 951

Matthews T. A., Sandage A. R., 1963, ApJ, 138, 30

M^{c}Hardy I.M. et al., 1998, MNRAS, 295, 641

M^{c}Hardy I.M. et al., 2003, MNRAS, 342,802

Miyazaki S., Sekiguchi M., Imi K., Okada N., Nakata F., Komiyama Y., 1998, Proc. SPIE Vol. 3355, p. 363, Optical Astronomical Instrumentation, Ed Sandro D'Odorico.

Mushotzky R. F., Cowie L. L., Barger A. J., Arnaud K. A., 2000, Nat, 404, 459

Muxlow T. W. B. et al., 2005, MNRAS, 358, 1159

Norris R. P. et al., 2005, AJ, 130, 1358

Norris R. P. et al., 2006, AJ, 132, 2409

O'dell S. L. et al., 1988, ApJ, 326, 668

Page M. J. et al., 2006, MNRAS, 369, 156

Peterson B.M., 1997, An Introduction to Active Galactic Nuclei. Cambridge University Press

Peacock J.A., 1998, Cosmological Physics. Cambridge University Press.

Polletta M., Courvoisier T. J.-L., 2000, in Boller T., ed, New Astronomy Review, Vol. 44, p.551

Prandoni I., Gregorini L., Parma P., de Ruiter H. R., Vettolani G., Wieringa M. H., Ekers R. D., 2000a, A&AS, 146, 31

Prandoni I., Gregorini L., Parma P., de Ruiter H. R., Vettolani G., Wieringa M. H., Ekers R. D., 2000b, A&AS, 146, 41

Prandoni I., Gregorini L., Parma P., de Ruiter H. R., Vettolani G., Wieringa M. H., Ekers R. D., 2001, A&A, 365, 392

Prandoni I., Parma P., Wieringa M. H., de Ruiter H. R., Gregorini L., Mignano A., Vettolani G., Ekers R. D., 2006, A&A, 457, 517

Richards E. A., 2000, ApJ, 533, 611

Rieke G.H., et al., 2004, ApJS, 154, 25

Rowan-Robinson M., 1970, MNRAS, 149, 365

Rowan-Robinson M., Benn C. R., Lawrence A., McMahon R. G., Broadhurst T. J., 1993, MNRAS, 263, 123

Rowan-Robinson M., 2000, Cosmology Third Edition. Oxford University Press

Ryle M., Vonberg D. D. 1946, Nature, 158, 462

Sadler E.M. et al., 2002, MNRAS, 329, 227

Salpeter E. E., 1964, ApJ, 140, 796

Saunders W., Rowan-Robinson M., Lawrence A., Efstathiou G., Kaiser N., Ellis R.S., Frenk C.S., 1990, MNRAS, 242, 318

Schinnerer E. et al., 2004, AJ, 128, 1974

Schmidt M., 1963, Nat, 197, 1040

Schwab F. R., 1984, AJ, 89, 1076

Searle L., Zinn R., 1978, ApJ, 225, 357

Seyfert C. K., 1943, ApJ, 97, 28

Seymour N., 2002, PhD Thesis, University of Southampton

Seymour N., McHardy, I.M., Gunn, 2004, MNRAS, 352, 131

Shakura N. I., Syunyaev R. A., 1973, A&A, 24, 337

Simpson C. et al., 2006, MNRAS, 372, 741

Snellen I. A. G., Lehnert M. D., Bremer M. N., Schilizzi R. T., 2002, MNRAS, 337, 981

Spergel D.N. et al., 2003, ApJS, 148, 175

Stern D. et al., 2005, ApJ, 631, 163

Taylor G. B., Carilli C. L., Perley A. R., eds, 1999, ASP Conf. Ser. Vol. 180, Synthesis Imaging in Radio Astronomy II. Astron. Soc. Pac.,San Francisco

Thompson T. A., Quataert E., Waxman E., Murray N., Martin C. L., 2006, ApJ, 645, 186

Tingay S. J., Edwards P. G., Tzioumis A. K., 2003, MNRAS, 346, 327

Ueda Y., Akiyama M., Ohta K., Miyaji T., 2003, ApJ, 598, 886

Urry C. M., Padovani P., 1995, PASP, 107, 803

Valentijn E.A., 1980, A&A, 89, 234

Warwick R. S., George I. M., McHardy I., Pounds K. A., 1986, MNRAS, 219, 39

Windhorst R.A., Miley G.K., Owen F.N., Kron R.G., Koo D.C., 1985, ApJ, 289, 494

Windhorst R., Mathis D., Neuschaefer L., 1990, in Kron R.G., ed, ASP Conf. Ser. Vol. 10, Evolution of the Universe of Galaxies. Astron. Soc. Pac.,San Francisco, p.389

White R. L., Becker R. H., Helfand D. J., Gregg M. D., 1997, ApJ, 475, 479

Yuan F., Narayan R., 2004, ApJ, 612, 724

Zheng Z., Coil A. L., Zehavi I., 2007, ApJ, 667, 760